Parameterisation of underwater light fields in the Arctic Ocean and associated impact on biological processes

Stacey Connan-McGinty
Department of Physics
University of Strathclyde, Glasgow

2023

A thesis submitted to the University of Strathclyde in accordance with the requirements for the degree of Doctor of Philosophy.

Declaration of Authenticity and Author's Rights

This thesis is the result of the author's original research. It has been composed by the author and has not been previously submitted for examination which has led to the award of a degree.

The copyright of this thesis belongs to the author under the terms of the United Kingdom Copyright Acts as qualified by University of Strathclyde Regulation 3.50. Due acknowledgement must always be made of the use of any material contained in, or derived from, this thesis.

Signed:

Date:

Abstract

Accurate characterisation of underwater light is an integral component in modelling the dynamics of marine ecosystems, particularly primary production and animal migration patterns. Existing methods of estimating light fields either rely on satellite data, *in situ* measurements or radiative transfer models that only operate when the sun is above the horizon. These methods are of limited use in Arctic waters, particular during Polar Night due to extended periods of extremely low light levels and prolonged periods when the sun remains below horizon. Estimating underwater light in the region is further hindered by the optical complexities introduced by widespread and seasonally varying snow and ice cover, and many current ecosystem models either simplify these under-ice light fields or excluding them entirely, potentially disregarding biologically significant light levels.

This work presents a model of spectrally resolved underwater light that demonstrates the ability to simulate light levels over the full year into the period of Polar Night and is validated by *in situ* data. Downwelling spectral irradiance in the photosynthetically active radiation (PAR, $400 - 700$nm) range is calculated in both open and ice-covered water columns and includes multiple reflection amplification effects of above surface irradiance between snow and cloud. Validation of downwelling broadband irradiance in open waters shows a mean absolute error of $<6\ \mu\mathrm{mol\,m^{-2}\,s^{-1}}$ over the water column and comparison of modelled to measured transmission through snow and ice shows a mean absolute error of 2% transmittance. During overcast conditions, multiple reflection amplification between snow and cloud induced an average increase of 65% in above surface downwelling irradiance. Application of the model on a Pan-Arctic scale in 2018 demonstrated the potential for >20% of above surface irradiance to penetrate through thin ice (<0.5m). When coupled to a broadband PAR model of primary production, model results showed the potential for under-ice light levels to be sufficiently high that under-ice productivity contributions may exceed 10% of total Pan-Arctic primary production in spring, and may reach saturation levels in summer, accounting for >20% of total productivity. In open waters, calculations of primary production were found to be highly sensitive to the parameterisation of the diffuse attenuation coefficient of light. Comparing the results of various light field models designed for use in the Arctic showed a factor 12 difference in calculated water column productivity when using output irradiances to drive a model of primary production. Comparing modelled underwater spectral irradiance to the diel vertical migration (DVM) patterns of Arctic krill in early spring 2018 showed that the spectral distribution of light may act as a trigger mechanism for DVM. Results appear to indicate that although diurnal changes in the magnitude of downwelling irradiance largely drives bulk migration patterns, the population of krill also responded to changes in the ratio of green to blue light, driven by changes in lunar and solar elevations, preferring to occupy regions of the water column with a dominant blue colour of underwater light.

Acknowledgements

I would first like to thank my supervisor Dr David McKee for his enthusiasm, his humour and his never ending confidence in my ability. Thank you for never letting me give up on this. Thank you also to Dr Neil Banas for his extremely helpful conversations and insights.

To my mum Diane Connan, thank you for continually showing me what true strength is and for being my biggest supporter in everything I do. Thank you to my friends Christopher Walsh and Michael Murphy for their unwavering humour in times when I needed it most, and to my grandmother Elizabeth McKellar for never doubting for a minute that this day would come.

Finally, thank you to my husband Steven McGinty, who continually put my career ahead of his own and sacrificed so much to lift me up. This wouldn't be possible without you.

Contents

Declaration of Authenticity and Author's Rights **i**

Abstract **ii**

Acknowledgements **iv**

Publications **ix**

1 Introduction **1**

1.1 Light in Aquatic Ecosystems 1

1.2 Marine Optics Overview 3

1.2.1 Radiometry of the Light Field 4

1.2.2 Inherent Optical Properties 5

1.2.3 Apparent Optical Properties 6

1.2.4 Optically Significant Constituents 8

1.3 Arctic Light Environment 11

1.4 Data Availability and Existing Light Parameterisations 12

1.5 Research Questions 14

2 Open Water Light Field Model **18**

2.1 Model Construction 19

2.1.1 Above Horizon Cloud-Free Solar Irradiance 20
2.1.2 Below Horizon Cloud-Free Solar Irradiance 20
2.1.3 Cloud-Free Lunar Irradiance 23
2.1.4 Cloud-Free Dark-Sky Irradiance 24
2.1.5 Cloud Cover Modulation 25
2.1.6 Air-Ocean Boundary Transmission 26
2.1.7 Underwater Attenuation 28
2.2 Model Validation 30
2.2.1 Above Surface Validation 31
2.2.2 Below Surface Validation 39
2.3 Comparisons to Current Models 55
2.4 Model Limitations 59
2.5 Conclusions 59

3 Attenuation of Spectral Irradiance by Snow and Ice 61
3.1 Background 62
3.1.1 Arctic Sea Ice 62
3.1.2 Sea Ice Type and Age 63
3.1.3 Sea Ice Extent and Concentration 63
3.1.4 Melt Ponds 64
3.1.5 Surface Scattering Layer 65
3.1.6 Snow 65
3.2 Model Construction 66
3.2.1 Model Coefficients 66
3.2.2 Attenuation Model 69
3.2.3 Open Water Element 71
3.2.4 Total Underwater Irradiance 71
3.3 Model Validation 73

3.3.1 Validation Datasets . . . 73
3.3.2 Validation Results . . . 74
3.4 Integration into the Open Water Model . . . 80
3.4.1 Satellite and Model Products . . . 80
3.4.2 *In Situ* Datasets . . . 81
3.4.3 Product Reliability . . . 82
3.5 Impact on Underwater Light . . . 90
3.5.1 Hierarchy of Impact on Transmittance . . . 99
3.6 Conclusions . . . 101

4 Amplification of Surface Irradiance by Multiple Reflection Effects 103
4.1 Background . . . 104
4.1.1 Arctic Cloud Cover . . . 104
4.1.2 Optical Properties of Cloud . . . 105
4.1.3 Existing Work . . . 105
4.2 Analysis of ArcLight Datasets . . . 106
4.2.1 PAR Irradiance Measurements . . . 106
4.2.2 Cloud Cover Data Comparison . . . 109
4.2.3 Comparison of Cloud Cover Data Sources . . . 120
4.2.4 PAR Irradiance After Cloud Correction . . . 122
4.2.5 Daylight Multiple Reflection . . . 125
4.2.6 ALAN Multiple Reflection . . . 130
4.3 Conclusions . . . 134

5 Parameterisation of Underwater Light Fields for Primary Production and Animal Behaviour 136
5.1 Primary Production . . . 137
5.1.1 Background . . . 137

5.1.2 Light Environment Impact on Primary Production 138
5.1.3 Pan-Arctic Primary Production Under Snow and Ice 141
5.1.4 Parameterisation of Attenuation - Impact on Primary Production . . 146
5.1.5 Conclusions 154
5.2 Animal Behavioural Response 157
5.2.1 Background 157
5.2.2 Perceived Surface PAR 158
5.2.3 Perceived Underwater PAR 165
5.2.4 Underwater Irradiance to Single Colour 170
5.2.5 Conclusions 172

6 Conclusions and Future Work **175**
6.1 Conclusions and Summary 175
6.2 Future Work 181

References **183**

Publications

Connan-McGinty, S., Banas, N. S., Berge, J., Cottier, F., Grant, S., Johnsen, G., Kopec, T. P., Porter, M., & McKee, D. (2022a). Midnight Sun to Polar Night: A Model of Seasonal Light in the Barents Sea. *Journal of Advances in Modeling Earth Systems*, *14*(10), 1–17. https://doi.org/10.1029/2022MS003198

Connan-McGinty, S., Banas, N. S., Berge, J., Cottier, F., Grant, S., Johnsen, G., Kopec, T. P., Porter, M., & McKee, D. (2022b). Midnight Sun to Polar Night: A model of seasonal light in the Barents Sea - HEIMDALL Model. *Zenodo*. https://doi.org/https://doi.org/10.5281/zenodo.7622686

Connan-McGinty, S., Banas, N. S., Berge, J., Cottier, F., Grant, S., Johnsen, G., Kopec, T. P., Porter, M., & McKee, D. (2022c). Midnight Sun to Polar Night: A model of seasonal light in the Barents Sea - Supplementary Data [Dataset]. *Zenodo*. https://doi.org/https://doi.org/10.5281/zenodo.7041939

Häfker, N. S., Connan-McGinty, S., Hobbs, L., McKee, D., Cohen, J. H., & Last, K. S. (2022). Animal behavior is central in shaping the realized diel light niche. *Communications Biology*, *5*(1), 1–8. https://doi.org/10.1038/s42003-022-03472-z

Castellani, G., Veyssière, G., Karcher, M., Stroeve, J., Banas, S. N., Bouman, A. H., Brierley, S. A., Connan, S., Cottier, F., Große, F., Hobbs, L., Katlein, C., Light, B., McKee, D., Orkney, A., Proud, R., & Schourup-Kristensen, V. (2022). Shine a light: Under-ice light and its ecological implications in a changing Arctic Ocean. *Ambio*, *51*(2), 307–317. https://doi.org/10.1007/s13280-021-01662-3

List of Abbreviations

Abbreviation	**Definition**	**Units**
ALAN	Artificial Light At Night	-
AOP	Apparent Optical Properties	-
$\alpha(\lambda)$	Spectral Albedo	dimensionless
α^B	Initial Slope of PP Curve	$\mathrm{mg\,C\,(mgB)^{-1}\,day^{-1}}$ $\mu\,\mathrm{mol\,m^{-2}\,day^{-1}}$
$a(\lambda)$	Spectral Absorption Coefficient	$\mathrm{m^{-1}}$
$b(\lambda)$	Spectral Scattering Coefficient	$\mathrm{m^{-1}}$
B	Chlorophyll Biomass	$\mathrm{mg\,m^{-3}}$
$b_b(\lambda)$	Spectral Backscattering Coefficient	$\mathrm{m^{-1}}$
$b_f(\lambda)$	Spectral Forward Scattering Coefficient	$\mathrm{m^{-1}}$
$\beta(\vartheta, \varphi, \lambda)$	Volume Scattering Function	$\mathrm{m^{-1}\,sr^{-1}}$
CDOM	Coloured Dissolved Organic Matter	-
C_F	Cloud Fraction	dimensionless
Chl	Chlorophyll a	$\mathrm{mg\,m^{-3}}$
CNN	Convolutional Neural Network	-
CoM	Centre of Mass	-

dir	Direct	-
dif	Diffuse	-
DVM	Diel Vertical Migration	-
$\mathrm{E_D}(\lambda)$	Downwelling Spectral Irradiance	$\mathrm{W\,m^{-2}\,nm^{-1}}$
$\mathrm{E_{D\,PAR}}$	Downwelling PAR Irradiance	$\mathrm{\mu\,mol\,m^{-2}\,s^{-1}}$
$\mathrm{E_K}$	Photoadaptation Parameter	$\mathrm{\mu\,mol\,m^{-2}\,s^{-1}}$
FYI	First Year Ice	-
GPP	Gross Primary Production	-
HEIMDALL	**H**ypersp**E**ctral **I**rradiance **M**odel for **D**iurn**A**l **L**ight **L**evels	-
IOP	Inherent Optical Properties	-
I	Ice	-
$\mathrm{K_d}$	Diffuse Attenuation Coefficient	$\mathrm{m^{-1}}$
$\mathrm{L}(\vartheta, \varphi, \lambda)$	Spectral Radiance	$\mathrm{W\,m^{-2}\,sr^{-1}\,nm^{-1}}$
MAE	Mean Absolute Error	-
MAPE	Mean Absolute Percentage Error	-
MBE	Mean Bias Error	-
MYI	Multi Year Ice	-
NAP	Non-algal Particulate Matter	-
NPP	Net Primary Production	-
OW	Open Water	-
PAR	Photosynthetically Active Radiation	-
p	Particulate Matter	-
P	Total Primary Productivity	$\mathrm{mg\,C\,m^{-2}\,day^{-1}}$
$\mathrm{P^B}$	Total P normalised to B	$\mathrm{mg\,C\,(mgB)^{-1}\,day^{-1}}$
$\mathrm{P^B_M}$	Assimilation Number of PP Curve	$\mathrm{mg\,C\,(mgB)^{-1}\,day^{-1}}$

PP	Primary Production	-
ρ	Density	$\mathrm{kg\,m^{-3}}$
ph	Phytoplankton	-
R	Reflectance	dimensionless
S	Snow	-
S_D	Snow Depth	m
SIC	Sea Ice Concentration	dimensionless
SIE	Sea Ice Extent	$\mathrm{km^2}$
SIT	Sea Ice Thickness	m
SSL	Surface Scattering Layer	-
T	Transmittance	dimensionless
$\bar{\mu}_D$	Mean Cosine of Downwelling Irradiance	dimensionless
w	Water	-
z	Depth	m

Chapter 1

Introduction

1.1 Light in Aquatic Ecosystems

Light availability is a key driver in aquatic ecosystems, influencing animal behaviour, supporting the marine food web through photosynthesis, and in the process facilitating the removal of carbon dioxide (CO_2) from the atmosphere. Increasing levels of atmospheric CO_2 have been identified as a main driver of anthropogenic climate change (Florides and Christodoulides, 2009), with current concentrations expected to double by the end of the 21st century (Li et al., 2012). However, marine microorganisms allow the ocean to act as a sink for atmospheric CO_2, and have removed around one third of anthropogenic CO_2 emissions (Sabine et al., 2004).

Phytoplankton are a collection of microscopic, autotrophic organisms found in aquatic environments. These small marine plants are found suspended beneath the ocean surface and use chlorophyll pigments to undergo photosynthesis, using sunlight and CO_2 to produce oxygen and carbohydrates. Marine phytoplankton account for around 50% of all global photosynthetic activity alongside terrestrial ecosystems (Simon et al., 2009). Not only does this process enable the transfer and deposition of carbon from the atmosphere to the ocean, but also supports growth and reproduction of the organisms when there is an abundance of additional key nutrients such as nitrate or phosphorous, resulting in phytoplankton blooms (Buchan et al., 2014). Determining the magnitude and timing of phytoplankton blooms is a key area of study in oceanography and is integrated into larger Ocean General Circulation Models (OGCMs) which describe both the biogeochemical and physical dynamics of ocean and atmospheric coupling (Popova et al., 2010, Popova et al., 2012).

In addition to their role in global carbon transfer, phytoplankton also serve as the base of the marine food web (Frederiksen et al., 2006), acting as a food source for primary consumers such as zooplankton. Zooplankton are microscopic marine animals of varying size that feed on free floating phytoplankton as their primary source of food, and in turn act as a food source for larger marine animals such as fish, small sharks and some types of whale (Beardsley et al., 1996). Any impact in phytoplankton availability can have a domino effect on the marine ecosystem, affecting organisms over many trophic levels.

All of these processes are significantly driven by light, which not only has an indirect effect on zooplankton by strongly influencing the availability of their primary food source, but also a direct influence on zooplankton movements in the water column. Phytoplankton are usually found in the euphotic zone where there is sufficient light to support photosynthetic growth, usually defined as the depth where light levels reach 1% of surface PAR (photosynthetically active radiation) (Marra et al., 2014). During daylight hours, zooplankton typically reside in the deeper mesopelagic zone of the ocean where there is very limited light penetration (Martin et al., 2020). Smaller zooplankton are generally very weak swimmers and rely on ocean currents to transport them across large-scale horizontal distances (Cyr and Sprules, 2022), however they do collectively perform vertical movement in the water column. This synchronised migration by the animals is known as diel vertical migration (DVM) and is primarily driven by ambient light levels (Berge et al., 2014, Last et al., 2016, Bandara et al., 2021). Zooplankton typically perform deep, vertical dives during daylight hours to the mesopelagic zone and emerge near the surface at night, into the euphotic zone to feed. This behaviour is theorised to be a cost-benefit trade off between avoiding detection by visual predators and accessing phytoplankton food sources (Fortier, 2001, Hays, 2003). This large-scale feeding depletes the concentration of free floating phytoplankton, and as a result zooplankton grazing habits are a key component in forecasting bloom dynamics.

Zooplankton not only act as an intermediary species in the marine food web, but also play a significant role themselves in carbon transfer. After consumption of phytoplankton, zooplankton and the larger animals that consume them transfer dissolved and particulate organic carbon to the deep ocean through egestion, respiration and decomposition (Steinberg and Landry, 2017). This coupled dynamic between phytoplankton and vertically migrating zooplankton forms the basis of the biological carbon pump, reducing atmospheric CO_2 concentrations.

Light availability is a significant driver both directly and indirectly in global biogeochemical processes. The amplitude and spectral composition of light entering the ocean can alter the timing and magnitude of under-ice and open water phytoplankton blooms (Shiozaki et al., 2014), and populations of ice-algae biomass in polar regions that have shown diverse latitudinal responses to simulations of climate change driven sea ice decline (Tedesco et al., 2019). This not only impacts atmospheric CO_2 transfer but also food availability for zooplankton, reverberating through the entire marine food web. Continual monitoring and forecasting of these biogeochemical processes requires an accurate quantification of underwater light levels, and will be of particular importance in response to a changing climate (Winder and Sommer, 2012).

1.2 Marine Optics Overview

This section will provide a brief overview of the optical processes significant in the marine environment, and how they are commonly quantified in oceanography research. Unless otherwise noted, the following mathematical derivations and theory follow the work of Mobley (2022).

1.2.1 Radiometry of the Light Field

Quantifying available light in the ocean begins with a description of spectral radiance. For a source emitting radiation, spectral radiance is defined as the radiant power (Φ) per unit solid angle (Ω) per unit area (A) at wavelength λ:

$$\mathrm{L}(\vartheta, \varphi, \lambda) = \frac{\mathrm{d}^3\Phi}{\mathrm{dA}\,\mathrm{d}\Omega\,\mathrm{d}\lambda} \tag{1.1}$$

where L is radiance in units of $\mathrm{W\,m^{-2}\,sr^{-1}\,nm^{-1}}$, and ϑ and φ are the zenith and azimuthal angles of the incident light. By integrating over all possible zenith and azimuthal angles, we can then quantify the spectrum of light incident ($\mathrm{E_D}(\lambda)$) on an element of area (dA) from one hemisphere of a sphere, i.e. all light incident from solar radiance:

$$\mathrm{E_d}(\lambda) = \int_0^{2\pi} \int_0^{\frac{\pi}{2}} \mathrm{L}(\vartheta, \varphi, \lambda) \cos\vartheta \sin\vartheta \, \mathrm{d}\vartheta \, \mathrm{d}\varphi \tag{1.2}$$

where $\mathrm{E_D}(\lambda)$ is the downwelling spectral planar irradiance at wavelength λ in units of $\mathrm{W\,m^{-2}\,nm^{-1}}$, describing all light travelling in a downward direction. Note the inclusion of $\cos\vartheta$ in Equation 1.2. This is a consequence of the Lambert cosine law, stating that the intensity of light incident on a surface is directly proportional to the cosine of the angle of incidence, relative to the surface normal of the receiving area.

Light incident upon the ocean surface is either reflected back into the atmosphere or transmitted into the water column. The degree of reflection and transmission is determined by the angle of incidence relative to the surface normal of the ocean, with smaller angles resulting in a larger proportion of light transmitted across the air-ocean boundary. This behaviour is well described by Fresnel equations and is explored in more detail in Chapter 2.

When light enters and interacts with the ocean, it undergoes an extinction process that is parameterised by a diffuse attenuation coefficient dependent on both the inherent optical properties of the medium and the angular distribution of the light field. This means that parameterisation of underwater light at various depths is dependent not only upon the optical features of the water and any optically significant substances present within the water, but also the geometric structure of the light field.

1.2.2 Inherent Optical Properties

Light passing through a medium is either absorbed, scattered, or transmitted. Inherent optical properties (IOPs) describe the absorption and scattering behaviour of the medium and are entirely independent of the incident light.

Consider an incident beam of radiant power φ_i passing through a volume of water ΔV with thickness Δr. Then the spectral absorption coefficient is the fraction of incident power absorbed in the ΔV per unit length and can be described as:

$$a(\lambda) = \lim_{\Delta r \to 0} \frac{\varphi_a(\lambda)/\varphi_i(\lambda)}{\Delta\, r} \tag{1.3}$$

where φ_a is the radiant power absorbed by the water and a(λ) is the the spectral absorption coefficient at wavelength λ in units of m^{-1}.

Similarly, the scattering coefficient is described as :

$$b(\lambda) = \lim_{\Delta r \to 0} \frac{\varphi_s(\lambda)/\varphi_i(\lambda)}{\Delta\, r} \tag{1.4}$$

where φ_s is the radiant power scattered by the water and b(λ) is the spectral scattering coefficient at wavelength λ in units of m^{-1}.

An important property of the scattering coefficient to consider is the direction that the light is scattered out of the beam. This behaviour is described by the volume scattering function, which defines the fraction of incident power scattered out of the beam path into a solid angle $\Delta\Omega$ at an angle described by (ϑ,φ):

$$\beta(\vartheta, \varphi, \lambda) = \lim_{\Delta r \to 0} \lim_{\Delta\Omega \to 0} \frac{\varphi_s(\lambda)/\varphi_i(\lambda)}{\Delta\, r \Delta\, \Omega} \tag{1.5}$$

where $\beta(\vartheta, \varphi, \lambda)$ is the volume scattering function at wavelength λ. By integration over all possible solid angles centred at (ϑ,φ), we can describe the scattering coefficient in the form:

$$\mathrm{b}(\lambda) = \int_0^{2\pi} \int_0^{\pi} \beta(\vartheta, \varphi, \lambda) \sin\vartheta \, d\vartheta \, d\varphi \tag{1.6}$$

By assuming that the scattering is azimuthally symmetric along the direction of propagation, it is then possible to separate Equation 1.6 into forward and backward scattering coefficients, $\mathrm{b_f}(\lambda)$ and $\mathrm{b_b}(\lambda)$ respectively, both in units of m^{-1}:

$$\mathrm{b_f}(\lambda) = 2\pi \int_0^{\frac{\pi}{2}} \beta(\vartheta, \varphi, \lambda) \sin\vartheta \, d\vartheta \tag{1.7}$$

$$\mathrm{b_b}(\lambda) = 2\pi \int_{\frac{\pi}{2}}^{\pi} \beta(\vartheta, \varphi, \lambda) \sin\vartheta \, d\vartheta \tag{1.8}$$

Inherent optical properties can be measured via water samples in a lab or *in situ* during field campaigns at sea. Due to the variety of optically significant constituents present in different types of water bodies during different seasons, IOPs vary both spatially and temporally (Bricaud et al., 1995, Bricaud et al., 1998b).

1.2.3 Apparent Optical Properties

Apparent optical properties (AOPs) depend on the inherent optical properties of the medium and on the structure of the light field. An example of an AOP is the diffuse attenuation coefficient, which describes how fast light diminishes through the water column. The downwelling spectral irradiance at a given depth z in the water column can be estimated using the Beer-Lambert Law:

$$\mathrm{E_d}(\lambda, \mathrm{z}) = \mathrm{E_d}(\lambda, 0) \exp(-\mathrm{K_d}(\lambda, \mathrm{z})\, \mathrm{z}) \tag{1.9}$$

where $\mathrm{E_D}(\lambda, \mathrm{z})$ is the downwelling spectral planar irradiance at depth z, $\mathrm{E_D}(\lambda, 0)$ is the downwelling spectral planar irradiance immediately below the ocean surface and $\mathrm{K_d(\lambda, z)}$ is the spectral diffuse attenuation coefficient, all at wavelength λ.

Rearranging for $\mathrm{K_d}$:

$$\mathrm{K_d(\lambda, z) = -\frac{1}{z} \ln \frac{E_d(\lambda, z)}{E_d(\lambda, 0)} = -\frac{1}{E_d(\lambda, z)} \frac{dE_d(\lambda, z)}{dz}} \tag{1.10}$$

If $\mathrm{E_D(\lambda, z)}$ changes suddenly at depth z due to a change in above surface cloud cover or change in solar angle then the magnitude of $\mathrm{K_d(\lambda, z)}$ also changes, and so diffuse attenuation is dependent on the geometric shape of the light field. Equations 1.9 and 1.10 assume that z is infinitesimally small to give accurate determination of diffuse attenuation at a specific depth, however this can be difficult to do in practice.

Average $\mathrm{K_d(\lambda)}$ can be determined *in situ* by measuring the downwelling spectral irradiance immediately below the surface and at larger depth z. However if we have no means to measure underwater spectral irradiance and want to predict $\mathrm{E_D(\lambda, z)}$, we can do so using information about the inherent optical properties and the geometric structure of the light field. Parameterisations of average $\mathrm{K_d(\lambda)}$ over depth z have typically been approximated using spectral absorption and backscattering coefficients ($\mathrm{a(\lambda)}$ and $\mathrm{b_b(\lambda)}$ respectively) similar to the following form (Sathyendranath and Platt, 1988, Sathyendranath et al., 1989):

$$\mathrm{K_d(\lambda) = \frac{a(\lambda) + b_b(\lambda)}{\bar{\mu_D}}} \tag{1.11}$$

where $\bar{\mu_D}$ is the mean cosine of the downwelling spectral irradiance and describes the angle of refraction of the light field after it has entered the water column. Snell's law describes the change of angle for a beam of light crossing the air water interface:

$$\mathrm{n_{air} sin\vartheta_{air} = n_{water} sin\vartheta_{water}} \tag{1.12}$$

where $\mathrm{n_{air}}$, $\mathrm{n_{water}}$ are the refractive index values of air and water respectively and ϑ_{air},

$\vartheta_{\mathrm{water}}$ are the angle of the light beam relative to the ocean surface normal in air and water respectively. Light can either be considered direct or diffuse. Direct light from the sun is comprised of photons that are travelling in parallel beams having undergone negligible scattering, and diffuse light are those photons that have undergone significant scattering by either the atmosphere or cloud cover. The mean cosine for direct light can be calculated directly by taking the cosine of the relevant solar zenith angle. However, the mean cosine for diffuse light is usually assigned an average value discussed in more detail in Chapter 2. This means that diffuse attenuation is not only dependent on the geometric shape of the light field, but of the optical properties of the medium and is considered an AOP.

1.2.4 Optically Significant Constituents

With knowledge of the inherent optical properties (IOPs) of the water column and above surface downwelling spectral irradiance, it is possible to predict the downwelling spectral irradiance at any given depth. In addition to the optical behaviour of water, it is also essential to consider the optical properties of particulate and dissolved matter that is distributed in the water column. The optically significant substances present in ocean waters are generally assumed to be phytoplankton (ph), non-algal particulate matter (NAP) and coloured dissolved organic matter (CDOM) (Morel and Prieur, 1977). Each of these substances absorb and scatter light in a different way.

Attenuation by water has been well studied, absorbing weakly in the blue-green region of the visible spectrum and strongly in the red (Pope and Fry, 1997), corresponding with vibrational transitions of the molecules. Absorption can vary depending on both the temperature and salinity content of the water with salinity having a more prominent effect (Röttgers et al., 2014). In contrast to absorption properties, scattering of light by water is stronger in the blue wavelengths and weaker in the red with some dependence on salinity and temperature (Zhang et al., 2009). Attenuation by water is dominated by absorption which has a spectrally averaged value 2 orders of magnitude higher than the equivalent scattering value (Pope and Fry, 1997).

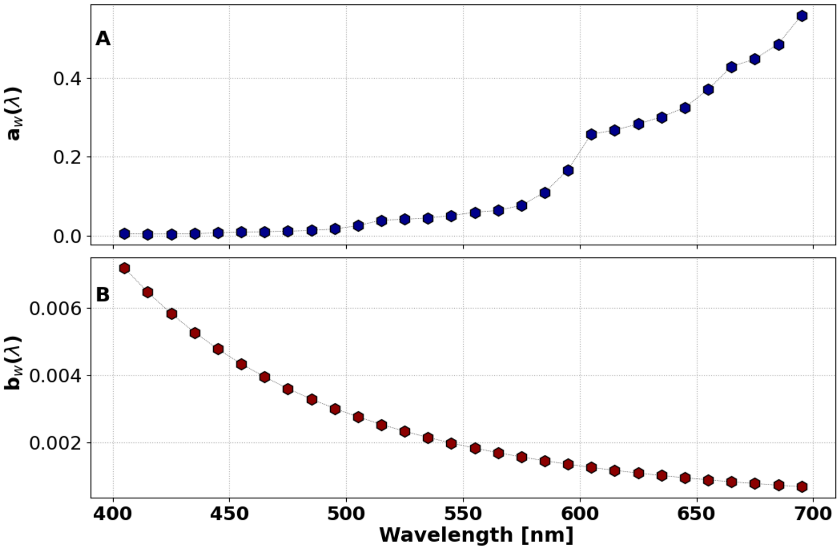

Figure 1.1: A) Spectral absorption coefficient ($a_w(\lambda)$) for pure water (Pope and Fry, 1997) and B) Spectral scattering coefficient ($b_w(\lambda)$) for pure water (Mobley, 2022).

Phytoplankton absorption spectra vary between different species, characterised by the light absorbing pigment composition. Most species have absorption peaks in the blue and red wavebands of the visible spectrum and lower absorption in the green, facilitated by chlorophyll pigments (Roy et al., 2006, Clementson and Wojtasiewicz, 2019). Absorption of light by chlorophyll can be affected by physiological characteristics of the pigments, in which they limit their light harvesting mechanisms during periods of increased light intensity to minimise cell damage (Rousso et al., 2021). Scattering by phytoplankton is highly dependent on the cell size and shape and is usually derived through theoretical means or by direct *in situ* measurements but is generally low due to real refractive indices close to that of water (Aas, 1996).

Non-algal particles (NAP) are particulate matter that don't have an extractable phytoplankton pigment, and can include detritus, mineral particles, bacteria and viruses. The absorption and scattering spectra of NAP can vary widely depending on what particulates are present in the water and to what degree, but the general behaviour is stronger absorption in the blue decaying exponentially towards the red (Bricaud et al., 1998a). Scattering properties of NAP are more difficult to generalise, with some showing a linear decrease with increasing wavelength and some with minimal wavelength dependence (Stramski et al., 2007).

Coloured dissolved organic matter (CDOM) is characteristically yellow in colour and is produced by decomposing organic material. It is usually driven by river runoff in coastal waters but can exist further from shore as a native constituent through local breakdown of plant material (Stedmon et al., 2011). CDOM absorption in the visible range dominates in the blue wavelengths, decreasing exponentially towards the red (Röttgers and Doerffer, 2007). There is no evidence currently that scattering by particles smaller than $<0.2\ \mu\mathrm{m}$ is significant; CDOM is classified beneath this size limit and so scattering contributions are generally neglected (Dall'Olmo et al., 2009).

Using *in situ* measurements or modelled values of the above properties, bulk inherent optical properties (IOPs) of the water column can then be defined as the sum of the contributions from constituent components, in the form:

$$\mathrm{a}(\lambda) = \mathrm{a_w}(\lambda) + \mathrm{a_{ph}}(\lambda) + \mathrm{a_{NAP}}(\lambda) + \mathrm{a_{CDOM}}(\lambda) \tag{1.13}$$

$$\mathrm{b}(\lambda) = \mathrm{b_w}(\lambda) + \mathrm{b_p}(\lambda) \tag{1.14}$$

$$\mathrm{b_b}(\lambda) = \mathrm{b_{b\,w}}(\lambda) + \mathrm{b_{b\,p}}(\lambda) \tag{1.15}$$

where ph is phytoplankton, NAP is non algal particulate matter, CDOM is coloured dissolved organic matter and p is particulate matter, including non algal particulates.

Not only can these values of spectral absorption a(λ), scattering b(λ) and backscattering $b_b(\lambda)$ be used to predict spectral irradiance at depth, but they can also describe the optical structure of the upper water column and are routinely inferred by satellites using remote sensing techniques to monitor global oceans (Werdell et al., 2018). To characterise the magnitude and spectral distribution of the light within the water column that is available for photosynthetic processes and for utilisation by marine animals, a detailed knowledge of the optical properties of both the water and constituents present is essential.

1.3 Arctic Light Environment

Arctic marine ecosystems are strongly influenced by the extreme seasonality of light in the region, where the light climate is primarily controlled by seasonal changes in solar elevation. With extended periods of 24-hr daylight (Polar Day) and 24-hr darkness (Polar Night), there exists extreme variations in both the magnitude and spectral composition of irradiance entering the ocean throughout the year. Whilst the sun remains below the horizon during the Polar Night, solar elevation still significantly controls spectral irradiance during much of this period through atmospheric scattering of light from the sun. However, throughout the darkest periods of the winter season, irradiance from the moon becomes the dominant source of illumination (Johnsen et al., 2021c).

Variations in light intensity have been shown to be an important environmental cue in the behavior of marine organisms as well as a key driver in the development of phytoplankton blooms, which form the base of the Arctic food chain (Castellani et al., 2022). Recent work has shown Arctic zooplankton performing vertical migrations in response to changes in both the position and phase of the moon during Polar Night (Last et al., 2016). In the absence of moonlight, some zooplankton may also be able to both detect and utilize ambient diffuse solar light at certain wavelengths down to a depth of around 30 m during the Polar Night (Cohen et al., 2015).

Examination of Arctic microalgae has also demonstrated that phytoplankton communities in the region exhibit rapid restoration of photosynthetic capacity when re-illuminated following the period of Polar Night or after ice retreat in the spring (Kvernvik et al., 2018, Sloughter et al., 2019). Although light levels through the winter season are generally believed to be insufficient for primary production to occur, phytoplankton species have been shown to maintain their ability for photosynthesis throughout extreme darkness and quickly respond to artificially increased light levels (Berge et al., 2015b). Likewise, living and growing brown, red, and green macroalgae have also been found during the Polar Night, such as in Kongsfjorden, Svalbard in January 2020 (Summers et al., 2022).

Parameterisation of underwater light in the Arctic can be challenging not only due to considerable complexities induced by the impact of consistently low sun angles and extremely low light levels, but also by widespread seasonal snow and ice cover and increasing levels of cloud. Spring-time cloud cover in the Arctic has been increasing linearly in recent decades (Schweiger, 2004) and cloud cover has been shown to significantly reduce surface irradiance levels (Pfister et al., 2003). Early summer cloud cover data have also been shown to be a predictor of sea ice concentration in the late summer in the Arctic (Choi et al., 2014), with high cloud coverage over sea ice covered oceans altering the albedo feedback (He et al., 2019), accelerating ice melt (Huang et al., 2019) and allowing more light to penetrate into the water column. Inclusion of the effects of cloud and ice cover on the magnitude of irradiance reaching the ocean surface will therefore be increasingly important as the region warms.

1.4 Data Availability and Existing Light Parameterisations

Current models of light parameterisation in Arctic ecosystem studies are generally focussed on above horizon solar irradiance using radiative transfer models that are dependent upon *in situ* radiometry measurements, the use of daily shortwave radiation (300–3000 nm) estimates from satellite observations, or atmospheric models and reanalyses (Hill et al., 2018, Randelhoff et al., 2020, Freer et al., 2021, Hobbs et al., 2021). Satellite or reanalysis products of daily downwelling shortwave or Photosynthetically Active Radiation (PAR) are widely available (Hersbach et al., 2018, NASA, 2014), however these datasets come with the significant limitations that they are not operational at high latitudes during winter months and are limited to broadband estimates only. Alternatively, the proprietary radiative transfer software Hydrolight (Mobley, 2022) is able to predict downwelling spectral irradiances at the ocean surface at any given location provided with knowledge about local solar position. Again however, this approach also has limitations for Pan-Arctic seasonal applications as irradiance estimates are limited to scenarios when the sun is above horizon. In such situations these light models may be missing periods of the year where there are biologically significant light levels. Assumptions in some current plankton models concerning underwater light during Polar Night and transitional periods are often extremely simple, introducing uncertainty and bias that likely affects large-scale reconstructions and predictions of primary productivity (Popova et al., 2010, Sloughter et al., 2019).

Recent modelling studies on Arctic underwater light fields have focussed on the complexities of light beneath variable ice and snow (Stroeve et al., 2021, Veyssière et al., 2022). Using a combination of satellite and modelled data or *in situ* measurements, these studies are able to provide under-ice light field estimates over large scales in the Arctic, but have also relied upon either irradiance measurements obtained during field campaigns or via satellites, and are subsequently restricted to seasons when the sun is sufficiently above horizon.

There have also been considerable field campaigns throughout various regions of the Arctic to measure *in situ* spectral downwelling irradiance under various snow and ice conditions (Light et al., 2008, Light et al., 2015, Rösel et al., 2018, Katlein et al., 2019). These studies have collected measurements of spectral transmission and attenuation over a range of temporal scales at various sites in the Arctic. However, a significant limitation of this approach is geographical restriction and/or a limited temporal range, in that measurements looking at the evolution of under-ice light fields may be available over time scales such as weeks or years but they are generally restricted in the spatial domain. *In situ* measurements undertaken by manually removing ice cores are extremely spatially and temporally constrained, but even the use of under-ice remotely operated vehicles (ROVs) and autonomous underwater vehicles (AUVs) does not entirely mitigate these issues. Although ROVs and AUVs have the ability to cover a large spatial-temporal domain, they generally follow transects and thus cannot provide a cost effective solution to scaling up to a Pan-Arctic level of under-ice light field mapping. Additionally, they are not equipped to accurately measure above surface irradiance or sea ice concentration, changes in which could introduce error into calculated transmission or attenuation values.

Continuous estimates of light fields to study various ecosystem responses remains challenging, particularly at the high latitudes of the Arctic. Difficulties arise from dark, cold, and icy conditions, inaccessibility of remote regions, and limitations on the sensitivity of available equipment to very low irradiance levels for much of the year. Although field campaigns and *in situ* measurements have demonstrated the impact that the optical properties of snow and ice have on light penetration into the water column, the fixed location and time limited nature of these datasets make them an inadequate solution for scaling up to a Pan-Arctic level. To understand both spatially and temporally varying under-ice light fields, a fast, accurate and inexpensive hyperspectral light model which can capture the seasonal behaviour of the Arctic light climate and fully extend throughout Polar Night would be a useful tool for many lines of both observation and model-based research that focus on assessing the impacts of underwater light fields on the marine environment.

1.5 Research Questions

This introductory chapter has outlined the significant influence of underwater light in global biogeochemical processes and highlighted complexities in characterising these light fields, with particular focus on the Arctic. In this region, significant challenges remain when modelling irradiance dependent marine ecosystems due to strong seasonality of light and widespread snow and ice cover. Current approaches for quantifying underwater light fields are limited to scenarios where the sun remains above the horizon, which excludes a considerable time period in the Arctic. A similar problem exists when relying on *in situ* measurements or satellite irradiance data. Commercially available radiometers are not generally sensitive enough to record surface irradiance values in winter, and satellites are unable to provide data at high latitudes in the winter months. These limitations mean there is currently no reliable method to quantify fully seasonal, Pan-Arctic underwater light availability that can accurately capture all optically significant components for continuous study of photosynthetic processes or animal behaviour.

To address these highlighted key gaps, this thesis will aim to answer the following questions:

- Is there a low-cost method of modelling fully seasonal, underwater Pan-Arctic light whilst maintaining accuracy?
- Which environmental factors impact light availability most?
- Are satellite products reliable in determining the quantity of snow, ice and cloud cover present?
- How much does the presence of snow and ice impact light availability for photosynthesis?
- Does the spectral distribution of light influence animal behaviour?

Chapter 2 will outline the construction of the **H**ypersp**E**ctral **I**rradiance **M**odel for **D**iurn**A**l **L**ight **L**evels (**HEIMDALL**) for ice-free conditions applied to the Barents Sea. The hyperspectral model accurately determines location-specific downwelling spectral irradiance $E_D(\lambda)$ contributions from solar, lunar, and galactic components throughout the year, with modulation using local cloud cover from satellite estimates and transmission across the air-ocean boundary that considers the optical behaviour of low sun angles. By incorporating a region-specific bio-optical model to accurately determine the optical properties of both homogeneous and inhomogeneous water columns, underwater validation is presented using broadband irradiance data measured by autonomous underwater vehicles from the Barents Sea.

Chapter 3 will outline the construction of a snow and sea ice spectral attenuation model to estimate spectrally resolved under-ice light, populated by parameters that can easily be obtained from satellite data, i.e. snow depth, sea ice thickness and sea ice concentration. Validation of the model is presented, comparing modelled outputs to *in situ* spectral transmission values from existing literature. The chapter will also discuss the hierarchy of controlling sea ice parameters that determine the magnitude of underwater light, and compare satellite derived values of sea ice thickness and snow depth with *in situ* measurements.

Chapter 4 will discuss the amplification of above surface visible irradiance due to multiple reflection induced by widespread snow cover and high fractional cloud cover. It will outline the use of a convolution neural network (CNN) applied to all-sky images obtained from the ArcLight Light Observatory in Ny Ålesund, Svalbard to assess the reliability of satellite data in determining local cloud cover fraction. Using cloud cover estimates determined via the CNN, the magnitude of this amplification effect is quantified and discussed in the context of existing literature.

Chapter 5 will use the HEIMDALL model to quantify seasonal, Pan-Arctic light availability for photosynthesis, including the effects of snow, sea ice and cloud cover using satellite data from 2018. The impact of varying snow and sea ice on primary production is quantified, followed by an impact assessment on the effects of disregarding under-ice primary production for varying seasons. Additionally, a comparison of various open water light field parameterisations against broadband irradiance measured by autonomous underwater vehicles from the Barents Sea will be discussed. Primary production is estimated using each of these models to assess the impact of a varying diffuse attenuation coefficient on estimating photosynthetic activity. The chapter concludes with a discussion on spectrally resolved underwater light fields in the context of diel vertical migration (DVM) of Arctic zooplankton. A time series of acoustic backscattering data measured from Kongsfjorden, Svalbard in March 2018 is presented with underwater light fields calculated by HEIMDALL. Vertical movement of the zooplankton is analysed with discussion of a possible trigger of DVM induced by spectral distribution of the perceived light field.

Chapter 2

Open Water Light Field Model

Introduction

Surface irradiance is primarily controlled by two drivers, solar elevation and cloud cover, closely followed by lunar elevation and phase (Kasten and Czeplak, 1980, Bartlett et al., 1998, Johnsen et al., 2021c). Propagation of the light field across the air-ocean boundary is dependent upon the geometric structure of the light field, controlled by local conditions, and attenuation of light down the water column is determined by the optical properties of the water and the concentration of optically significant constituents present within the column (Bricaud et al., 1995, Pope and Fry, 1997, Bricaud et al., 1998b, Mobley, 2022). As each of these components have both spatial and temporal dependence, any parameterisation of local light levels must be a function of global location, date and time.

This chapter will describe in detail the construction of the **H**ypersp**E**ctral **I**rradiance **M**odel for **D**iurn**A**l **L**ight **L**evels (**HEIMDALL**), an ice-free, open water hyperspectral light field model used to characterise spectrally resolved underwater seasonal light in the Barents Sea. It will further outline the results of model performance against current state of the art radiative transfer software and demonstrate validation using *in situ* radiometry datasets from above and below the ocean surface. Finally, a comparison of the HEIMDALL model against existing light data products will be discussed.

A significant proportion of the material presented in this chapter has recently been published (Connan-McGinty et al., 2022a).

2.1 Model Construction

The HEIMDALL model can accurately determine location-specific downwelling spectral irradiance ($E_D(\lambda)$) contributions from solar, lunar, and galactic components throughout the year, modulated by local cloud cover. Provided with a latitude, longitude, date and time, it will determine the local solar zenith angle, lunar zenith angle and phase, and will extract satellite cloud cover data for historical light levels or request user specified cloud cover values for predictive modelling. Also incorporated is a baseline irradiance value representing dark-sky conditions in the absence of significant solar and lunar illumination, where the dominant sources of light shift to scattered starlight, sunlight scattered by interplanetary dust (zodiacal light), and the faint emission of light from atomic processes in the atmosphere (airglow) (Kolláth et al., 2020). Direct and diffuse components of light are preserved separately and transmitted across the air-ocean boundary, with consideration of the optical behaviour of low sun angles typical in the region. Finally, the diffuse and direct light fields are propagated down the water column via the Beer-Lambert Law, with attenuation determined via an incorporated Barents Sea bio-optical model that accurately determines the optical properties of both homogeneous and inhomogeneous water columns. Requiring only salinity and chlorophyll *a* concentration profiles to populate the bio-optical model, $E_D(\lambda)$ is calculated at 10 nm resolution in the photosynthetically active radiation (PAR, 400–700 nm) range at user specified depth and temporal resolution. Through a combination of available measured and modelled data sources, HEIMDALL provides continuous underwater hyperspectral light field estimates uninterrupted from Polar Day to Polar Night. All modelled light data are in units of $\mathrm{Wm^{-2}\,nm^{-1}}$, at central wavelength values of 405–695 nm at 10nm intervals. Using the photon energy at each central wavelength, outputs can be converted into quantised units of $E_{D\,PAR}$ ($\mu\,mol\,m^{-2}\,s^{-1}$) covering a 10 nm bandwidth. Total underwater irradiance is calculated as the sum of the direct and diffuse light fields, as detailed in sections 2.1.1 to 2.1.7.

2.1.1 Above Horizon Cloud-Free Solar Irradiance

The radiative transfer software Hydrolight calculates above surface solar radiance distributions using the physical laws governing radiative transfer (Mobley, 2022). By executing an extension of the RADTRAN model (Gregg and Carder, 1990), Hydrolight determines direct and diffuse spectral irradiance in the 300–1000 nm range up to a maximum solar zenith value of 89°. Using Hydrolight, clear sky spectral irradiance values were extracted at solar zenith angles in the range 0° to 80° at 10° intervals, for wavelengths 405–695 nm at 10 nm intervals. One final run was executed at the upper limit of 89° to act as boundary value for interpolation of zenith angles $> 80°$. Local solar zenith angle is determined via a high precision solar position algorithm using latitude, longitude, date and time (Reda and Andreas, 2004). Local direct and diffuse spectral irradiances are then linearly interpolated from the binned values obtained from Hydrolight in units of $Wm^{-2}\,nm^{-1}$. For modelling direct irradiance, HEIMDALL assumes no direct irradiance when solar zenith exceeds 89°.

2.1.2 Below Horizon Cloud-Free Solar Irradiance

As the sun moves below the horizon and zenith angle exceeds 90°, the light field is comprised only of diffuse light scattered through the Earth's atmosphere. Although the sun is no longer visible, there still exists a significant amount of light reaching the ocean surface. To account for this diffuse light field, HEIMDALL makes use of empirical irradiance measurements recorded from the period of sunset to astronomical twilight.

Downwelling spectral irradiance ($E_D(\lambda)$) was measured by Spitschan et al. (2016) at Cherry Springs State Park in Pennsylvania, USA (41.6646°N, 77.8125°W) over a period of approximately 8 days in the summer of 2014. Measurements were recorded on an elevated site within the Susquehannock State Forest. $\mathrm{E_D}(\lambda)$ was recorded in the visible range of 400–800 nm at 1 nm resolution. One remarkable feature of this dataset is that when $\mathrm{E_D}(\lambda)$ is integrated over the wavelength range and represented as a function of solar elevation angle, there appears to be an unexpected dependence upon time of day, shown in Figure 2.1A. This apparent dependence upon solar azimuth results in a variation of integrated irradiance values up to 1.5 orders of magnitude for similar sun angles. Spitschan et al. (2016) attributed this behaviour to possible differences in atmospheric conditions at dawn and dusk, however when independently calculating solar elevation and re-plotting the data, the feature was eliminated. Figure 2.1B shows the dataset with solar elevation angles that have been recalculated for known times and positions using Reda and Andreas (2004), the high precision solar position algorithm integrated into HEIMDALL. Both datasets show irradiance values binned into the nearest solar elevation angle within 2° and averaged. Additionally, the data presented represents only those measurements where lunar irradiance was minimised. The removal of the apparent dependence upon solar azimuth strongly suggests a calculation error in the original dataset in regards to solar elevation. As the authors specified that measurements were taken from an elevated position within the site, it is assumed that local topography is not impacting irradiance measurements. The authors of Spitschan et al. (2016) have been notified of this issue and intend to update their data (Manuel Spitschan, personal communication 08 October 2022).

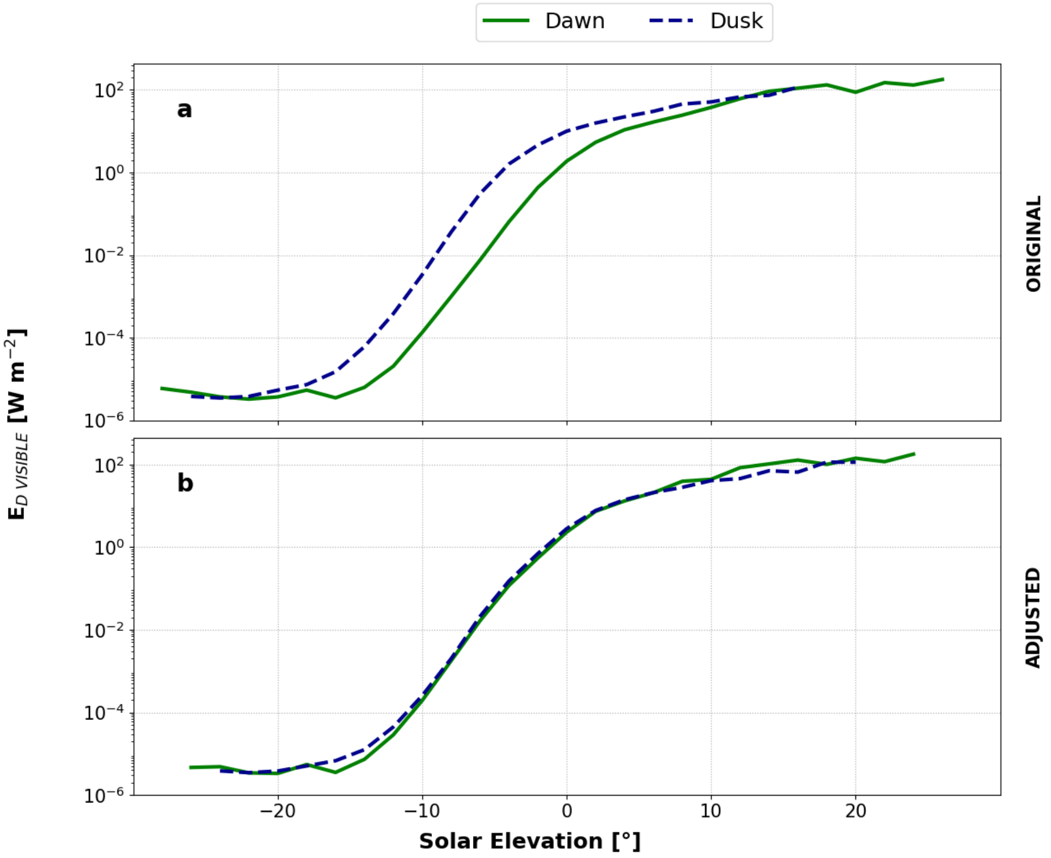

Figure 2.1: Total integrated downwelling irradiance (400–800 nm) measured by Spitschan et al. (2016) as a function of (A) solar elevation as determined by Spitschan et al. (2016) (ORIGINAL), and (B) solar elevation determined using Reda and Andreas (2004) (ADJUSTED).

For incorporation into HEIMDALL, the adjusted dataset was further filtered for recorded timestamps where local cloud cover was ≤ 10%, using the approach discussed in Section 2.1.5, with wavelengths extracted to match those of Section 2.1.1. Values from the dawn and dusk datasets from Figure 2.1B were averaged and appended to existing above horizon data set (Section 2.1.1). Converting from solar elevation to solar zenith provides clear sky solar irradiance over the solar zenith range 0° to 110°.

Note that there is no attempt to account for the Novaya Zemlya effect, a phenomenon in which atmospheric refraction results in direct rays of sunlight being visible from a solar disk that is below the horizon (Lehn, 1979). Since these direct rays of sunlight are travelling almost parallel to the ocean surface, only a negligible fraction will cross the air-ocean boundary into the water column.

2.1.3 Cloud-Free Lunar Irradiance

Lunar spectral irradiance is integrated into HEIMDALL using existing direct and diffuse solar irradiance values. Lunar zenith, phase and distance for the given location and time are first calculated using a high precision position calculator (Rhodes, 2019).

Assuming a Lambertian surface reflecting equally in all directions with an apparent full-moon radiance at lunar zenith angle (ϑ_L) of:

$$L_{FM}(\lambda, \vartheta_L) = \frac{\alpha(\lambda) H_D(\lambda, \vartheta_L)}{\pi} \tag{2.1}$$

where $L_{FM}(\lambda, \vartheta_L)$ is the total apparent full-moon lunar spectral radiance, $H_D(\lambda, \vartheta_L)$ is the equivalent total solar irradiance at lunar zenith angle ϑ_L, and $\alpha(\lambda)$ is the lunar spectral albedo determined by Shkuratov et al. (1999). $L_{FM}(\lambda, \vartheta_L)$ is then multiplied by the solid angle subtended by the moon (Ω_L) at a distance calculated from the centre of the Earth for the given date, and a phase factor (F) relating lunar phase angle (φ) to fraction of illumination (Miller & Turner, 2009), such that spectral lunar irradiance is then:

$$E_{D\,\mathrm{lunar}}(\lambda, \vartheta_L, \varphi) = L_{FM}(\lambda, \vartheta_L) F(\varphi) \Omega_L \tag{2.2}$$

Using the solar irradiance at zenith ϑ_L, rather than the solar constant, allows preservation of the direct and diffuse components of lunar irradiance separately, preserving the consistency with the solar component, and avoiding the need for additional inclusion of atmospheric properties.

2.1.4 Cloud-Free Dark-Sky Irradiance

As shown in Figure 2.1, irradiance levels appear to reach a baseline value of order $10^{-6}\,\mathrm{W\,m^{-2}}$, at which time solar zenith is no longer a dependent variable. To determine where the upper limit of solar zenith angle should be fixed for this baseline value, irradiance measurements from a dark sky site were analysed.

Light levels recorded at Zselic Starry Sky Park in Hungary (46.2366°N, 17.7653°E) by Kolláth et al. (2020) detail spectral radiance at a solar zenith angle of approximately 140°. Measurements were taken at a site that is subject to minimal impact from artificial light sources. Through spectral decomposition, Kolláth et al. (2020) concluded that the continuous part of the night sky spectrum, that which is comprised of spectral radiance contributions from starlight, sunlight scattered by interplanetary dust (zodiacal light), and the faint emission of light from atomic processes in the atmosphere (airglow), exhibited a flat curve of $\approx 2\,\mathrm{nW\,m^{-2}\,sr^{-1}\,nm^{-1}}$. A single hemisphere of 2π steradians integrated over the 400-700 nm range gives a broadband baseline irradiance value in the region $3\,\mathrm{\mu W\,m^{-2}}$. This lower limit of broadband irradiance is consistent with observations from Cherry Springs National Park (Section 2.1.2), where baseline irradiance values of order $10^{-6}\,\mathrm{W\,m^{-2}}$ were observed.

In the HEIMDALL model, a spectrally flat baseline irradiance value of $4\pi\,\mathrm{nW\,m^{-2}\,nm^{-1}}$ ($2\,\mathrm{nW\,m^{-2}\,sr^{-1}\,nm^{-1}} * 2\pi$) is applied to diffuse solar irradiance when solar zenith angle exceeds 106° (solar elevation $< -16°$). This upper limit zenith angle was chosen by averaging the dawn and dusk datasets from Figure 2.1B and determining the associated baseline elevation, as shown in Figure 2.2. Note that the baseline irradiance value for this dataset is expected to be around the value of $5\,\mathrm{\mu W\,m^{-2}}$ due to the larger bandwidth of measured data (400-800 nm) compared to the bandwidth used in HEIMDALL (400-700 nm).

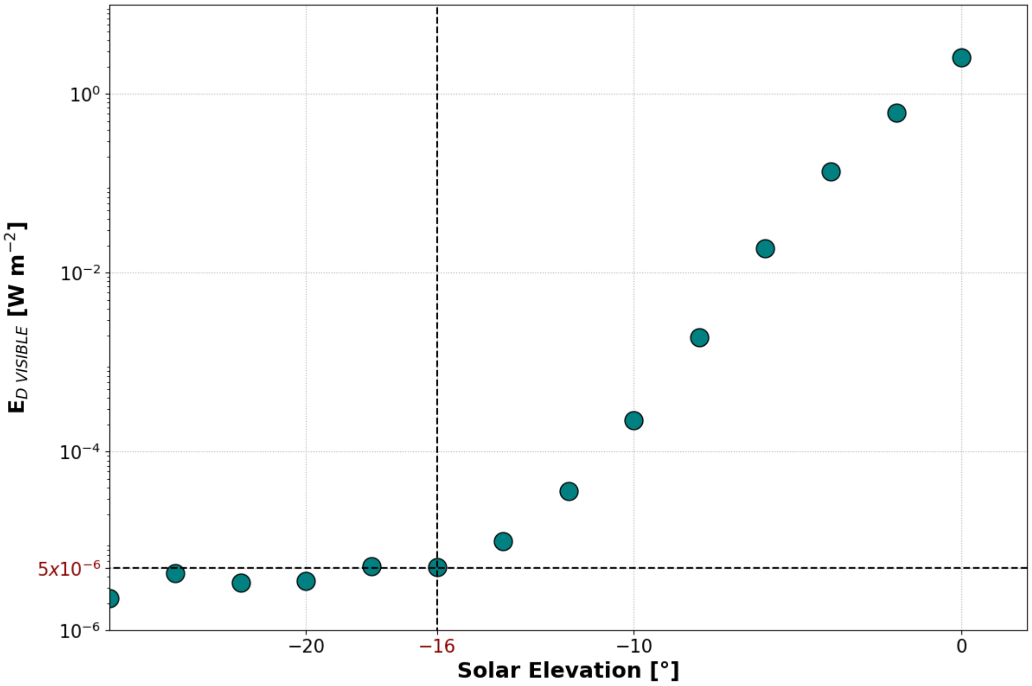

Figure 2.2: Total integrated downwelling irradiance (400–800 nm) measured by Spitschan et al. (2016) as a function of solar elevation determined using Reda and Andreas (2004). Values shown are an average of the dawn and dusk datasets. Baseline irradiance value and associated solar elevation noted in red.

2.1.5 Cloud Cover Modulation

The behaviour of light propagating through cloud can be optically complex, with dependencies such as cloud type, thickness, and precipitation state (Davies, 1978, Bartlett et al., 1998, Josefsson and Landelius, 2000). To model all dependent variables affecting the transmission of light through clouds with high precision would require computationally expensive full radiative transfer simulations. An objective of the HEIMDALL model is to retain simplicity without sacrificing significant accuracy. As such, a spectrally flat approximation of irradiance reduction first proposed by Kasten and Czeplak (1980) is implemented to account for the presence of cloud cover.

$$\mathrm{E_D(C_F) = E_D(0)\,(1 - 0.75\,C_F^{3.4})} \tag{2.3}$$

$$\mathrm{E_{D\,dif}(C_F) = E_D(C_F)\,(0.3 - 0.7\,C_F^{2})} \tag{2.4}$$

$$\mathrm{E_{D\,dir}(C_F) = E_D(C_F) - E_{D\,dif}(C_F)} \tag{2.5}$$

where $\mathrm{E_D(0)}$, $\mathrm{E_D(C_F)}$ are total downwelling irradiance summed from all sources for a clear sky and at cloud fraction $\mathrm{C_F}$ respectively. $\mathrm{E_{D\,dif}}$, $\mathrm{E_{D\,dir}}$ are the diffuse and direct components respectively. When the sun and moon are both below the horizon, there is no direct clear sky light field and Equation 2.3 only is applied.

Cloud cover is imported into HEIMDALL from the Copernicus Climate Change Service (C3S) Climate Data Store (Hersbach et al., 2018). Hourly averaged fractional cloud cover data is available on a grid size of 0.25° x 0.25° spatial resolution from 1979 until present. User supplied latitude and longitude is rounded to the nearest 0.25° with cloud cover data extracted for the required date and time and applied to Equations 2.3–2.5.

2.1.6 Air-Ocean Boundary Transmission

As the above surface downwelling irradiance field is preserved as separate direct and diffuse components, each must be independently transferred across the air-ocean boundary.

The direct component of the light field is transmitted across the air-ocean boundary using Fresnel coefficients and using the local solar or lunar zenith ($\vartheta_\mathrm{S}/\vartheta_\mathrm{L}$ respectively) as the angle of incidence (ϑ_i).

$$\mathrm{R_s} = \left| \frac{\mathrm{n_{air}} \cos\vartheta\mathrm{i} - \mathrm{n_{water}}\sqrt{1 - (\frac{\mathrm{n_{air}}}{\mathrm{n_{water}}}\sin\vartheta_\mathrm{i})^2}}{\mathrm{n_{air}} \cos\vartheta\mathrm{i} + \mathrm{n_{water}}\sqrt{1 - (\frac{\mathrm{n_{air}}}{\mathrm{n_{water}}}\sin\vartheta_\mathrm{i})^2}} \right|^2 \tag{2.6}$$

$$R_p = \left| \frac{n_{air}\sqrt{1-(\frac{n_{air}}{n_{water}}\sin\vartheta_i)^2} - n_{water}\cos\vartheta_i}{n_{air}\sqrt{1-(\frac{n_{air}}{n_{water}}\sin\vartheta_i)^2} + n_{water}\cos\vartheta_i} \right|^2 \tag{2.7}$$

where n_{air}, n_{water} are the refractive indices of air and water respectively, and R_S, R_P are the reflection coefficients of the s and p polarisation planes of the incident light field respectively. For unpolarised light, it is assumed there is an equal amount of power in both s-polarisation and p-polarisation planes. The total reflectance, R_{Total}, is then an average of these and total transmission (T) is:

$$T = 1 - R_{Total} = 1 - \frac{1}{2}(R_s + R_p) \tag{2.8}$$

Note that the complex component of the refraction index has been ignored as its contribution is negligible in the visible region (Mobley, 2022).

The diffuse light field is comprised of photons with random direction of travel, with an angle of incidence on the ocean surface in the range $0° \leq \vartheta_i < 90°$. Assuming an average incidence angle of 45° applied to Equations 2.6–2.8 gives a transmission fraction of 0.97 for diffuse light. This constant value is applied to the diffuse component of the downwelling irradiance.

Analysis of clear sky direct and diffuse light transmission across the air-ocean boundary for increasing surface roughness was undertaken using modelled output from Hydrolight. Varying wind speed from $0\,\mathrm{m\,s^{-1}}$ to $15\,\mathrm{m\,s^{-1}}$ in $2.5\,\mathrm{m\,s^{-1}}$ steps showed only a modest relative increase in underwater light for the diffuse component (1.7% increase at $15\,\mathrm{m\,s^{-1}}$ compared to $0\,\mathrm{m\,s^{-1}}$) for all solar zenith angles. The direct component saw minimal variation for zenith angles $\leq$ 80° (4% increase at $15\,\mathrm{m\,s^{-1}}$), however exhibited a relative increase of factor 3 at zenith angle 89°. However at this angle, the sun is so close to the horizon that the direct component of light accounts for $< 0.003\%$ of the total light field. The air-ocean boundary is therefore treated as flat since calculating surface roughness to account for a modest increase in total underwater downwelling irradiance would not be computationally efficient.

2.1.7 Underwater Attenuation

Propagation of light down the water column is dependent upon both the inherent optical properties (IOPs) of the water and constituent optical components, as well as the geometrical structure of the light field, an apparent optical property (AOP).

The IOPs of water bodies can vary globally and depend on the concentration of different types of optically significant constituents (Bengil et al., 2016, Cota et al., 2003). Using a bio-optical model developed specifically for the Barents Sea (Kostakis et al., 2020), the IOPs of the water column are parameterised only by chlorophyll *a* concentration (Chl) and salinity (Sal) profile inputs. However, the bio-optical component of HEIMDALL can easily be modified to include optically significant components for use in other regional waters.

In addition to the IOPs of the seawater, each optical component in the water column also has an associated value of wavelength dependent absorption ($a(\lambda)$), scattering ($b(\lambda)$) and backscattering ($b_b(\lambda)$). The total value of each is defined as:

$$a(\lambda) = a_w(\lambda) + a_{CDOM}(\lambda, Sal) + a_{NAP}(\lambda, Chl) + a_{ph}(\lambda, Chl) \tag{2.9}$$

$$b(\lambda) = b_w(\lambda) + b_p(\lambda, Chl) \tag{2.10}$$

$$b_b(\lambda) = b_{bw}(\lambda) + b_{bp}(\lambda, Chl) \tag{2.11}$$

where subscripts w, CDOM, NAP, ph and p refer to water, coloured dissolved organic matter, non-algal particles, phytoplankton, and particulate matter respectively. The bio-optical model uses chlorophyll *a* concentration (photosynthetic phytoplankton biomass) and relates all particle properties to it. It also establishes a link between salinity content and CDOM. Values for a_{CDOM}, a_{NAP}, b_p and b_{bp} are determined from Kostakis et al. (2020), a_{ph} from Bricaud et al. (1995) and a_w, b_w, b_{bw} from Pope and Fry (1997) and Morel (1974).

Both the diffuse and direct light field are attenuated separately down the water column to depth z using the Beer-Lambert law.

$$\mathrm{E_{D\,dir}}(\lambda, \mathrm{z}) = \mathrm{E_{D\,dir}}(\lambda, 0)\exp(-\mathrm{K_{dir}}(\lambda)\mathrm{z}) \tag{2.12}$$

$$\mathrm{E_{D\,dif}}(\lambda, \mathrm{z}) = \mathrm{E_{D\,dif}}(\lambda, 0)\exp(-\mathrm{K_{dif}}(\lambda)\mathrm{z}) \tag{2.13}$$

$$\mathrm{K_{dir}}(\lambda) = \frac{\mathrm{a}(\lambda) + \mathrm{b_b}(\lambda)}{\bar{\mu}_{\mathrm{dir}}} \tag{2.14}$$

$$\mathrm{K_{dif}}(\lambda) = \frac{\mathrm{a}(\lambda) + \mathrm{b_b}(\lambda)}{\bar{\mu}_{\mathrm{dif}}} \tag{2.15}$$

where $\mathrm{K_{dir}}(\lambda)$, $\mathrm{K_{dif}}(\lambda)$ are the diffuse attenuation coefficients of direct and diffuse light respectively and $\bar{\mu}_{\mathrm{dir}}$, $\bar{\mu}_{\mathrm{dif}}$ are the mean cosine values for direct and diffuse light.

Following the approach taken by Sathyendranath and Platt (1988), the value of $\bar{\mu}_{\mathrm{dif}}$ is set to a constant value. Incident diffuse light can impact the ocean surface at an incidence angle ranging from 0 to 90°. Using Snell's law, this constrains the underwater angle of refraction to 0–48°, with mean cosine value ranging from approximately 0.67–1. Assuming the midpoint value is representative of typical underwater diffuse light, $\bar{\mu}_{\mathrm{dif}}$ is assigned a constant value of 0.83. Similarly, the value of $\bar{\mu}_{\mathrm{dir}}$ is also calculated via Snell's Law, where the angle of incidence is either the solar or lunar zenith angle.

To maintain the ability to process structured profiles, the water column is divided into layers of depth z' determined by the user-specified depth resolution. The depth layer is always constant at z'. The surface value of $\mathrm{E_D}$ for layer k is equal to the value of $\mathrm{E_D}$ at the bottom of layer $\mathrm{k} - 1$. The model is implemented via the open source programming language Python version 3.7, with the full HEIMDALL open water hyperspectral light model and supplementary data available under the Creative Commons Attribution 4.0 License (Connan-McGinty et al., 2022b, Connan-McGinty et al., 2022c). A typical 200 m depth profile is produced by HEIMDALL in approximately 15 seconds using an Intel® Core™ i7-9750H CPU at 2.60 GHz.

2.2 Model Validation

Validation of the above surface irradiance field was undertaken for both $E_D(\lambda)$ and $E_{D\,PAR}$ using separate and independent instruments located at the ArcLight Light Observatory in Ny-Ålesund, Svalbard (78.94116°N, 11.84207°E), location shown in Figure 2.3.

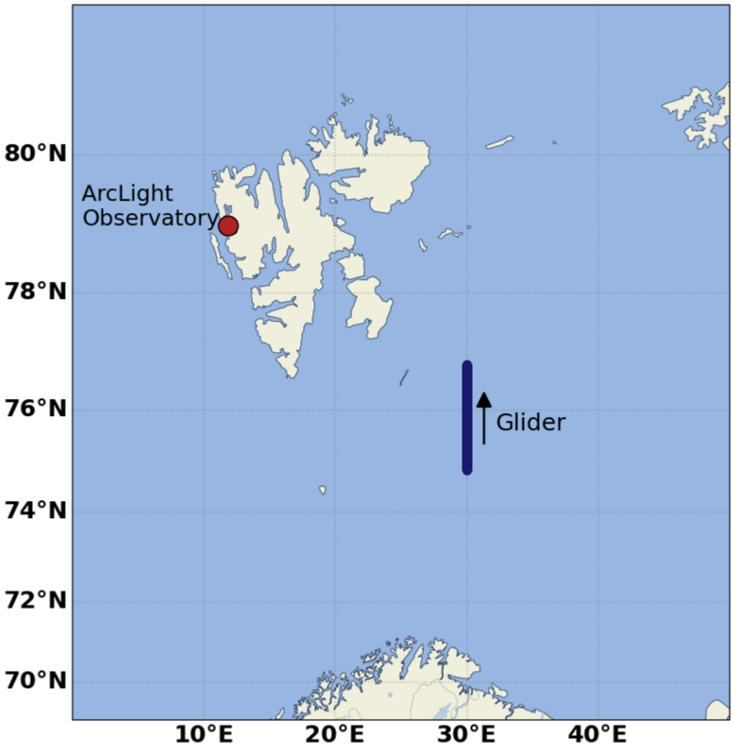

Figure 2.3: Location of the ArcLight Light Observatory and representative path along 30°E transect traversed by autonomous glider.

Underwater validation was undertaken using modelled results from the Hydrolight radiative transfer software for a variety of optical conditions for both $\mathrm{E_{D\,PAR}}$ and $\mathrm{E_D}(\lambda)$. Additional validation of underwater $\mathrm{E_{D\,PAR}}$ was undertaken using results from a PAR sensor attached to an underwater autonomous glider deployed in the Barents Sea along 30°E (Figure 2.3).

2.2.1 Above Surface Validation

Spectral Domain

Downwelling spectral irradiance ($\mathrm{E_D}(\lambda)$) was measured at the ArcLight Light Observatory using an USSIMO (In-situ Marine Optics, Perth, WA, Australia) hyperspectral radiometer designed for light collection in daylight conditions (Berge et al., 2021b). As the instrument was situated beneath a plexiglass dome, all recorded values of $\mathrm{E_D}(\lambda)$ were adjusted to account for dome transmission (Johnsen et al., 2021c).

Measurements were taken at 30-minute intervals over the range 300 – 1100 nm at 10 nm resolution in units of $\mathrm{W\,m^{-2}\,nm^{-1}}$. Solar zenith angle was then calculated using the method of Reda and Andreas (2004) for the observatory location and timestamp recorded by the instrument, adjusted to UTC. Figure 2.4 shows selected spectral irradiances as a function of solar zenith angle. Data show a clear sensitivity limit of the spectroradiometer occurring around 10^{-4} $\mathrm{W\,m^{-2}\,nm^{-1}}$ as confirmed by Johnsen et al. (2021c). This restricts suitable validation measurements to zenith angles $\leq 97°$, and so measurements recorded at greater zenith angles have been excluded for the validation process.

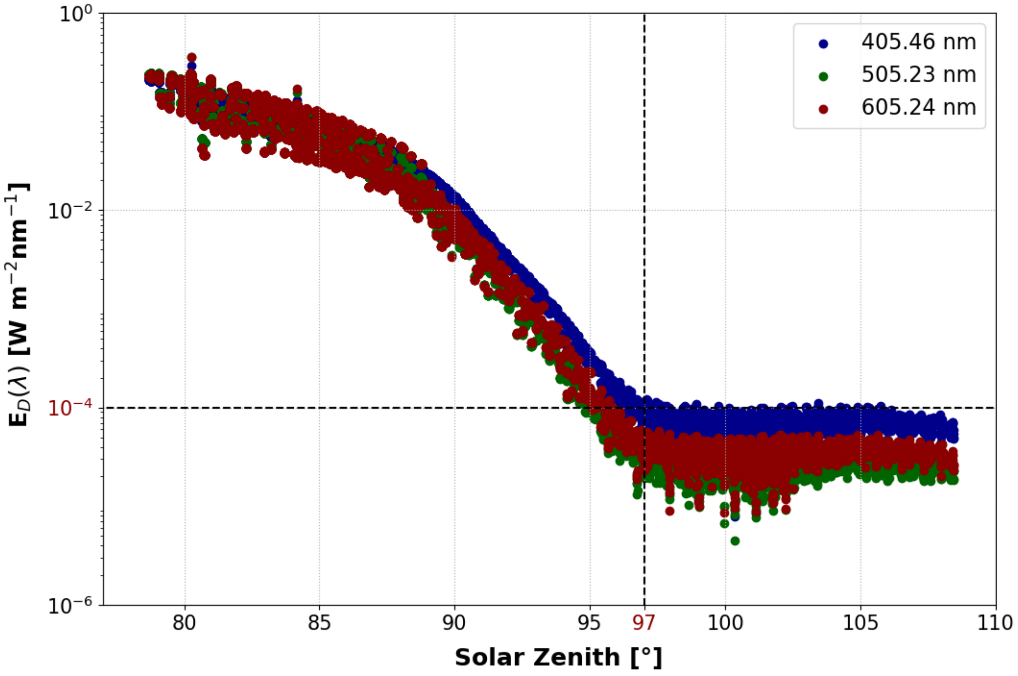

Figure 2.4: Subset of spectral irradiance measured at the ArcLight Light Observatory (78.94116°N, 11.84207°E). Dashed lines show sensor limitation for shortest wavelength required for HEIMDALL validation and associated zenith angle this occurs.

To validate the approach of HEIMDALL to estimate cloud-free solar spectral irradiance after sunset (Section 2.1.2), measurements recorded by USSIMO during February and March 2018 were extracted in the 400 – 700 nm range, filtered for cloud and moon free conditions using techniques described in Sections 2.1.5 and 2.1.3, and linearly interpolated to match selected wavelengths described in Sections 2.1.1–2.1.4 (405 – 695 nm in 10 nm intervals).

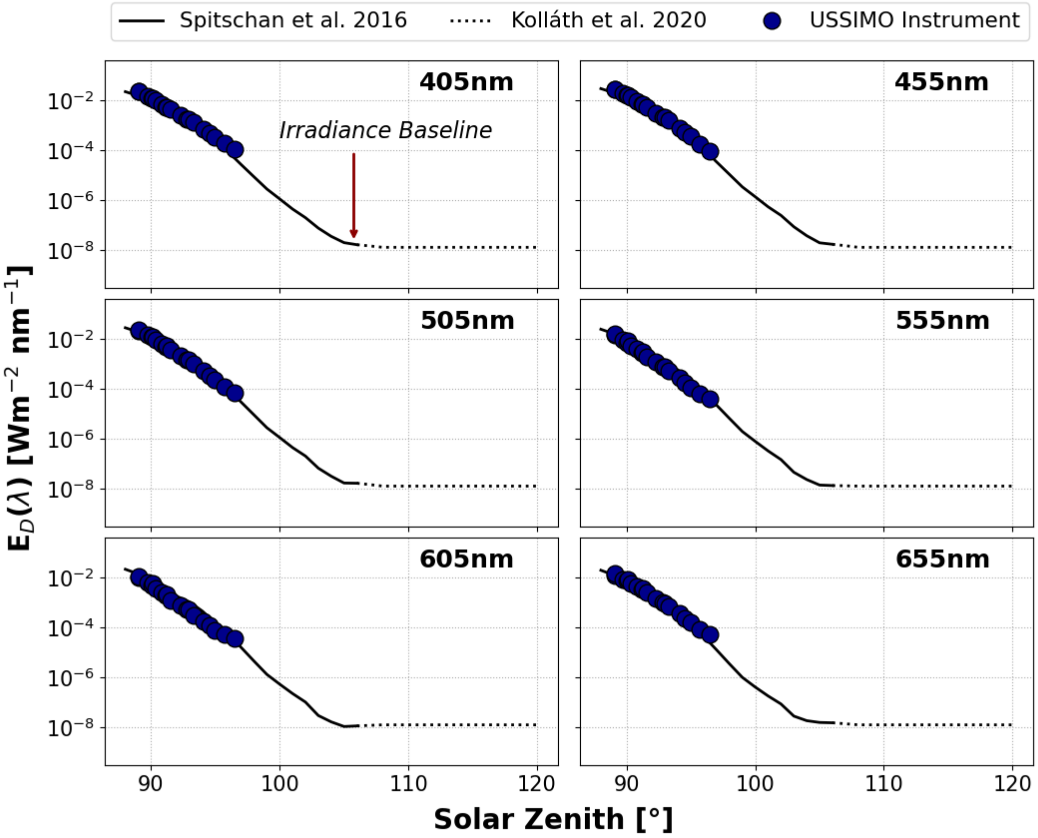

Figure 2.5: Spectral irradiance($E_D(\lambda)$) measured at ArcLight Light Observatory (symbols) and $E_D(\lambda)$ values from the literature (black solid and black dotted) used in HEIMDALL.

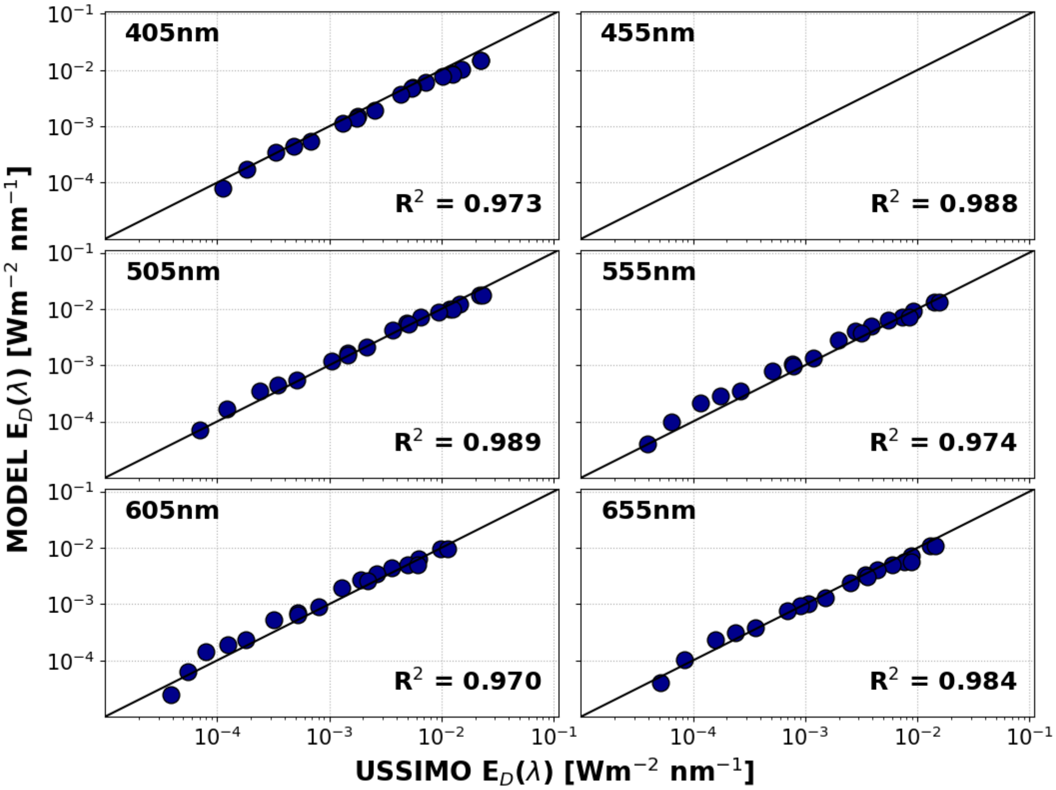

Figure 2.6: Spectral irradiance($E_D(\lambda)$) measured at ArcLight Light Observatory (USSIMO) and $E_D(\lambda)$ predicted by HEIMDALL (MODEL) using data from Spitschan et al. (2016). Coefficient of determination (R^2) noted for each wavelength.

As shown in Figures 2.5 and 2.6, measurements at the ArcLight Light Observatory at 79°N are in agreement ($R^2 \geq 0.97$) with those recorded at Cherry Springs State Park at 42°N (Spitschan et al., 2016) when both are filtered for the same clear sky conditions and binned as a function of solar zenith angle. The USSIMO instrument reaches a sensitivity limit at approximately 97° zenith and as a consequence irradiance comparisons cannot be made beyond this value. Since we see a strong agreement between valid measurements and modelled data (Figure 2.6), it is assumed the full range of values collected at 42°N up to a maximum solar zenith angle of 106° are valid for use in HEIMDALL. When solar zenith angle exceeds 106°, the spectrally flat clear sky baseline irradiance value described in Section 2.1.4 is applied. Note that Figure 2.6 shows a tendency for the model to slightly underestimate irradiance in the blue more than other wavelengths. As shown in the results from Spitschan et al. (2016), the shorter wavelengths dominate the spectral irradiance distribution at these solar angles and local topography may be impacting model results here. Localised snow covered terrain may be causing an unexpected increase in recorded irradiance levels at the ArcLight Light Observatory location. Amplification of above surface irradiance by snow will be explored in Chapter 4.

Broadband Domain

Above surface $E_{\mathrm{D\,PAR}}$ was also recorded at the ArcLight Light Observatory using a Canon D5 Mark III EOS camera (Canon Inc., Tokyo, Japan) in units of $\mathrm{W\,m^{-2}}$ at 60 minute intervals (Johnsen et al., 2021c, Johnsen et al., 2021b). To compare modelled and measured irradiance, the HEIMDALL light model was run at the observatory location and at timestamps recorded by the instrument, and compared with measured irradiance from 2018. Modelled spectral irradiance in the PAR range was integrated to calculate broadband irradiance ($E_{\mathrm{D\,PAR}}$) and converted from $\mathrm{\mu\,mol\,m^{-2}\,s^{-1}}$ to $\mathrm{W\,m^{-2}}$. Figure 2.7 shows modelled and measured $E_{\mathrm{D\,PAR}}$ from January, April and July 2018. These months have been chosen to reflect the period of Polar Night (JAN), day/night cycling (APR) and Polar Day (JUL). Modelled output includes contributions from solar and lunar spectral irradiance, modulated by local cloud cover estimates.

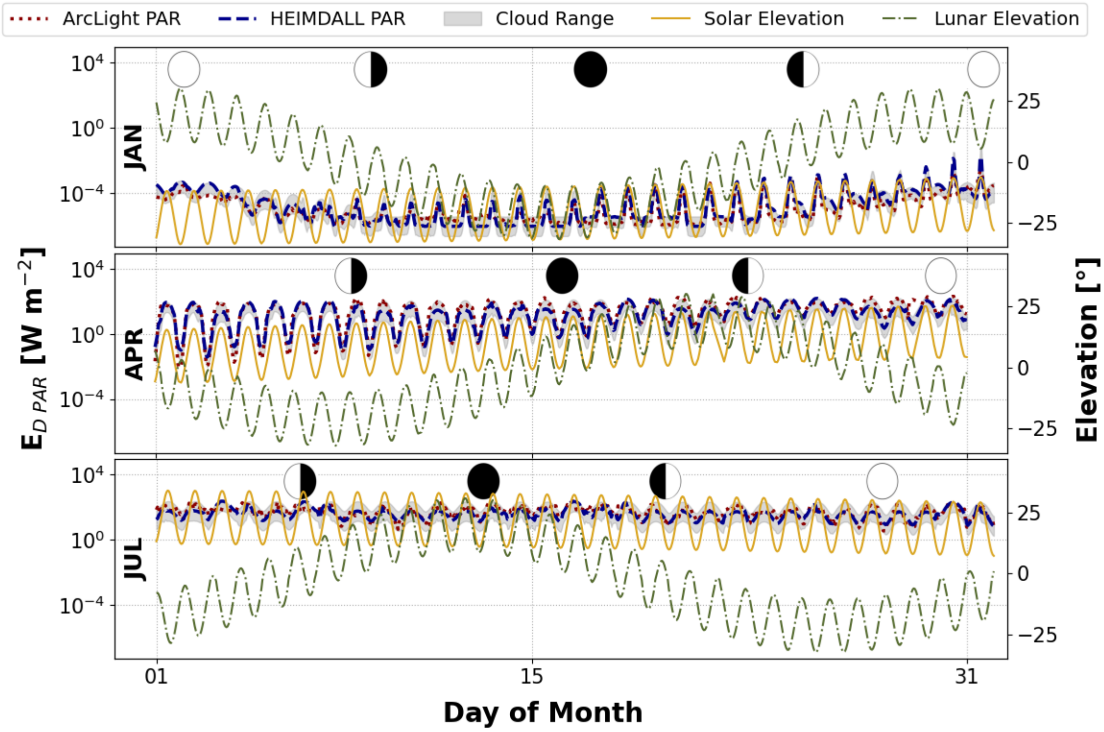

Figure 2.7: Modelled (dashed) and measured (dotted) PAR at 79°N in Ny-Ålesund, Svalbard in 2018. Grey shading indicates the range of variability that can be attributed to variation in cloud cover. Solar elevation (solid) and lunar elevation (dash-dot) are shown along with fractional lunar illumination.

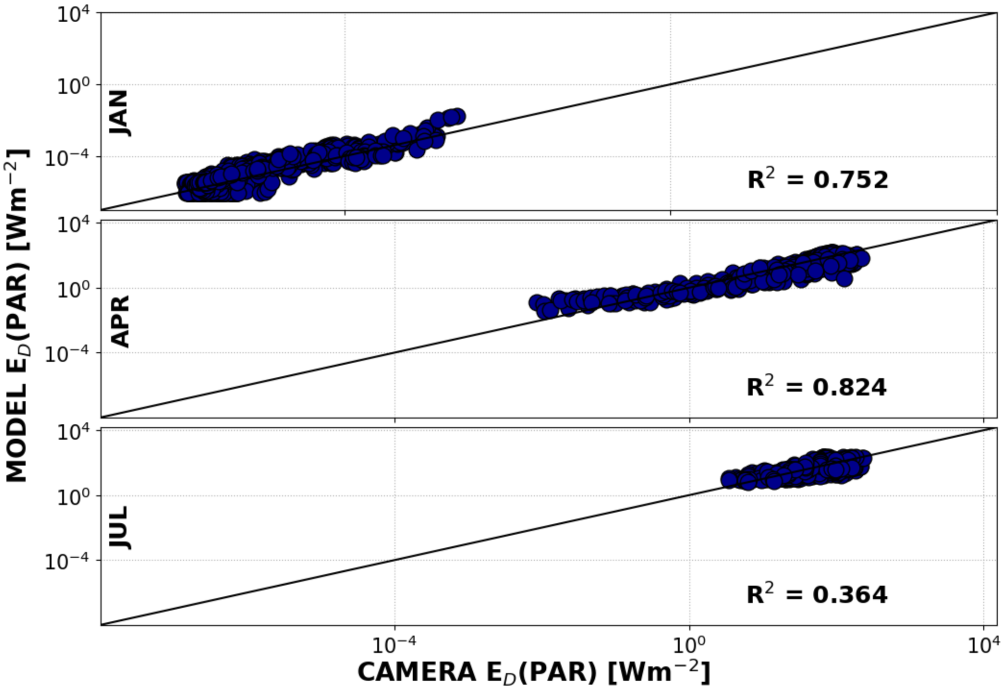

Figure 2.8: PAR irradiance(E_D(PAR)) measured at ArcLight Light Observatory (CAMERA) and E_D(PAR) predicted by HEIMDALL (MODEL). Coefficient of determination (R^2) noted for each season.

Fractional cloud cover data imported into HEIMDALL is an hourly average for the location over the preceding 60 min. Since this average value may not reflect the true cloud cover during an instantaneous measurement, Figure 2.7 also includes an estimated range within which real-time measurements may fall (Cloud Range). The upper and lower bounds of this range represent clear sky and overcast conditions, respectively. The Arctic generally experiences high levels of cloud (Schweiger, 2004, so overestimation of modelled irradiance is more likely if satellite estimates are incorrect. This is explored further in Chapter 4.

There are occasional periods of mismatch where the measured value falls outside of the range of possible modelled irradiance. This may be a result of several factors which cannot currently be accounted for within HEIMDALL, for example, active precipitation, heavy fog, snow cover, aurora or local light pollution. In general, there is a good degree of match up with the model output and the measured data from the ArcLight Light Observatory particularly for January and April (Figure 2.8) with $R^2 = 0.752$ and 0.824 respectively. The model demonstrates the ability to capture the behaviour of the moonlight during the Polar Night both in magnitude and time. This is particularly evident in the first panel of Figure 2.7 where a circumpolar full moon is the dominant source of irradiance at the beginning of the month, before transitioning to a new moon on January 17th. The moon then remains below the horizon (elevation $< 0°$) from January 11th–19th inclusive and midday solar irradiance is dominating $E_{D\,PAR}$. Although the sun is still below the horizon over this period, it has a midday zenith angle of around 100° and so has not yet reached the zenith angle for baseline irradiance (Section 2.1.2). As the month progresses, the moon emerges back above the horizon and to full moon phase on the 31st. Simultaneously, the midday sun moves closer to the horizon, where it begins to overtake as the dominant irradiance source. In the absence of moonlight, a noticeable baseline value of $E_{D\,PAR}$ is reached of order 10^{-6} W m^{-2}, consistent with the measured background dark-sky irradiance discussed in Section 2.1.4. There is more variation in modelled data for July (Figure 2.8), with a lower $R^2 = 0.364$. During this period, the sun is continually above horizon and so local topography may be inducing an azimuthal component in irradiance values, with surrounding terrain perhaps partially blocking direct irradiance. Both April and July show model underestimation at the higher magnitudes, indicating more variance during clear days or when the sun is at a higher elevation. The impacts of local topography are discussed further in Chapter 4.

2.2.2 Below Surface Validation

Spectral Domain

State of the art radiative transfer models for predicting underwater light fields are available, such as the widely use proprietary software Hydrolight (Numerical Optics Ltd, Devon, UK). Although Hydrolight can provide very precise estimates of underwater irradiances, the process can be time expensive, is limited to above horizon solar irradiance only, and is not optimized to operate over dynamic spatial-temporal domains. To assess the capability of HEIMDALL to perform in realistic marine environments, performance has been compared against Hydrolight for a range of optical and environmental conditions. Well-mixed, surface maximum and sub-surface maximum chlorophyll *a* profiles were extracted from data gathered by gliders deployed in the Barents Sea to be used as test cases as shown in Figure 2.9.

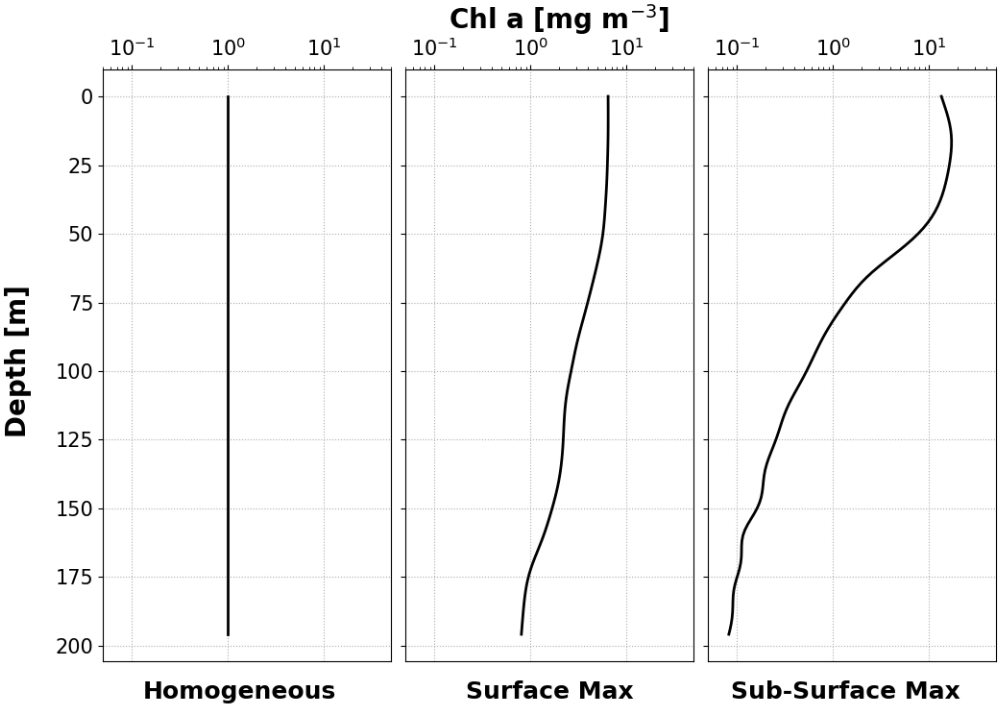

Figure 2.9: Input chlorophyll *a* profiles used to test HEIMDALL against Hydrolight.

For each of the three profiles, salinity was kept at a constant value of 35 PSU, a typical value for the Barents Sea region that also experiences minimal seasonal variation (Kostakis et al., 2020). Inherent optical properties were provided to both HEIMDALL and Hydrolight using the Barents Sea bio-optical model described in Section 2.1.7 and run for solar zenith angles of 30°, 60°, 80° and 0%, 50%, 100% cloud cover.

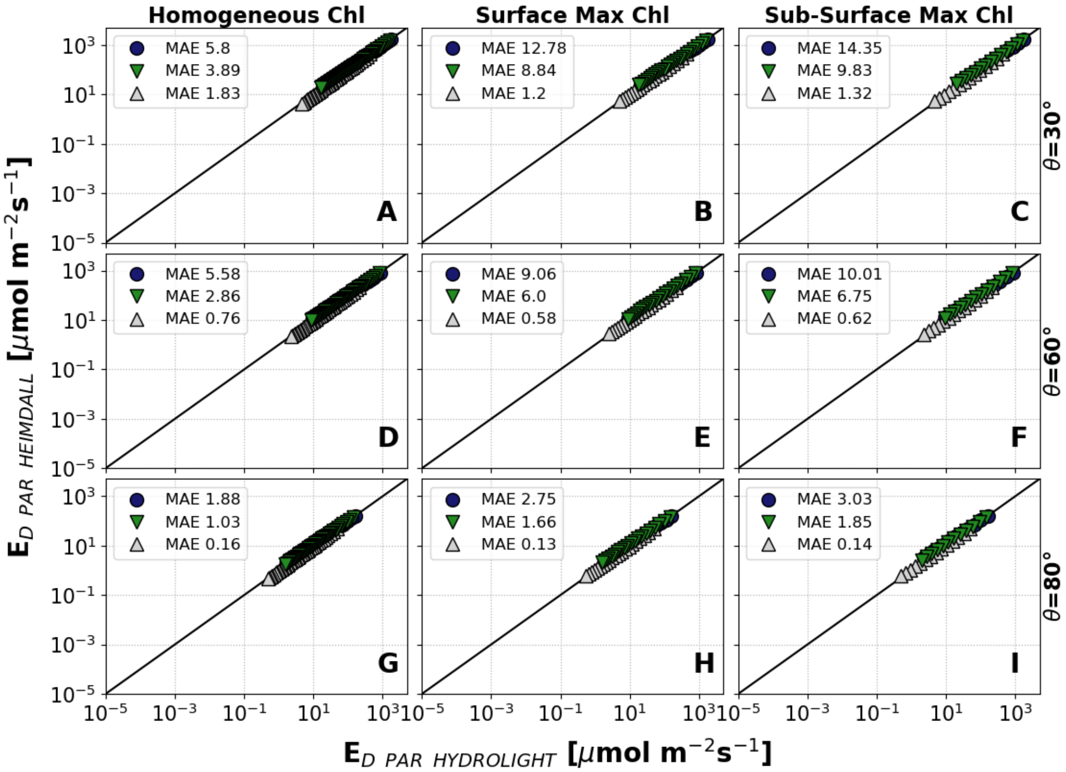

Figure 2.10: $E_{D\,PAR}$ from Hydrolight and HEIMDALL for various optical and environmental conditions. 0% Cloud (blue circle), 50% Cloud (green triangle down) and 100% Cloud (grey triangle up). Values shown cover depth from surface to 1% surface light level. Mean absolute error (MAE) shown for each run, in units of $\mu\,\mathrm{mol}\,\mathrm{m}^{-2}\,\mathrm{s}^{-1}$.

Figure 2.10 shows estimates of $E_{D\,PAR}$ from HEIMDALL and Hydrolight at 1m depth resolution over the euphotic zone (from surface down to depth z at which $E_{D\,PAR}(z) = 1\%$ $E_{D\,PAR}(z = 0)$ level). The mean absolute error (MAE) for each run is shown in units of $\mu\,\mathrm{mol\,m^{-2}\,s^{-1}}$. As expected, this decreases as the cloud cover increases for each simulation due to the smaller surface light levels. For a range of optical and environmental conditions, there is minimal variability in the performance of HEIMDALL compared with Hydrolight. MAE was chosen as a preferred performance indicator due to the large range of magnitudes.

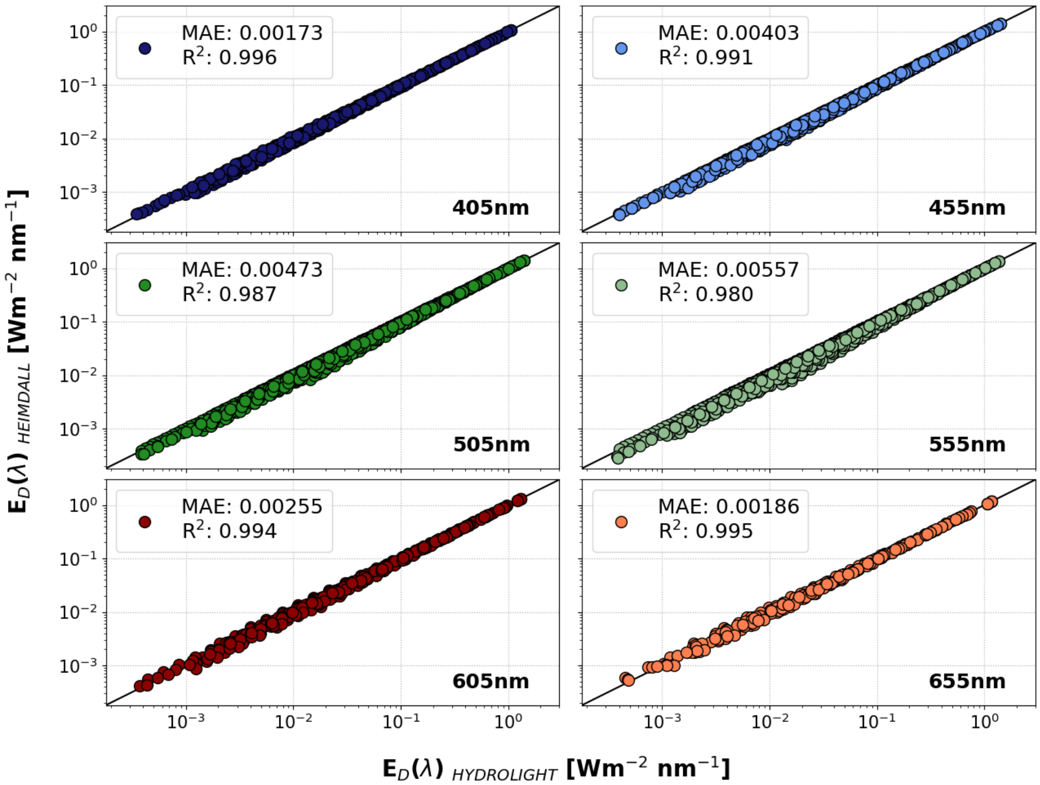

Figure 2.11: Aggregated $E_D(\lambda)$ from Hydrolight and HEIMDALL for selected wavelengths. Mean absolute error (MAE) shown in units of $\mathrm{W\,m^{-2}\,nm^{-1}}$ and coefficient of determination (R^2) shown. Values shown cover depth from surface to 1% surface light level.

Figure 2.11 shows aggregate spectral irradiances from HEIMDALL compared to Hydrolight values for selected wavelengths and for all optical and environmental conditions tested. Mean absolute error (MAE) for $\mathrm{E_D}(\lambda)$ is shown for each wavelength in units of $\mathrm{W\,m^{-2}\,nm^{-1}}$. MAE is lower for red wavelengths as rapid absorption in surface layers leads to generally small values. For each of the wavelengths shown the MAE is in the region $10^{-3}\ \mathrm{W\,m^{-2}\,nm^{-1}}$ for each wavelength, relatively small compared to overall irradiance which ranges from $10^{-4}\ \mathrm{W\,m^{-2}\,nm^{-1}}$ at the bottom of the euphotic zone to $10^{0}\ \mathrm{W\,m^{-2}\,nm^{-1}}$ at the surface. These results are typical for all wavelengths in the PAR range. Results predicted by HEIMDALL show excellent agreement with those predicted by Hydrolight, with all wavelengths demonstrating $\mathrm{R}^2 \geq 0.98$ over the euphotic zone.

Extending both comparisons of $\mathrm{E_{D\,PAR}}$ and $\mathrm{E_D}(\lambda)$ to a test depth of 100m results in similar performance in HEIMDALL compared to Hydrolight.

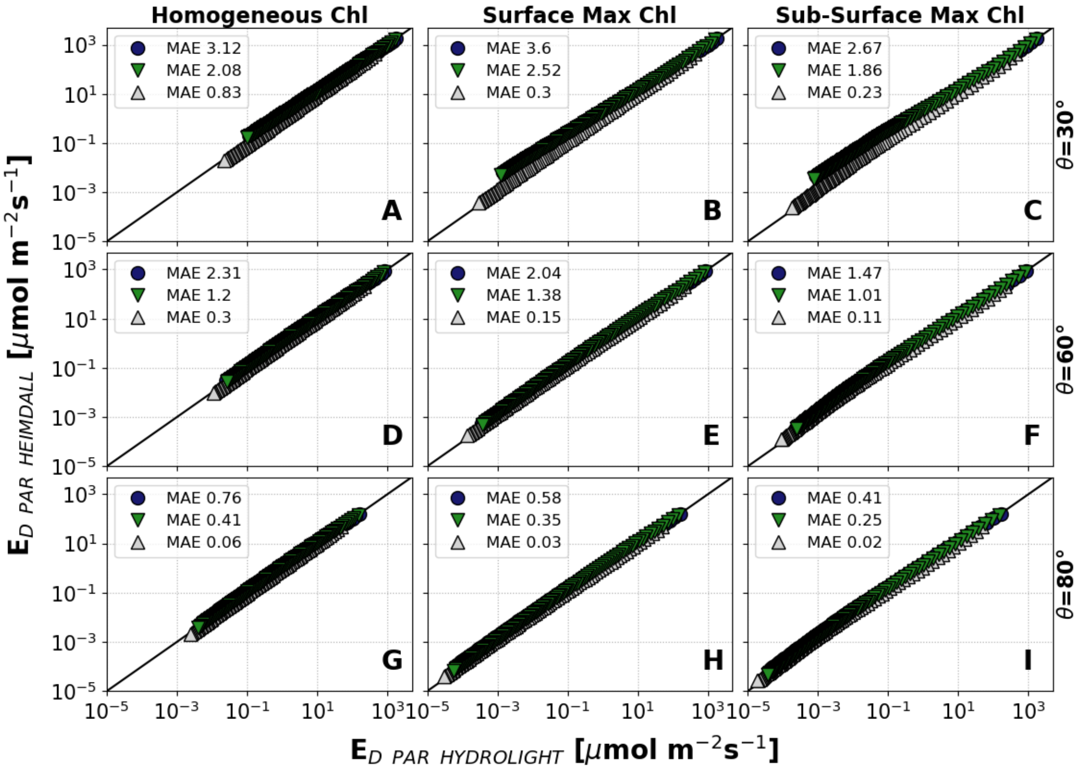

Figure 2.12: $E_{\mathrm{D\,PAR}}$ from Hydrolight and HEIMDALL for various optical and environmental conditions. 0% Cloud (blue circle), 50% Cloud (green triangle down) and 100% Cloud (grey triangle up). Values shown cover depth from surface to 100m. Mean absolute error (MAE) shown for each run, in units of $\mu\,\mathrm{mol\,m^{-2}\,s^{-1}}$.

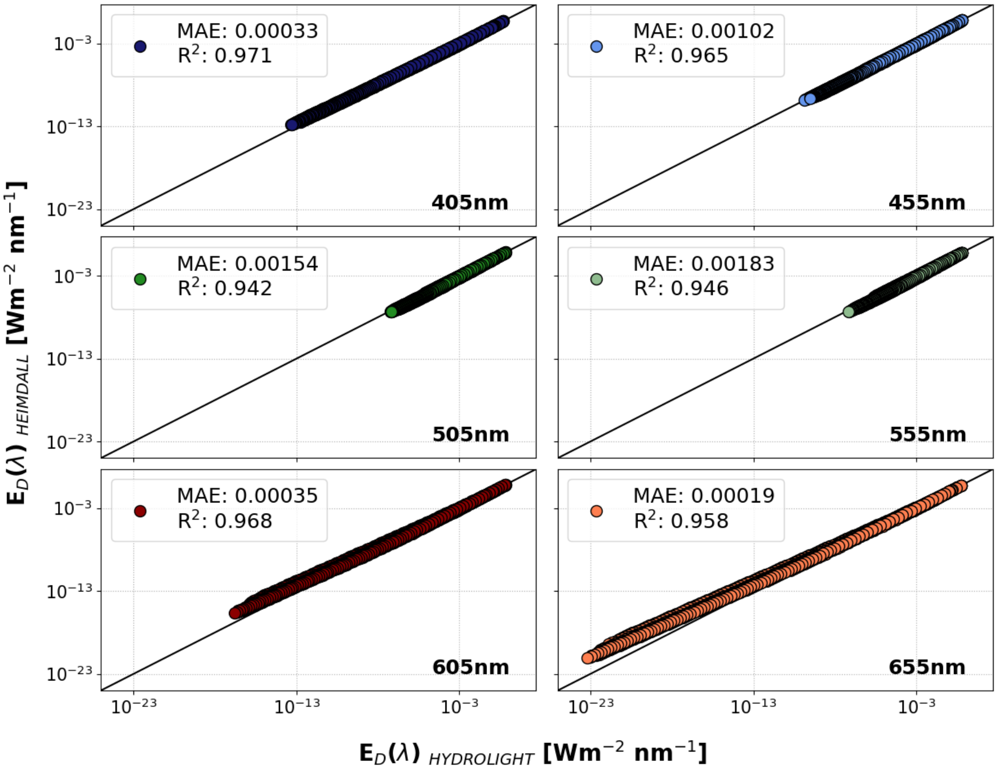

Figure 2.13: Aggregated $E_D(\lambda)$ from Hydrolight and HEIMDALL for selected wavelengths. Values shown cover depth from surface to 100m. Mean absolute error (MAE) shown in units of $W\,m^{-2}\,nm^{-1}$ and coefficient of determination (R^2) shown.

Figures 2.12 and 2.13 show HEIMDALL performance over 100m water columns with mean absolute error (MAE) and coefficient of determination (R^2) noted for each wavelength. Results show more of a divergence in HEIMDALL modelled $E_D(\lambda)$ compared with Hydrolight $E_D(\lambda)$ for the longer wavelengths. Since these wavelengths attenuate more rapidly in the water column, it may be the case that the random nature of individual photon scattering interactions is more important when predicting irradiance levels with such low magnitudes (in the region 10^{20}).

Hydrolight is designed to provide a full representation of the light field while HEIMDALL is restricted to downwards irradiance only. As a result, HEIMDALL is able to produce E_D profiles faster than Hydrolight. A typical 200 m depth profile is produced by HEIMDALL in approximately 15 seconds and is independent of column structure, compared to > 23 seconds for Hydrolight for a homogeneous water column and >300 s for a structured column. Simulations were run using an Intel® Core™ i7-9750H CPU at 2.60 GHz.

Broadband Domain

Model output was also compared against $E_{D\,PAR}$ data collected from underwater gliders in the Barents Sea (Porter et al., 2020). Autonomous G2 Slocum gliders (Teledyne, California, USA) were deployed along 30°E (Figure 2.3) from January to June 2018 equipped with an $E_{D\,PAR}$ sensor (Biospherical Instruments Inc, San Diego, USA), a CTD sensor for temperature, salinity, and depth (Sea-bird Scientific, Washington, USA) and an ECO-triplet sensor to estimate concentration of chlorophyll *a*, CDOM and total backscattering at 700 nm (WET Labs Inc, Oregon, USA).

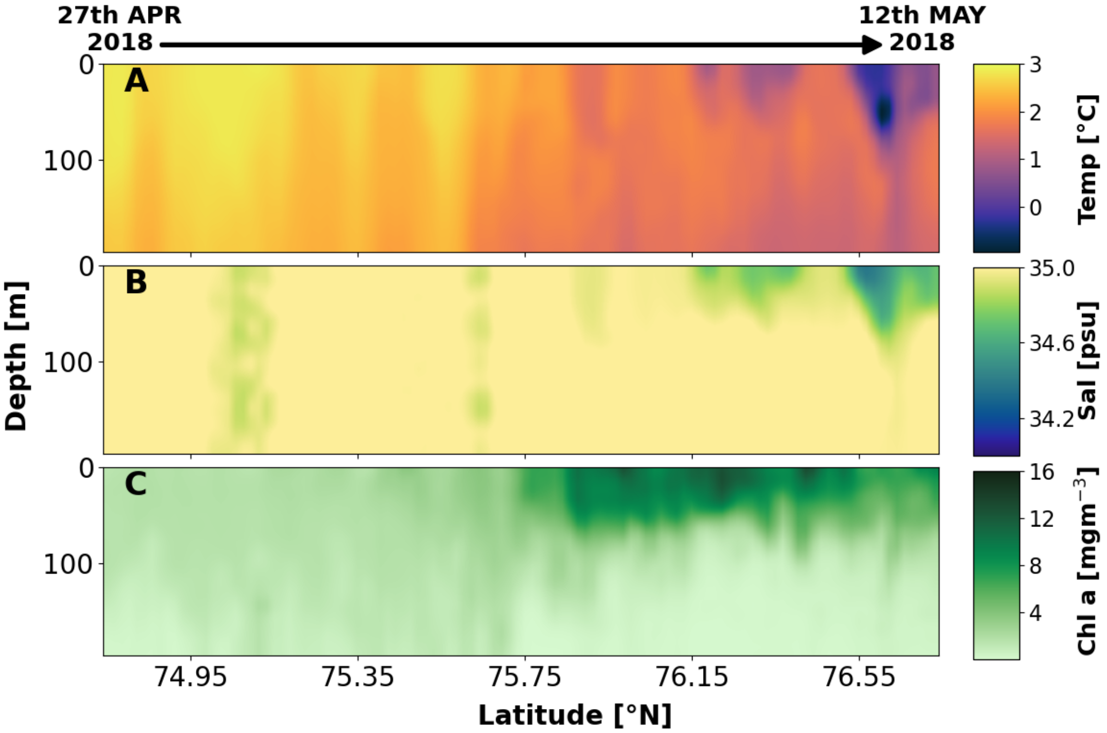

Figure 2.14: Profiles of (A) temperature, (B) salinity, and (C) chlorophyll *a* concentration (determined via a combination of fluorescence and backscatter measurements) collected via autonomous glider in the Barents Sea during Spring 2018. Note the occurrence of the spring bloom north of 75.75°N.

The period of 27 April 2018 – 12 May 2018 covers 406 individual depth profiles collected in a sawtooth pattern from 74.75°N to 76.73°N, where one depth profile is defined as surface to depth and back to surface. This time period was chosen for validation as it contained the largest data set collected from a single transect during the campaign. Data collected and used as inputs for testing the HEIMDALL model were salinity, chlorophyll *a* concentration and backscatter at 700 nm. Chlorophyll *a* concentration was determined by *in situ* chlorophyll *a* fluorescence ($\mathrm{Chl_{fl}}$) when $\mathrm{Chl_{fl}} < 2\,\mathrm{mg\,m^{-3}}$ and via backscattering when $\mathrm{Chl_{fl}} \geq 2\,\mathrm{mg\,m^{-3}}$ as described by Kostakis et al. (2020). This approach is to mitigate the effects of solar quenching in chlorophyll *a* concentration measured by fluorescence. Inherent optical properties were then calculated using the bio-optical model for the region described in Section 2.1.7.

Figure 2.14 shows the measured profiles across the collection period after undergoing a gridding process. Due to constraints of the battery on board the autonomous glider, salinity, fluorescence and backscattering were not measured at consistent depths and required interpolation into equidistant latitudes and depths. This was undertaken by Porter et al. (2020) before the data was acquired for this research.

Recorded timestamps from individual raw profiles were imported into HEIMDALL to calculate local solar and lunar positions and cloud cover, with the pressure measurements in decibars from the CTD used as output depths in meters.

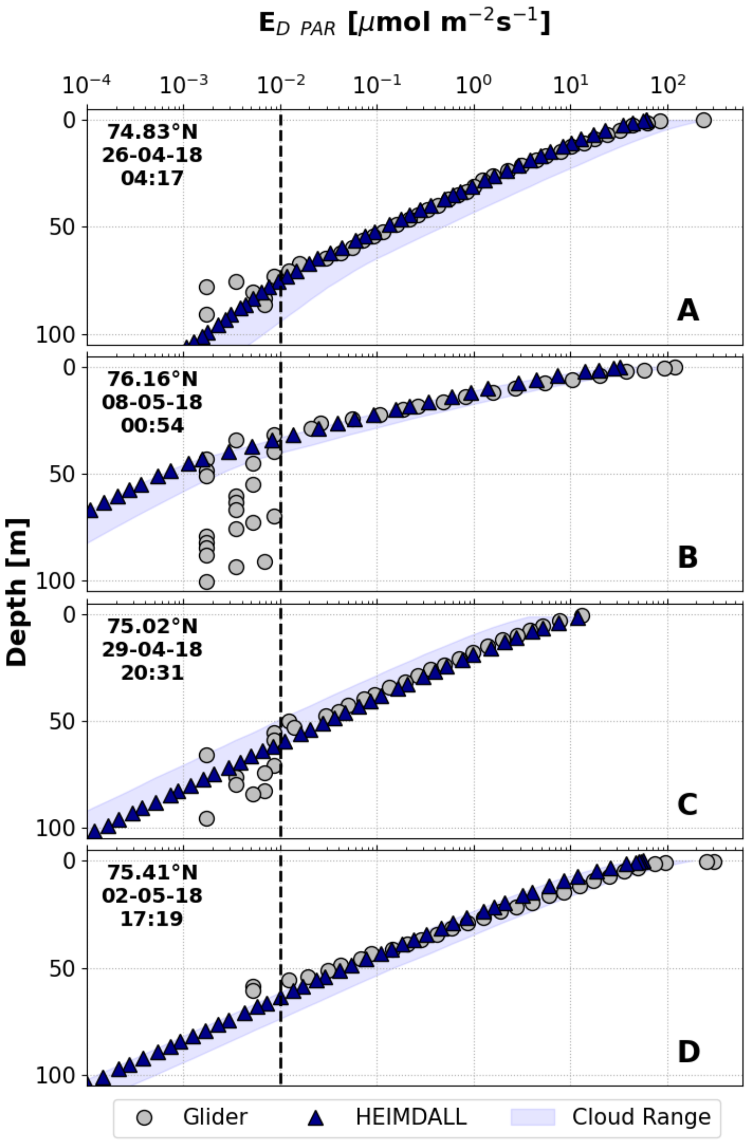

Figure 2.15: Modelled and measured $E_{\mathrm{D\,PAR}}$ from the Barents Sea during 2018. Shaded blue area is possible range of $E_{\mathrm{D\,PAR}}$ depending on local cloud cover. Dashed vertical line represents lower limit of reliability of glider measured $E_{\mathrm{D\,PAR}}$.

A comparison of modelled and measured $\mathrm{E_{D\,PAR}}$ is shown in Figure 2.15. A sample of 4 of the 406 measured profiles have been shown for comparison, chosen via a pseudo-random number generator.

Since glider data bio-optical data and PAR data were not collected at the same depths, a direct comparison of modelled and measured light cannot be made in terms of quantifying error for in Figure 2.15. Measured $\mathrm{E_{D\,PAR}}$ appears to hit a sensitivity baseline value of order $10^{-2}\,\mu\mathrm{mol\,m^{-2}\,s^{-1}}$. It can be challenging to quantify exactly where the data is no longer reliable, but it is likely from Figure 2.15 that this is the approximate sensitivity baseline of the $\mathrm{E_{D\,PAR}}$ sensor on board. HEIMDALL modelled values were calculated at depths where bio-optical data were measured by the glider, which did not always correspond to the same depths where PAR was measured. By interpolating modelled values to match those depths where PAR was measured, a direct comparison between modelled and measured data can be explored as shown in Figure 2.16. Note that glider PAR values that fall below the sensitivity baseline ($10^{-2}\,\mu\mathrm{mol\,m^{-2}\,s^{-1}}$) have been excluded. For all profiles shown, modelled and measured PAR values exhibit strong agreement with $\mathrm{R}^2 \geq 0.939$, demonstrating the ability of HEIMDALL to accurately predict underwater PAR over large spatial temporal ranges in structured water columns.

For a large-scale overview of modelled and measured $\mathrm{E_{D\,PAR}}$, data from HEIMDALL and the glider were both gridded using a Barnes Objective Analysis approach for irregularly spaced data. Each of the modelled and measured datasets were interpolated using the same method and parameters, obtained from Porter et al. (2020). Figure 2.17 shows both modelled and measured $\mathrm{E_{D\,PAR}}$ that has been mapped for equidistant latitudes and depths. Measured data $< 10^{-2}\,\mu\mathrm{mol\,m^{-2}\,s^{-1}}$ has been masked due to unreliability of data.

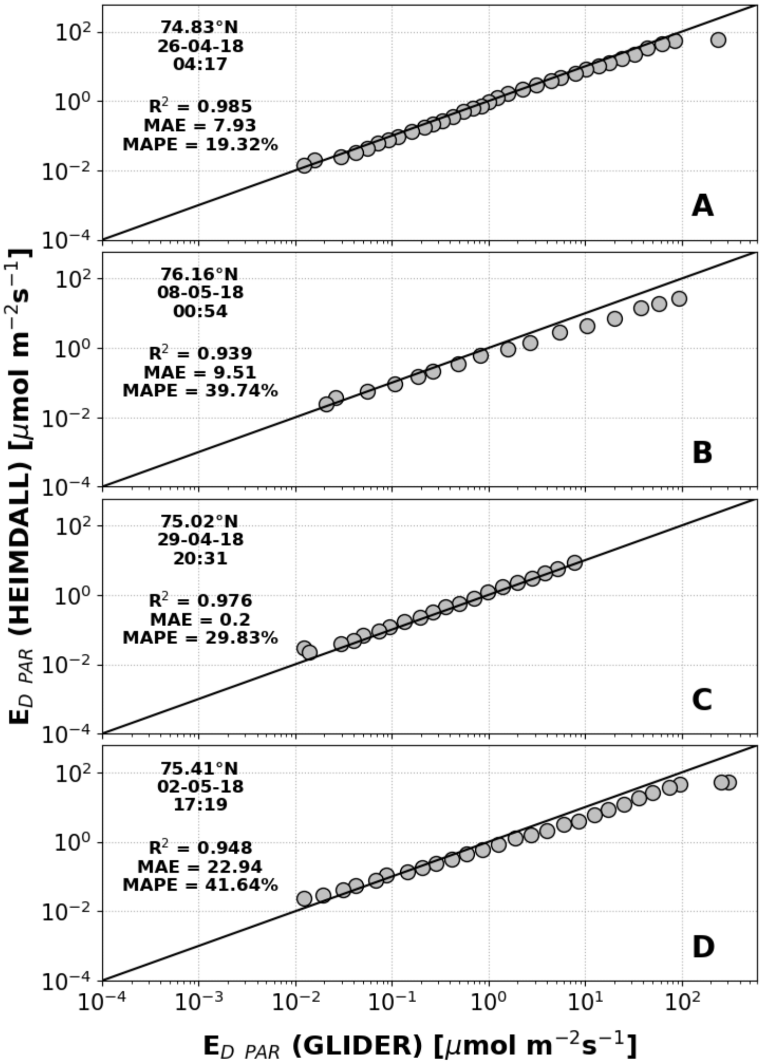

Figure 2.16: Modelled and measured $E_{\mathrm{D\,PAR}}$ from the Barents Sea during 2018, with MAPE, coefficient of determination (R^2) and MAE in units of $\mu\,\mathrm{mol\,m^{-2}\,s^{-1}}$ shown for each profile. Note that HEIMDALL $E_{\mathrm{D\,PAR}}$ have been interpolated to match depths where a valid PAR measurement was recorded by the glider.

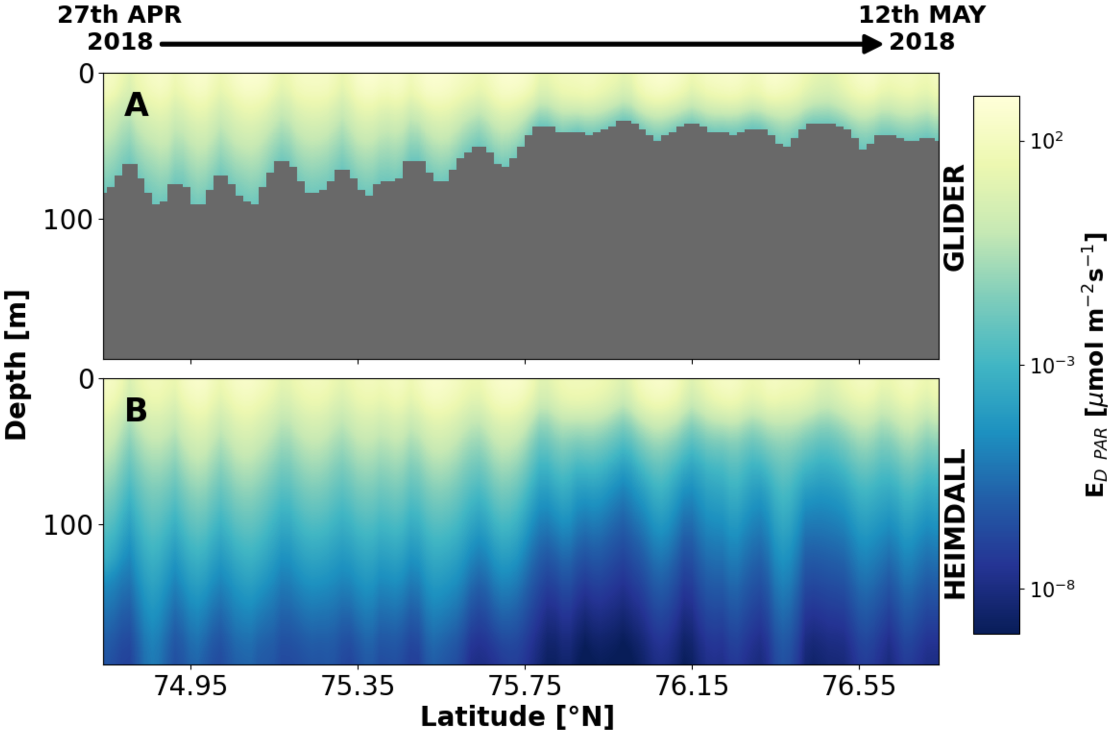

Figure 2.17: (A) Measured (GLIDER) and (B) modelled (HEIMDALL) $E_{\mathrm{D\,PAR}}$ from the Barents Sea during 2018 after gridding process. Data shown is for equidistant latitudes and depths. Measured data below the light sensor sensitivity limit has been masked.

The modelled data demonstrate good agreement in both time and magnitude of measured underwater $E_{D\,PAR}$. Figure 2.17 also highlights the ability of HEIMDALL to substantially extend data availability several orders of magnitude beyond the sensitivity limit of the on-board $E_{D\,PAR}$ sensor.

Figure 2.18 demonstrates a direct comparison between the measured and modelled $E_{D\,PAR}$ profiles after gridding with associated MAE. Note that the gridded data profiles presented in Figure 2.18 are not directly comparable to the raw data profiles presented in Figure 2.15. The data shown in Figure 2.15 are a comparison of $E_{D\,PAR}$ measured *in situ* against $E_{D\,PAR}$ modelled using measured bio-optical data collected at specific depths. Data presented in Figure 2.18 are a comparison of two interpolated datasets. Disagreement between these data at larger magnitudes is likely due to cloud cover variation (Section 2.1.5), highlighted in Figure 2.15. At lower magnitudes, it is likely that erroneous measurements were recorded by the $E_{D\,PAR}$ sensor due to limitations in equipment sensitivity, and those measurements have introduced biases during the interpolation process. Data obtained from Porter et al. (2020) show that occasionally the sensor would reach a measurement plateau at depth (as seen in Figure 2.15B), however more frequently it would record negative $E_{D\,PAR}$ values, resulting in an excessive reduction in nearby interpolated data. Note that the MAPE displayed in Figure 2.18 appears to be large and it should be expected that variation in local cloud cover alone could introduce a variation of up to factor 4 (Section 2.1.5). Despite this, the model appears to show significant agreement ($R^2 = 0.945$) with PAR measurements from the Barents Sea for a variety of weather and water column conditions.

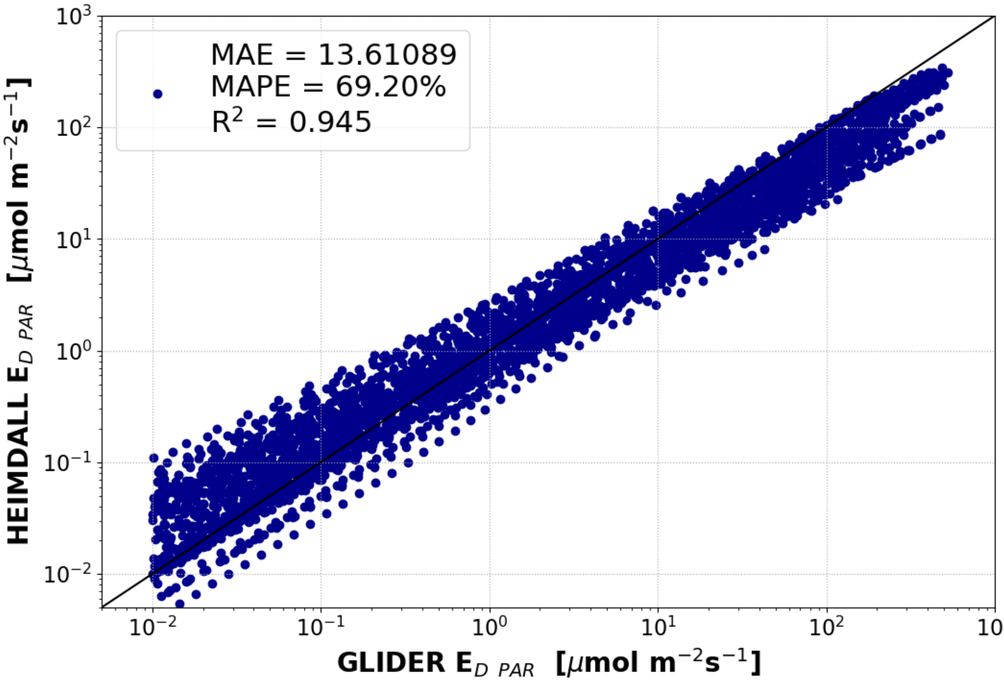

Figure 2.18: Comparison of measured and modelled $E_{D\,PAR}$ from the Barents Sea. MAPE and coefficient of determination (R^2) shown with MAE noted in units of $\mu\,mol\,m^{-2}\,s^{-1}$.

2.3 Comparisons to Current Models

Many ecosystem models that rely on light as a key driver currently parameterise light fields through the use of radiative transfer software such as Hydrolight, or satellite estimates of daily radiation (Hill et al., 2018, Freer et al., 2021). Available sources to estimate PAR include the NASA MODIS-AQUA satellite and the Copernicus Climate Change ERA5 Data Reanalysis (NASA, 2014, Hersbach et al., 2018). These data products provide PAR estimates at detailed spatial and temporal resolution but struggle at high latitudes, particularly in winter months. Figures 2.19 and 2.20 show Pan-Arctic light maps using both of these products during a period of Polar Night in the Arctic. Note that data below the sensitivity limit of the sensors has been masked.

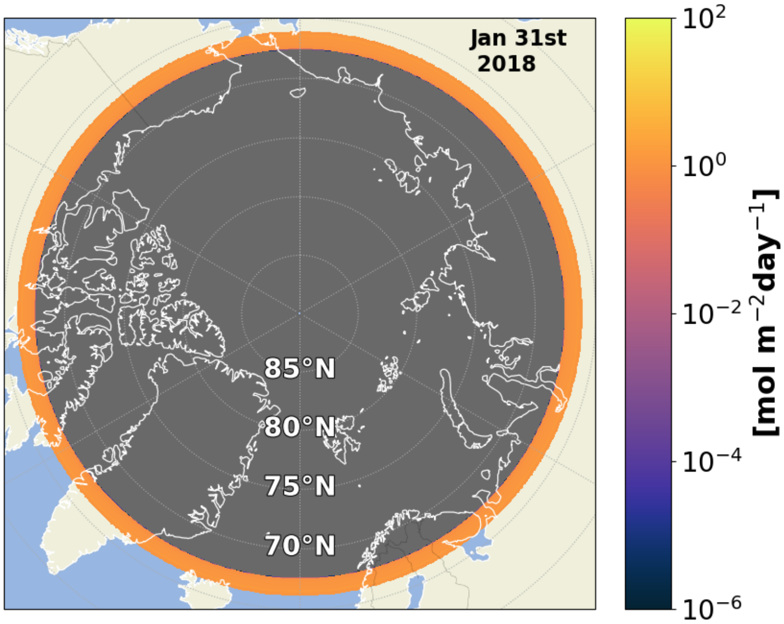

Figure 2.19: Pan-Arctic map of measured daily $E_{D\,PAR}$ determined by NASA MODIS-AQUA Satellite Data in photon count units of mol m^{-2} day^{-1}. Data from NASA (2014).

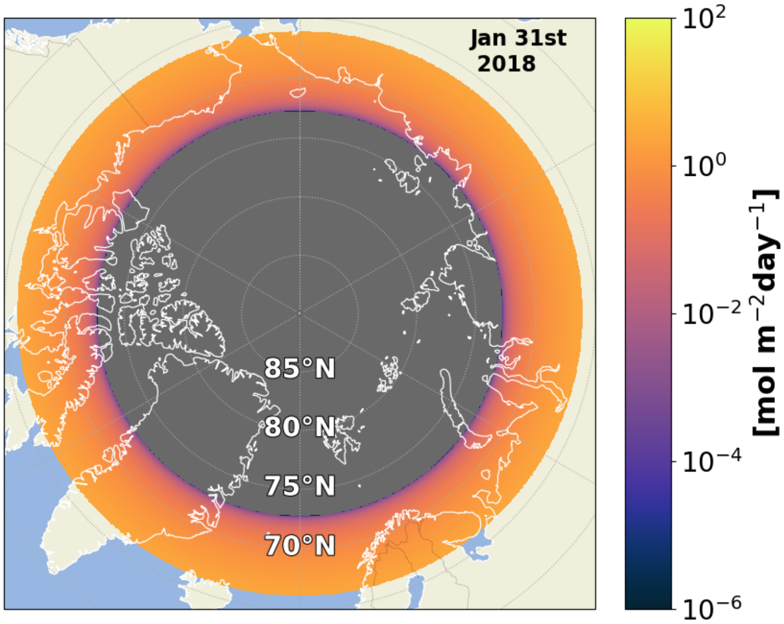

Figure 2.20: Pan-Arctic map of clear sky daily $E_{D\,PAR}$ determined by Copernicus Climate Change Service Reanalysis Data in photon count units of mol m^{-2} day^{-1}. Data from Hersbach et al. (2018).

Data from Figure 2.7 demonstrate that in late January, although the sun remained below horizon, it was the dominant source of irradiance at a latitude of ≈ 79°N. During this time period, MODIS is unable to measure PAR data above ≈ 67.5°N (Figure 2.19), and the Copernicus ERA5 Reanalysis is unable to model above ≈ 72.5°N (Figure 2.20).

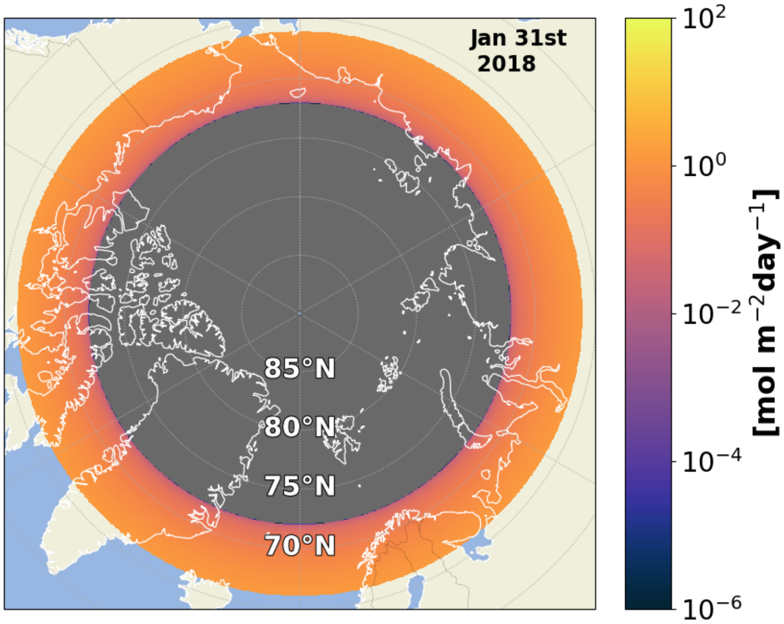

Figure 2.21: Pan-Arctic map of clear sky daily $E_{D\,PAR}$ determined by Hydrolight in photon count units of mol m^{-2} day^{-1}. Data from Mobley (2022).

Hydrolight daily PAR (Figure 2.21) demonstrates similar performance to the Copernicus ERA5 Reanalysis Data (Figure 2.20), reaching a limitation at ≈ 72°N. Data outside the limitations of Hydrolight have been masked.

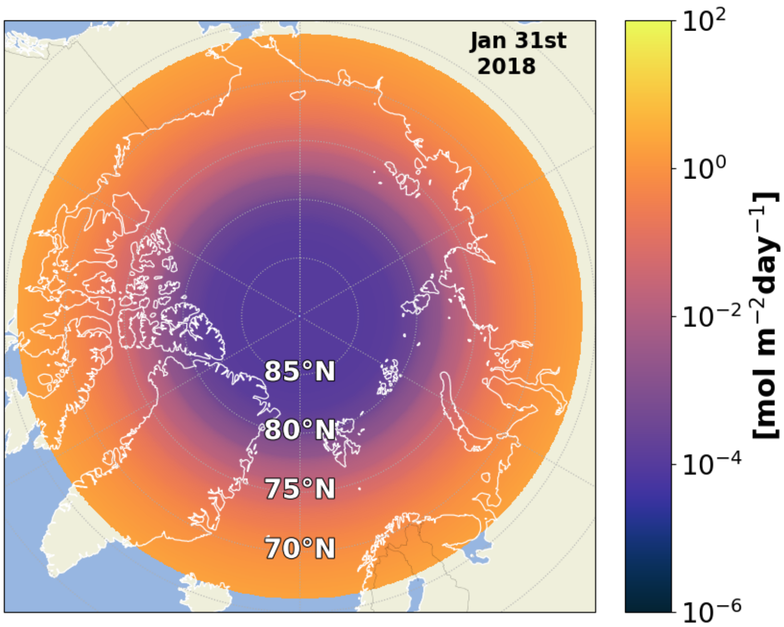

Figure 2.22: Pan-Arctic map of clear sky daily $E_{D\,PAR}$ determined by HEIMDALL in photon count units of mol m^{-2} day^{-1}.

Pan-Arctic light modelling using the HEIMDALL model (Figure 2.22) shows uninterrupted estimates of PAR during Polar Night. Due to their evident limitations, current light field parameterisations could potentially be missing biologically significant activity that could now be explored using HEIMDALL outputs. Work done by Berge et al. (2015a) reported that Arctic phytoplankton demonstrate rapid restoration of photosynthetic ability, with lab-based measurements of primary production detectable at 0.5 µmol m^{-2} s^{-1}. These light levels are typical for daytime in mid February at 80°N when the sun remains below horizon. Arctic zooplankton also exhibit a large-scale response to moonlight in the form of mass vertical migration correlated to lunar light (Last et al., 2016).

2.4 Model Limitations

Although HEIMDALL has global application in principle, one key limitation is a need to populate and define a suitable bio-optical model for the region of interest. This chapter has demonstrated that the bio-optical model for the Barents Sea proposed by Kostakis et al. (2020) performs well in this region and can be adequately populated using information provided by commonly deployed *in situ* sensors (CTD and ECO-triplet). However, as noted in Section 2.1.7, bio-optical model parameters are not universal. Accurate determination of optically significant constituent concentrations and associated IOPs would be required for optimal performance of HEIMDALL outside of the Barents Sea region.

An additional obstacle may be dependence on using satellite cloud cover data that operates on hourly averages, both in spatial and temporal dimensions. An hourly average cloud cover value may not accurately reflect the conditions during a single instantaneous measurement. Similarly, an average value covering a grid size of 0.25°x0.25° may not be indicative of cloud cover at a relatively small measurement location. These issues result in a modelled irradiance that can vary by a factor of 4 (Kasten and Czeplak, 1980).

2.5 Conclusions

Light measurement in Arctic waters continues to be a challenge due to extended periods of low light conditions, requiring sensitive equipment as well as difficulty in accessing many areas. This chapter has presented a hyperspectral model of underwater light that is able to provide fast and accurate light field estimates for the Barents Sea ($R^2 \geq 0.939$ for a range of environmental and water column conditions), capturing seasonal solar and lunar irradiance with modulation by local cloud conditions. HEIMDALL extends the range of light conditions that can be modelled beyond the capacity of Hydrolight, enabling estimation of underwater light levels during Polar Night when the sun is below the horizon. This is achieved whilst maintaining broad agreement with the more sophisticated Hydrolight radiative transfer model and providing a computationally efficient solution.

The ability to predict spectrally resolved light fields to depth and inclusion of a complete solar, lunar and dark-sky surface light model means HEIMDALL could be a useful tool in the study of estimating light-induced primary production as a function of time and space, providing depth resolved primary production estimates with the provision of either a spectral or broadband primary production model. Furthermore, HEIMDALL can be directly integrated into models of phytoplankton bloom dynamics and animal behaviour studies across the full annual cycle, filling gaps in existing datasets, particularly at high latitudes. Fully customisable depth and time resolution steps mean it should be possible to provide useful information for static positions (e.g., observatories on land, fixed moorings at sea) or for mobile operations (e.g., autonomous vehicles or tagged animals).

Chapter 3

Attenuation of Spectral Irradiance by Snow and Ice

Introduction

Characterising underwater diffuse attenuation coefficients ($\mathrm{K_d}$) in open water can be relatively straightforward, provided all optically significant constituents present in the water column have been identified and parameterised. The presence of sea ice and snow makes the task of estimating underwater $\mathrm{K_d}$ far more complex due not only to varying snow depth, sea ice thickness and leads in the ice, but also due to an inhomogeneous optical structure caused by properties such as snow grain size, the presence of bubbles or brine, or the stage of melt (Perovich et al., 2009, Light et al., 2008, Warren, 2019). High-precision calculation of the light field under a highly variable icescape is usually undertaken via various 3-D modelling approaches that account for melt ponds, ice leads etc. (Katlein et al., 2014, Massicotte et al., 2018). However, parameterising the presence and size of these features using satellite data or aerial imagery can be challenging, particularly at high latitudes, due to low spatial resolution imagery or insufficient solar illumination (Rösel and Kaleschke, 2011).

This chapter will outline the construction of a snow and sea ice spectral attenuation model to estimate spectrally resolved under-ice light. To facilitate an approach that can be applied on a Pan-Arctic basis, the attenuation model will be populated by parameters that can easily be obtained from satellite imagery, i.e. snow depth, sea ice thickness and sea ice concentration. No attempt will be made to address the complex structure of snow and sea ice since this information is difficult to obtain on a local basis and so is not available on the scales over which this model is intended to be used. A discussion of model validation results will follow, comparing modelled spectral transmission against *in situ* spectral transmission data from existing literature, measured at several locations and under varying snow and ice conditions. Finally, an overview of available satellite products used to populate the model will be discussed, concluding with analysis on how typical seasonal conditions impact the underwater light field.

3.1 Background

3.1.1 Arctic Sea Ice

In addition to regulating ocean-atmospheric heat transfer, the presence of sea ice also controls the magnitude and spectral distribution of the light penetrating into the water column, altering light availability for Arctic primary production (Kurtz et al., 2011, Popova et al., 2012). The Arctic experiences both regional and seasonal variability in sea ice cover, with recent trends showing a notable decline in both extent and melt onset timing (Perovich and Richter-Menge, 2009, Stroeve et al., 2014b, Stroeve and Notz, 2018). Studies of historic sea ice data have shown a linear decrease in sea ice extent from 1979-2014 (Serreze and Stroeve, 2015). Earlier onset of the melt season for the majority of Arctic regions has been observed, ranging from 1.0 days decade^{-1} in the Bering Sea, to 7.3 days decade^{-1} in the East Greenland Sea. Coupled with a later onset of freeze up, this has resulted in an increased melt season of approximately 20 days over the period 1978-2009 (Markus et al., 2009). The Arctic icescape is also trending towards a younger, thinner ice type. From mid 1980–2011, Multi Year Ice (MYI) as a proportion of the total ice extent reduced from around 75% to 45% (Maslanik et al., 2011). These evolving sea ice properties result in several characteristics that must be accounted for when estimating spectral transmission through an ice-covered Arctic Ocean.

3.1.2 Sea Ice Type and Age

Sea ice type is generally categorised as either Multi Year Ice (MYI) or First Year Ice (FYI). MYI is usually defined as ice that has survived at least two melt seasons and is associated with having a typical thickness of 2-4m. FYI thickness is generally greater than 0.3m but the ice sheet has not survived a melt season. These definitions mean there is a strong correlation between ice age and ice thickness. Although explicit data is not required on sea ice age to populate light transmission models, it can be a useful proxy to help determine the ice type and associated inherent optical properties.

There is little variation in the spectral albedo and transmittance of bare FYI and MYI, however it has been observed that when the ice becomes ponded, FYI has lower spectral albedo and diffuse attenuation compared with MYI (Light et al., 2015). This is likely due to FYI decaying at a quicker rate during melt season due to the higher liquid water content, resulting in increased light transmission (Veyssière et al., 2022).

3.1.3 Sea Ice Extent and Concentration

Sea Ice Extent (SIE) describes the area of ocean covered with ice, usually expressed in $\mathrm{km}^2\,\mathrm{yr}^{-1}$. Closely related is Sea Ice Concentration (SIC), which identifies the relative ice coverage of a particular area of ocean, expressed in %. The evolution of SIE and SIC in the Arctic has been the subject of several recent studies, documenting the clear decline in sea ice cover since the late 1970s (Stroeve et al., 2008, Maslanik et al., 2011, Cavalieri and Parkinson, 2012, Stroeve et al., 2012). The depletion in extent has resulted in a substantial reduction in SIC, with the Barents Sea particularly affected. Between 1979 and 2010, the Barents Sea saw an estimated yearly extent loss trend of $13.5 \times 10^3\,\mathrm{km}^2\,\mathrm{yr}^{-1}$ (Cavalieri and Parkinson, 2012). This is a significant decline when expressed in terms of SIC. When assessed in 2016, concentration in the Barents Sea had declined at a maximum rate of 0.56% per annum from 1979, with the largest rate of decline seen in the month of September (Wang et al., 2019), the period of time which would usually be expected to coincide with the onset of refreeze.

Sea ice concentration is a particularly important parameter to include when modelling the penetration of light into the upper ocean. Although characterising the optical properties of ice is an integral component of under-ice light modelling, it is expected that the proportion of open water in a given area of ocean will be the dominant controlling variable in the magnitude of light propagating down the water column.

3.1.4 Melt Ponds

Melt ponds form on the surface of sea ice during the melt season and result in increased transmission of light into the water column. Spectral attenuation of light by melt ponds has been extensively studied at various locations in the Arctic (Perovich, 2002, Grenfell et al., 2006, Light et al., 2008, Light et al., 2015, Katlein et al., 2019). Relative to bare (non-ponded) ice, measurements by Light et al. (2015) during the ICESCAPE campaign over summer 2010 and 2011 found that the presence of melt ponds resulted in a 4.4 factor increase in light transmission.

Although melt ponds are optically significant in describing the underwater light field with high precision during melt season, data on melt ponds are particularly difficult to obtain using satellite based data. Snow and ice depth are usually measured by satellites using radar and laser altimeters which struggle to distinguish melt ponds from open water leads, and so attempts to characterise the existence of melt ponds have usually involved visible satellite imagery and application of artificial neural networks (Rösel et al., 2012, Lee et al., 2020, Tilling et al., 2020). This approach can make it difficult to predict under-ice light fields at specific locations and times, as it would rely on cloudless images, as well as low sun angles adding more uncertainty to satellite backscattering data. As a result, melt ponds are not included in the snow and ice transmission model described in Section 3.2 due to the lack of available data on their spatial and temporal distribution.

3.1.5 Surface Scattering Layer

The presence of a Surface Scattering Layer (SSL) has been documented during melt season in the Arctic, and has been characterised as a highly scattering top layer that forms on melting ice, causing drainage of water into the lower layers of the ice column (Light et al., 2008, Light et al., 2015). Recent work by Smith et al. (2022) has shown that the albedo of this layer is generally correlated with the SSL thickness, although little is known about the mechanism behind this correlation.

Existing transmission models of light through summer Arctic ice have included the effects of the SSL in the form of a constant transmission parameter (Stroeve et al., 2021). However, as with melt ponds, this optical feature that persists in summer Arctic ice is difficult to parameterise via satellite data. At present, there is no method to quantify SSL thickness on a Pan-Arctic basis without wide-scale *in situ* measurements. As such, this feature has been excluded from the model described in Section 3.2.

3.1.6 Snow

The attenuation of light through snow can be affected by snow grain size, liquid water content and optically significant components within the snow such as dust or soot (Warren, 2019, Warren and Wiscombe, 1980). Snow has a significantly high albedo, reflecting around 90% of light incident upon it, with spectrally flat shape. Attenuation coefficients for snow are an order of magnitude greater than those of ice and attenuate red wavelengths more than in the blue (Grenfell and Maykut, 1977, Meirold-Mautner and Lehning, 2004, Light et al., 2008). Recent long term trends have shown that snow cover extent in the Northern hemisphere is trending upward during the autumn and winter, with increasing extent 0.26 million km^{-2} decade^{-1} and 0.19 million km^{-2} decade^{-1} respectively, with summer and spring trends falling (Estilow et al., 2015). The presence of snow on sea ice is likely to be a significantly controlling parameter in quantifying the under-ice light field.

3.2 Model Construction

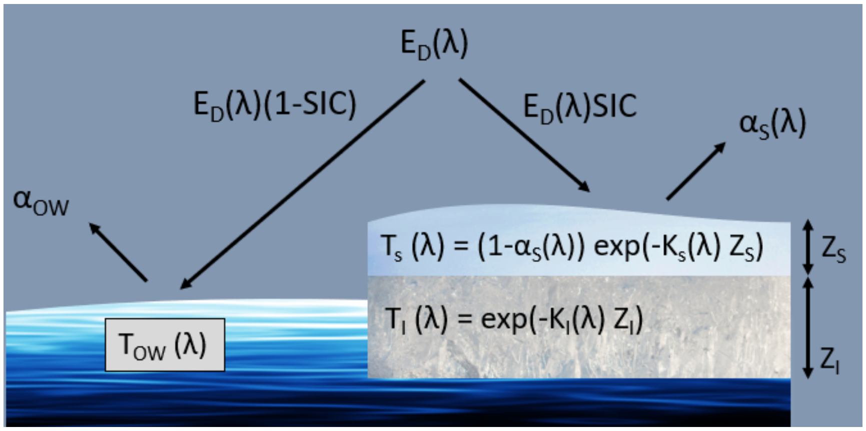

Figure 3.1: Overview of transmission model.

Figure 3.1 presents a visual overview of how light is transmitted across the air-ice/air-ocean boundary. The above surface spectral irradiance, $E_D(\lambda)$, is proportioned according to the sea ice concentration (SIC). Transmission of the open water component (T_{OW}) is executed via the attenuation model described in Chapter 2. Transmission of the ice-covered portion is described in detail in Section 3.2.2.

3.2.1 Model Coefficients

To facilitate a snow and ice transmission model that can be utilised on a Pan-Arctic basis with potential for global coverage, spectral albedo and diffuse attenuation measurements for Snow, First Year Ice (FYI) and Multi Year Ice (MYI) were compiled from a variety of field campaigns undertaken at independent sites.

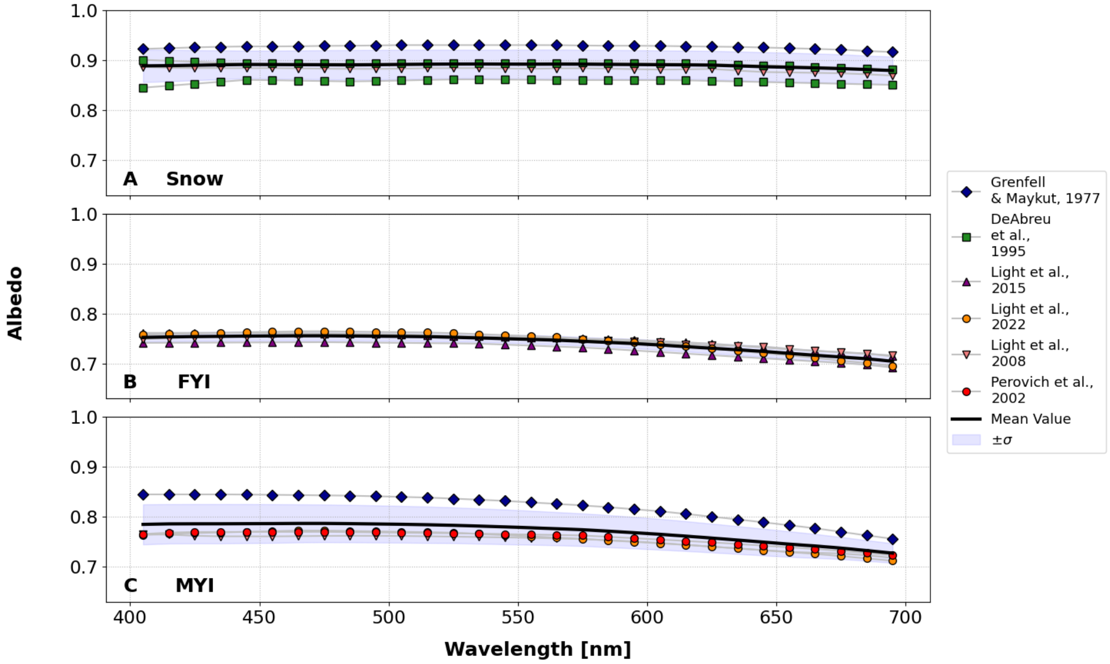

Figure 3.2: Spectral albedo measured across various campaigns and locations, for A) Snow, B) First Year Ice (FYI) and C) Multi Year Ice (MYI). Mean value across measurements is shown in solid black, with standard deviations highlighted in shaded areas.

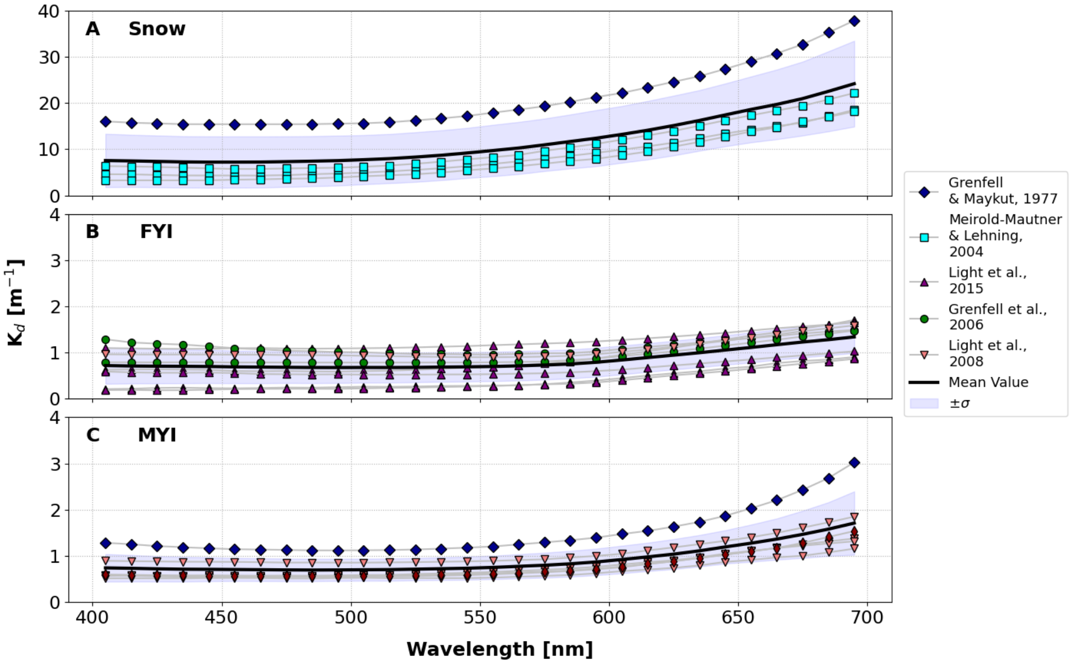

Figure 3.3: Spectral diffuse attenuation measured across various campaigns and locations, for A) Snow, B) First Year Ice (FYI) and C) Multi Year Ice (MYI). Note the factor of 10 difference in scale for Snow. Mean value across measurements is shown in in solid black, with standard deviations highlighted.

Figures 3.2 and 3.3 show measured spectral albedo and diffuse attenuation coefficients recorded throughout a range of field campaigns undertaken in the Arctic. The optical properties of snow and ice are difficult to measure during the winter period due to difficulties accessing the region and limitations on the sensitivity of radiometers and low light availability. As a result, these measurements have been made during the traditional melt season (May - September inclusive), with some recorded during the early onset of melt (Grenfell et al., 2006) and others specifically targeting the height of melt season (Light et al., 2015). Note however that all values for MYI and FYI shown in Figures 3.2 and 3.3 were recorded during bare ice conditions only. For the analysis to follow, only measured transmission values recorded underneath bare ice have been used and those retrieved under the presence of melt ponds have been excluded.

Accurate representation of the behaviour of light propagating through the complex optical structures of snow and ice can be challenging. Localised changes affecting light attenuation can be difficult to quantify, such as snow drift and degree of liquid water content. As a consequence, mean spectral albedo and diffuse attenuation coefficients are used to populate the attenuation model described in Section 3.2.2. This allows for representation of the bulk transmission of light on a Pan-Arctic scale and across a range of conditions with minimal input data required.

Note that although the surface-scattering layer (SSL) has been shown to contribute towards the extinction of the light field (Light et al., 2008, Smith et al., 2022), the presence and depth of the SSL cannot be quantified using aerial photography or satellite data. As a result, it has been excluded from this analysis.

3.2.2 Attenuation Model

In the HEIMDALL open water model (Chapter 2), diffuse attenuation of light was characterised using the Inherent Optical Properties (IOPs) of the water and optically significant constituents. A similar approach taken to snow and ice can be difficult due to the heterogeneity of their structures. As a result, directly measured IOPs are not widely available. A frequent approach to mitigate this issue is to use measured Apparent Optical Properties (AOPs) to populate a light transmission model (Hamre et al., 2004, Ehn et al., 2008, Katlein et al., 2019, Cooper et al., 2021).

Attenuation by snow and sea ice is parameterised via a double exponential Beer-Lambert Law, similar to the approach taken by existing models (Castellani et al., 2017, Stroeve et al., 2021). Using the albedo and attenuation coefficients described in Section 3.2.1, total spectral transmission is parameterised as the product of transmission through ice (T_I) and snow (T_S) depending on local conditions.

$$T_I(\lambda) = (1 - \alpha_I(\lambda)) \exp(-K_I(\lambda)\, z_I) \tag{3.1}$$

$$T_S(\lambda) = (1 - \alpha_S(\lambda)) \exp(-K_S(\lambda)\, z_S) \tag{3.2}$$

$$T_{S,I}(\lambda) = (1 - \alpha_S(\lambda)) \exp(-K_S(\lambda)\, z_S) \exp(-K_I(\lambda)\, z_I) \tag{3.3}$$

where α_S, α_I are the albedos, K_S, K_I are the diffuse attenuation coefficients and z_S, z_I are the depths of snow and ice respectively. Equation 3.1 will be implemented for bare ice only and Equation 3.3 will be used for conditions where a layer of snow is present on top of the ice. It is assumed that in the latter scenario, albedo loss will only occur at the surface level air-snow interface with no loss at the snow-ice interface.

The spectrally resolved values of $\alpha_{S/I}$ and $K_{S/I}$ are obtained from the mean values of the datasets described in Section 3.2.1. Snow and ice depth values can be user provided or populated using satellite estimates, described in more detail in Section 3.4.1. Note that the choice of K_I is determined by z_I. Recent work by Melling (2022) demonstrated that the average thickness of Multi Year Ice (MYI) in the Arctic is approximately 2.33m. The transmission model will implement MYI K_I values when ice depth is greater than or equal to 2.33m, and First Year Ice (FYI) K_I values when ice depth is less than 2.33m. During melt season, MYI may decay to become thinner than the 2.33m threshold value used in the transmission model and this may introduce some error in attenuation calculations. However the impact of switching between FYI and MYI K_I is like to be substantially smaller than the impact introduced by the presence of melt ponds (Light et al., 2015).

3.2.3 Open Water Element

Ice cover in the Arctic Ocean is not static. Ocean currents and atmospheric winds mean that ice not fastened to a fixed object is constantly in motion. Measured drift speeds can be as high as $1ms^{-1}$, with many regions of the Arctic exhibiting positive trends in these speeds in recent decades (Spreen et al., 2011, Kwok et al., 2013, Lund et al., 2018). Coupled with ice melt, this results in spatial and temporal variations in local sea ice cover.

Sea ice concentration (SIC) is defined as the fractional value of a specified area of ocean covered in ice, ranging from 0-1. For integration into the open water HEIMDALL model, the above surface light field (E_D) is partitioned according to a localised value of SIC, retrieved from satellite data (Section 3.4.1). The open water (OW) element of the light field, defined as $E_{D\,OW} = E_d\,(1\text{-SIC})$, is transmitted across the air-ocean boundary per the procedures described in Chapter 2, with the remainder transmitted via Equation 3.1 or Equation 3.3.

3.2.4 Total Underwater Irradiance

Total underwater spectral irradiance will be the sum of the open water and ice-covered elements at depth z defined by the user. In the open water, the light will travel through the water column to depth z and in the ice-covered portion, the light will travel to depth z'. This is to account for the space that the ice occupies in the water column and ensures the final output depth is consistent for both elements. A visual overview of this can be seen in Figure 3.4.

Assuming the density of water is $\rho_w \approx 1000\,\mathrm{kg\,m^{-3}}$ and the density of ice is $\rho_i \approx 900\,\mathrm{kg\,m^{-3}}$ (Timco and Frederking, 1996), the fraction of the ice submerged in water (f) can be described by the ratio of densities:

$$f = \frac{\rho_i}{\rho_w} \approx 0.9 \tag{3.4}$$

After transmission through snow and ice, the spectral irradiance component immediately beneath the surface of the ice is attenuated a distance of $z' = z - (0.9 * \mathrm{SIT})$, where SIT is the sea ice thickness determined via satellite or reanalysis. Note the ice is considered to have a constant density and no consideration is given to the presence liquid water content altering this. Additionally, there is assumed to be no albedo loss between the snow and ice boundary. As snow has a higher albedo than ice, it is assumed that any light reflected upward at the snow-ice boundary would then be reflected back in the downward direction by the snow layer.

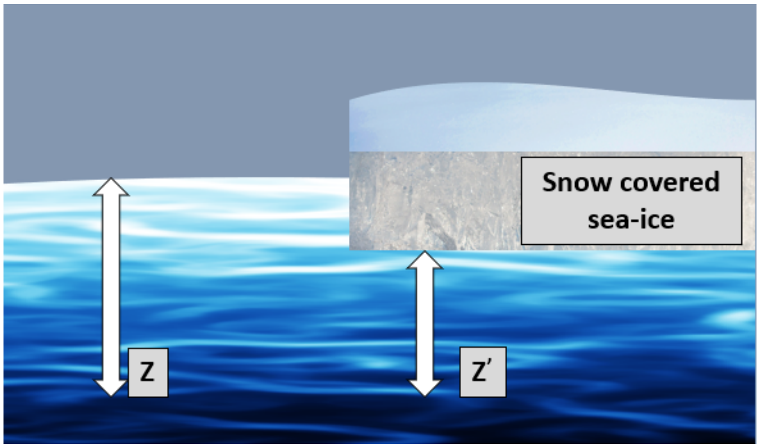

Figure 3.4: Overview of model depth adjustment for submerged sea ice.

3.3 Model Validation

3.3.1 Validation Datasets

To validate the snow and ice transmission model detailed in Section 3.2, three independent datasets of spectral transmission were used.

For light transmission through ice only, modelled spectral transmission was compared with measurements taken during the ICESCAPE field campaign (Light et al., 2015) and the Surface Heat Budget of the Arctic Ocean (SHEBA) project (Uttal et al., 2002, Perovich, 2007). The ICESCAPE field campaign recorded spectral transmission during two research cruises in the summers of 2010 and 2011, under ponded and bare ice conditions. Measurements were made at 19 field stations in the Chukchi and Beaufort Seas using a customised Analytical Spectral Devices (ASD) FieldSpec Pro spectrophotometer coupled to an ASD cosine collector (Malvern Panalytical Ltd, Malvern, UK) capable of recording simultaneous surface downwelling irradiance and under-ice downwelling irradiance, with spectral resolution of 0.5nm. A total of 24,039 bare ice data points in the PAR range (400-700nm) were used for validation, for ice depths in the range 0.86-2.04m. The SHEBA project comprised of 581 datapoints recorded under a bare ice depth of 0.17m. Spectral transmittance was measured in the Chukchi Sea during April 1998 using an ASD ICE-1 spectroradiometer (Malvern Panalytical Ltd, Malvern, UK), with a spectral range of 400 to 750 nm at 0.5nm resolution. Measurements in the PAR range only were used for validation.

Validation through snow and ice was undertaken using spectral transmission values recorded under landfast sea ice in Barrow, Alaska (Nicolaus et al., 2013). Spectral transmittance was measured in spring 2010 at 1nm resolution, with a total of 33,756 data points in the PAR range extracted for validation. Surface and under-ice irradiance was measured simultaneously with two upward-looking Ramses spectral radiometers with cosine collectors (Ramses ACC, Trios GmbH, Rastede, Germany). Ice depths were in the range 1.09-1.42m and snow in the range 0.04-0.43m. Additionally, a dataset of 581 data points recorded under 0.02m of snow and 0.17m of ice during the SHEBA project were included in the validation process (Uttal et al., 2002, Perovich, 2007). Spectral transmittance was measured in the Chukchi Sea during April 1998 using an ASD ICE-1 spectroradiometer (Malvern Panalytical Ltd, Malvern, UK), with a spectral range of 400 to 750 nm at 0.5nm resolution. Measurements in the PAR range only were used for validation.

3.3.2 Validation Results

Each validation dataset provides spectral transmission in addition to measured ice and snow depth, as appropriate. To calculate modelled transmission, depths provided in each dataset were used to populate $z_{S/I}$ in Equations 3.1-3.3, with spectral $\alpha_{S/I}$ and $K_{S/I}$ obtained from the mean spectra shown in Figures 3.2 and 3.3.

Calculations of modelled transmission shown in Figures 3.5-3.8 have an accompanying range of possible values. This range was obtained by modelling transmission using the maximum and minimum spectral $\alpha_{S/I}$ and $K_{S/I}$ from Figures 3.2 and 3.3. The range of $\alpha_{S/I}$ and $K_{S/I}$ used to generate the mean values populating the transmission model were measured over a range of locations and conditions, and show notable variation, particularly $K_{S/I}$. This range of variation should encompass the features of the validation datasets. It is expected that since a generalised approach is taken here using mean values, there will be some disagreement in the comparison of modelled and measured values. However if results do fall within the possible range of transmission values, it can be assumed that the modelling approach is robust enough to reasonably represent spectral transmission through snow and ice.

Results of modelled to measured spectral transmission for bare ice conditions show good agreement. Figure 3.5 shows a tendency for modelled values to be too high in the longer red wavelengths, and too low in the shorter blue wavelengths. Since measured values were recorded during melt season, this may be a result of an elevated amount of liquid water content within the ice. There may also be influence from nearby melt

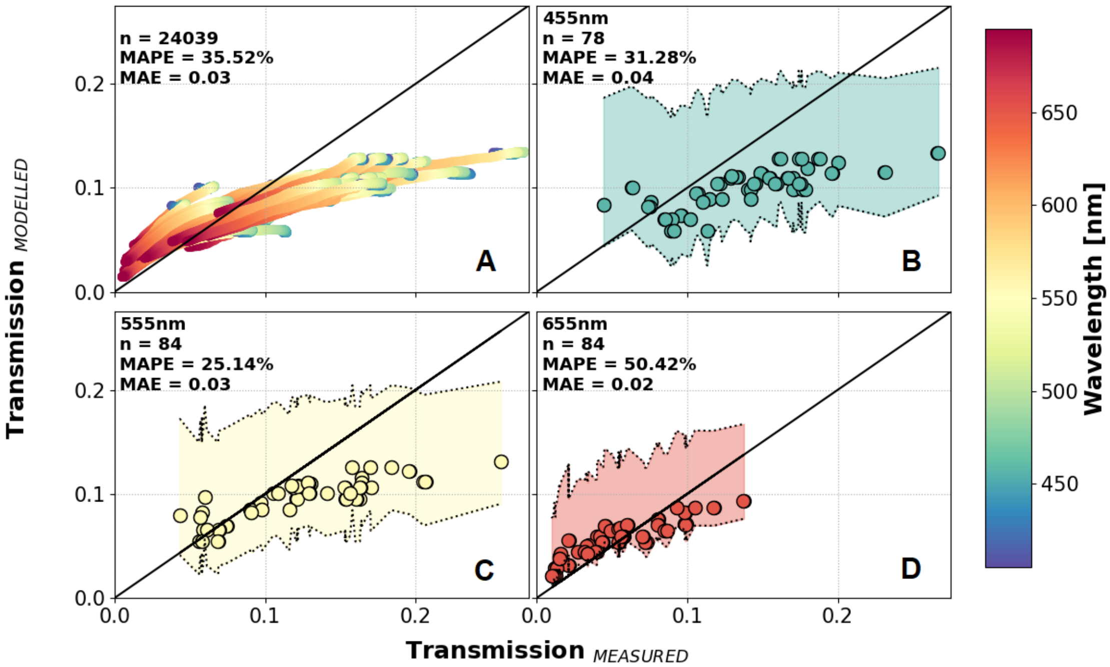

Figure 3.5: Measured and modelled spectral transmission in the PAR range for bare ice conditions during the ICESCAPE field campaign. Selected wavelengths shown with range of possible modelled transmission due to varying AOPs (shaded). Mean absolute percentage error (MAPE) and Mean Absolute Error (MAE) noted for full dataset and selected wavelengths. A) all wavelengths, B) 455nm, C) 555nm, D) 655nm.

ponds allowing additional light under the ice. Although validation results were filtered for bare ice conditions only, it is not possible to rule out the effect adjacent melt ponds may have on transmission. Figure 3.6 demonstrates the expected variation in results, appearing to show that the mean $\alpha_{S/I}$ and $K_{S/I}$ used are too high to represent the specific circumstances under which the SHEBA measurements were taken. However, results of both datasets consistently fall within the range of expected values, showing a mean absolute error (MAE) of approximately 0.03, or 3 percentage points difference in modelled to measured transmission.

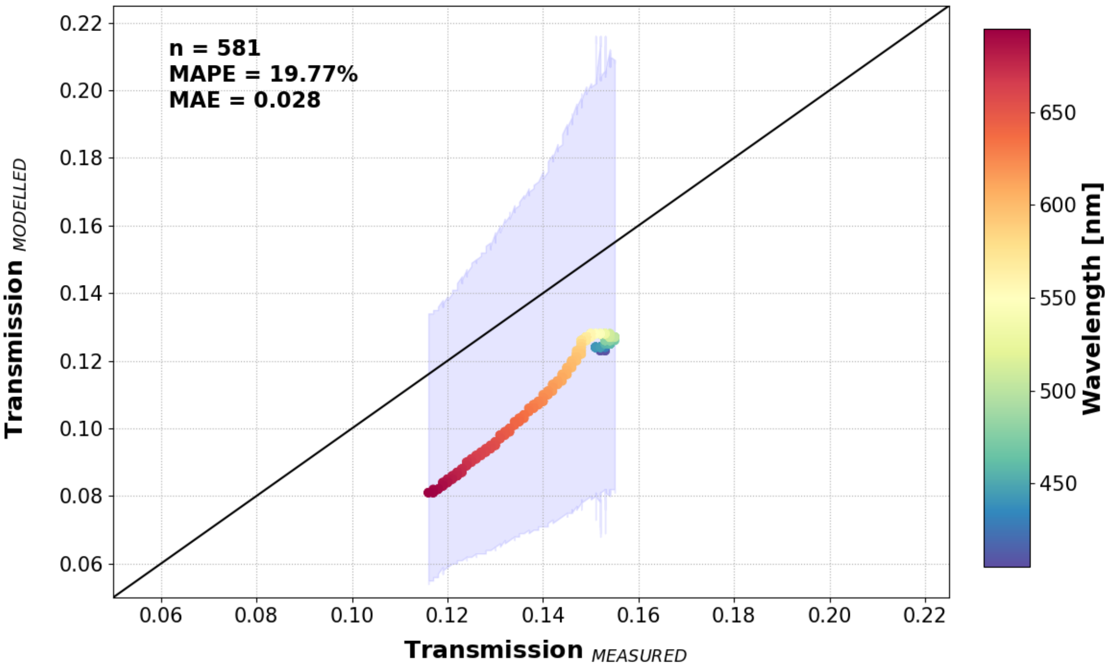

Figure 3.6: Measured and modelled spectral transmission in the PAR range for bare ice conditions during the SHEBA project, shown with range of possible modelled transmission due to varying AOPs (shaded). Mean absolute percentage error (MAPE) and Mean Absolute Error (MAE) noted for full dataset.

Similar results can be seen for transmission through snow and ice. Figure 3.7 demonstrates a large variation in transmission values, spanning 5 orders of magnitude. Results here show a trend of model underestimation in the red, and overestimation in the blue. One important point to note is that the study providing this validation dataset noted concentrations of chlorophyll present in ice and snow cores sampled at the site in Barrow, Alaska (Nicolaus et al., 2013). The presence of these pigments likely resulted in a substantial absorption of blue light, resulting in lower measured transmission values and consistent overestimation of modelled transmission with higher mean absolute percentage error (MAPE) for wavelength 455nm shown in Figure 3.7. Results in Figure 3.8 demonstrate

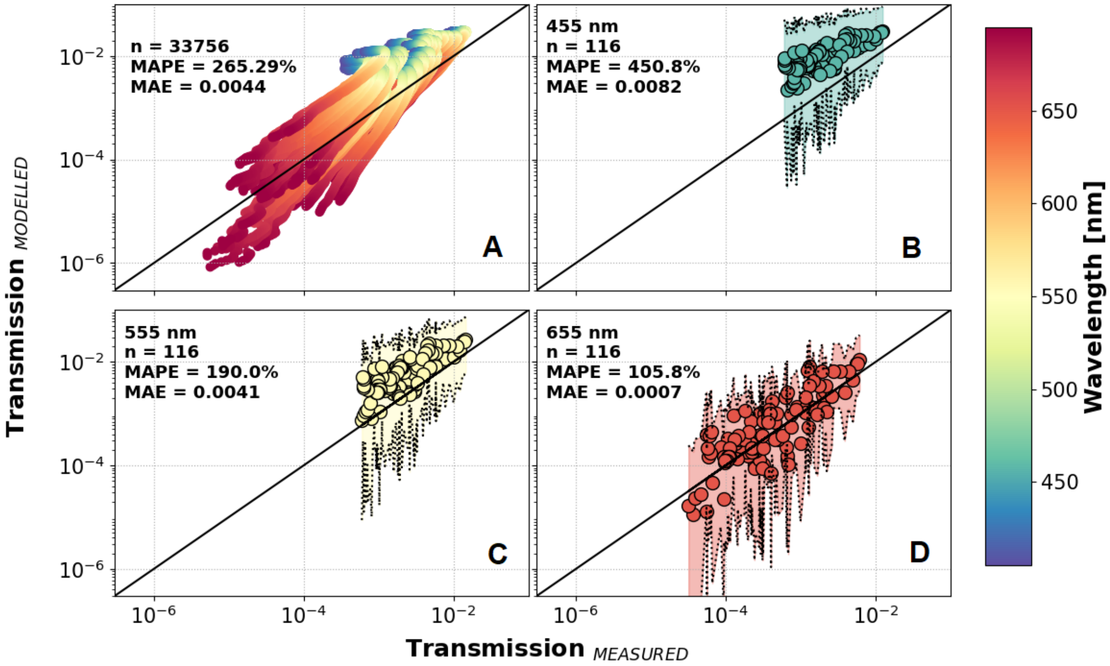

Figure 3.7: Measured and modelled spectral transmission in the PAR range for snow and ice conditions recorded at Barrow, Alaska. Selected wavelengths shown with range of possible modelled transmission due to varying AOPs (shaded). Mean absolute percentage error (MAPE) and Mean Absolute Error (MAE) noted for full dataset and selected wavelengths. A) all wavelengths, B) 455nm, C) 555nm, D) 655nm.

excellent agreement between modelled and measured values from the SHEBA dataset, with the lowest MAPE of all validation datasets. For these particular measurements, the mean values of $\alpha_{S/I}$ and $K_{S/I}$ appear to be very close to the site conditions.

Results of modelled to measured transmission for aggregated validation datasets are displayed in Figure 3.9. All modelled data appear to fall within the expected possible range of transmission values, and although mean absolute percentage error (MAPE) appears to be high at 166.61% over all datasets, this is heavily skewed by values in the lower range of transmission. As mean absolute error (MAE) across all datasets is <2%, it is assumed

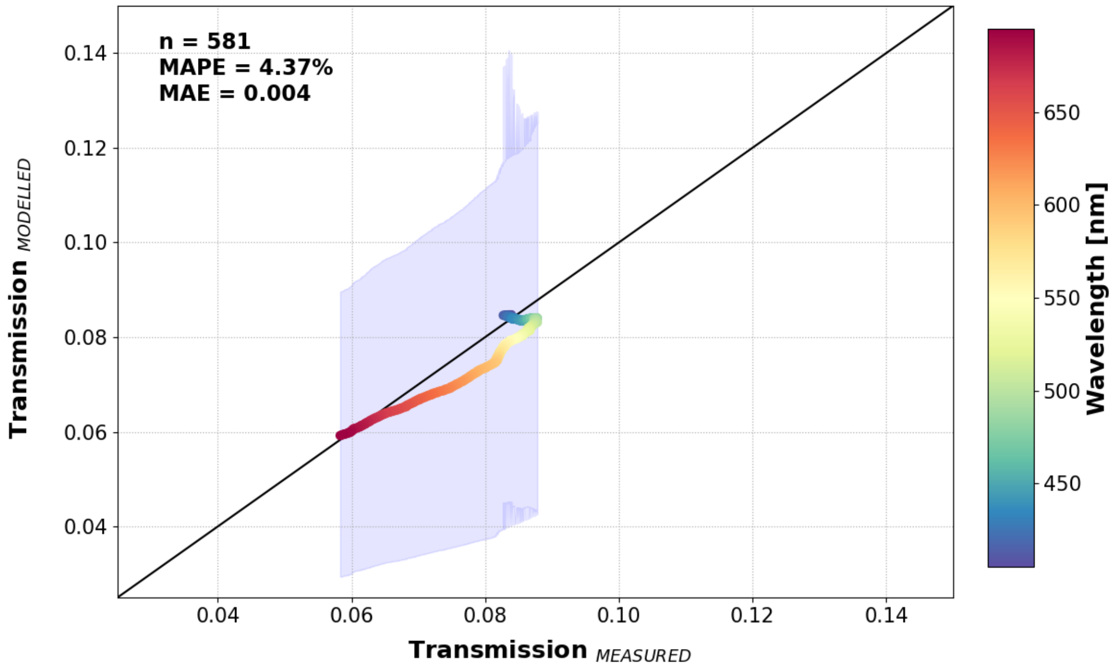

Figure 3.8: Measured and modelled spectral transmission in the PAR range for snow and ice conditions during the SHEBA project, shown with range of possible modelled transmission due to varying AOPs (shaded). Mean absolute percentage error (MAPE) and Mean Absolute Error (MAE) noted for full dataset and selected wavelengths.

that this approach to modelling the spectral transmission of light through snow and ice is sufficiently accurate to assess the impact on underwater light availability.

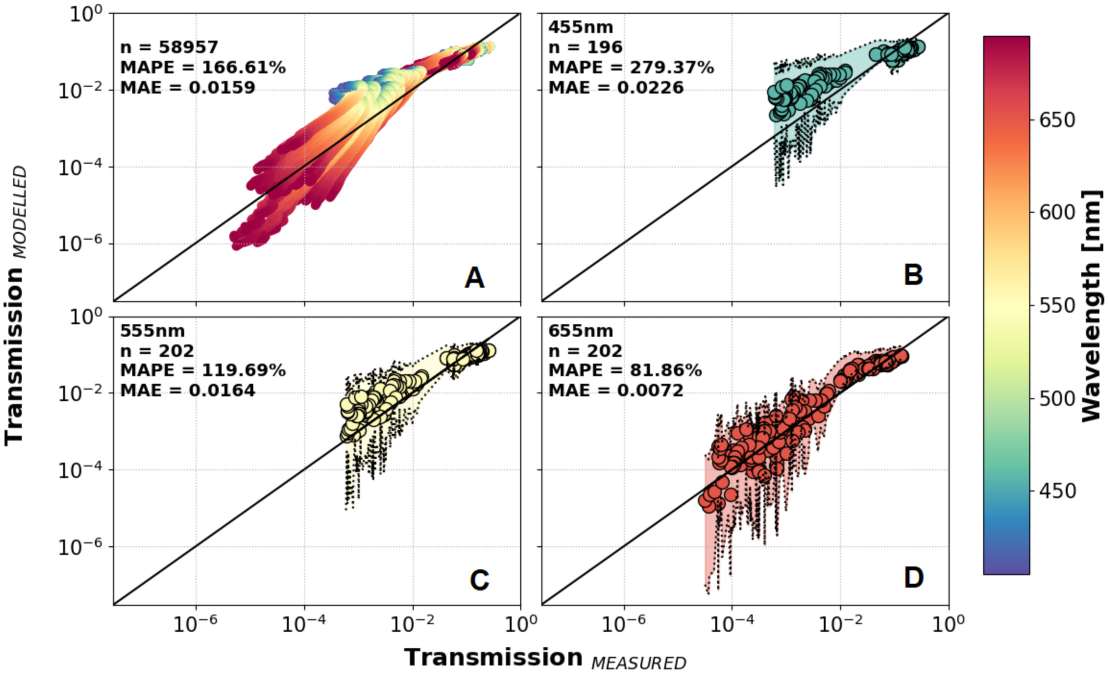

Figure 3.9: Measured and modelled spectral transmission in the PAR range for all data shown in Figures 3.5-3.8. Mean Absolute Percentage Error (MAPE) and Mean Absolute Error (MAE) analysed over aggregated datasets. A) all wavelengths, B) 455nm, C) 555nm, D) 655nm.

3.4 Integration into the Open Water Model

For incorporation into the HEIMDALL model, it is proposed that satellite observations and model predictions on sea ice concentration, snow depth and ice thickness can be used to calculate transmission. An overview of potential products able to provide this information is detailed below.

3.4.1 Satellite and Model Products

Estimates of sea ice and snow cover are available from satellite products making direct measurements, or reanalysis products combining observed data and models.

The National Snow and Ice Data Center (NSIDC) provides a catalogue of available datasets from NASA, NSF, NOAA and others. Products are available over a range of spatial and temporal scales, with typical resolution varying from daily to monthly coverage over a 12.5-25km square grid. Widely used models are also available to provide information on sea ice and snow. The PIOMAS Arctic Sea Ice Volume Reanalysis product is continuously updated with daily resolution and is widely used to estimate sea ice thickness, extent and snow depth (Zhang and Rothrock, 2003). Several reanalysis products are also available for estimating snow depth and density over defined time periods with daily resolution (Petty et al., 2018, Liston et al., 2020, Stroeve et al., 2020).

Satellite data on snow and ice depth is generally unavailable during the melt season (May-September inclusive) due to the presence of surface melt ponds affecting measurements. Reanalysis models usually extend throughout the melt season and provide a means to estimate snow and ice depth over the calendar year. To assess the reliability of these products to represent local conditions, their outputs were compared with *in situ* data measured at several locations in the Arctic.

Data products assessed are detailed in Table 3.1. Note that only ice and snow depth are assessed. Sea ice concentration (SIC) can be difficult to validate with local *in situ* measurements. Data sourced from the NSIDC on SIC is obtained from a combination of passive microwave satellite measurements from the Nimbus-7 satellite and the Defense Meteorological Satellite Program satellites, and has been independently validated against other passive microwave measurements (Meier et al., 2014, Meier et al., 2021).

Table 3.1: Overview of products assessed for use in snow and ice transmission model.

Variable	Resolution	Product	Shorthand	Ref.
Ice Depth	22km/Daily	PIOMAS	PIOMAS	Zhang and Rothrock, 2003
Ice Depth	25km/Daily	Cryosat-2/SMOS Merged	CryoSat/SMOS	Ricker et al., 2017
Snow Depth	25km/Monthly	CryoSat-2	CryoSat	Kurtz and Harbeck, 2017
Snow Depth	22km/Daily	PIOMAS	PIOMAS	Zhang and Rothrock, 2003
Snow Depth	25km/Daily	SnowModel-LG	LG	Stroeve et al., 2020

3.4.2 *In Situ* Datasets

Comparison of sea ice thickness (SIT) determined via available products was carried out against SIT measured *in situ*. A total of 45 ice depths were measured by Light et al. (2015) during the ICESCAPE field campaign in the summers of 2010 and 2011 in the Chukchi and Beaufort Seas. Ice thickness was determined by removing ice cores and measuring thickness using a thickness gauge (Kovacs Enterprise, Roseburg, United States). Additionally, a total of 508 SIT values were recorded by Rösel et al. (2018) through ice drilling or coring and measured with a flexible thickness gauge. Thickness values were recorded in the spring of 2015 in the Arctic Ocean north of Svalbard. 508 snow depth (S_D) measurements were also obtained from Rösel et al. (2018) using a Magnaprobe snow probe (Snow-Hydro, Fairbanks, AK, USA). These *in situ* measurements were used to assess satellite and reanalysis snow and sea ice depth products. Sea ice concentration (SIC) data are obtained from Meier et al. (2021).

3.4.3 Product Reliability

The PIOMAS Arctic Sea Ice Volume Reanalysis product is a widely used and a particularly valuable tool in estimating year round SIT due to its ability to operate over the melt season. PIOMAS operates on a generalised curvilinear coordinate system over the domain 45-90°N, with mean spatial resolution of 22km and daily temporal resolution (Zhang and Rothrock, 2003). PIOMAS SIT estimates have previously been validated against submarine measurements, with a root mean square error of 0.6m (Zhang and Rothrock, 2003). Figure 3.10 shows PIOMAS SIT estimates compared to the merged SIT reference dataset described in Section 3.4.2, with symbols coloured by corresponding SIC values. Three data points were determined to have a SIC=0 by the NSIDC passive microwave satellite at the location where Light et al. (2015) measured SIT, however this measured *in situ* data may have been collected near the perimeter of the ice. There are varying levels of agreement between modelled and measured SIT data, with no clear pattern of bias towards specific SIC values. Mean absolute error (MAE) demonstrates similar performance to validation results noted by the creators of PIOMAS, however there is a clear tendency for PIOMAS to overestimate local SIT, with a mean bias error (MBE) of 0.65m. Existing literature has documented that compared with *in situ* measurements, PIOMAS tends to overestimate thin ice ($\leq$ 1m) and underestimate thicker ice (Stroeve et al., 2014a, Wang et al., 2016), consistent with results in Figure 3.10. The creators of PIOMAS have also acknowledged this, but do not provide a definitive reason why this behaviour occurs and speculate that some error may be attributed to systematic errors in measurement (https://psc.apl.uw.edu/research/projects/arctic-sea-ice-volume-anomaly/validation/).

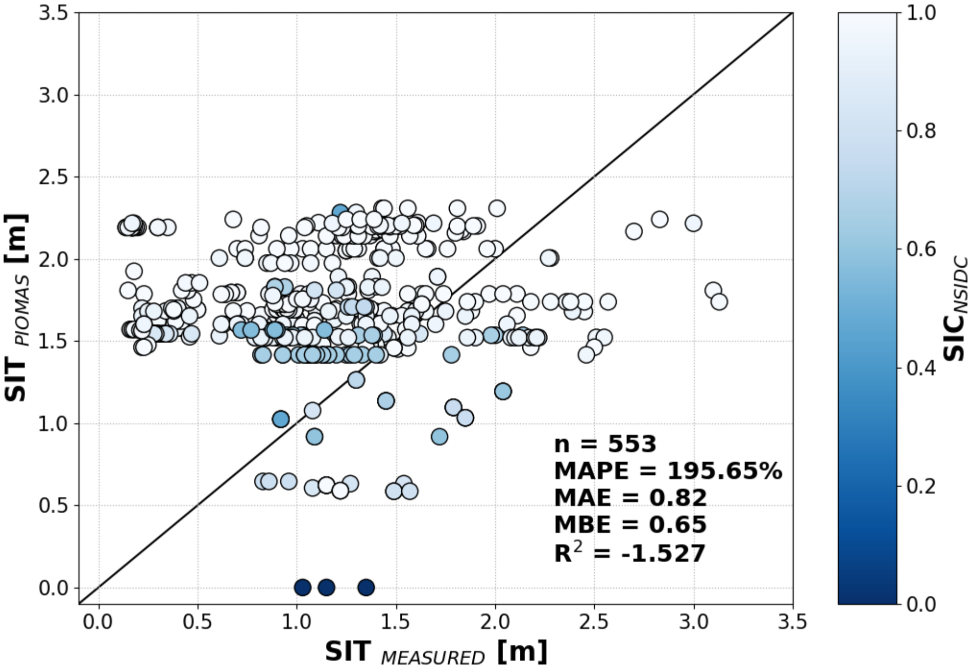

Figure 3.10: Comparison of Sea Ice Thickness (SIT) obtained from PIOMAS Reanalysis Model (PIOMAS) and *in situ* measurements (MEASURED). Sea ice concentration (SIC) is noted on colourbar, obtained from NSIDC passive microwave satellite data.

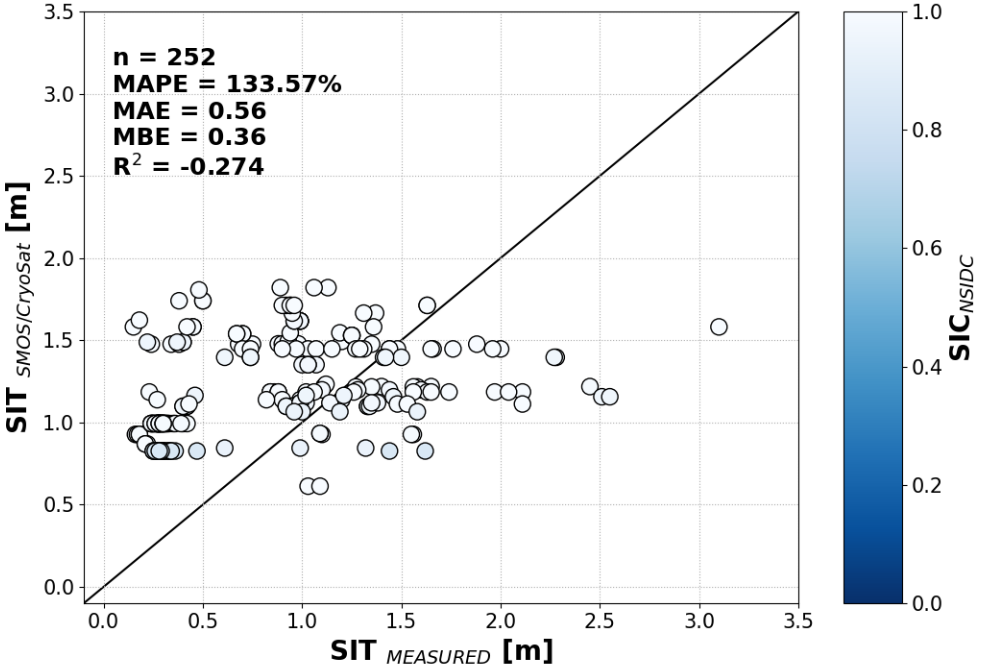

Figure 3.11: Comparison of Sea Ice Thickness (SIT) obtained from CryoSat-2 SMOS merged satellite product (CryoSat/SMOS) and *in situ* measurements (MEASURED). Sea ice concentration (SIC) is noted on colourbar, obtained from NSIDC passive microwave satellite data. Data is restricted to pre-melt season.

Similar analysis was carried out comparing *in situ* measured data with estimates from the CryoSat-2/SMOS merged SIT product at 25km spatial resolution. This product is blended of observations from the CryoSat-2 satellite and the Soil Moisture and Ocean Salinity (SMOS) satellite. CryoSat-2 uses altimetry to measure the height of ice above sea water and converts this to ice thickness, this method loses reliability when ice is thin ($<$ 0.5m) due to uncertainty (Ricker et al., 2017). The SMOS satellite uses surface brightness temperature to estimate SIT, and loses sensitivity at ice thickness $>$ 1m (Ricker et al., 2017). Due to the limitations of these products, the merged CryoSat-2/SMOS product was developed by the Alfred Wegener Institute (AWI) to provide continuous SIT estimates over a range of thickness values. Data is available daily from late 2010 onwards, and spans the full Northern hemisphere. As satellite data is not available throughout melt season, comparisons were only made against *in situ* data for time periods where valid satellite estimates were available. Figure 3.11 shows similar results to the PIOMAS product, with varying levels of agreement and a tendency to overestimate SIT with a mean bias error (MBE) of 0.36m. However, the satellite data has a lower mean absolute error (MAE) of 0.56m compared with 0.82m using PIOMAS data.

Although each of the products appears to show little correlation with *in situ* point measurements of SIT, their estimates are over large spatial scales and were likely not intended to replace the precision that comes with measurements from fieldwork. Caution should be exercised when relying upon these products to determine SIT on small spatially resolved scales. The CryoSat-2 merged product in particular has been shown to perform particularly well for thin ice when comparing average seasonal SIT over large spatial areas (Sallila et al., 2019), and so would likely be the preferred product to use outside of melt season when data is available.

PIOMAS also provides daily snow depth estimates. Snow depth is parameterised as a water equivalent depth ($\mathrm{D_{WE}}$). This means the depth of water that the accumulated snow would occupy if it melted over the given grid area. Depth of snow is therefore dependent upon snow density and is calculated as:

$$\mathrm{S_D} = \frac{\varrho_{\mathrm{W}}\,\mathrm{D_{WE}}}{\varrho_{\mathrm{S}}} \tag{3.5}$$

where ϱ_{W} is the density of water, $\mathrm{D_{WE}}$ is the water equivalent depth and ϱ_{S} is the density of snow.

Snow density values are not provided with PIOMAS snow depths, and creators of PIOMAS have advised they would normally treat snow density as one third of water density (Jinlun Zhang, personal communication, 29 November 2022). Recent work on the variation of snow over Arctic sea ice reports values in the range 120-494 $\mathrm{kg\,m^{-3}}$, with

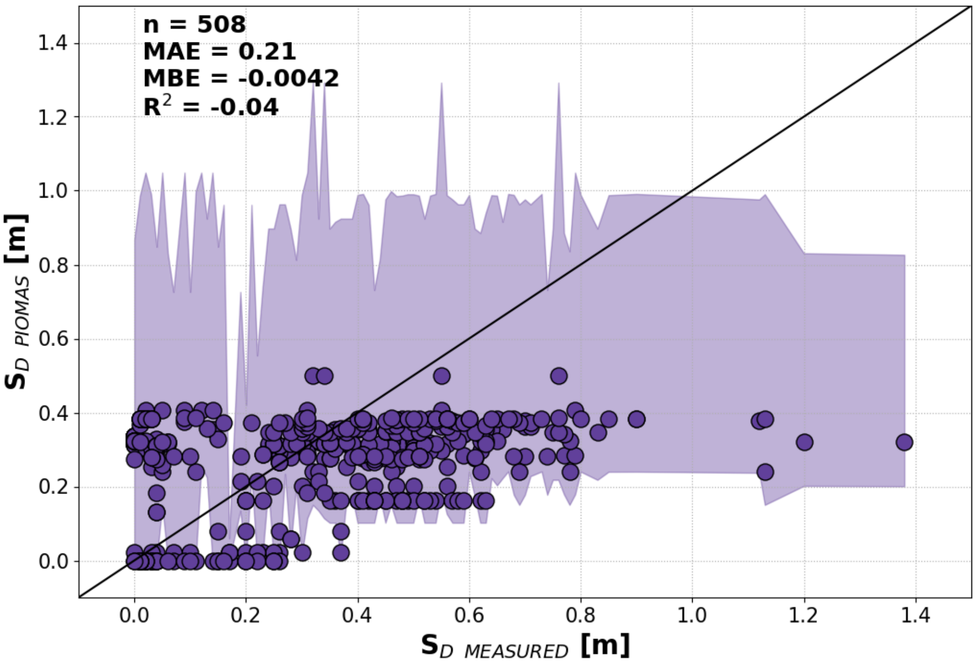

Figure 3.12: Comparison of Snow Depth (S_D) obtained from PIOMAS Reanalysis Model (PIOMAS) and *in situ* measurements (MEASURED)(Rösel et al., 2018). Shaded area represents range of variability as a result of varying snow density.

an average value of 310 $\mathrm{kg\,m^{-3}}$ (King et al., 2020). Snow depth data shown in Figure 3.12 were calculated using the average snow density of 310$\mathrm{kg\,m^{-3}}$, with possible depth ranges bound by the minimum and maximum recorded by King et al. (2020). Using these values, results show that PIOMAS exhibits little bias, with a mean absolute error of 21cm when compared to *in situ* point measurements. As with the SIT comparison, there is little agreement between the two datasets. Garnier et al. (2021) recently compared PIOMAS snow depth estimates with airborne derived snow depth measurements recorded during NASA's Operation IceBridge (Kurtz et al., 2013, Newman et al., 2014) and found PIOMAS to have RMSE of 0.10m and MBE of 0.043m. Their comparisons were done using validation data on a Pan-Arctic basis and averaged seasonally.

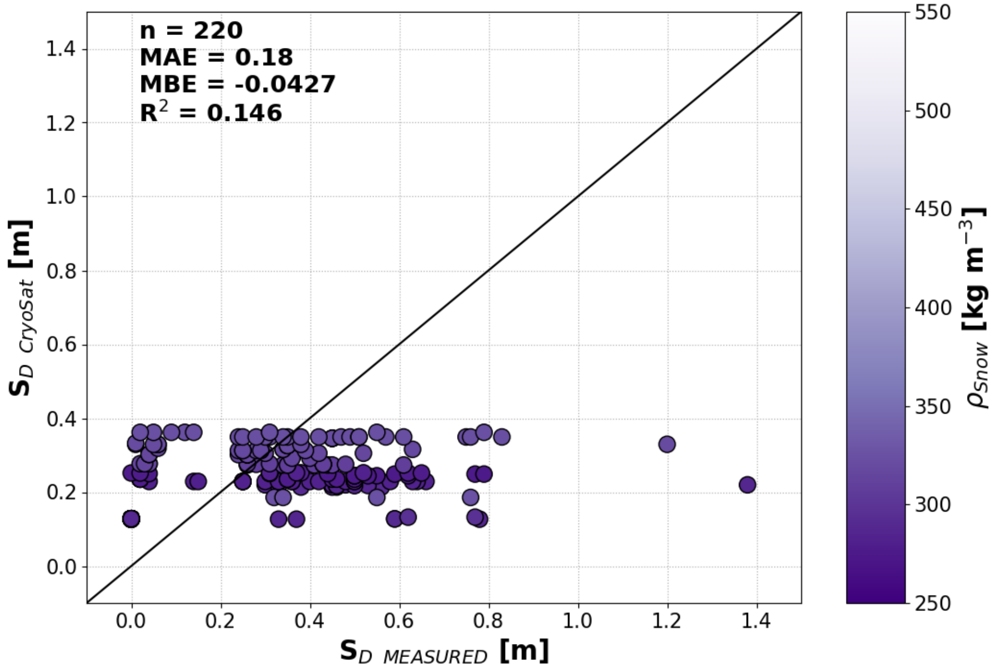

Figure 3.13: Comparison of Snow Depth (S_D) obtained from CryoSat-2 product (CryoSat) and *in situ* measurements (MEASURED). Snow density (ρ_{snow}) is noted on colourbar, also obtained from CryoSat-2 product. Data is restricted to pre-melt season.

The CryoSat-2 satellite also provides estimates of snow depth with accompanying snow density on a monthly basis over the range 55-90°N at 25km spatial resolution. Again the data is restricted to those times outside of melt season and as a result, *in situ* data has been filtered accordingly. Results in Figure 3.13 demonstrate a reduced mean absolute error (MAE) of 18cm compared to the PIOMAS MAE of 21cm, however CryoSat shows a tendency to underestimate snow depth with a mean bias error (MBE) of approximately 4cm. Quantifying location-specific snow density does not appear to significantly improve local snow depth measurements. The snow depth and density product from CryoSat-2 is constructed using a modified snow climatology from Warren et al. (1999), based on *in situ* snow depth measurements from pre-1991 (USER GUIDE: CryoSat-2 Level-4 Sea Ice Elevation, Freeboard, and Thickness, Version 1 [https://nsidc.org/sites/default/files/rdeft4-v001-userguide_1.pdf], last access: March 2023). This historical data is unlikely to represent the current climatology of the Arctic. Additionally, the large spatial and temporal resolution of this data product make it a poor candidate for estimating local snow depth.

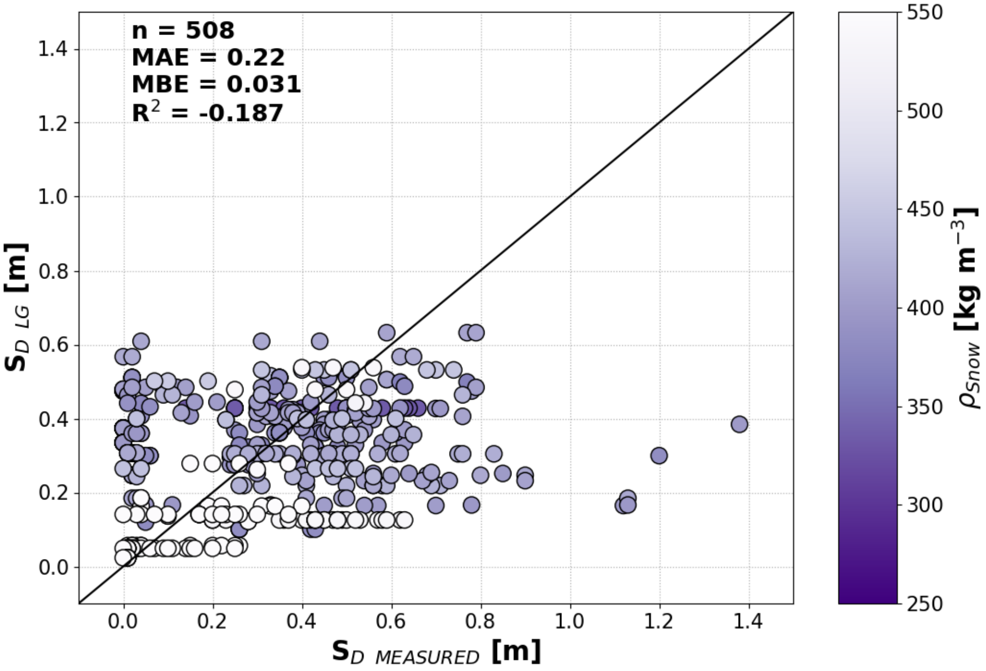

Figure 3.14: Comparison of Snow Depth (S_D) obtained from SnowModel-LG Model (LG) and *in situ* measurements (MEASURED). Snow density (ρ_{snow}) is noted on colourbar, also obtained from SnowModel-LG Model.

Finally, the performance of the SnowModel-LG model was assessed against *in situ* measurements. The SnowModel-LG model provides daily snow depth and accompanying density measurements on a daily basis at 25km resolution. Currently data are only available from August 1980 - July 2018, however the model does benefit from being able to operate throughout the melt season. Results of the SnowModel-LG model performance in Figure 3.14 show a similar mean absolute error (MAE) to that obtained by the PIOMAS model (Figure 3.12) and mean bias error (MBE) of approximately 3cm. Zhou et al. (2021) compared the performance of the SnowModel-LG model snow depth estimates with NASA's Operation IceBridge (Kurtz et al., 2013, Newman et al., 2014) airborne measurements and reported a RMSE of 0.09m. However, these comparisons were made over 100x100km grids and averaged monthly.

The results outlined here have highlighted a significant issue with relying upon large-scale satellite data or model re-analyses to predict sea ice and snow characteristics on small scales. Although these products have been independently validated, it has been carried out on larger spatial-temporal scales than the *in situ* data presented here. These products are likely suitable for Pan-Arctic analyses but are not intended to inform local conditions. The following section will explore the impact that snow and ice has on seasonal underwater light, with sea ice concentration (SIC) obtained from the NSIDC passive microwave satellite data product (Meier et al., 2021), snow depth (S_D) from the CryoSat satellite data product (Kurtz and Harbeck, 2017) and sea ice thickness (SIT) from the CryoSat/SMOS merged satellite data product (Zhang and Rothrock, 2003).

3.5 Impact on Underwater Light

Light transmission through snow and sea ice has been modelled in various ways, ranging from implementing transmission models to estimate underwater light fields to assuming zero transmission under any areas of sea ice (Castellani et al., 2017, Sloughter et al., 2019, Stroeve et al., 2021). One consistent limitation however is usually the restriction of Polar Night. Above surface light fields are generally populated by satellite estimates of downwelling shortwave radiation, data which is not available during the period of Polar Night (see Chapter 2). Here we can extend simulations of under-ice light fields across the entire Arctic region throughout the full season and into the winter months, building on the light field model developed in Chapter 2. Figure 3.15 shows the monthly averaged daily surface PAR for January, April, July and October 2018 respectively. Above surface irradiance was calculated by the HEIMDALL model, assuming clear sky conditions. Downwelling spectral irradiance was calculated on an hourly basis, and integrated over the broadband PAR range ($400 - 700$nm) and 24 hours per day. Daily downwelling surface PAR was totalled and divided by the number of days in a given month to provide monthly averaged daily surface PAR for January, April, July and October. The period of Polar Night is evident in Figure 3.15A, with extremely low surface irradiance levels at most latitudes, particularly impacting high latitudes. Conversely, the monthly of July (Figure 3.15C) exhibits a comparable daily PAR irrespective of latitude, consistent with the period of Polar Day when the sun persistently remains above the local horizon. This behaviour is similarly seen in April (Figure 3.15B), where the sun spends much time above the horizon at high latitudes but with some day and night cycling. The dependence on observer latitude is most prominent in October (Figure 3.15D), where the most northern latitudes experience very little daily surface PAR.

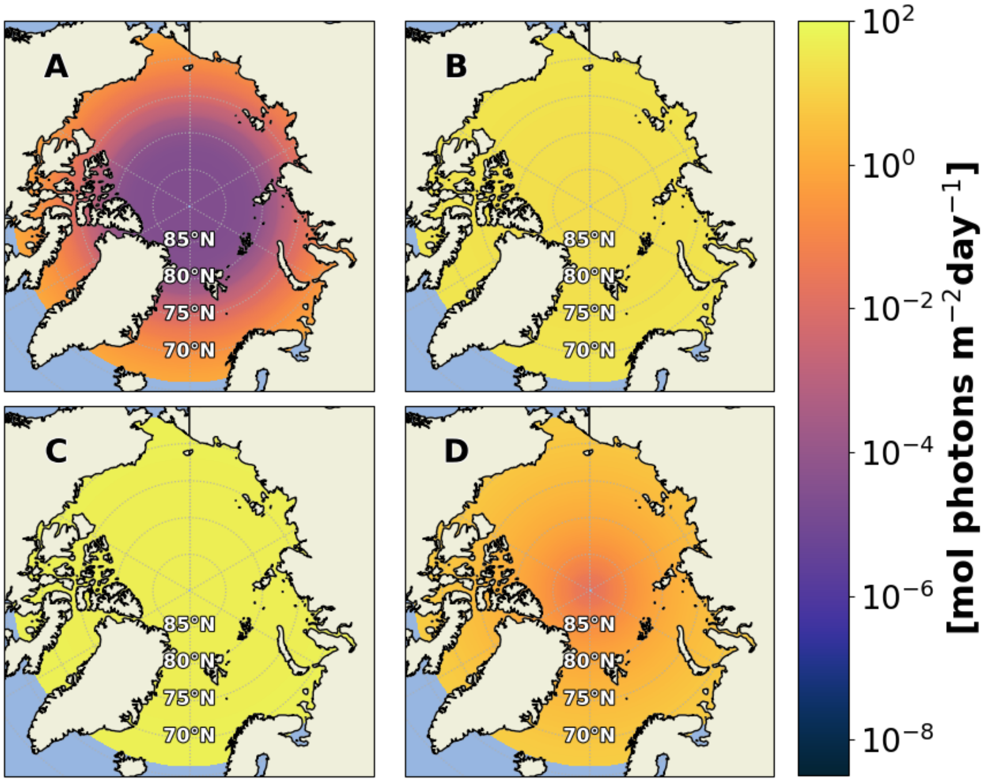

Figure 3.15: Monthly averaged daily surface PAR calculated using the HEIMDALL model for A) January, B) April, C) July and D) October 2018. Clear sky conditions are assumed.

To assess the impact snow and ice has on the light field during the transition between Polar Night and Polar Day, monthly averaged under-ice irradiance was calculated for January, April, July and October 2018 using satellite retrieved sea ice concentration (SIT), sea ice thickness (SIT) and snow depth (S_D). Note that due to independent datasets being used to quantify sea ice characteristics, the model has a quality control in place to stop erroneous scenarios such as the presence of snow but no ice. The presence of SIC is checked first, after which SIT can only exist if SIC does, and finally snow can only exist where SIT is present. Each calculation of Pan-Arctic monthly averaged daily underwater PAR took approximately 28 minutes to complete.

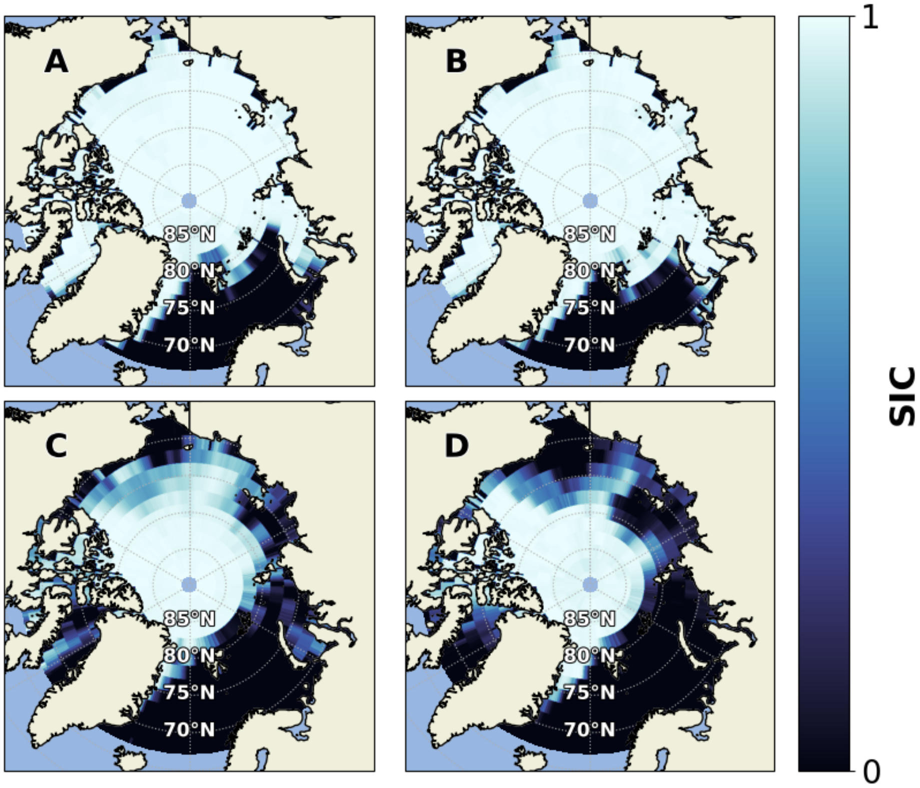

Figure 3.16: Monthly averaged Sea Ice Concentration (SIC) obtained from NSIDC passive microwave satellite data for A) January, B) April, C) July and D) October 2018.

Figure 3.16 shows monthly averaged sea ice concentration (SIC) from the NSIDC Nimbus-7/Defense Meteorological Satellite Program satellite for January, April, July and October 2018 respectively.

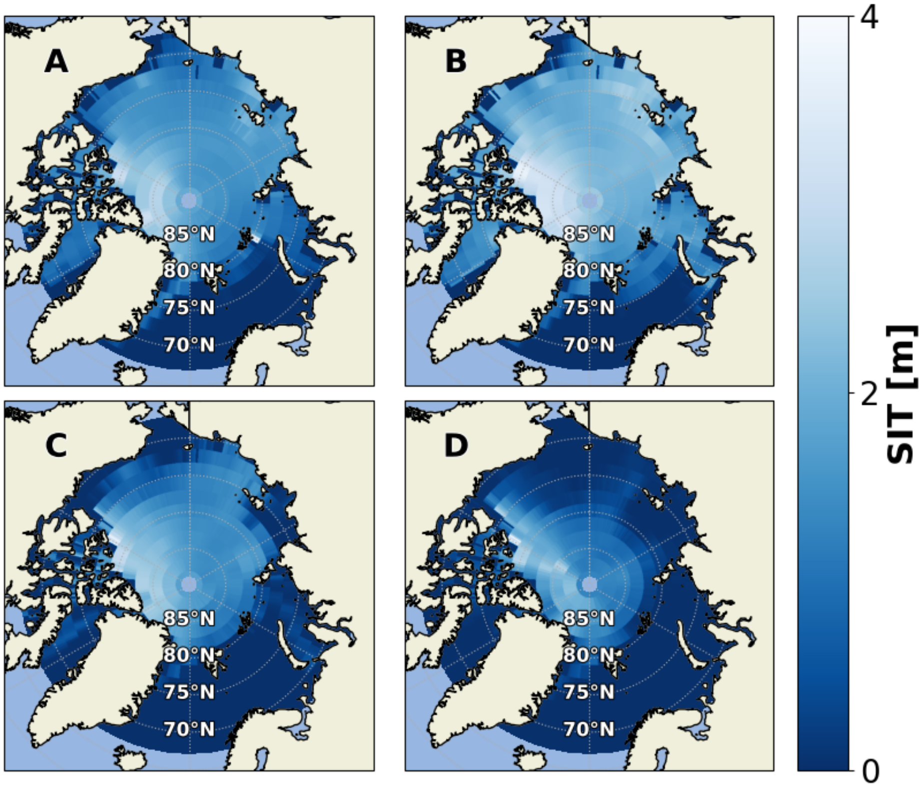

Figure 3.17: Monthly averaged Sea Ice Thickness (SIT) obtained from CryoSat/SMOS merged satellite data for A) January, B) April, C) July and D) October 2018.

Figure 3.17 shows monthly averaged sea ice thickness (SIT) for January, April, July and October 2018 respectively, obtained from the CryoSat/SMOS merged product satellite data.

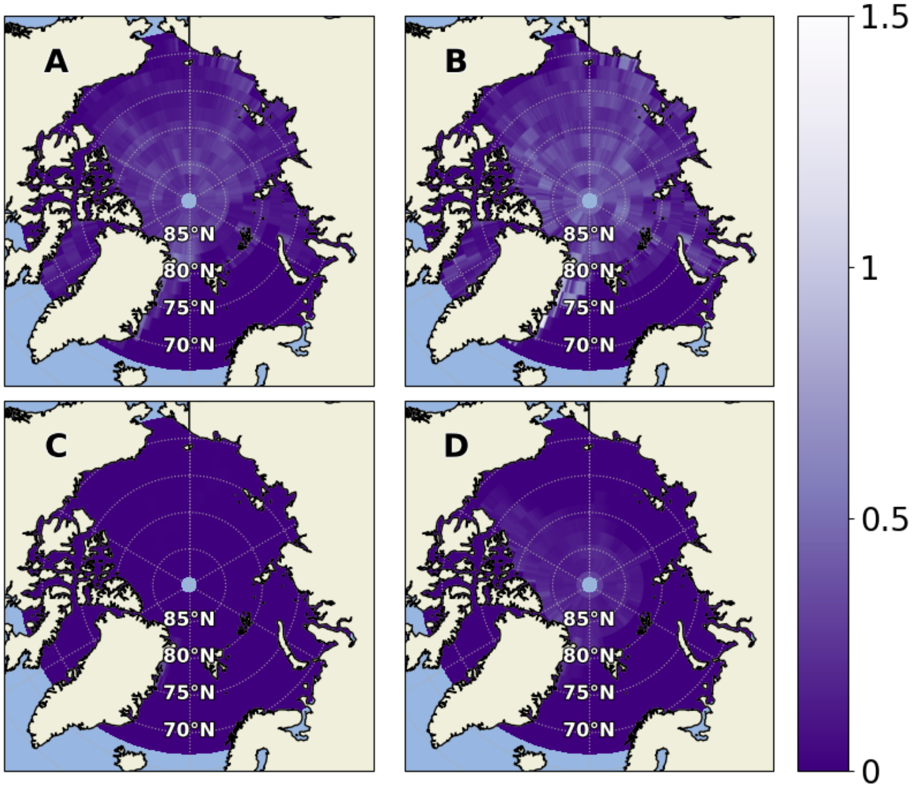

Figure 3.18: Monthly averaged Snow Depth (S_D) obtained from CryoSat satellite data for A) January, B) April, C) July and D) October 2018.

Figure 3.18 shows monthly averaged snow depth (S_D) for January, April, July and October 2018 respectively, obtained from CryoSat satellite data.

Figure 3.19 shows the monthly averaged daily under-ice PAR light fields for January, April, July and October 2018 respectively using the SIC, SIT and S_D data presented in Figures 3.16 to 3.18. Values shown are for PAR calculated immediately beneath the surface of the ice and include no attenuation by water. Since transmission of the above surface light field is dependent on solar zenith angle, the light field (Figure 3.15) was transmitted across the air-ocean boundary on an hourly basis according to the SIC fraction. Note that satellite data is not available directly over the pole, and linear interpolation was carried out on the final light field data to attain the smoothed data in Figure 3.19. Light was calculated on an hourly basis to ensure the correct transmission factor for the open water component (a function of solar zenith). SIC, SIT were extracted daily, and monthly averaged S_D was used as per satellite availability.

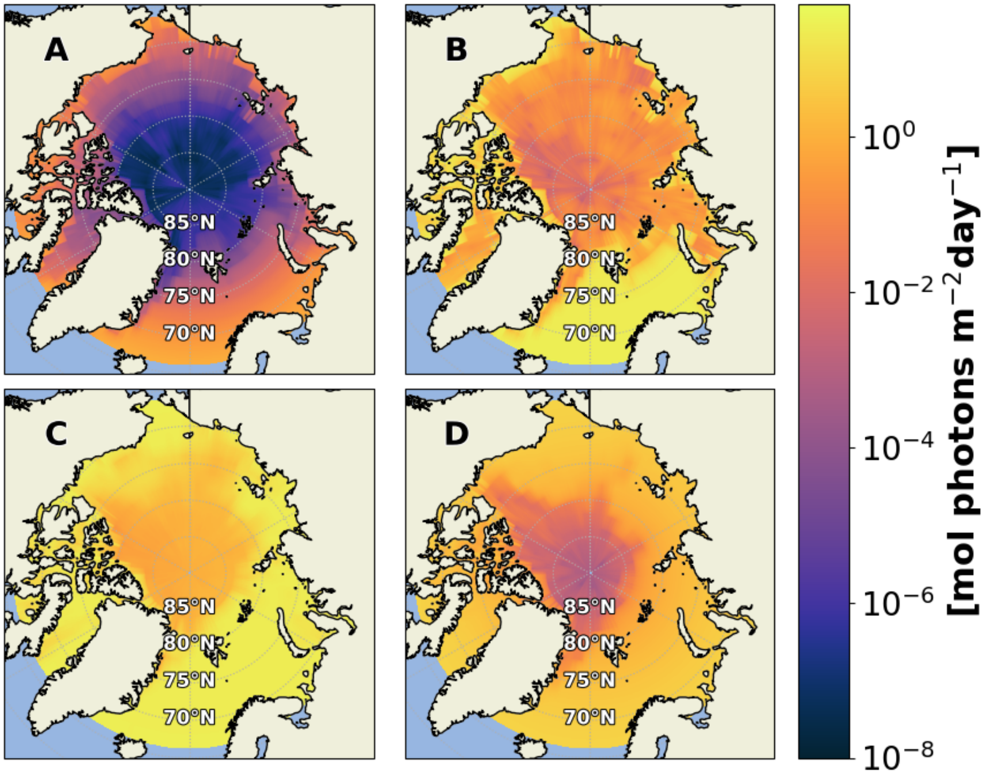

Figure 3.19: Monthly averaged daily underwater PAR calculated using the HEIMDALL model and snow and ice transmission model for A) January, B) April, C) July and D) October 2018. Clear sky conditions are assumed with daily SIC, SIT and monthly averaged S_D.

Light data results shown in Figure 3.19 demonstrate that the approach of attributing the under-ice light field to zero during Polar Night or in the presence of sea ice concentration is not entirely accurate. However it may be the case that although light is present under-ice, magnitudes are sufficiently low enough that the approximation of zero is adequate. Assessing the potential for these light levels to stimulate biological activity will be the focus of Chapter 5.

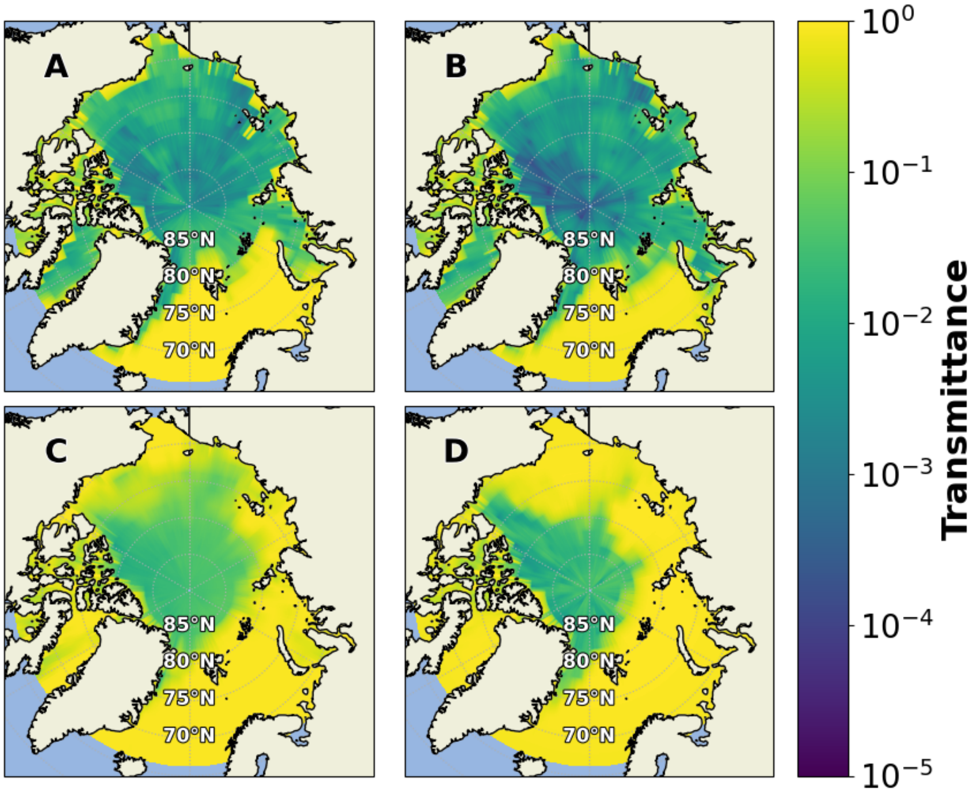

Figure 3.20: Monthly averaged daily PAR transmittance for A) January, B) April, C) July and D) October 2018. Clear sky conditions are assumed with daily SIC, SIT and monthly averaged S_D.

Figure 3.20 highlights the proportion of light that transmits into the ocean for January, April, July and October 2018 respectively. Due to greater SIT and S_D (Figures 3.17 and 3.18), spatially averaged transmission of light into the ocean is lower in April compared with January, with Pan-Arctic transmittance values of 31% and 38% respectively. July has a spatially averaged transmittance of 48%, with October seeing the highest proportion of light entering the ocean at 54%, suggesting that the primary predictor of light transmission is sea ice concentration. Note that these results have assumed that there is no seasonal bias in the satellite data used to predict transmitted light and reliability issues of satellite data previously highlighted may impact on transmittance values.

3.5.1 Hierarchy of Impact on Transmittance

This section will assess the hierarchy of controlling sea ice parameters that determine the magnitude of underwater light.

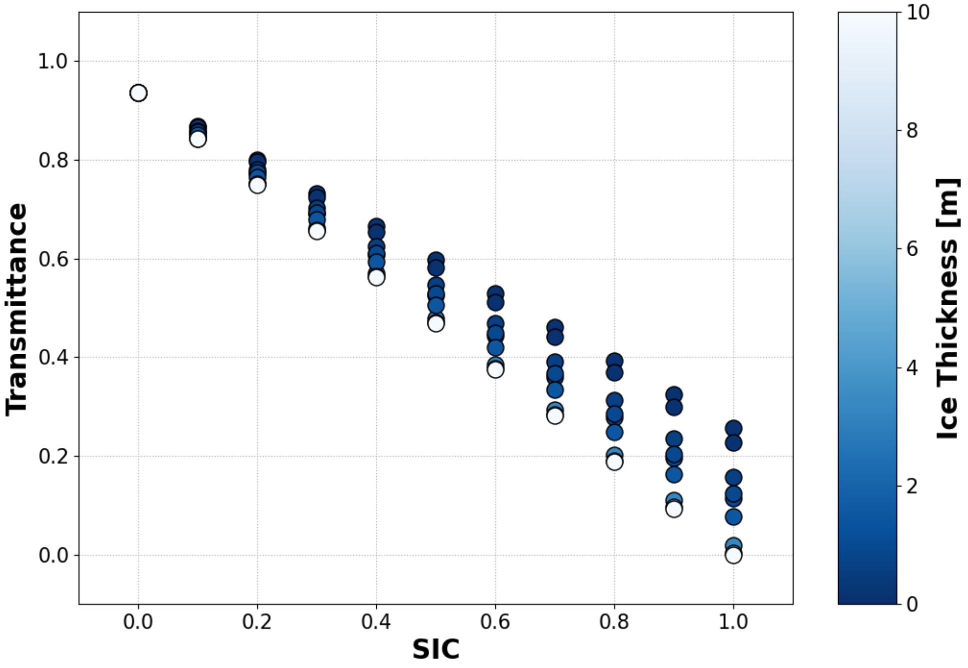

Figure 3.21: Transmission reduction as a function of Sea Ice Concentration (SIC), and Sea Ice Thickness (SIT).

Light transmission as a function of sea ice concentration (SIC) and sea ice thickness (SIT) is shown in Figure 3.21. These results clearly demonstrate that the most influential variable on under-ice light availability is SIC. Open water transmittance (SIC = 0) is > 0.9. Increasing SIC rapidly reduces transmittance by a factor that also depends on SIT. Very thick ice will transmit almost zero light when SIC = 1, but thinner ice (SIT < 0.5m) still transmits at least 20% of the above surface irradiance. This is equivalent to the impact that overcast conditions have on clear sky irradiance. Sea ice is still widespread even during the spring and summer seasons, and so biological models that discount under-ice light entirely could potentially be substantially underestimating light availability and subsequent biological responses.

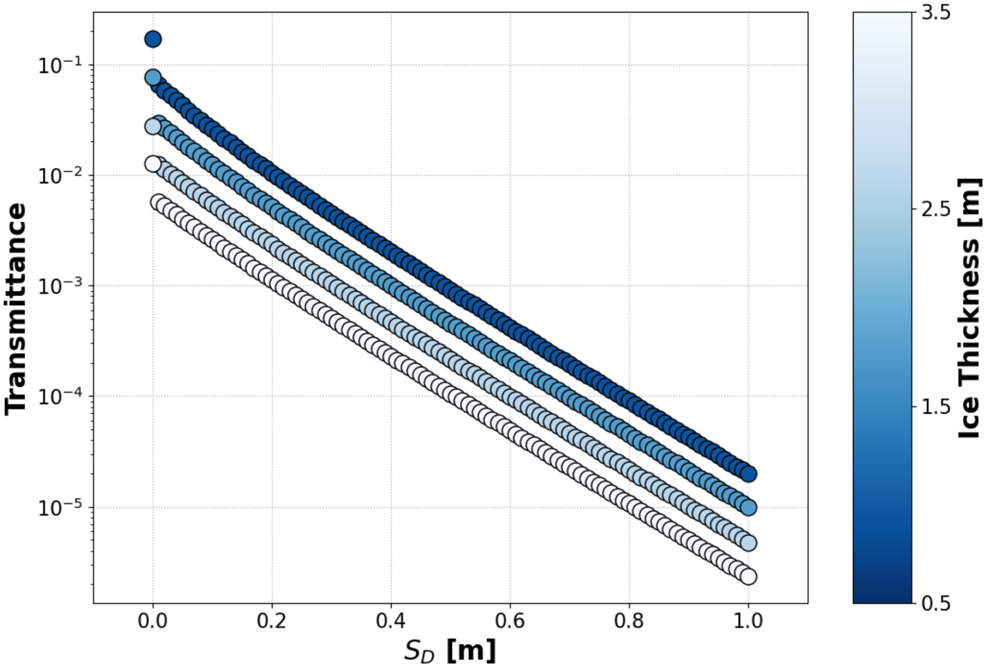

Figure 3.22: Transmission reduction as a function of Snow Depth (S_D) and Sea Ice Thickness (SIT) for constant Sea Ice Concentration (SIC) = 1.

The presence of snow on sea ice has a demonstrably larger effect on light field attenuation as seen in Figure 3.22. At 0m snow coverage, increasing the SIT depth from 0.5m to 3.5m results in a drop in transmittance from 0.17 to 0.01. For a fixed SIT of 0.5m, only 20cm of snow is required to have the same impact on transmittance that 3m of additional ice has. For each of the 4 displayed SIT values ($0.5\,\text{m}, 1.5\,\text{m}, 2.5\,\text{m}, 3.5\,\text{m}$), 1cm of snow results in a drop in transmittance of $\approx 60\%$. Figures 3.21 and 3.22 clearly demonstrate a hierarchy of influence on transmittance by snow and sea ice, with SIC being the dominant factor, followed by S_D and finally SIT.

3.6 Conclusions

Although under-ice light fields are generally considered to be zero during the period of Polar Night, or may have been ignored in the presence of sea ice (Perovich et al., 2007, Sloughter et al., 2019), these results show that even with 100% sea ice cover, there is potential for $> 20\%$ transmission of light to interface with the ocean.

Melt ponds present a challenging obstacle in retrieval of satellite estimates of SIT and S_D in the Northern Hemisphere during the May-September melt period. Recent notable work has shown progress in this area. Application of convolution neural networks (CNN) to CryoSat images has allowed for the identification of melt ponds and subsequent estimates of SIT underneath (Landy et al., 2022). Although this type of year round product is in the early stages, sufficient spatial resolution would make it possible to flag melt ponds in images and adjust spectral transmission to values measured by Light et al. (2015).

The surface scattering layer (SSL) has also been shown to persist over the melt season on the surface of both ice and snow, however it is not fully understood how this layer forms, nor are the resulting optical features. This feature cannot currently be parameterised via satellite measurements for Pan-Arctic study. As a consequence, any attempt to model the transmission of light throughout the melt season may result in some overestimation of available light due to the exclusion of attenuation by the SSL.

The most dominant limitation is the difficulty in relying upon satellite or reanalysis data to quantify local features and populate the snow and ice transmission model. Although these products are widely used and have been validated over large spatial-temporal ranges, Section 3.4.3 highlights substantial risk with using this data to inform under-ice light field parameterisation at specific locations, since there is no significant agreement between satellite or reanalysis estimates and local *in situ* measurements ($R^2 \leq 0.146$ for all products). The results in Section 3.5 demonstrate a hierarchy of considerations when quantifying the under-ice light field. Sea ice concentration is the dominant controlling parameter, followed by snow depth and finally sea ice thickness. As the Arctic continues to warm, the need for improved estimates of under-ice light fields is likely to increase as the homogeneity of the Arctic icescape reduces with ice structures experiencing increased melt and fracture. Satellite and reanalysis estimates of snow depth in this chapter have a mean average error (MAE) of $\approx$0.2m. Results in Figure 3.22 show that this error alone impacts the under-ice light field by an order of magnitude. It is likely that the spatial resolution of available SIT and $\mathrm{S_D}$ products are unable to capture the spatial heterogeneity of snow and ice on local scales, which may change rapidly as a result of local wind and precipitation. Due to these obvious limitations, the HEIMDALL model features the ability for user provided SIC, SIT and $\mathrm{S_D}$ inputs if such local measurements exists, and the use of satellite data to populate the snow and ice transmission model should be restricted to Pan-Arctic studies. The biological impacts of snow and ice on under-ice light will be assessed in Chapter 5.

Chapter 4

Amplification of Surface Irradiance by Multiple Reflection Effects

Introduction

Quantifying underwater spectral light is dependent on two main factors, accurate determination of the above surface light field and correctly parameterising attenuation of that light down the water column. It seems a logical assumption that one follows the other, and the above surface light field should be calculated before any attempt is made to address transmission of light through snow and ice, or across an open water air-ocean boundary. However, there are conditions in which the presence of snow and ice can alter the above surface light field.

Arctic Amplification is a well studied phenomenon, in which warming in the Arctic is occurring at a notably higher rate than global averages (Rantanen et al., 2022). Cloud cover has been proposed as a significant contributing factor to this mechanism (Pithan and Mauritsen, 2014, Taylor et al., 2013). Depending on what time of the year they are present, clouds can either cool or warm a region. Cloud cover can act to prevent solar irradiance reaching the surface by reflecting light back into space, whilst also allowing for multiple reflection of surface irradiance between cloud and snow. Analysis by Choi et al. (2020) and Alkama et al. (2020) suggests that cloud cover may contribute to regulating the melt speed of Arctic sea ice and as a result, dampen the rate of Arctic sea ice loss in summer. However, Pithan and Mauritsen (2014) found that Arctic Amplification is influenced primarily by temperature feedback mechanisms induced by cloud cover, causing warming in the region.

This chapter will discuss the amplification of above surface visible irradiance in the presence of snow and high fractional cloud cover. Firstly the chapter will focus on the reliability of satellites to accurately retrieve cloud cover estimates over snow-covered terrain. It will then outline the use of a convolutional neural network applied to all sky-images taken at the ArcLight Light Observatory in Ny Ålesund, Svalbard to retrieve accurate local cloud cover, and finally the use of associated irradiance data to quantify the magnitude of the amplification effect.

4.1 Background

4.1.1 Arctic Cloud Cover

Cloud cover is a ubiquitous feature in the Arctic, with many regions experiencing an average cloud cover value >50% for most of the year (Eastman and Warren, 2010). Observations made between 1980-2001 show a linear increase in spring cloud cover at a rate of $\approx 5\%$ decade^{-1}, a more modest increase of $\approx 0.4\%$ decade^{-1} for both summer and autumn, and a decrease of $\approx 4\%$ decade^{-1} for winter (Schweiger, 2004). However a more recent analysis using satellite and reanalysis data shows a shift in winter cloud cover towards a positive trend, with some areas of the Arctic showing an increase of $\approx 3\%$ year^{-1} between 1998-2013 (Jun et al., 2016).

4.1.2 Optical Properties of Cloud

Accurate determination of the attenuation of light through clouds depends on many factors such as liquid water content, black carbon content, ice crystal content and cloud droplet size (Kondratyev et al., 1998, Baran, 2004). Inhomogeneous structure also means extinction coefficients can vary by height within the cloud (Cairns et al., 2000). Terrestrial clouds can be highly reflective. Depending on the cloud type and associated thickness, albedo measurements can range from 0.1-0.9 (Conover, 1965, Liu et al., 2011, Xie and Liu, 2013). Although individual cloud properties will not be discriminated in this work, it is important to note that their highly complex structure results in large variances in optical behaviour.

4.1.3 Existing Work

Modelling of surface net radiation balance as a function of cloud over a snow-covered transect in the Greenland Ice Sheet was carried out by Cawkwell and Bamber (2002). They found that in comparison to a cloud-free day, surface net radiation reduced universally over the spectral range by a factor of around 1.4-1.5 under 100% cloud cover. Similarly, Barber and Thomas (1998) reported similar results from snow-covered ice in the Canadian Arctic. Downwelling shortwave radiation reduced by a factor of approximately 1.5 under 100% cloud cover compared to cloud-free conditions. This result was consistent over snow-covered First Year Ice and Multi Year Ice. Continuous shortwave radiation measurements made in Antarctica during continually overcast conditions showed downwelling radiation increased by approximately 85% when measured at a snow-covered sea ice site, compared with an open water site (Wendler et al., 2004).

A recent study by Jechow and Hölker (2019) claims to report the first results of amplification of Artificial Light At Night (ALAN) by ground snow and high cloud cover. This study assessed all-sky images to estimate scalar irradiance at one suburban site in Germany and one rural sub-Arctic site in Finland. At the suburban site during overcast conditions, the presence of ground snow resulted in an increase in downwelling scalar irradiance by a factor of approximately 31, compared with snow-free conditions. At the rural site during ground snow conditions, the presence of cloud cover increased downwelling scalar irradiance by a factor of approximately 10 compared to cloud-free conditions. This amplification effect is clearly enhanced in the presence of artificial light sources under cloud.

Although the impact of multiple reflection effects have been highlighted in literature (Schneider and Dickinson, 1976, Wendler et al., 1981, Rouse, 1987), this feature is not widely integrated to ecosystem models that use light as a key driver. Capturing this complex behaviour on a large scale can present many challenges due to the varying albedo of different surfaces, with water, ice and snow exhibiting average values around 0.03, 0.75 and 0.9 respectively (see Chapter 3). The surface albedo of land largely varies, from 0.05 for rainforests to 0.6 for sand dunes (Ponce et al., 1997). A visual description of multiple reflection can be seen in Figure 4.1.

4.2 Analysis of ArcLight Datasets

4.2.1 PAR Irradiance Measurements

The USSIMO instrument located at the ArcLight Light Observatory in Ny Ålesund, Svalbard (78.94°N, 11.84°E) records continuous spectral irradiance measurements at intervals of approximately 30 minutes. Spectral measurements integrated in the PAR range are used here to analyse multiple scattering amplification (Berge et al., 2021a). Also located at the ArcLight Light Observatory is a digital all-sky camera. The Canon EOS 5D Mark III camera is fitted with a fish-eye lens, allowing full 180° image capture of the sky overhead (Johnsen et al., 2021a). All-sky images were recorded at 60 minute intervals over several years. Data from both devices were extracted for the 2020 year. An example all-sky image is shown in Figure 4.2.

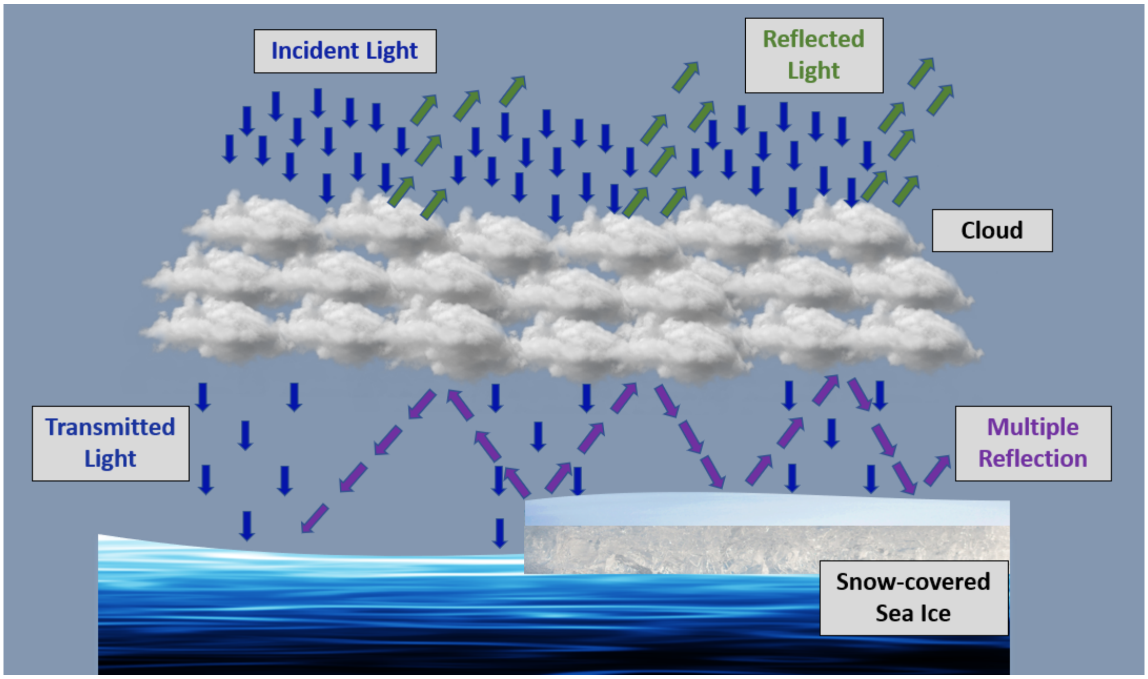

Figure 4.1: Diagram of enhanced irradiance reaching ocean surface due to multiple reflection between snow-covered sea ice and cloud. Above cloud blue and green arrows represent incoming and reflected irradiance respectively. Below cloud blue arrows represent transmitted irradiance, and purple arrows indicate multiple reflection of irradiance between snow and cloud.

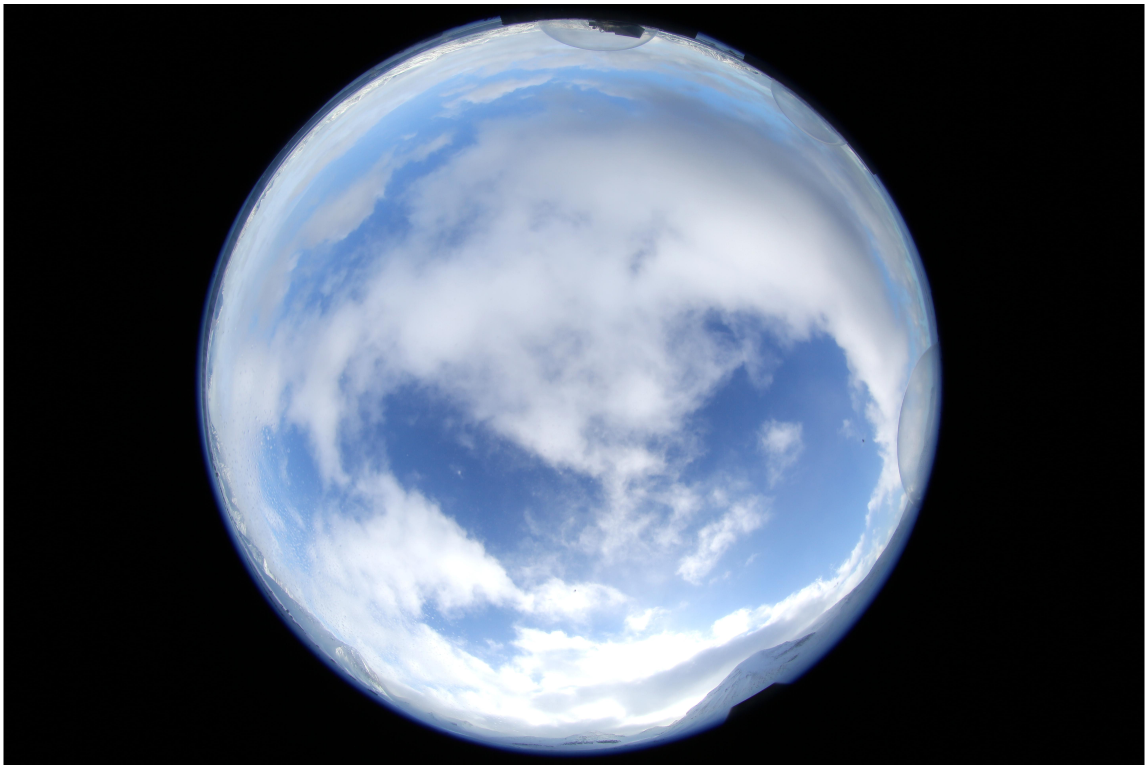

Figure 4.2: Example all-sky image from the ArcLight Light Observatory in Ny Ålesund.

Data from the ArcLight Light Observatory have previously been used to validate the above surface irradiance output from the HEIMDALL model. While model and measured outputs exhibited a good degree of match up in terms of order of magnitude, relatively small variances in modelled output were expected due to uncertainties in local cloud cover during the moment of instantaneous measurement. To assess the impact of multiple reflection amplification, accurate cloud cover data is a necessity.

4.2.2 Cloud Cover Data Comparison

Cloud Data Overview

Using timestamps recorded by the camera, cloud cover data for the observatory location was retrieved from the Copernicus Climate Change Service (C3S) Climate Data Store ERA5 Reanalysis (ERA5) (Hersbach et al., 2018). Reanalysis datasets are a popular choice for many climate research areas, as traditional satellite imagery suffers from both spatial and temporal discontinuities. To assess the performance of the ERA5 data to accurately predict local cloud cover under varying conditions, particularly during the presence of a highly reflecting surface albedo, reanalysis data is required during a period of ground snow, and a period of snow-free conditions.

The high latitude of Ny Ålesund, Svalbard means that the region generally experiences some form of snow presence year round, particularly at high altitudes. Mountainous terrain surrounding the town is usually continually snow-covered at the peaks. Due to this, the all-sky images from ArcLight are not entirely indicative of ground snow conditions.

The Zeppelin Observatory (78.91°N, 11.88°E) run by The Norwegian Polar Institute overlooks the town of Ny Ålesund, near to where the ArcLight Light Observatory is located (78.94°N, 11.84°E). One instrument located at the Zeppelin Observatory is a webcam that captures images every 10 minutes (Pedersen, 2013). These images were used to choose time periods that represent the weather conditions required to test the accuracy of ERA5 cloud cover data. The month of April was chosen for ground snow conditions, and July for snow-free conditions.

Figure 4.3: Webcam images overlooking Ny Ålesund during (A) April 2020 and (B) July 2020 obtained from the Zeppelin Observatory (Pedersen, 2013).

Figure 4.3 shows examples from the webcam image dataset. Daily images for each month were manually checked to ensure conditions met the requirements, i.e. all data used in April occurred during a period of snow cover, and all data for July was snow-free at ground level. Note that snow is present on the terrain surrounding Ny Ålesund in Figure 4.3B (July), however as this location is never snow-free, July represents a period of minimal snow cover through the year. All-sky images, PAR irradiance data and satellite cloud cover data were extracted for the months of April and July 2020.

The open-water HEIMDALL model described in Chapter 2 was initially run for both time periods at the ArcLight Light Observatory location, using cloud data imported from the Copernicus Climate Change ERA5 Reanalysis. For multiple reflection to be occurring due to the presence of ground snow, results should demonstrate a higher than expected amplitude of measured light during periods of high cloud cover for April. This feature should be less noticeable for July but may still be present due to snow-covered mountains adjacent to the detectors, and the reflection from snow-free land which has an albedo value one order of magnitude higher than open water (Ponce et al., 1997). Results are shown in Figures 4.4 and 4.5 respectively.

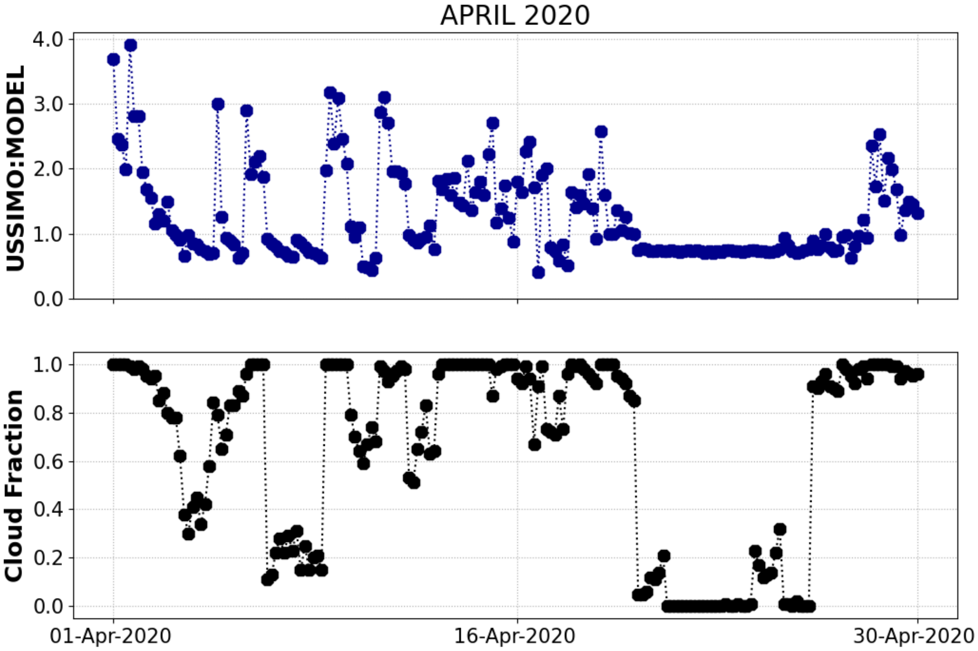

Figure 4.4: Ratio of measured (USSIMO) to modelled (MODEL) downwelling PAR irradiance at the ArcLight Light Observatory during April 2020. Cloud fraction (lower panel) for modelled light is determined via Copernicus Climate Change Service ERA5 Reanalysis. During periods of high fractional cloud cover, the USSIMO sensor recorded irradiance signals up to 4 times higher than predicted by HEIMDALL.

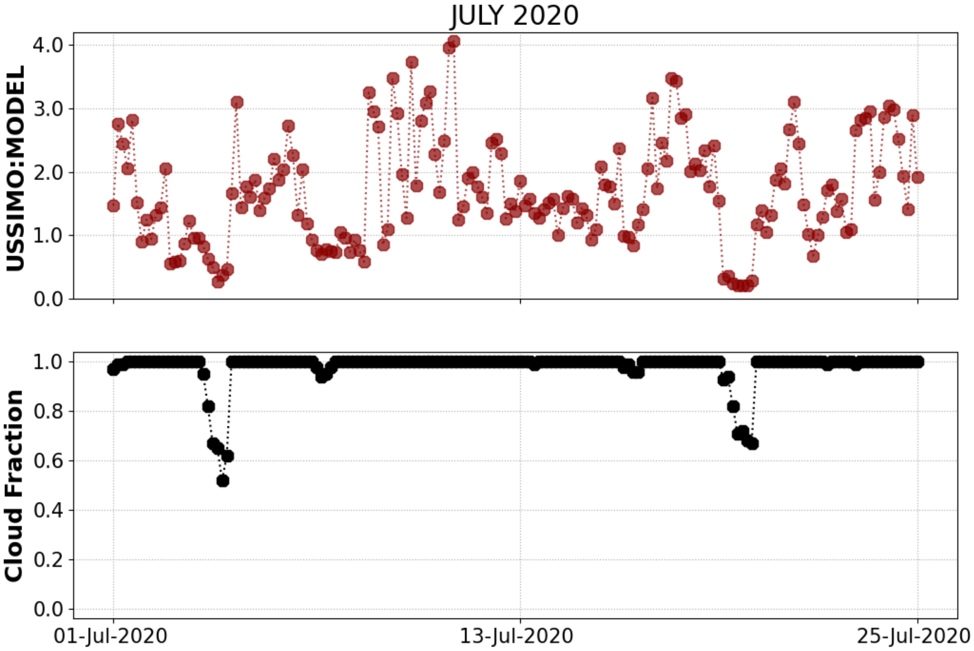

Figure 4.5: Ratio of measured (USSIMO) to modelled (MODEL) downwelling PAR irradiance at the ArcLight Light Observatory during July 2020. Cloud fraction (lower panel) for modelled light is determined via Copernicus Climate Change Service ERA5 Reanalysis. During periods of high fractional cloud cover, the USSIMO sensor recorded irradiance signals up to 4 times higher than predicted by HEIMDALL.

Figures 4.4 and 4.5 show the ratio of measured to modelled light. The results appear to demonstrate some evidence of multiple reflection, but no obvious and consistent correlation with high cloud cover. As cloud cover data from ERA5 are averaged both temporally and spatially, improved accuracy on local cloud cover is required for a more robust analysis of multiple reflection.

Local Cloud Cover Estimation

Estimating local cloud cover can be difficult to carry out manually by eye. To obtain a more accurate estimate, image analysis techniques have been shown to be successful, particularly the application of neural networks (Luo and Ding, 2019, Zhang et al., 2018, Xie et al., 2020). One drawback of such an approach is the requirement of an adequate training dataset. In order to train a neural network to automatically detect features in images, a training dataset of source images and label images are required. This involves manually annotating the label images to inform the neural network of certain features present in the source images, such as the presence of cloud. This task can be time consuming as training requires a sufficiently large dataset. Xie et al. (2020) recently reported results of a custom built deep learning convolutional neural network to estimate cloud cover from all-sky images. Although the proposed model is not accessible for community use, the database of training images are available to download (https://github.com/CV-Application/WSISEG-Database: Accessed 27 May 2022). This database of 400 all-sky images and associated annotated label images were used as a training dataset to estimate cloud cover from all-sky images taken at the ArcLight Light Observatory.

The convolution neural network (CNN) used to estimate cloud cover is known as a U-net, named after the architectural shape of the network and first proposed by Ronneberger et al. (2015) for applications in bio-medical image segmentation. These machine learning techniques usually rely upon thousands of training images. This particular type of network was built to provide a fast image segmentation process with much fewer training images, as access to thousands of image samples is not always feasible in the medical field (Ronneberger et al., 2015). Implementation of the CNN was done via the TensorFlow open source machine learning platform packages imported into Python.

To prepare the input image dataset, all images were standardised for brightness levels, i.e. darkest value assigned a value of 0 and bright assigned a value of 255. Brightness values were then normalised to values between 0-1 to accelerate model convergence, and images were cropped to a size of 512x512 pixels to comply with the U-net requirements. The process of cropping the images only impacted the black background pixels and did not affect the actual all-sky dome images. Training and validation datasets were split into 90% and 10% proportions respectively.

Input images were run through the CNN for 90 epochs, at this value the error had begun fluctuating around a minimum and convergence was reached. The parameters determined during training and validation were then applied to infer cloud cover values on the ArcLight (target) dataset. As with the input dataset, all images in the target dataset had brightness values adjusted and normalised, and were cropped to 512x512 pixels.

The output of the CNN is an all-sky grayscale mask that represents areas of the image where cloud is present. An example target image and output mask can be seen in Figure 4.6. Once this mask has been generated, the brightness values are rescaled back to a range of 0-255 in order to threshold cloud and sky pixels.

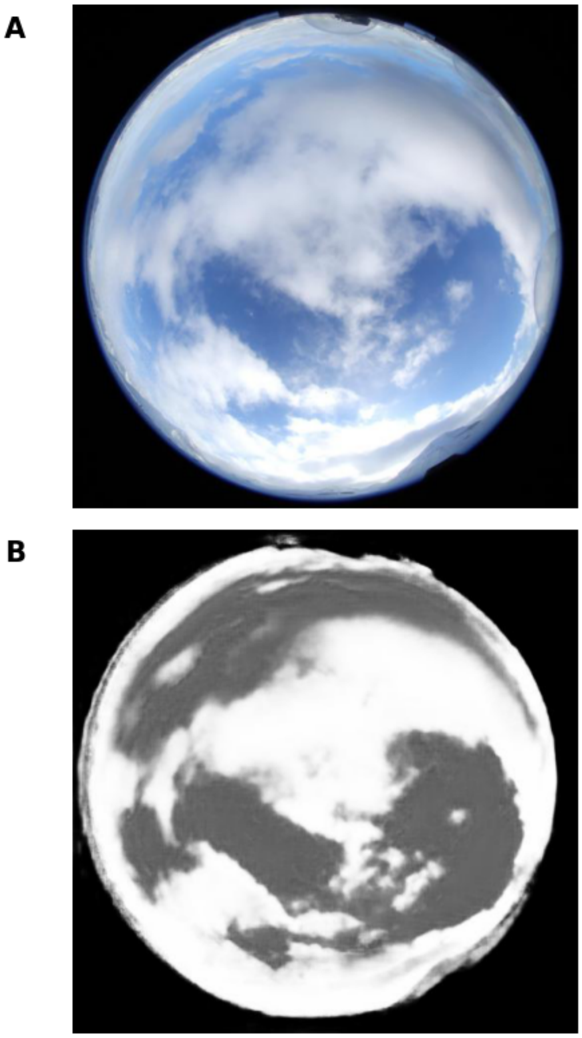

Figure 4.6: Example of target all-sky image from ArcLight Light Observatory (A) and output cloud mask from CNN (B).

To determine fractional cloud cover, each pixel value is binned into an RGB value depending on which grayscale range they fell within. Pixels with value < 10 (indicating the black background) were assigned to (0, 0, 0) to remain black. Pixels with values $\geq$10 and <140 were assigned blue (0, 0, 255) to represent sky and the remaining pixel values red (255, 0, 0) indicating cloud.

The final stage of processing was to crop out the outer perimeter of each all sky RGB mask image. As seen in Figure 4.6, parts of the snow-covered mountain terrain surrounding the camera apparatus is being mistaken for cloud cover due to the brightness of the snow. The same outer perimeter area was removed from each all-sky image RGB mask. Finally, the fractional cloud cover value is defined as the ratio of red pixels to red + blue pixels. Note that there was no correction for image distortion, however as the camera irradiance detector was cosine corrected this step shouldn't be needed as the cloud cover data are being used to determine a relationship between measured irradiance and fractional cloud cover.

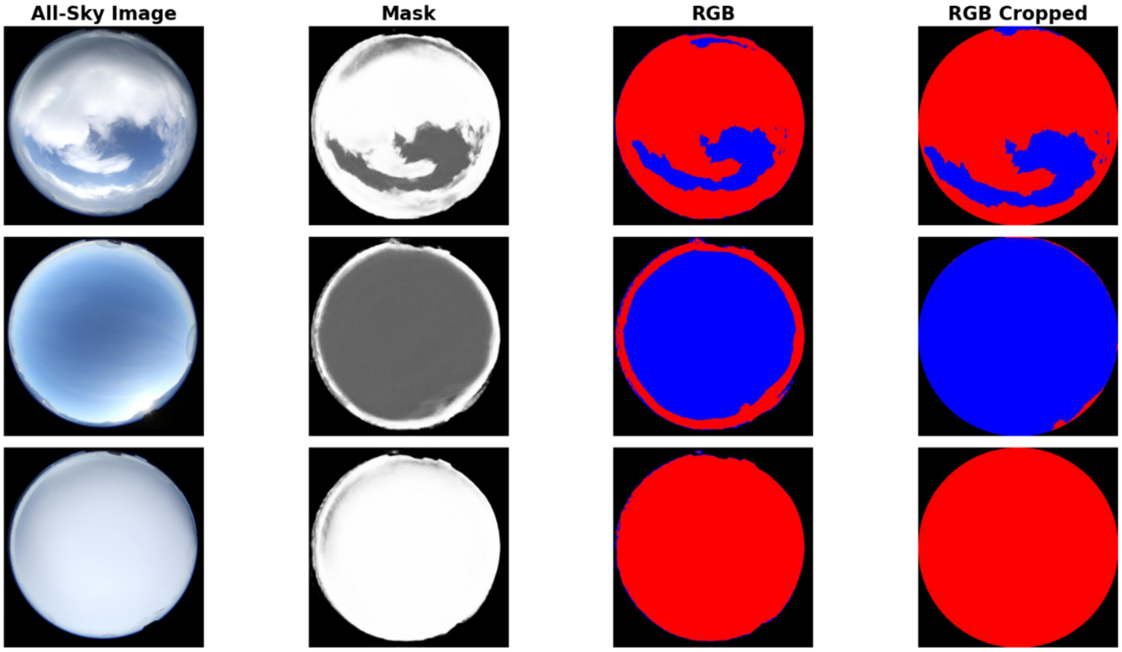

Figure 4.7: Examples of full process using CNN to determine cloud cover from all-sky images.

The all-sky camera captured continuous images throughout the full day, however as the training dataset only included images when the sun was above the horizon, analysis on the ArcLight dataset was restricted to images recorded during daylight hours only.

Note that some images were removed from analysis. Data from July 26th - July 31st inclusive have been excluded due to an obstruction on the dome housing the camera that caused erroneous classification of clouds (Figure 4.8). During April, 16 images were excluded due to active snow precipitation or ice covering the dome. For the July dataset, 4 images were excluded due to optical artefacts caused by refraction of sunlight through the dome inducing errors in the CNN application. The total target dataset consisted of 194 images for April and 171 for July.

Figure 4.8: Ornithological obstruction and unfortunate aftermath on July 26th.

4.2.3 Comparison of Cloud Cover Data Sources

A comparison of cloud cover data retrieved from reanalysis data (ERA5) and inferred from the all-sky images via convolutional neural network (CNN) can be seen in Figure 4.9, with associated Mean Bias Error (MBE) noted for each month.

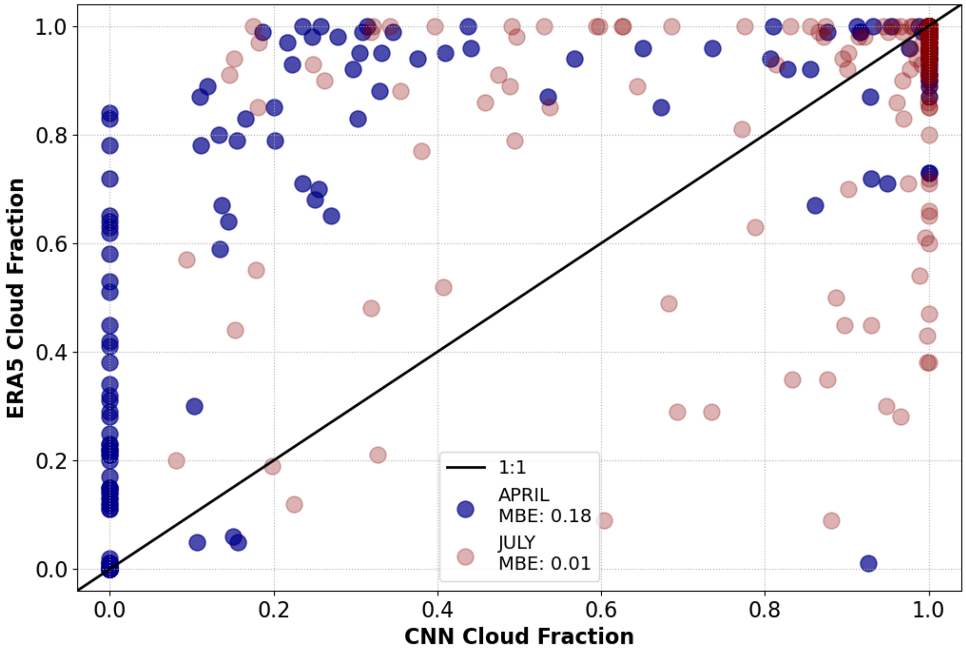

Figure 4.9: Comparison of cloud cover determined by Convolution Neutral Network (CNN) and Copernicus Climate Change ERA5 Reanalysis. Mean Bias Error (MBE) noted for each month.

Data from Figure 4.9 show that there is a clear tendency for the ERA5 data to overestimate cloud cover in April (MBE = 0.18) compared with July (MBE = 0.01). This is particularly evident when local cloud cover determined via the CNN method is zero. As the ERA5 data are averaged over a time period of 60 minutes and 0.25° squared grid, the expectation would be an approximately equal over and under-estimation, a feature seen in the data from July. It appears from Figure 4.9 that a clear bias is being introduced to the ERA5 reanalysis method when ground snow is present.

Previous work has shown that the ERA5 reanalysis can struggle to accurately determine fractional cloud, particularly during winter months. Ansari et al. (2021) analysed the results of fractional cloud cover retrieved from ERA5 compared with 96 visual observation stations across South Korea between 2010-2019. Their results show a large variation in visual data compared with ERA5 data, with a percentage deviation as large as -70% during winter, confirming the tendency of ERA5 to overestimate at this time of year. They speculate that poor performance in winter may be attributed to the presence of snow or incorrect detection of cloud due to lower temperatures.

Satellites in general appear to struggle to discriminate between cloud and snow-covered terrain (Irish et al., 2006, Hall and Riggs, 2007). Error analysis by Stillinger et al. (2019) assessed the performance of the MODIS satellite at classifying cloud cover during periods of ground snow, compared with 26 manually labelled satellite images. Results showed overall precision and recall values of 0.17 and 0.72 respectively. This essentially means that 28% of cloud present in images was missed entirely, and 83% of pixels identified as cloud were snow.

Discriminating between cloud and snow is particularly important at the poles, where snow cover is ubiquitous throughout the year. Reliance upon satellite data to quantify local cloud cover even at high temporal resolution may induce errors in above surface light field estimations due to ground snow or snow-covered ice being erroneously classified as cloud.

4.2.4 PAR Irradiance After Cloud Correction

The above surface component of the HEIMDALL open water light field model was re-run at the ArcLight Light Observatory location using cloud cover values obtained via image analyses of all-sky images. Comparison of measured to modelled light was re-analysed, with results shown in Figures 4.10 and 4.11.

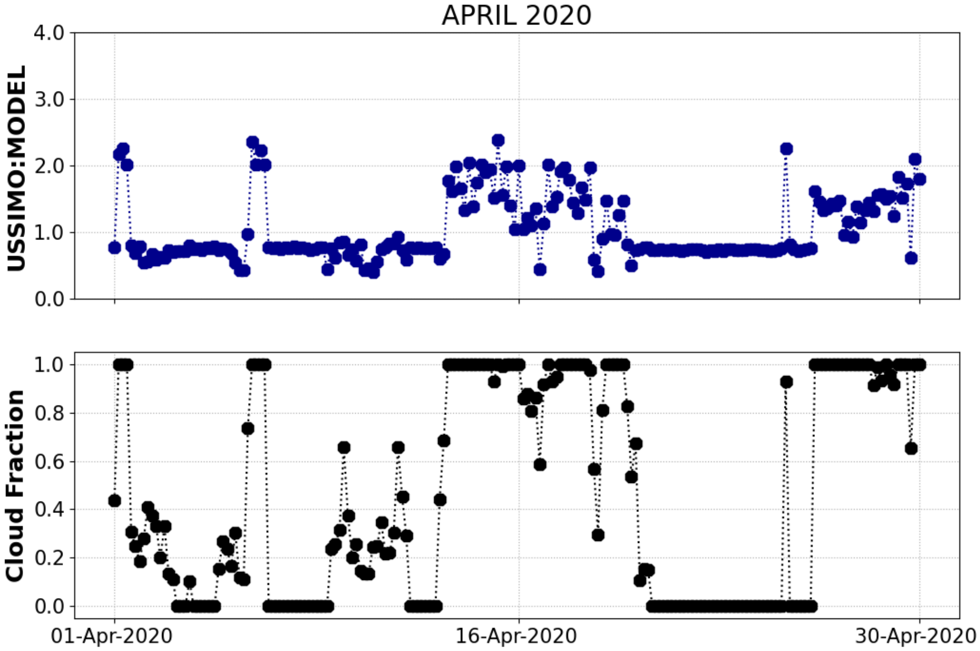

Figure 4.10: Ratio of measured (USSIMO) to modelled (MODEL) downwelling PAR irradiance at the ArcLight Light Observatory during April 2020. Cloud fraction (lower panel) for modelled light is determined via Convolutional Neural Network (CNN) applied to all-sky images. There still remains a discrepancy between measured and modelled irradiance by a factor ≈ 2 during periods of high cloud cover.

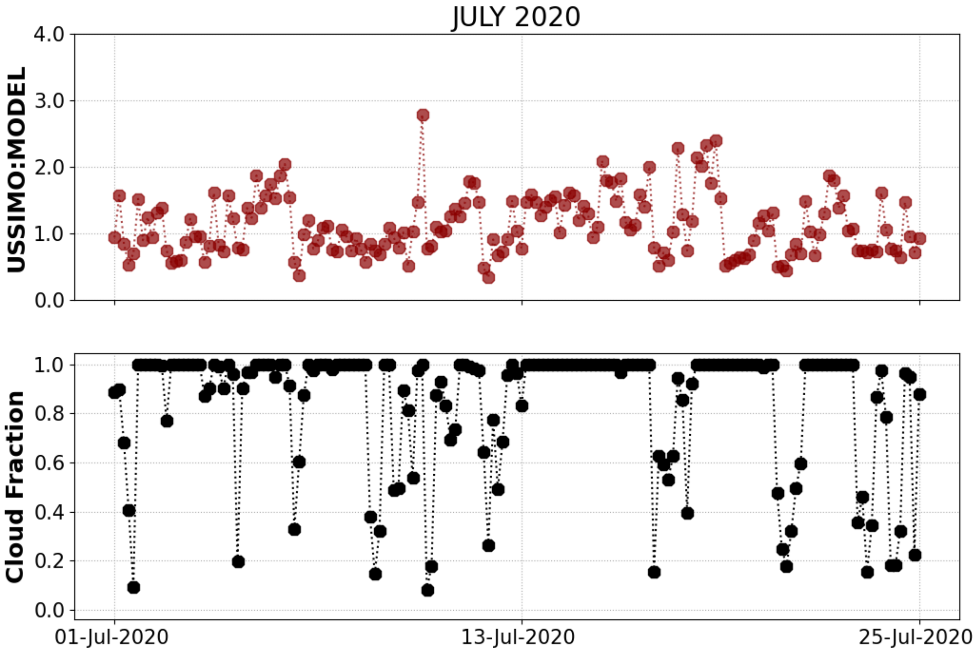

Figure 4.11: Ratio of measured (USSIMO) to modelled (MODEL) downwelling PAR irradiance at the ArcLight Light Observatory during July 2020. Cloud fraction (lower panel) for modelled light is determined via Convolutional Neural Network (CNN) applied to all-sky images. There still remains a varying discrepancy between measured and modelled irradiance during periods of high cloud cover.

Implementing accurate cloud cover values into HEIMDALL appears to result in more consistent behaviour of the ratio of measured to modelled light. During the period of snow cover in April (Figure 4.10), overcast conditions generally lead to an increase in expected light levels by a factor of ≈ 2. Note that during clear sky conditions, there is evidence of a tendency for the model to overestimate the measured light field. This is likely due to the surrounding terrain blocking out a fraction of the direct light field, as seen in Figure 4.7, All-Sky Image number 2. Maximum solar elevation throughout April at this latitude ranges from 15° to 25°, resulting in the solar disc being partially obscured by surrounding terrain. Both datasets are also likely to show some of the measured diffuse atmospheric light being blocked out, resulting in an overestimation of modelled light compared with measurements.

Results for July are less clear in quantifying multiple reflection amplification effects. Overcast conditions are more common during the July period. Whilst fractional cloud cover is high, visual inspection of the all-sky images does appear to show a thinner cloud type compared with that of April.

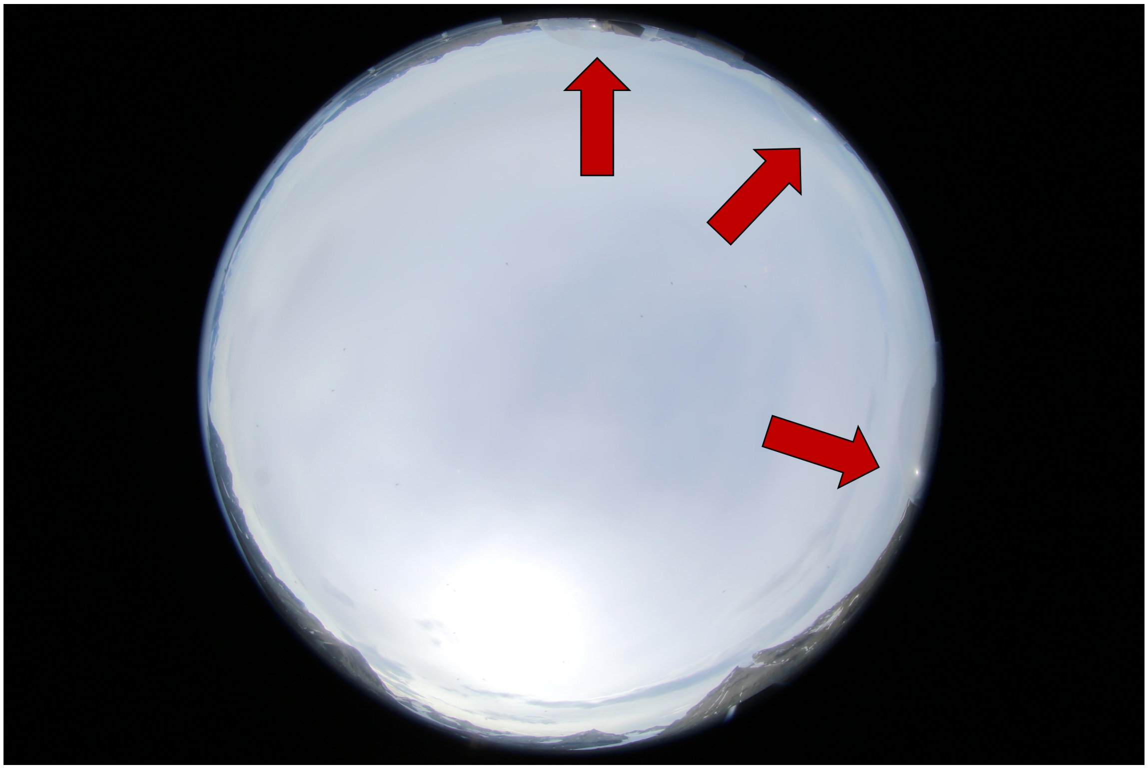

Figure 4.12: All-sky image from July 2020. Conditions appear to be overcast, however cloud is sufficiently thin that solar disc can be viewed, as well as optical artefacts in adjacent domes (red arrow labels).

Figure 4.12 shows the solar disc reflecting in the perspex dome covers placed on top of the instruments at the ArcLight Light Observatory. These conditions would be classified as overcast by the CNN, however the cloud is sufficiently translucent that the image of the solar disc is penetrating the cloud, as the solar position can clearly be seen in the image. These thin cloud conditions were more common in the July image dataset.

Observations made as part of the SHEBA campaign from 1982-1999 indicate that during this period, cloud cover in the Arctic was generally thinner in summer compared with spring, however this excludes the Barents Sea and Nansen Basin regions where clouds were thicker in summer (Wang and Key, 2005). In contrast, more recent observations from Andenes in the Norwegian Arctic reported ground-based measurements of cloud properties between 2011-2017. They noted a decrease in cloud thickness with higher cloud base height in July compared with April (Schäfer et al., 2022).

Although a thinner cloud type may be contributing to higher than expected irradiance values during overcast conditions in July, data from Figure 4.11 suggest that there are still amplification effects occurring during the summer period, as ground albedo is not reduced to zero in the absence of snow.

4.2.5 Daylight Multiple Reflection

Visualising the data as a function of cloud cover shows the ratio of measured to modelled light linearly increasing for both months after a fractional cloud cover value of ≈ 0.65 is met. Figures 4.13 and 4.14 both exhibit this behaviour, with a much larger gradient of increase for the April dataset.

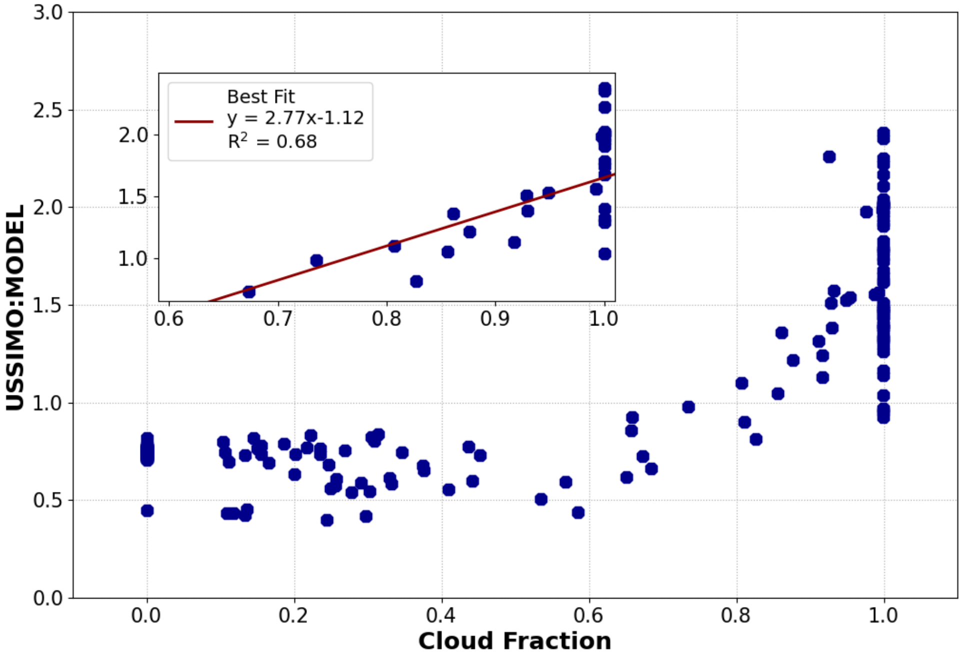

Figure 4.13: Ratio of measured (USSIMO) to modelled (MODEL) light for April 2020 as a function of fractional cloud cover determined by convolutional neural network (CNN). Insert plot shows linear increase in ratio after cloud cover reaches ≈ 0.65 with associated R^2 of model fit noted.

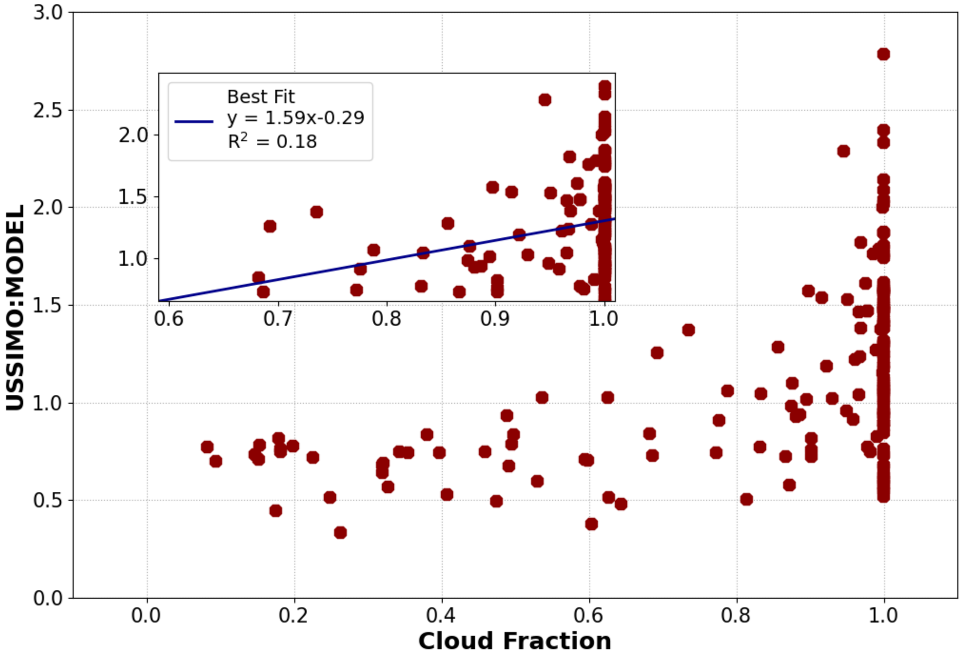

Figure 4.14: Ratio of measured (USSIMO) to modelled (MODEL) light for July 2020 as a function of fractional cloud cover determined by convolutional neural network (CNN). Insert plot shows linear increase in ratio after cloud cover reaches ≈ 0.65 with associated R^2 of model fit noted.

There is a clear relationship demonstrated in Figure 4.13 ($R^2 = 0.68$) between increasing cloud cover and amplification of the irradiance that is predicted using current modelling approaches, with a weaker correlation in July shown in Figure 4.14 ($R^2 = 0.18$). This suggests the presence of ground snow is inducing a stronger effect. It is also evident that the magnitude of the amplification by ground snow is not stable and varies during periods of overcast conditions (cloud fraction = 1.0), which may be a result of changing surface albedo. Throughout April, the coverage of ground snow was not static, cycling between melt and re-cover. Periods of snow-covered sea ice over the nearby fjord were also noted, as seen in Figure 4.15.

Figure 4.15: Webcam images overlooking Ny Ålesund during (A) late April 2020 and (B) early April 2020 obtained from the Zeppelin Observatory (Pedersen, 2013). Images show the variation in surface albedo due to changing snow cover.

This changing surface albedo likely contributes substantially to the range of values at high cloud cover shown in Figure 4.13. It is speculated that larger ratios are more likely after periods of heavy snowfall and lower values after melt, although there is no robust data on active precipitation or sea ice melt at the site location to corroborate this.

Data from July also demonstrate the existence of multiple reflection events (Figure 4.14). A linear increase of measured to modelled light is present, but with smaller gradient and larger variance in the data. As discussed in Section 4.2.4, differences in cloud thickness during July may contribute to the range of values seen in Figure 4.14, however this is likely also being driven by multiple reflection events between snow-free land and cloud, occurring on a smaller scale than reflections between cloud and snow.

Both datasets may also be influenced by local topography. Multiple reflections occurring between clouds and snow capped mountains influence ground level irradiance even in the absence of ground snow at the detector. Radiative transfer simulations carried out by Rozwadowska and Górecka (2012) noted that cloud base height above a snow topped mountain controls the horizontal distance a photon undergoing multiple reflection can travel, with higher base height allowing for further distance. An increased irradiance of approximately 20% was noted when topography was taken into account, compared with a plane parallel surface assumption of multiple reflection. Dependent variables also included solar azimuth and zenith angles. The effect is also possible during cloudless skies, with multiple reflections occurring between the atmosphere and mountain tops, with increased irradiance of around 11% (Rozwadowska and Górecka, 2017).

Data from Figures 4.10 and 4.11 suggest that there likely exists a range of amplification factors that depend on both cloud coverage and a varying surface albedo. As the focus of this work is on light fields beneath sea ice and snow, the data from April provide the best representation of conditions in a cloudy and snow-covered sea ice environment where bare land albedo and local topography are not of relevance. Following the linear relationship from the April dataset (Figure 4.13 insert), an average amplification factor of around 1.65 would typically be expected during overcast conditions. This is similar to the results reported by Wendler et al. (2004), who described an average increase of 85% in surface irradiance for the same conditions.

The HEIMDALL model calculates surface irradiance as a function of cloud fraction ($\mathrm{C_F}$) (Kasten and Czeplak, 1980) as:

$$\mathrm{E_D}\,(\mathrm{C_F}) = \mathrm{E_D}\,(0)\,(1 - 0.75\,\mathrm{C_F^{3.4}}) \tag{4.1}$$

where $\mathrm{E_D}\,(\mathrm{C_F})$ is surface irradiance at cloud fraction $\mathrm{C_F}$, and $\mathrm{E_D}\,(0)$ is surface irradiance at 0% cloud. In the presence of snow-covered sea ice, multiple reflection effects will be included when $\mathrm{C_F} \geq 0.65$ (65% coverage) with Equation 4.1 adjusted as per the linear relationship determined by the April dataset (Figure 4.13 insert) as follows:

$$\mathrm{E_{D\,GS}}\,(\mathrm{C_F}) = \mathrm{E_D}\,(0)\,(2.77\,\mathrm{C_F} - 1.12)\,(1 - 0.75\,\mathrm{C_F^{3.4}}) \tag{4.2}$$

where $\mathrm{E_{D\,GS}}\,(\mathrm{C_F})$ is surface irradiance at cloud fraction $\mathrm{C_F}$, under conditions of snow-covered sea ice. The impact of this amplification effect on under-ice light availability for biological processes will be discussed in Chapter 5.

4.2.6 ALAN Multiple Reflection

As noted in Section 4.2.2, the convolutional neural network (CNN) cannot be applied to all-sky images taken when the sun is below the horizon. To assess the presence of multiple reflection amplification from artificial light at night (ALAN), two all-sky images and associated irradiance measurements from January 2020 were chosen to represent clear sky and overcast conditions. Assessment of cloud cover was done manually by eye, and ground snow conditions were confirmed using the Norwegian Polar Institute webcam.

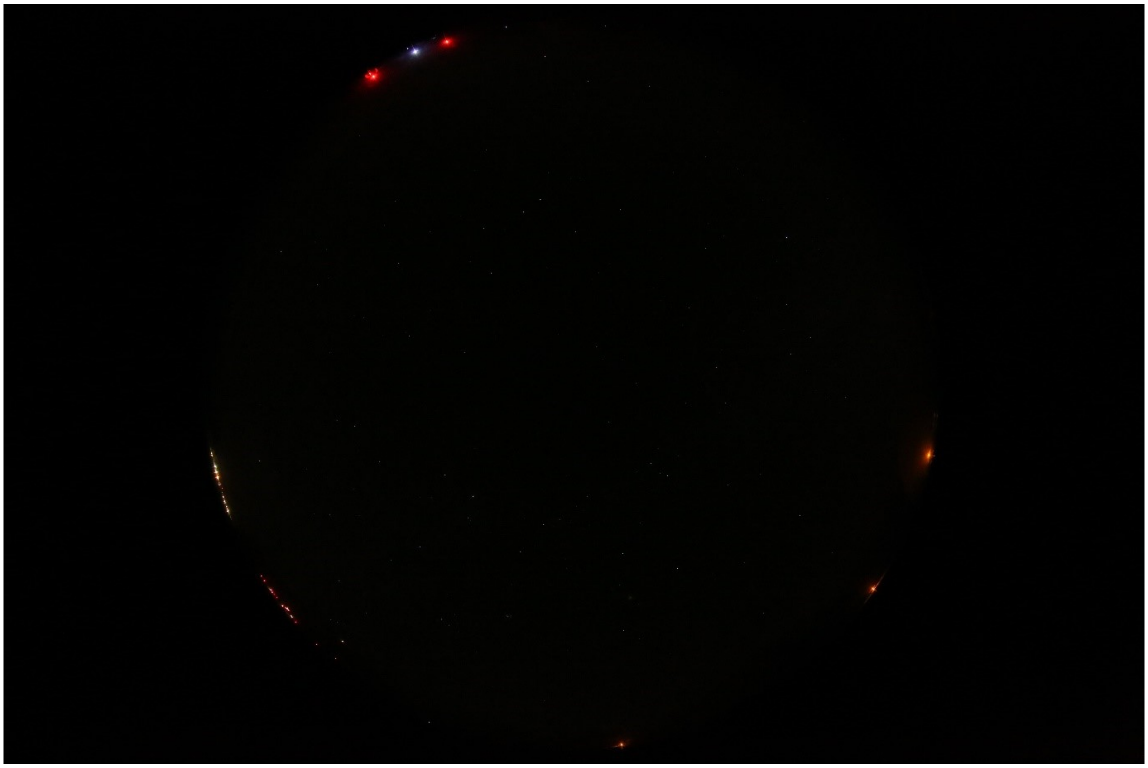

Figure 4.16: All-sky image from January 2020 showing clear sky conditions. Note the presence of starlight in the image. Direct sources of artificial light can be seen around the perimeter with limited sky glow near the zenith.

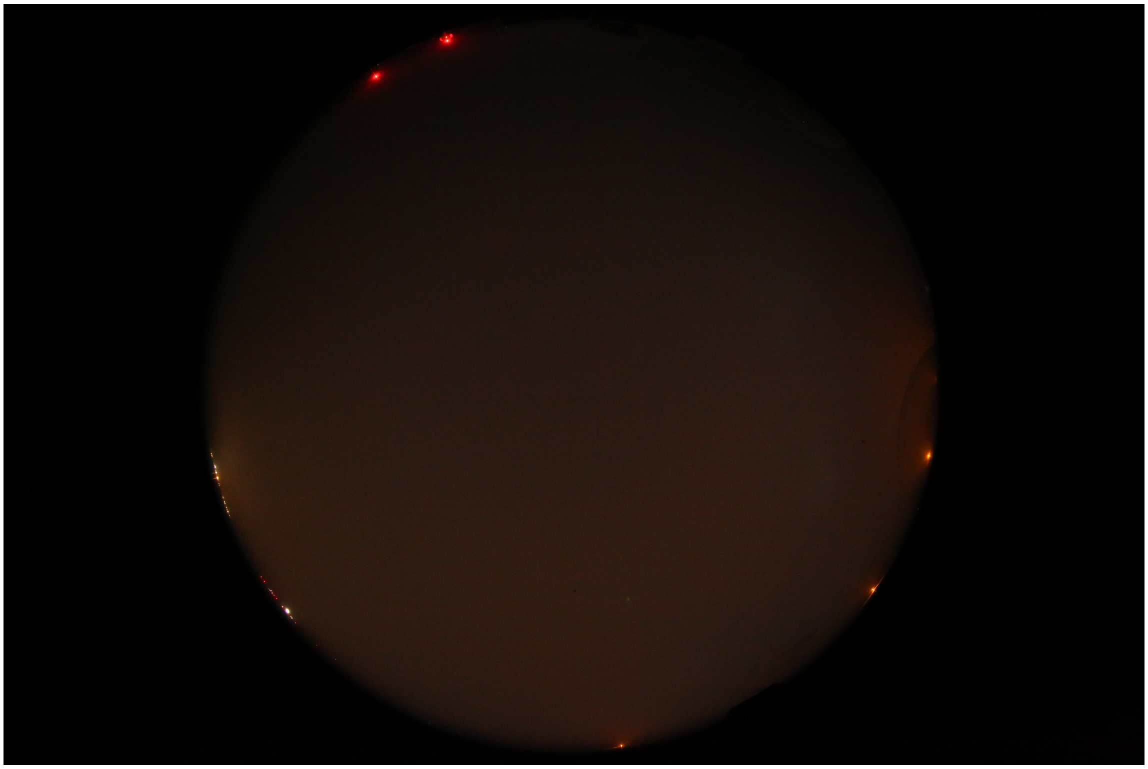

Figure 4.17: All-sky image from January 2020 showing overcast conditions. Direct sources of artificial light can be seen around the perimeter with more significant sky glow compared to Figure 4.16.

Figure 4.16 and 4.17 show all-sky images for clear and overcast conditions respectively. Note the presence of starlight in Figure 4.16 and glowing clouds due to light pollution in Figure 4.17. In both images, the perimeter shows artificial light sources from the neighbouring town of Ny Ålesund.

Note that during the Polar Night, the USSIMO instrument is not sensitive enough to detect irradiance. Light levels for this analysis were derived from the Canon camera capturing the all-sky images (Johnsen et al., 2021b).

Table 4.1: Irradiance measurements from the ArcLight Light Observatory during ground snow conditions.

Irradiance Measurements January 2020		
	Clear Sky	Overcast
Irradiance [Wm^{-2}]	$1.42x10^{-6}$	$3.02x10^{-6}$
Date/Time	16/01/2020 20:00	18/01/2020 20:00
Solar Zenith [°]	117.7	117.3
Lunar Zenith [°]	99.8	112.9

Results can be seen in Table 4.1. Dates were chosen due to the similarity in conditions, particularly the below-horizon solar zenith angle. It was not possible to get equivalent lunar conditions due to the lunar cycle, however on both occasions the moon was significantly below the horizon and lunar light should not affect results.

Irradiance results show that during overcast conditions, the camera detected $\approx$ 2.1x as much light as it measured during clear sky conditions. As noted in Equation 4.1, irradiance under overcast conditions should be around a quarter of the equivalent clear sky measurement. These results show a snow and cloud multiple reflection amplification factor of approximately 8.5 when artificial light is a consideration. Again, these results are very similar to those from Jechow and Hölker (2019), who reported an amplification factor of approximately 10 during similar conditions at their rural site. Any attempt to parameterise the local light field, particularly near coastal areas where biological processes are being studied, should therefore consider the presence of ALAN amplification.

4.3 Conclusions

Amplification of light by the simultaneous presence of ground snow and cloud cover due to multiple reflections has been demonstrated using the ArcLight dataset. Multiple reflection amplification between cloud and snow is a key factor in determining light levels in the Arctic, with amplification factors ranging of ≈ 1.65 for natural light and ≈ 8.5 for artificial light. Increasing cloud cover and thickness, and year round snow coverage in many areas of the region mean that this phenomenon should be considered when modelling light fields. The effect is particularly influential during periods of artificial light at night.

This chapter has highlighted that multiple reflections during daylight conditions can vary even on small temporal scales. Amplification factors largely depend on the spatial distribution of surface albedo and degree of cloud cover, with increasing snow and cloud coverage resulting in higher amplification.

One issue emphasised is the difficulty in obtaining accurate cloud cover data via satellite or reanalysis products for these conditions. There appears to be a clear bias in these products when estimating cloud fraction over areas with ground snow, as algorithms applied to images incorrectly interpret snow as cloud and consequently overestimate cloud cover. The application of image analysis techniques to all-sky images has been shown as a viable alternative for estimating local cloud cover, however this type of data is rarely available especially at sea.

For high precision parameterisation of this effect, it would be necessary to carry out more sophisticated computational modelling that can account for many variables that are beyond the scope of this work. Particularly cloud base height, thickness, and liquid water content. It would also be necessary to include the spatial and temporal distribution of surface albedo, in addition to reflection effects induced by local topography.

For the purposes of assessing this phenomenon at sea, it should be sufficient to include a spectrally flat amplification of light level estimations, with an appropriate caveat of variance induced by error in detecting cloud cover fraction as both snow and cloud albedo are generally spectrally flat (Chapter 3, Bartlett et al., 1998). For areas of the ocean containing partial snow-topped ice cover and partial open water, this amplification will be a key component in determining underwater light fields, substantially increasing the amount of expected light entering both the ice-covered and adjacent open ocean areas.

Chapter 5

Parameterisation of Underwater Light Fields for Primary Production and Animal Behaviour

Introduction

Light is a key driver in many biotic ecosystems such as phytoplankton bloom dynamics, primary production and animal migration patterns (Platt et al., 2008, Banas et al., 2016, Last et al., 2016, Bouman et al., 2018, Häfker et al., 2022). Continuous analysis of these systems in the Arctic can be challenging. Although many biological processes still occur during extremely low light conditions (Berge et al., 2015b), the prolonged Polar Night period and seasonal sea ice cover make it difficult to estimate the magnitude and spectral distribution of the light available to these organisms on a Pan-Arctic and fully seasonal basis. This chapter will first focus on the parameterisation of underwater light fields for estimating primary production. An initial discussion will be presented on the impact that varying snow depth and sea ice thickness could have on underwater primary productivity, using a general broadband primary production model. Following that, analysis of Pan-Arctic seasonal primary production will be outlined for varying light conditions, including the impact of snow/cloud light amplification (Chapter 4) using sea ice data obtained from modelled data and satellite observations. An impact assessment will then be carried out to determine the fraction of total primary production that is unaccounted for when under-ice light is neglected. To conclude the section on primary production, a comparison of open water light field parameterisations against Photosynthetically Active Radiation (PAR) measured by an autonomous underwater glider in the Barents Sea in 2018 is presented. Using bio-optical data measured *in situ* by the glider and a broadband primary production model, primary production is estimated using each of these light field parameterisations. The chapter will conclude with a discussion on spectrally resolved underwater light fields in the context of diel vertical migration (DVM) of Arctic zooplankton. Using acoustic backscattering data, two time series of the migration patterns of the *Thysanoessa* genus of Arctic krill in Kongsfjorden, Svalbard from March 2018 are presented alongside underwater irradiances predicted by the HEIMDALL model. By adjusting the light fields for the spectral sensitivity of the visual receptors of zooplankton, a possible trigger of DVM induced by spectral distribution of the perceived light field is explored.

5.1 Primary Production

5.1.1 Background

Phytoplankton are a collection of microscopic, autotrophic organisms found in marine environments. These small marine plants use chlorophyll pigments to absorb sunlight and through the process of photosynthesis, consume carbon dioxide to produce oxygen and carbohydrates, removing carbon from the atmosphere. The rate at which this process occurs is known as primary productivity, driven by light and nutrient availability. Estimates of modelled global net marine primary productivity (NPP) range from ~ 40 to ~ 70

Pg C year^{-1} (Behrenfeld and Falkowski, 1997, Behrenfeld et al., 2005, Carr et al., 2006, Westberry et al., 2008).

Many existing approaches of quantifying the underwater light climate to populate primary production models rely on daily satellite estimates of surface irradiance (Smyth et al., 2005, Popova et al., 2010, Saba et al., 2011, Lee et al., 2015, Stroeve et al., 2021). The presence of sea ice introduces further complexities, with some studies relying on large-scale *in situ* under-ice light measurements (Castellani et al., 2020), while others assume that no light reaches the ocean surface under areas covered by sea ice (Perovich et al., 2007, Sloughter et al., 2019). Each of these approaches present a challenge for continuous under-ice light estimation in the Arctic. During the period of Polar Night, satellites are generally unable to determine surface irradiance (see Chapter 2). The seasonal, large-scale presence of sea ice makes the region difficult to access to record *in situ* measurements, and neglecting under-ice light results in discarding the vast majority of the lightscape, particularly in spring during the onset of phytoplankton blooms.

This section will first focus on estimating seasonal Pan-Arctic primary production using the HEIMDALL light model, satellite or reanalysis derived snow and ice estimates and a general broadband model for primary production. The relative impact of neglecting under-ice primary production will be discussed. Finally, open water primary production will be analysed with a focus on how varying the underwater light field parameterisation can impact the magnitude of modelled daily primary production.

5.1.2 Light Environment Impact on Primary Production

Primary production can be described by a photosynthesis-irradiance curve (Figure 5.1), graphically representing the correlation between incident irradiance and photosynthesis. To estimate total primary production (P) immediately below the ocean surface, the following broadband model (Platt et al., 1990) was used:

$$\mathrm{P} = \mathrm{B}\mathrm{P}_{\mathrm{M}}^{\mathrm{B}}\left(1 - \exp\left(-\frac{\alpha^{\mathrm{B}}\mathrm{E}}{\mathrm{P}_{\mathrm{M}}^{\mathrm{B}}}\right)\right) \tag{5.1}$$

where P is total primary production, B is biomass (assumed here to be concentration of chlorophyll *a*), $\mathrm{P}_{\mathrm{M}}^{\mathrm{B}}$ is the assimilation number representing the maximum P normalised to biomass, α^{B} is the initial slope of the light curve and E the irradiance in the PAR range. Note that the effects of photo-inhibition and respiration have not been included as this analysis is focussed on the relative differences in gross primary productivity and not net primary productivity. Analysis presented here has a focus on large-scale relative differences in potential primary productivity when varying the light parameter, and to include these features in sufficient detail would require large-scale sampling of various phytoplankton species present in the marine environment.

The parameters α^{B} and $\mathrm{P}_{\mathrm{M}}^{\mathrm{B}}$ are assigned values $0.05\ \mathrm{mgC}\,(\mathrm{mg\,Chl})^{-1}\mathrm{h}^{-1}\,(\mu\,\mathrm{mol\,m}^{-2}\,\mathrm{s}^{-1})^{-1}$ and $1.73\ \mathrm{mgC}\,(\mathrm{mg\,Chl})^{-1}\mathrm{h}^{-1}$ respectively, and are average values from data collected during field campaigns in the Arctic (H. Boumann, personal communication, 26 September 2021). To maximise accuracy in modelling primary production, ideally a spectrally resolved model of both E and α^{B} should be used, however in the absence of data a broadband model has been implemented (Kyewalyanga et al., 1992).

Figure 5.1 shows instantaneous primary production per unit *Chl a* ($\mathrm{P}^{\mathrm{B}} = \frac{\mathrm{P}}{\mathrm{B}}$) normalised to $\mathrm{P}_{\mathrm{M}}^{\mathrm{B}}$, calculated using Equation 5.1 with E assumed to be noon-time irradiance conditions at 80°N on April 1st. P^{B} is calculated for varying sea ice conditions and is estimated as P^{B} immediately below the surface of the open water or ice, with darker green colour indicating higher primary production. For lower magnitudes of PAR, primary productivity is heavily dependent on irradiance. As PAR increases, P^{B} becomes less dependent on available light, eventually becoming independent of incident irradiance. The magnitude of PAR that constrains the region of light-limiting conditions for photosynthesis to occur is known as the photoadaptation parameter (E_{K}), described as:

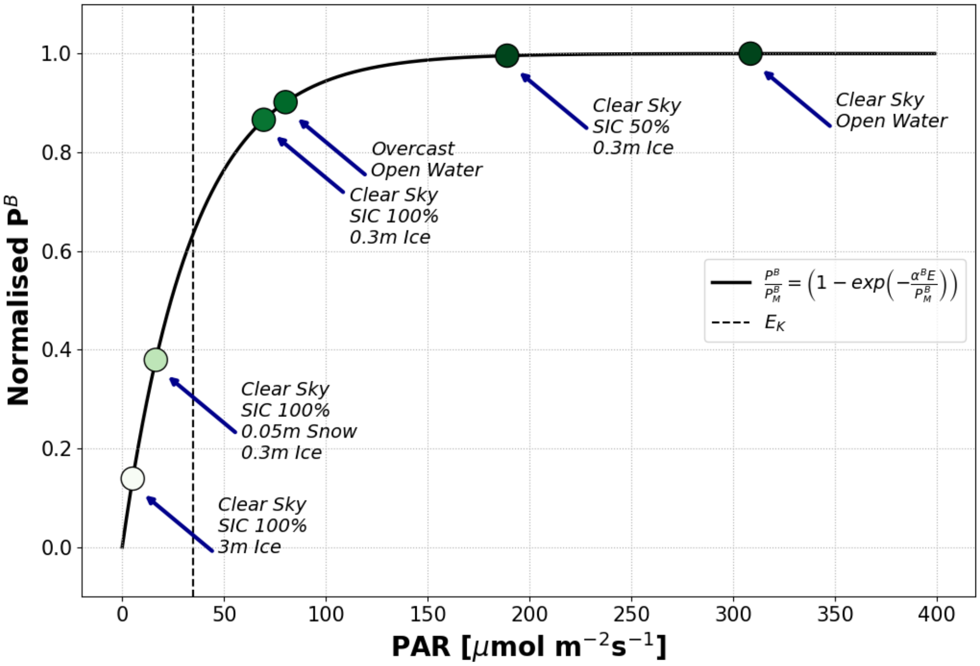

Figure 5.1: Instantaneous Primary Production per unit *Chl a* immediately beneath the surface of open water or ice (normalised to P^B_M) for various snow and ice conditions. Light conditions calculated for solar zenith angle 75° (noon-time angle on 1st April at 80°N). Normalised P^B (black solid) determined using Equation 5.1, and photoadaptation parameter E_K (black dashed) shown for model parameters $\alpha^B = 0.05$ and $P^B_M = 1.73$.

$$E_K = \frac{P^B_M}{\alpha^B} \tag{5.2}$$

When PAR exceeds E_K the growth of the curve begins to slow, deviating from the initial slope and eventually reaching a plateau value of P^B_M where saturation occurs. Evident in Figure 5.1 is that even in areas of 100% sea ice concentration (SIC), the presence of thinner ice allows sufficient light to enter the water such that light-saturation conditions have almost been met for P^B. However, only 5cm of snow on top of thinner ice sufficiently impacts the underwater light that P^B is reduced by more than 50%. Also noteworthy is the impact that cloud clover has on P^B. Cloud cover is usually implicitly included when calculating primary production, as irradiance is generally obtained from daily satellite or reanalysis estimates. Figure 5.1 shows that overcast conditions result in a similar rate of P^B compared with clear sky conditions and 100% SIC of thin ice. This indicates that a significant proportion of productivity could be erroneously disregarded if under-ice P^B is ignored. Note that these results are specific to the parameters that populate the primary production model (Equation 5.1) and a different value of α^B may yield different results.

5.1.3 Pan-Arctic Primary Production Under Snow and Ice

To assess the impact of varying light parameterisations on daily integrated Pan-Arctic primary production, satellite and model reanalysis sea ice data was obtained for January, April, July and October 2018. Sea ice concentration (SIC) was sourced from NSIDC passive microwave satellite data (Meier et al., 2021), sea ice thickness (SIT) from the PIOMAS Arctic Sea Ice Volume Reanalysis product (Zhang and Rothrock, 2003) and snow depth (S_D) from the SnowModel-LG model (Stroeve et al., 2020). Reanalysis products for SIT and S_D were favoured due to their ability to predict sea ice characteristics during melt season. Above surface spectral irradiance was calculated using the HEIMDALL light field model at hourly intervals to account for changes in solar elevation and transmitted through the snow and ice as per the procedures described in Equations 3.1 and 3.3 of Chapter 3. Equation 5.1 was used to estimate primary production immediately beneath the surface of the ice. Under-ice light and associated primary production was calculated on an hourly basis, summed over a 24-hour period for each day of the associated month and averaged by number of days in the month. Pan-Arctic primary production was calculated for both clear skies and overcast conditions with amplification effects included and excluded. Results are summarised in Table 5.1 and Figures 5.2 and 5.3.

During clear sky conditions in January, there is very little photosynthetic productivity occurring in the region. Extensive SIC coupled with very low ambient light levels mean

Table 5.1: Proportion of under-ice Pan-Arctic Primary Productivity.

Month	**Clear sky**	**Overcast**	**Overcast incl. amplification**
January	1.8%	1.8%	2.0%
April	11.0%	5.8%	7.3%
July	22.6%	10.5%	10.6%
October	1.4%	1.1%	1.3%

that there is insufficient light to support primary production, with values several orders of magnitude below saturation ($\mathrm{P}_{\mathrm{M}}^{\mathrm{B}} = 1.73$). However despite widespread sea ice coverage in July, an adequate amount of irradiance is penetrating the ice to support primary production levels that have either reached or are approaching $\mathrm{P}_{\mathrm{M}}^{\mathrm{B}}$, with continual above-horizon solar elevation during the summer season producing high levels of ambient irradiance. Although the average SIT over the Pan-Arctic region is thickest in April, the daily cycling of the sun between day and night results in substantially more photosynthetic productivity in April compared with January despite the thicker sea ice.

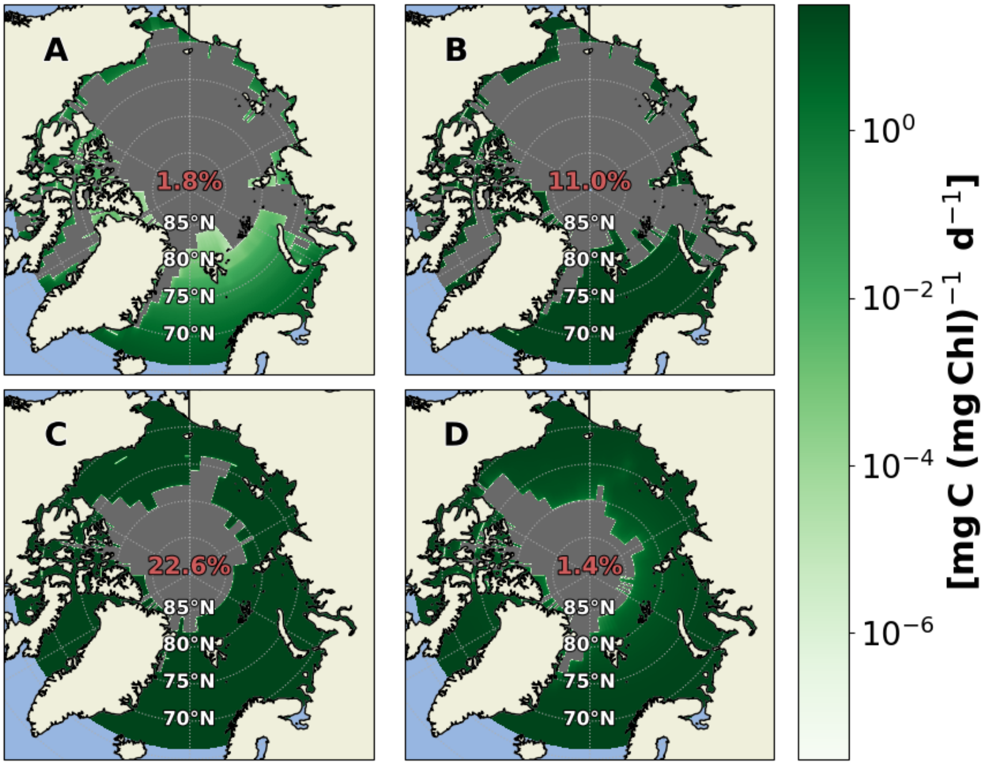

Figure 5.2: Average Daily Primary Production per unit *Chl a* immediately beneath the surface for A) January, B) April, C) July and D) October 2018. **Clear sky conditions assumed**. Open water only, ice-covered regions masked in grey. Fraction of total daily primary production occurring under-ice noted as % in red.

In January and October (Figures 5.2A and 5.2D), extremely low ambient light levels mean that total Pan-Arctic primary production is already very low, and primary productivity occurring under the ice may account for <2%. The onset of the spring phytoplankton bloom in the high Arctic usually occurs around mid to late April (Kostakis et al., 2020, Vernet et al., 2021) and can extend until late summer (Lowry et al., 2017). During the spring period (Figure 5.2B), sufficient levels of light can support low levels of under-ice productivity, accounting for around 11% of the total Pan-Arctic primary production. In July (Figure 5.2C), the contribution from under-ice productivity more than doubles compared with April, accounting for more than 22%, highlighting a significant fraction of total photosynthetic productivity.

As highlighted in Chapter 4, the presence of overlying snow during overcast conditions can substantially increase the quantity of above surface irradiance. Analysis of multiple reflection of light at the ArcLight Light Observatory in Ny Ålesund, Svalbard showed that the presence of ground snow under clouded skies increases above surface irradiance levels on average by $\sim 65\%$. To assess how this might impact primary production occurring beneath the ice, this amplification factor of 1.65 was integrated into the HEIMDALL model. Figure 5.3 shows the same analysis as in Figure 5.2 but with overcast conditions for above surface irradiance and includes amplification effects.

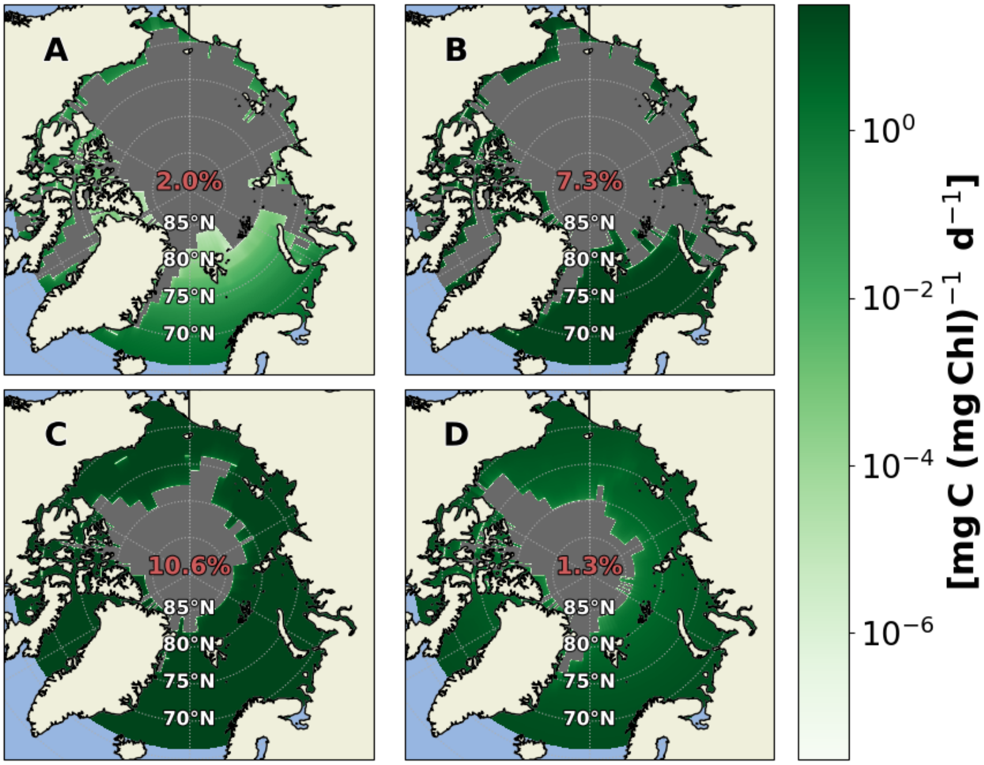

Figure 5.3: Average Daily Primary Production per unit *Chl a* immediately beneath the surface for A) January, B) April, C) July and D) October 2018. **Overcast conditions and snow/cloud feedback amplification factor of 1.65 assumed**. Open water only, ice-covered regions masked in grey. Proportion of total daily primary production occurring under-ice noted as % in red.

Amplification effects during overcast conditions in January only modestly impact the fraction of primary production occurring under-ice (Figure 5.3A). This is likely due to the lack of direct sunlight occurring in the Arctic during this time. In January, the sun remains below the horizon entirely for latitudes north of $\sim$ 73°N. In October however, latitudes north of 80°N still experience some direct sunlight resulting in a slight reduction in the fraction of primary production occurring under-ice (5.3D). Although adjusting above surface irradiance for cloud cover in the HEIMDALL model results in the same factor in reduction irrespective of solar zenith, the non-linear nature of the photosynthesis-irradiance curve (Figure 5.1) means that this does not correlate with the same factor reduction in productivity, i.e. a 50% reduction in light does not translate to a 50% reduction in primary production. This behaviour is particularly evident during April and July (Table 5.1 - Overcast) where the above surface irradiance has been reduced by 75% (Chapter 2) but the under-ice primary production has reduced by only ~50%. Calculating above surface irradiance with an amplification factor of 1.65 and transmitting through the snow and ice shows an increase in under-ice primary production across all seasons compared with exclusion of this amplification effect (Table 5.1).

Results in Table 5.1 show July is the least affected by multiple reflection, due to little accumulation of snow during the summer season and high abundance of saturation levels already being reached. However in April, multiple reflection of the light field means under-ice productivity as a fraction of Pan-Arctic productivity increases by around 25%, and productivity in January exceeds clear sky conditions, however Pan-Arctic productivity as a whole remains extremely low during winter.

The results shown here indicate that even in the presence of widespread ice cover, it is possible for a sufficient level of light to penetrate into the ocean to not only support primary production, but to facilitate saturation levels. A substantial amount of productivity may be unaccounted for in the summer months when under-ice primary production is neglected. This effect may be further enhanced in the spring months when widespread snow is present. Multiple reflection of above surface light fields may induce uncertainties in underwater light field parameterisations, introducing errors in current approaches to model spring phytoplankton bloom dynamics.

5.1.4 Parameterisation of Attenuation - Impact on Primary Production

Parameterisation of the underwater light field is normally approximated by a Beer-Lambert Law (Gordon, 1989), driven by an attenuation value that usually varies in each study. The Beer-Lambert law is of the form:

$$E_D(z) = E_D(0)\exp(-K_d z) \tag{5.3}$$

where $E_D(z)$ is the downwelling irradiance at depth z, $E_D(0)$ is the downwelling irradiance immediately beneath the ocean surface and K_d is the diffuse attenuation coefficient. Estimating underwater irradiance using Equation 5.3 is common in many ecosystem models (Wassmann et al., 2006, Zhang et al., 2010, Banas et al., 2016), with varying values of K_d. Note that this type of light field modelling typically operates on broadband PAR irradiance, E_{PAR}. To assess the impact of varying the K_d parameter, underwater PAR measurements were compared against several models for predicting underwater light, each constructed for use in the Arctic.

Table 5.2: Overview of light models assessed against *in situ* PAR measurements.

K_d **Model**	**Inputs**	**Model Name**	**Ref.**
$= K_w + K_{ph}Chl$	$K_w = 0.05, K_{ph} = 0.003$	Banas et al., 2016	Banas et al., 2016
$= \frac{K_w + 0.0088Chl + 0.054Chl^{\frac{2}{3}}}{\bar{\mu}_D}$	$K_w = 0.04, \bar{\mu}_D = 0.6$	Wassmann et al., 2006	Wassmann et al., 2006
$= K_w + K_{ph}Chl$	$K_w = 0.04, K_{ph} = 0.35$	Zhang et al., 2010	Zhang et al., 2010
$= K_w + K_{ph}Chl$	$K_w = 0.04, K_{ph} = 0.03$	Tuned K_d	-
Equations 2.14 and 2.15	Equations 2.9 and 2.11	HEIMDALL	Connan-McGinty et al., 2022a

As discussed in Chapter 2, autonomous gliders were deployed in the Barents Sea along a 30°E transect during spring 2018 continually measuring PAR. Light field measurements were compared with an ensemble of light field models used in various ecosystem models, each with a different parameterisation of the diffuse attenuation coefficient, K_d (see Table 5.2).

In addition to the light field models from the literature, including the spectrally resolved HEIMDALL model, results of a basic broadband model of K_d (Tuned K_d) are shown, which is of the same form as Banas et al. (2016) with K_{ph} specifically tuned for conditions in the Barents Sea. To tune K_{ph}, 406 glider profiles of chlorophyll *a* and PAR measurements were used. Total K_d was determined using the ratio of PAR at the bottom of the water column divided by PAR just below the surface, for each of the profiles. The bottom of the water column was defined as the depth immediately before the PAR sensor reached the sensitivity baseline discussed in Chapter 2 ($10^{-2}\,\mu\mathrm{mol\,m^{-2}\,s^{-1}}$). K_w was defined as 0.04 to remain consistent with the models from the literature as the sensitivity of K_{ph} was the focus of the analysis. K_w was then removed from total K_d for each profile to provide attenuation only by optically significant constituents in the water. Since the light field models from the literature parameterise this only as a function of chlorophyll *a* concentration, the remaining attenuation (K_d-K_w) was divided by the average chlorophyll *a* concentration measured in the water column for each profile, resulting in 406 K_{ph} values. The distribution of values for the full transect provided a median value of 0.03 for K_{ph}.

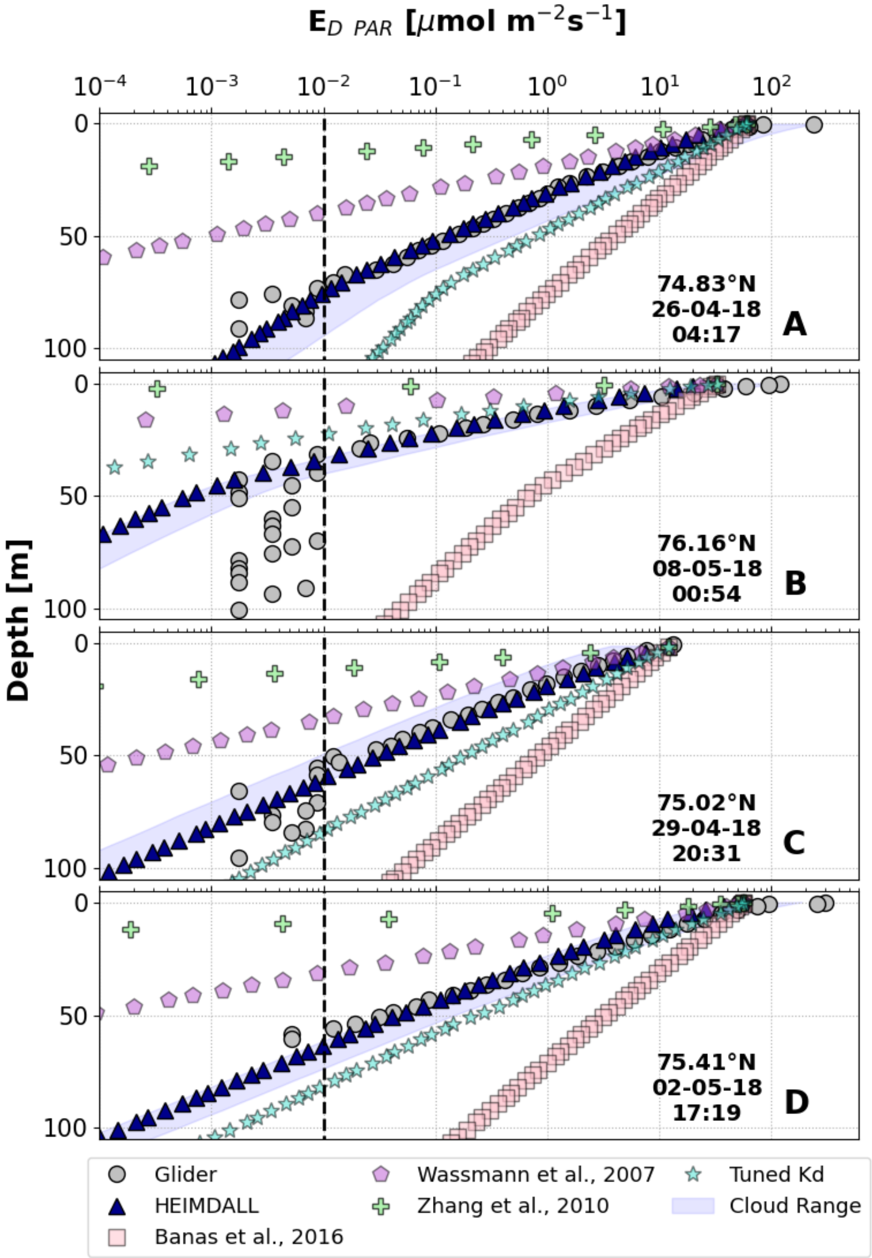

Figure 5.4: Underwater PAR calculated by various models of broadband attenuation compared with PAR measurements from glider observations in the Barents Sea. Panels A, B, C and D are results from glider profiles with date, time and location noted.

Results using each of the models in Table 5.2 to predict underwater light in the Barents Sea is shown in Figure 5.4. The same profiles used in Chapter 2 were selected for consistency. Each model was populated with glider-based measurements of vertically resolved chlorophyll *a* concentration and a surface irradiance value calculated by HEIMDALL, and propagated 100m down the water column. As discussed in Chapter 2, glider PAR and chlorophyll *a* data were not collected at the same depths. To facilitate a direct comparison between modelled and measured PAR, modelled results have been interpolated match depths where PAR was measured by the glider. Results of average R^2, mean absolute error (MAE) and mean absolute percentage error (MAPE) across all profiles are summarised in Table 5.3.

Table 5.3: Results of light models assessed against *in situ* PAR measurements.

Model Name	R^2	**MAE** $[\mu\,\mathrm{mol\,m^{-2}\,s^{-1}}]$	**MAPE** [%]
Banas et al., 2016	-0.163	14.03	2411.73
Wassmann et al., 2006	-2.230	11.23	83.9
Zhang et al., 2010	-18.920	13.63	96.40
Tuned K_d	0.630	10.36	244.62
Connan-McGinty et al., 2022a	0.962	10.14	32.63

Results in Figure 5.4 do indicate a persistent tendency for the model used in Banas et al., 2016 to overestimate PAR, and both the models of Wassmann et al., 2006 and Zhang et al., 2010 to underestimate. Of the broadband models shown, the Tuned K_d appears to perform the best when predicting underwater light, generally overestimating PAR but not exclusively. Figure 5.4 does highlight that even a K_d parameter specifically adjusted to the environmental conditions is still unable to perform as well as the HEIMDALL model. Results demonstrate that the Beer-Lambert Law is a valid approach to estimating the underwater light field but is sensitive to parameterisation of the diffuse attenuation coefficient K_d (Gordon, 1989).

Using chlorophyll *a* concentration profiles measured by the glider (Figure 5.5), surface PAR estimated from HEIMDALL simulations and underwater light levels predicted by each model, depth resolved and column integrated primary production using Equation 5.1 was estimated for the Barents Sea transect previously shown in Chapter 2.

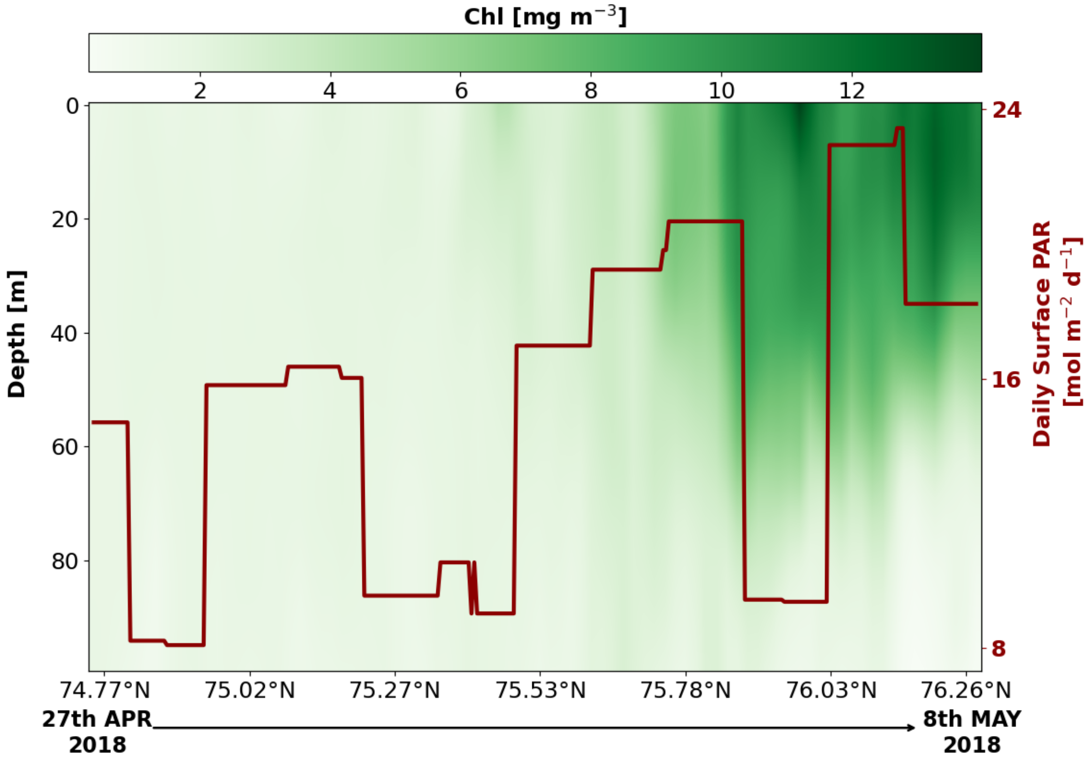

Figure 5.5: Measured *Chl a* concentration from transect in the Barents Sea in 2018, and associated daily surface PAR as modelled by HEIMDALL (red line).

Results of estimated primary production for each model are displayed in Figure 5.6. As expected, the model used in Banas et al. (2016) in these conditions substantially overestimates primary production (Figure 5.6B) compared with the HEIMDALL model (Figure 5.6A), due to overestimation of PAR (Figure 5.4). As a result, column integrated daily primary production during bloom conditions (north of ~ 75.8°N) is a factor of 3 higher. Conversely, primary production predicted using the light models of Wassmann et al. (2006) and Zhang et al. (2010) (Figures 5.6C and D) during bloom conditions are underestimated by factors of $\sim$2 and $\sim$4 respectively with the latter model predicting the lowest levels of photosynthetic productivity.

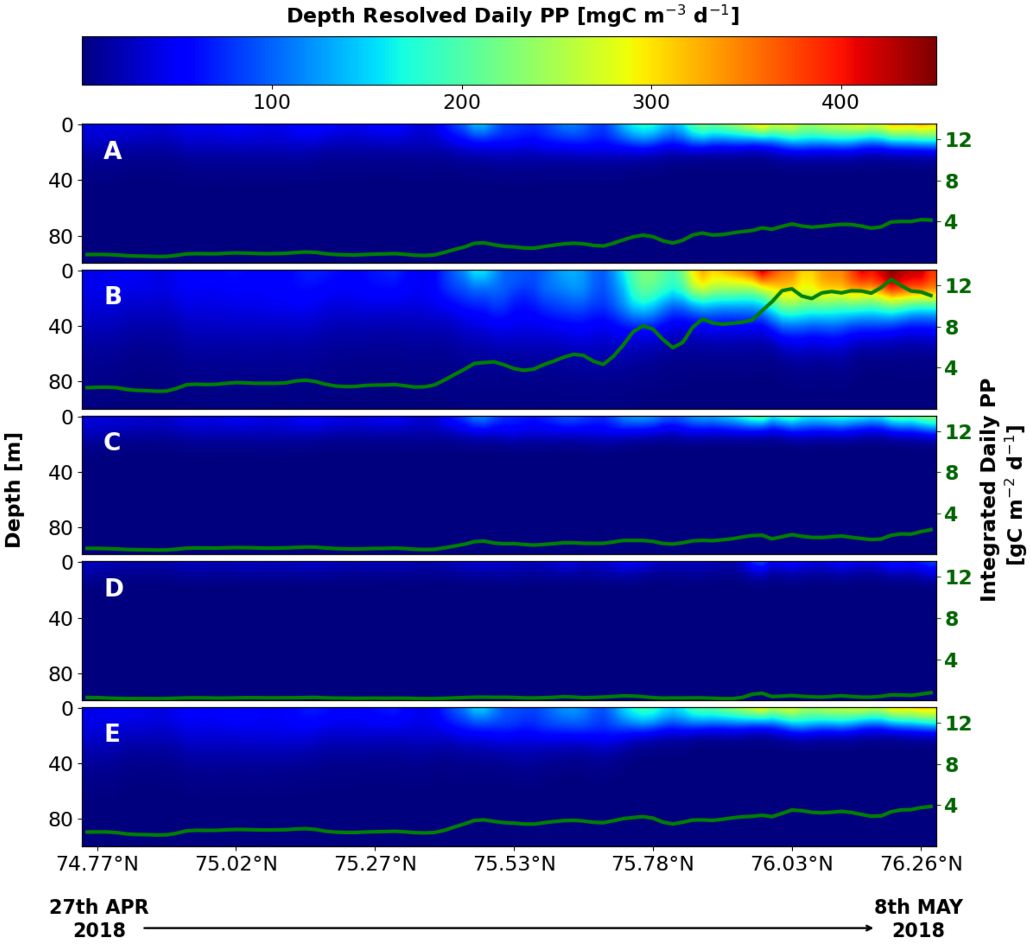

Figure 5.6: Depth resolved (colourmap) and column integrated (green solid line) Daily Primary Production (PP) per unit *Chl a* in Barents Sea glider transect, using measured *Chl a* and light as calculated by models in Figure 5.4. A) HEIMDALL, B) Banas et al., 2016, C) Wassmann et al., 2007, D) Zhang et al., 2010, E) Kd tuned to transect conditions.

The Tuned K_d model (Figure 5.6E) appears to provide a reasonable estimate of column integrated daily primary production, with some overestimation in depth resolved calculations earlier in the transect.

Since the HEIMDALL light model shows very good agreement with underwater PAR measurements, and the parameter values for α^B and P_M^B used throughout this chapter are specific to this region, it is expected that Figure 5.6A should represent primary productivity over this transect reasonably well and should be the benchmark for comparison. Although some of the other models presented do not perform as well as HEIMDALL, it may be the case that while they have previously been used for Arctic phytoplankton ecosystems, their parametersiation of K_{ph} may be so finely tuned for their specified models that they are not appropriate for this particular transect region at this specific time. However, results indicate that using a Beer-Lambert model with a fully tuned K_d may be useful if computation costs are critical and spatial variation is not important to the study.

5.1.5 Conclusions

Analysis of Pan-Arctic seasonal primary production has shown that a non-trivial quantity of photosynthesis can still occur beneath the ice, particularly during the spring and summer months. Clear sky conditions in April and July result in under-ice productivity accounting for 11.0% and 22.6% of Pan-Arctic primary production respectively, reducing to 5.8% and 10.5% during overcast conditions. In the spring season, widespread snow coverage in April during overcast conditions induces an amplification of above surface irradiance in the region of 65%, increasing the proportion of under-ice primary production to 7.3%. During January, extremely low light levels mean that total Pan-Arctic photosynthesis is very low, with the maximum under-ice fraction being $\leq$2% for all light conditions. Similarly for October, a substantial majority of photosynthesis occurs at lower, open water latitudes where the sun is regularly cycling between day and night, and ice at higher latitudes rapidly depletes the very small amount of available light.

Results here show that during the Polar Night and surrounding time periods, under-ice primary production accounts for very little total productivity in the Arctic, and to disregard this contribution is likely a reasonable approximation due to the extremely low light levels. However, many studies focus on phytoplankton dynamics during the spring and summer seasons (Banas et al., 2016, Lowry et al., 2017) and results shown here suggest they would benefit by accounting for not only light transmission through snow and ice, but multiple reflection induced irradiance amplification effects.

There are notable limitations to this approach at quantifying how much primary production is occurring seasonally beneath the ice. The first is that a single primary production model has been used which populates the parameters based on measurements from one area of the Arctic Ocean. Different species of phytoplankton may behave in such a way that their α^B and P_M^B parameters are not well described by the values implemented here. Another drawback is that this analysis has not included the presence of melt ponds. As discussed in Chapter 3, melt ponds are currently very difficult to identify via satellite, but *in situ* measurements have shown that they can transmit around 70% of incident irradiance, more than double the transmittance of bare ice (Light et al., 2015).

It is worth highlighting that this analysis has relied on biomass normalised calculations. Satellite observations of near surface chlorophyll concentrations rely on remote sensing reflectance relationships and are not available at high latitudes during the period of Polar Night (Jamet et al., 2019). Even if both an appropriate light field model and a primary production model for Pan-Arctic analysis are available, spatial temporal maps of biomass are not available to populate these models for much of the year. Additionally, satellite biomass data are also generally only reliable for cloud free pixels (Hu et al., 2012), and cannot observe under-ice blooms making full seasonal analysis without *in situ* data very challenging. Furthermore, without spectral measurements of biomass absorption parameters, the full potential of hyperspectral light field models is not exploited. However, the results do highlight the potential impact of disregarding under-ice primary production, particularly during the summer months when saturation levels may be achieved despite ubiquitous ice cover.

Some of these considerations may be of particular importance for future conditions in the Arctic. Although the Arctic is expected to become progressively cloudier (Liu et al., 2012), springtime snow cover in some regions has been projected to reduce by around 1.5cm year^{-1}, meaning that amplification effects may eventually become greatly reduced (Lee et al., 2021, Mallett et al., 2021). However, clouds are believed to be a driver of sea ice melting (Huang et al., 2019), and analysis of sea ice loss between 2003 and 2018 reported an average reduction of sea ice volume by 2870km^{-3} decade^{-1} in February-March and 5130km^{-3} decade^{-1} in October-November with the proportion of thick, multi-year ice decreasing by more than 50% (Kwok, 2018). This trend is expected to accelerate (Wei et al., 2020, Mallett et al., 2021), resulting in a younger, thinner Arctic icescape allowing more light to penetrate into the water column and stimulate primary production.

Results here also highlight the importance of choosing an appropriate value for K_d when estimating underwater light fields. Comparisons of *in situ* PAR measurements against light fields predicted by 5 different models all designed for the Arctic have yielded very different results, with some consistently over and under estimating the light field substantially. When calculating column integrated daily primary production using these predicted light fields, the gap between the two models with the largest variance was a factor of $\sim$12. Such curated constraints of parameters for specific environmental conditions may limit the scope of model applications, particularly in a geographical region where *in situ* data is difficult to obtain, and modelled outputs are so heavily relied upon for many areas of study.

5.2 Animal Behavioural Response

5.2.1 Background

Not only are phytoplankton an integral component in global carbon transfer dynamics, they also form the base of the aquatic food chain providing sustenance to microscopic aquatic animals known as zooplankton, which are in turn consumed by larger marine species (Fenchel, 1988). The consumption of phytoplankton biomass by zooplankton is a key element of global carbon transport and is broadly accounted for in many ecosystem forecasting models (Kettle and Merchant, 2008, Popova et al., 2012, Banas et al., 2016).

Zooplankton are horizontally transported through advection and passively travel with ocean currents, however active vertical migration by the organisms is a well documented and geographically widespread behaviour (Cohen and Forward, 2002, Cottier et al., 2006, Berge et al., 2014, Last et al., 2016, Bandara et al., 2021, Häfker et al., 2022). The action of diel vertical migration (DVM) by zooplankton generally follows local irradiance levels with the organisms rising at night and retreating to depth during daylight, and has been theorised to be driven by the goal of avoiding visual predators while accessing food sources (Fortier, 2001, Hays, 2003). Although several factors have been hypothesised to trigger DVM in zooplankton, such as temperature or ultraviolet radiation levels (Cooke et al., 2008, Williamson et al., 2011), light levels are believed to be the main driver in triggering large-scale DVM in zooplankton populations, with some even responding to artificial light sources (Cohen and Forward, 2016, Ludvigsen et al., 2018).

This section will focus on the diel vertical migration patterns of a population of Arctic zooplankton in response to changing light conditions over two time periods in March 2018. Acoustic backscattering data collected from a mooring site in Kongsfjorden, Svalbard documents the vertical movement of the organisms, which are analysed in the context of modelled and measured irradiance levels. Initial discussion will focus around the differences between the physical and perceived light levels taking into account the spectral sensitivity of the zooplankton photoreceptors, and how local light conditions driven by solar and lunar positions can impact this perceived light field. Finally, depth resolved hyperspectral light field modelling will discuss possible DVM trigger mechanisms relating to the spectral distribution of the light field.

The material presented in this section builds upon recently published work (Häfker et al., 2022).

5.2.2 Perceived Surface PAR

To analyse the dynamic vertical distribution of zooplankton in response to changes in spectrally resolved light, the diel vertical migration (DVM) patterns of the *Thysanoessa* genus of Arctic krill was studied. Zooplankton acoustic backscattering data were measured at a mooring site in Kongsfjorden, Svalbard (78.959°N, 11.824°E) using two 300kHz Acoustic Doppler Current Profilers (ADCPs) mounted at a depth of approximately 120m with one facing upward and the other downward (Häfker et al., 2022). Data were extracted at 20-minute time intervals. The taxonomy of the zooplankton biomass was dominated by the *Thysanoessa* krill, which was used as a proxy to represent the community throughout analysis. To define zooplankton position in the water column, Centre of Mass (CoM) was used and reflected the depth with the highest density of biomass (Urmy et al., 2012).

Two periods of time were chosen: the first was 3-13 March 2018 and the second 20-26 March 2018. The period of 3-13 March was chosen for both the lunar characteristics and cloud free conditions. The moon was progressing from full moon to a waning phase, with decreasing elevation and initial phase shift of $\sim 180°$ with the solar path. During this time period, irradiance levels were below the sensitivity limit of many commercially available radiometers for a majority of the days. The HEIMDALL model was used to calculate above surface irradiance, with a window of consecutive cloud free days chosen to mitigate uncertainty introduced by spatially and temporally averaged cloud cover reanalysis data (see Chapter 4). Cloud conditions were verified by visual inspection of all-sky images taken on an hourly basis from the Ny-Ålesund Light Observatory in Svalbard (78.941°N, 11.842°E) (Johnsen et al., 2021b). As described in Häfker et al. (2022), hyperspectral irradiance for the period of 20-26 March was obtained from an USSIMO (In-situ Marine Optics, Perth, WA, Australia) hyperspectral radiometer designed for light collection in daylight conditions (Berge et al., 2021b). The instrument was sufficiently sensitive at this time to provide valid *in situ* above surface irradiance measurements to populate the HEIMDALL model. *In situ* irradiance measurements were chosen over modelled light to mitigate uncertainty in local cloud cover. During this period, the orbit of the moon followed closely with the sun through the ecliptic plane, with only a small phase shift between the two initially. The moon was also progressing from new moon to a waxing phase, with increasing elevation throughout. Salinity at the mooring site was recorded by a SBE 16plus V2 SeaCAT (Sea-bird Scientific, Washington, USA) mounted at 21m, recording an average value of ~34.5 PSU. In the absence of further data, this time-averaged value was used for full depth light attenuation calculations since the region generally experiences little variation in salinity (Kostakis et al., 2020). Chlorophyll *a* fluorescence was also measured by the same instrument, however for both time periods the phytoplankton concentration was undetectable and thus was not included when attenuating the light field.

Underwater spectral irradiance determined by the HEIMDALL model, or any model that attenuates the above surface light field, is not representative of the irradiance perceived by zooplankton due to the limited spectral sensitivity of their visual receptors (Cohen et al., 2015). Results presented here took this distinction into consideration by weighting the calculated spectral irradiance field by the normalised visual spectral sensitivity spectrum ($\mathrm{S}(\lambda)$) of the *Thysanoessa* genus of krill (peaking around 495nm) as determined by Cohen et al. (2015), and integrated over the Photosynthetically Active Radiation (PAR) range to determine perceived PAR irradiance ($\mathrm{E}_{\mathrm{PAR,Perceived}}$).

$$\mathrm{E}_{\mathrm{PAR,Perceived}} = \int_{400\mathrm{nm}}^{700\mathrm{nm}} \mathrm{E}(\lambda)\,\mathrm{S}(\lambda)\mathrm{d}\lambda \tag{5.4}$$

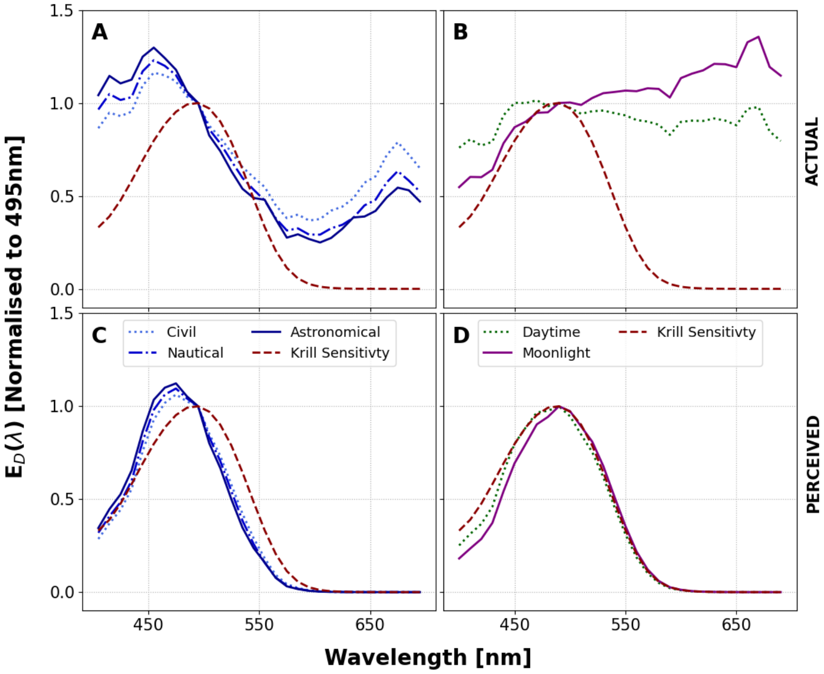

Figure 5.7: Visual sensitivity spectrum of the *Thysanoessa* krill (red dashed) normalised to 495nm. Spectral distribution of light field during moonless civil, nautical and astronomical twilight (Panel A) and from the sun at 10° elevation (green dotted) and moon at 10° elevation (purple solid)(Panel B). Spectral distribution of light field weighted by visual sensitivity of the *Thysanoessa* krill during moonless civil, nautical and astronomical twilight (Panel C) and from the sun (green dotted) and moon (purple solid)(Panel D). All values normalised to 495nm.

The spectral sensitivity function of the *Thysanoessa* krill can be seen in Figure 5.7, normalised to their approximate peak sensitivity wavelength of 495nm. Light in the blue-green range (400∼600 nm) is the most abundantly detected with wavelengths >600nm showing very little contribution towards the perceived light field. Also shown is the spectral distribution of the ambient light field at various times, all normalised to 495nm. Figure 5.7A shows normalised spectral irradiance during astronomical, nautical and civil twilight when the solar elevation angle is -13°, -7° and -4° respectively, for clear sky and moon free conditions. During these periods, shorter blue-green wavelengths dominate the composition of the light field. When this spectral distribution is present, the krill would perceive a higher proportion of PAR due to the overlap with their spectral sensitivity function. Figure 5.7B shows spectral distribution of ambient light during daylight (solar elevation 10°) and full moon conditions (lunar elevation 10°). When a direct source of light is present, the spectral distribution of the light field shifts, becoming more spectrally flat during periods of daylight and stronger in the red wavelengths during full moon periods due to the spectral albedo of the moon (Shkuratov et al., 1999). The resulting effect is that the proportion of PAR perceived by the krill is lower during these conditions compared with twilight conditions. Panels C and D in Figure 5.7 weight the spectral distribution of the ambient light field to the visual sensitivity of the *Thysanoessa* krill, demonstrating a shift in peak perceived irradiance from blue to green when the light field changes between twilight conditions to those with direct solar or lunar light.

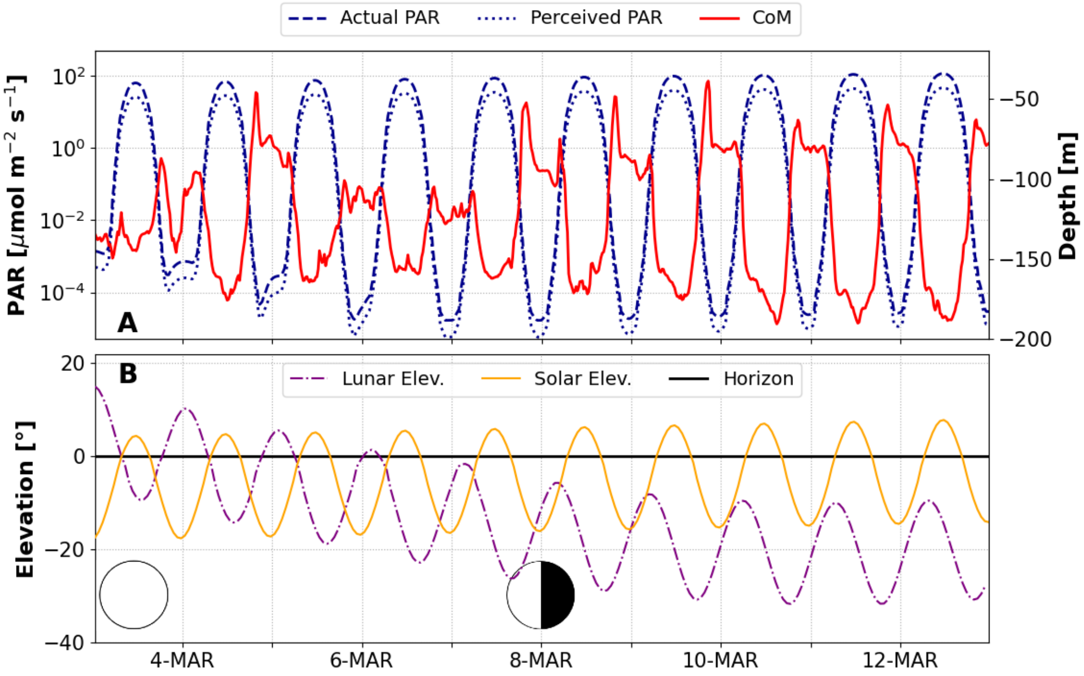

Figure 5.8: Measured Centre of Mass (CoM) of calanus (red solid), modelled surface PAR (blue dashed) and perceived surface PAR (blue dotted) from Kongsfjorden in early March 2018. Perceived PAR calculated by weighting the modelled surface PAR by the spectral sensitivity of *Thysanoessa* krill. Lunar (purple dashdot) and solar elevation (yellow solid) displayed in lower panel, alongside pictorial representation of lunar phase.

Figure 5.8 (Panel A) shows above surface PAR as calculated by the HEIMDALL light model (actual PAR), surface PAR weighted by zooplankton visual sensitivity (perceived PAR), zooplankton centre of mass (CoM) and (Panel B) local solar and lunar elevations at the site of the mooring for the period 3-13 March 2018. Diel vertical migration (DVM) patterns by the zooplankton (red solid line, Figure 5.8A) exhibit the typical movement of inverse cycling with surface irradiance (Berge et al., 2014, Darnis et al., 2017), but demonstrate unusual behaviour or suddenly retreating to depth when approaching their maximum height in the water column at night. Referencing the solar and lunar positions in Figure 5.8B does not appear to show any immediate indication of a consistent trigger for this change in migration to a lower depth in the water column.

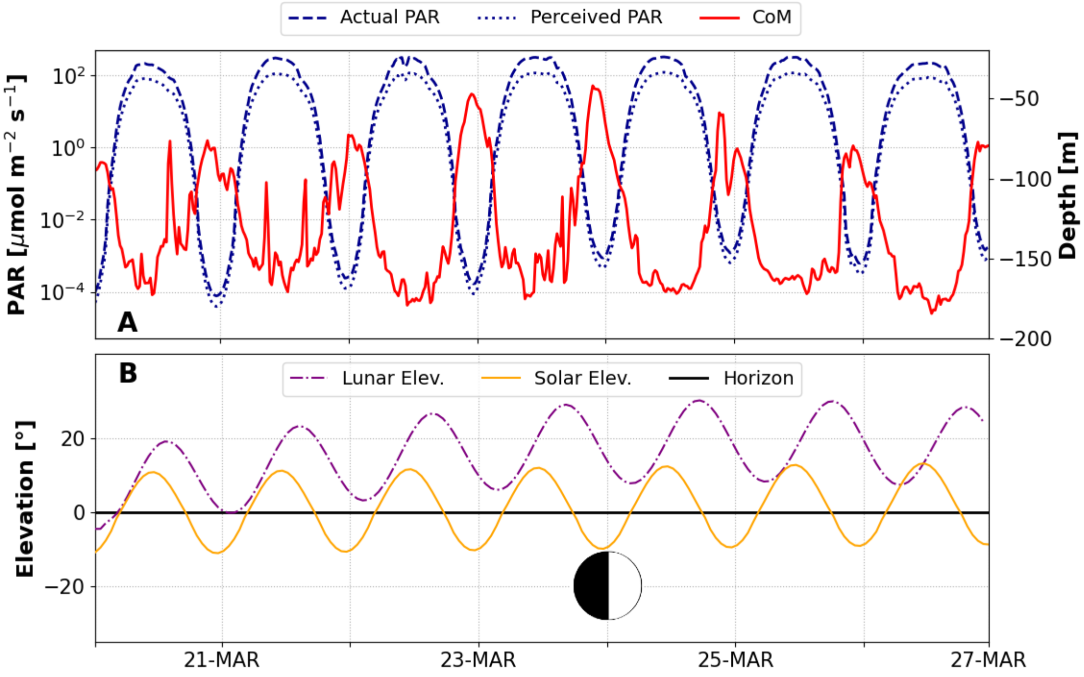

Figure 5.9: Measured Centre of Mass (CoM) of calanus (red solid), modelled surface PAR (blue dashed) and perceived surface PAR (blue dotted) from Kongsfjorden in late March 2018. Perceived PAR calculated by weighting the modelled surface PAR by the spectral sensitivity of the *Thysanoessa* krill. Lunar (purple dashdot) and solar elevation (yellow solid) displayed in lower panel, alongside pictorial representation of lunar phase. Note that new moon occurred on March 17th, outside the range of data displayed.

Similar analysis for the period 20-27 March 2018 can be seen in Figure 5.9. Again, the inverse cycling of DVM with surface irradiance is evident. Although not as periodically regular as the behaviour during 3-13 March (Figure 5.8A), there remains some unusual movement of the krill during periods of both maximum and minimum surface irradiance (Figure 5.9A).

When weighting the spectrally resolved surface PAR field by the visual sensitivity spectrum of the zooplankton over both time periods, the perceived surface PAR as a percentage of actual surface PAR varies from 34-56% depending on the light conditions. To explore this further, the fraction of perceived PAR was investigated as a possible correlation mechanism for DVM movements.

5.2.3 Perceived Underwater PAR

Underwater hyperspectral irradiance was calculated for each of the two time periods using the HEIMDALL model. Above surface irradiance was modelled for the period 3-13 March 2018, and measured *in situ* for the period 20-27 March 2018. Irradiance was propagated down the water column at 1m intervals using the bio-optical model integrated into HEIMDALL, assuming a constant salinity value of 34.5 PSU and chlorophyll *a* concentration of 0 $\mathrm{mg\,m^{-3}}$, both determined by *in situ* measurements.

Figure 5.10 shows underwater perceived PAR as a fraction of actual PAR for the period 3-13 March 2018, with Centre of Mass (CoM) of the krill biomass overlaid. From Figure 5.7, it is evident that when the sun is at an elevation within the definition of astronomical twilight ($<$ -12°), the ratio of blue-green to red light at the surface is highest. As the sun progresses towards the horizon, this ratio begins to decrease until a more flat spectral shape is reached when the sun rises above the horizon. This effect is more pronounced for lunar light due to high albedo at the longer, red wavelengths. Early in this time period, the moon is inverse cycling with the sun and is above horizon at minimum solar elevation, with near full moon phase. For the period 3-8 March inclusive, when the moon is at maximum elevation, the solar elevation falls below the baseline value of -16° where a spectrally flat background irradiance is used by HEIMDALL (see Chapter 2). As a result, spectral distribution at night during these dates is dominated by lunar irradiance with higher amounts of red light, decreasing the fraction of perceived PAR. As the moon sets, the solar minimum elevation progressively moves closer to the horizon. The sun then takes over as the controlling source of spectral distribution, but either remains in the bounds of astronomical twilight at night or moves sufficiently below the horizon that the background, spectrally flat galactic light becomes the main irradiance driver. There appears to be an aversion to areas where the perceived fraction of PAR is minimised. Although this fractional change is not something the krill can perceive, it does indicate that a change in actual spectral distribution may be driving some response in the animals. Several instances can be seen where the population of krill move towards the surface at night and suddenly revert to deeper waters, coinciding with a decrease in the fraction of perceived PAR. This means the magnitude of light the krill perceive is lower than the magnitude of PAR that would be measured *in situ* or predicted by current light field models, an approach which is usually taken in studying DVM (Hobbs et al., 2021, Häfker et al., 2022). As the light is propagated down the water column, the optical properties of the seawater and constituent components results in attenuation of both blue light (absorbed by CDOM and scattered by water) and red light (absorbed by water), leaving predominantly green light progressing with depth. Due to the spectral sensitivity of the *Thysanoessa* krill peaking in the blue-green waveband range, this results in a large proportion of remaining PAR being perceived at depth ($\sim$ 97%).

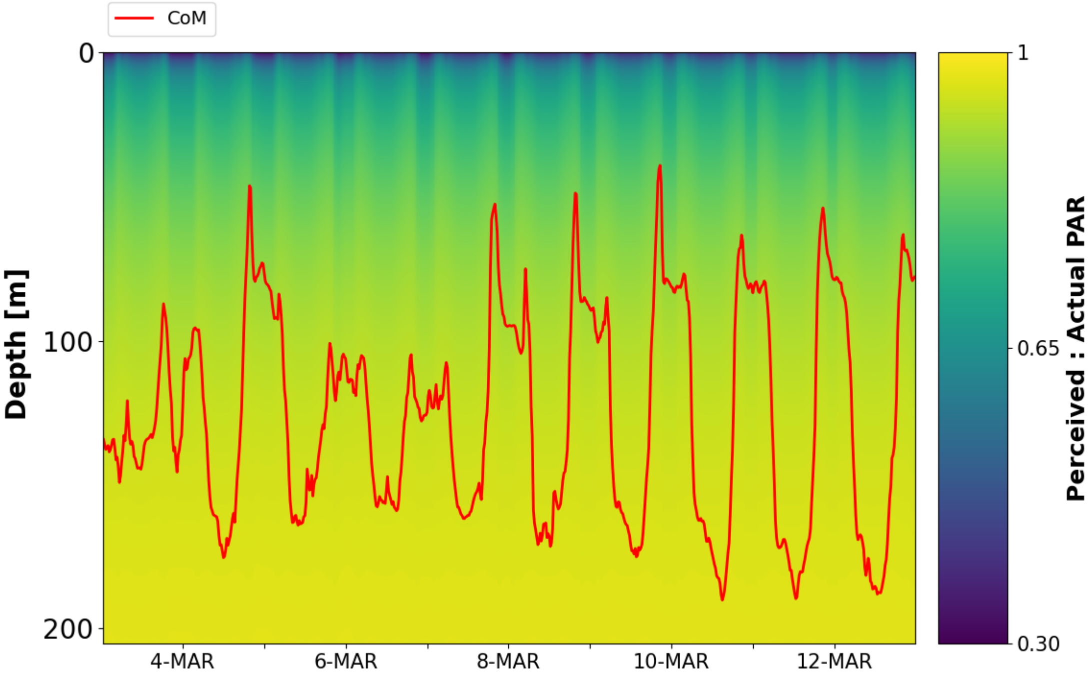

Figure 5.10: Ratio of underwater PAR perceived by *Thysanoessa* krill to actual PAR as modelled by HEIMDALL, from Kongsfjorden in early March 2018. Measured Centre of Mass (CoM) of krill (red solid) also shown.

The same analysis was carried out for the period of 20-27 March 2018. During this time, the moon is above horizon initially cycling concurrently with the sun and progressing towards first quarter phase. The solar irradiance largely dominates the spectral distribution of the light field. During daylight hours, it is again evident that the fraction of perceived PAR is reduced due to the higher presence of red wavelengths from direct solar light. When the sun moves below the horizon, the moon is still visible in the night sky. In these conditions, it might be expected that fraction of perceived at night would be similar to early March (Figure 5.10) due to similar lunar characteristics. However, this is not the case and the fraction of perceived PAR during 20-27 March is much higher at night compared with the period 3-13 March. This is due to the elevation of the sun. Although the solar disc has moved below the horizon, minimum solar elevation only reaches -10° at night (compared with -18° for the earlier period), meaning conditions cycle between daylight, into civil twilight and finally to nautical twilight. At no point is there a transition into astronomical twilight (as in early March) where a substantially large portion of the light field is in the short blue wavelengths that are not fully perceived by krill. Figure 5.7A suggests that when the sun remains below horizon, civil twilight conditions are when fractional perceived PAR due is optimised to the distribution of wavelengths. The diffuse light from the sun at this solar elevation is >1 order of magnitude higher than irradiance from the moon, meaning spectral distribution of light is largely governed by solar irradiance. Due to a spectral irradiance field dominated by blue-green light at night, there is no regular sudden change in perceived PAR nor associated change in migration depth. Some irregular DVM movements do remain though. There may be some correlation with sporadic changes in perceived PAR that may be a result of local changes in cloud cover, since above surface irradiance for this period was obtained from *in situ* measurements. Previous work on spectral irradiance changes by cloud has suggested that the spectral effects of clouds on PAR are relatively small and can generally be neglected (Bartlett et al., 1998), however more recent work suggests there may be a notable enhancement by clouds on clear sky solar irradiance in the wavelength range 400-450nm (Durand et al., 2021, Parisi et al., 2020). These changes in perceived PAR may be too subtle to identify here but obvious to the ocular receptor of the krill.

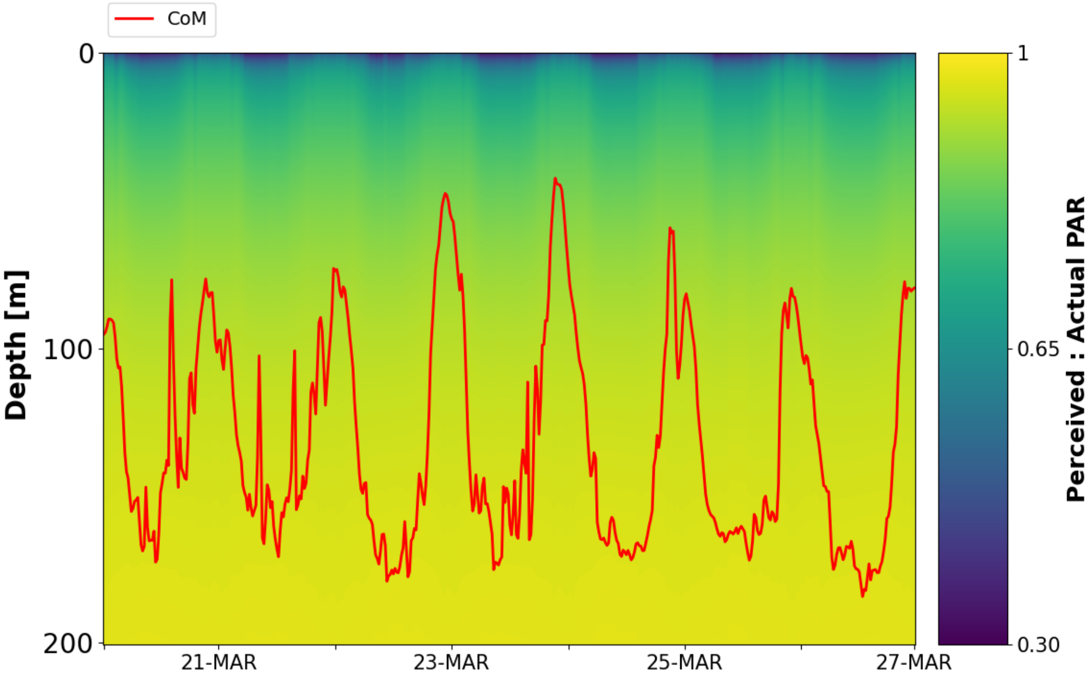

Figure 5.11: Ratio of underwater PAR perceived by the *Thysanoessa* krill to actual PAR as modelled by HEIMDALL, from Kongsfjorden in late March 2018. Measured Centre of Mass (CoM) of krill (red solid) also shown.

5.2.4 Underwater Irradiance to Single Colour

To further contextualise these results in relation to krill spectral sensitivity function, perceived PAR was deconstructed into separate blue, green and red wavebands spanning the wavelength ranges 400-500nm (B), 501-600nm (G), 601-700nm (R) and converted to single colour. In 1931, the Commission Internationale de l'Eclairage (CIE) published colour matching functions $(\bar{\mathrm{x}}(\lambda), \bar{\mathrm{y}}(\lambda), \bar{\mathrm{z}}(\lambda))$ which map a spectrum of wavelengths $(\mathrm{S}(\lambda))$ into tristimulus values $(\mathrm{X}, \mathrm{Y}, \mathrm{Z})$, corresponding to response functions of the cones in the human eye, determined via colour matching experiments (Smith and Guild, 1931).

$$\mathrm{X} = \int_{400}^{700} \mathrm{S}(\lambda)\bar{\mathrm{x}}(\lambda)\mathrm{d}\lambda \tag{5.5}$$

$$\mathrm{Y} = \int_{400}^{700} \mathrm{S}(\lambda)\bar{\mathrm{y}}(\lambda)\mathrm{d}\lambda \tag{5.6}$$

$$\mathrm{Z} = \int_{400}^{700} \mathrm{S}(\lambda)\bar{\mathrm{z}}(\lambda)\mathrm{d}\lambda \tag{5.7}$$

These X,Y,Z values essentially describe the unique co-ordinates of single colour of a given spectrum $\mathrm{S}(\lambda)$. These X,Y,Z values can be further converted into a default RGB colour space as described in Mobley (2022), using the following:

$$\begin{bmatrix} \mathrm{R} \\ \mathrm{G} \\ \mathrm{B} \end{bmatrix} = \begin{bmatrix} 3.2410 & 1.5374 & 0.4986 \\ 0.9692 & 1.8760 & 0.0416 \\ 0.0556 & 0.2040 & 1.0570 \end{bmatrix} \begin{bmatrix} \mathrm{X} \\ \mathrm{Y} \\ \mathrm{Z} \end{bmatrix}$$

Once RGB values are obtained, they can be used to represent a single colour visually via any data visualisation plotting software.

Figure 5.12 shows the result of this process on the underwater perceived spectral irradiance determined by HEIMDALL for both periods, with associated CoM of krill overlaid and perceived surface PAR. Although the spectral irradiance has been weighted in accordance with the spectral sensitivity of the krill, it is important to note that this single colour is not necessarily representative of what the krill would see. CIE functions are inherently determined using the spectral sensitivity of the human eye. The results presented here are better described as what a human eye would see, if the underwater light field was weighted to the spectral sensitivity of the *Thysanoessa* krill and is an exploration of how the light field is changing in terms of blue and green wavebands.

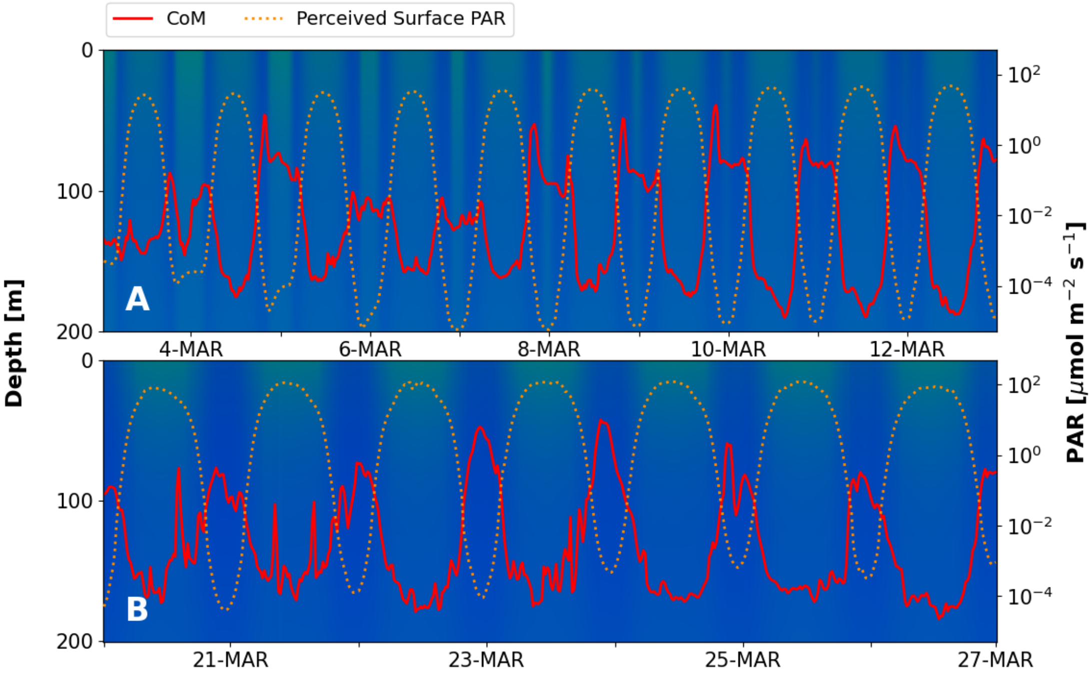

Figure 5.12: Dominant colour of underwater irradiance weighted by the visual sensitivity of *Thysanoessa* krill, perceived surface PAR (yellow dotted) and measured Centre of Mass (COM) of krill (red solid) for A) early March and B) late March 2018.

The results in Figure 5.12 show the conversion of the perceived spectra at each 1m depth and 20 minute time interval into a single colour. Note that the the intensity of the colour does not represent the magnitude of the light, only the dominant colour of the localised spectra as it would be perceived by the human eye. The results appear to indicate that the krill biomass is responding to changes in the ratio of green to blue light, preferring to occupy regions of the water column when this ratio is <1, with a dominant blue colour. Earlier in the month (Panel A) shows a DVM trigger occurring at night when there is a shift in the perceived dominant colour of light. This feature is largely absent later in the month (Panel B), when the night-time light field is dominated by blue wavelengths. Previous work has investigated the response of zooplankton migration to changes in the magnitude of specific wavelengths of light or magnitude of the PAR irradiance (Häfker et al., 2022, Daase et al., 2016), however results here indicate that spectral distribution may be another significant driver in DVM trigger mechanisms.

5.2.5 Conclusions

Analysing diel vertical migration (DVM) of the *Thysanoessa* genus of Arctic krill in response to changing environmental conditions has highlighted that using photosynthetically active radiation (PAR) as a predictor of DVM may not be appropriate. When accounting for the visual sensitivity of the animals, light levels that would be perceived by the krill can be an order of magnitude lower than actual light levels that would be modelled or measured *in situ*. Moreover, the fraction of irradiance that they can perceive varies with solar and lunar positions as well as depth in the water column, varying in this study between 33% to 97%. The attenuation characteristics of seawater mean that the further ambient light penetrates the water column, the more aligned the spectral distribution becomes with the spectral sensitivity of the krill. This results in the fraction of perceived PAR increasing with depth.

Exploring changes in perceived PAR in the context of changing environmental conditions has shown that the elevation of the sun and moon, as well as lunar phase play a vital role in determining the fraction of light that is sensed by krill. The abundance of irradiance in the red wavelengths from direct solar and lunar light results in a drop in perceived light levels. When both are below the local horizon, perceived fraction of PAR near the surface is maximised during astronomical twilight conditions, when the spectral distribution of ambient light most closely aligns with spectral sensitivity of the krill. Transforming these spectral irradiance curves into a single colour indicates that the ratio of green to blue light may play a role in determining DVM movements. Results from both time periods presented here have shown that lower absolute irradiance levels at night may not always a predictor of migration depth, although to properly assess this relationship other factors influencing vertical movements of krill would need to be considered. Night-time perceived surface irradiance levels in late March were in the region of 10^{-4} mol photons $\mathrm{m}^{-2}\,\mathrm{s}^{-1}$, and saw a CoM migration depth for the population of krill as high as 50m in the water column. In earlier March, night-time perceived surface irradiance reached as low as 10^{-6} mol photons $\mathrm{m}^{-2}\,\mathrm{s}^{-1}$ and saw a CoM depth around 100m. However, the dominance of spectral irradiance distribution by the moon earlier in the month meant that the perceived light field was more weighted to the green wavelengths, a feature that was absent in later March due to the proximity of the sun to local horizon at night. If absolute light levels were the only predictor of migration depth, it would be expected that the krill population would migrate to a more shallow depth in the water column earlier in the month. However it should be noted that the analysis presented here has not taken into consideration the abundance of krill, predator or food sources which add more complexity to predicting migration patterns.

A limitation to using the HEIMDALL model for further studies in this context is the manner in which local cloud cover is integrated into the light field model. In its current form, HEIMDALL implements a broadband reduction factor to spectral irradiance in the presence of cloud. Studies have shown that the spectral effects of clouds on PAR are relatively small and can generally be neglected (Bartlett et al., 1998), however recent work reports some enhancement of irradiance in the wavelength range 400-450nm by clouds (Durand et al., 2021, Parisi et al., 2020). This subtle change may be sufficient enough to be identified by the visual receptors of zooplankton and induce vertical mirgration which cannot currently be predicted by HEIMDALL.

Existing studies have focussed on DVM in response to PAR, with some suggesting the animals are tracking an isolume in the water column as a visual cue (Last et al., 2016, Hobbs et al., 2021), while others have taken into account the spectral resolution of the light field and appropriately weighted by animal eye response function to account for only those wavelengths that can be utilised by the krill (Cohen et al., 2015, Ludvigsen et al., 2018, Häfker et al., 2022). These approaches generally focus on a changing intensity of either broadband or specified wavelengths of light without consideration of the spectral distribution that evolves as a function of solar and lunar characteristics. Overall irradiance levels are a clear driver for DVM in zooplankton, however results here show that spectral distribution of light may also be a controlling factor in animal behaviour and should be explored in future studies.

Chapter 6

Conclusions and Future Work

6.1 Conclusions and Summary

The work presented here has focussed on the construction of a computational model to estimate fully seasonal, underwater hyperspectral light fields in the Arctic and the associated biological impacts in relation to primary production and animal migration patterns.

The first stage of the project was the development of a spectrally resolved underwater light field model for ice-free conditions in the Barents Sea. The HEIMDALL hyperspectral light field model demonstrated the ability to accurately determine location-specific above surface downwelling spectral irradiance contributions from solar, lunar and dark sky components by combining modelled irradiance values from Hydrolight (Mobley, 2022), *in situ* measurements for twilight and dark sky conditions (Spitschan et al., 2016, Kolláth et al., 2020), and a newly developed model of lunar spectral irradiance using lunar albedo measurements (Shkuratov et al., 1999), all modulated by satellite retrieved cloud cover data. By incorporating a region-specific bio-optical model (Kostakis et al., 2020), results showed accurate calculations of underwater irradiance to depth for inhomogeneous water columns over a spatial-temporal range, validated against time series irradiance data from the ArcLight Light Observatory in Ny Ålesund, Svalbard and *in situ* irradiance sensors deployed in the Barents Sea. In comparison to state-of-the-art radiative transfer models, on average over the water column the model demonstrated a typical mean absolute error of $< 1\,\mu\mathrm{mol\,m^{-2}\,s^{-1}}$ for overcast conditions and $< 6\,\mu\mathrm{mol\,m^{-2}\,s^{-1}}$ for clear conditions, with a reduced execution time of factor 20.

Following the validation of the open water component of the light field model, a snow and ice module was developed to simulate the transmission of spectrally resolved light through snow and ice, accounting for fractional ice cover on the water. Using a collection of field data from existing literature, a Pan-Arctic model of spectral attenuation was developed which is populated by snow depth, ice depth, ice age and sea ice concentration estimates from satellite or modelled data. Comparison with *in situ* measurements of spectral transmission (Uttal et al., 2002, Perovich, 2007, Nicolaus et al., 2013, Light et al., 2015) showed a mean absolute transmission error of 0.03 for bare ice and <0.005 for snow-covered ice transmission, averaged over all wavelengths. Results demonstrated a clear hierarchy of controlling parameters when determining under-ice light fields, with sea ice concentration having the largest effect on the fraction of light entering into the water column, followed by snow depth and then ice depth. However, results also showed that even during periods of 100% ice cover, sufficiently thin bare ice ($<$ 0.5m) still allows more than 20% of the above surface irradiance to penetrate into the water, highlighting a potential issue with disregarding under-ice light fields. Substantial limitations were also discussed, particularly the inability for current modelling approaches to include the effects of melt ponds or the surface scattering layer that persists in the Arctic during the melt season, as these cannot be parameterised via satellite measurements. Furthermore, issues were identified with using satellite, reanalysis or modelled data to quantify location-specific sea ice characteristics. Comparisons of available snow and sea ice products (Zhang and Rothrock, 2003, Ricker et al., 2017, Kurtz and Harbeck, 2017, Stroeve et al., 2020) with *in situ* measurements (Light et al., 2015, Rösel et al., 2018) showed a mean absolute error of $>$ 0.8m for ice depth and $>$ 0.2m for snow depth. This potential error was particularly significant for snow depth estimates, as an uncertainty of 0.2m was shown to impact under-ice light by an order of magnitude.

The above surface light field was then revisited to explore the impact of multiple reflection effects between ground snow and cloud on surface irradiance levels. Using a convolutional neural network (CNN) (Ronneberger et al., 2015) applied to daytime all-sky images from the ArcLight Light Observatory in Ny Ålesund (Johnsen et al., 2021a), accurate cloud cover values were determined over a two separate months in 2020, one with significant snow cover (April) and one with minimal snow cover (July). These cloud cover values were compared with satellite retrieved cloud cover estimates from the Copernicus Climate Change Service ERA5 Reanalysis product, provided on an hourly basis (Hersbach et al., 2018). Results showed a higher mean bias error in the dataset from April (0.18) compared to July (0.01), suggesting that the satellite data may be struggling to distinguish cloud cover from ground snow. Using cloud cover values determined via CNN and imported into the HEIMDALL open water light field model, estimates of modelled irradiance were compared with daytime irradiance measured *in situ* from the ArcLight Light Observatory (Berge et al., 2021a). During April, a clear relationship was seen between high cloud cover values and higher than expected *in situ* irradiance measurements. When cloud cover fraction exceeded 0.6 (60% coverage), a linear relationship between cloud fraction and amplification factor was determined, with an average amplification of ∼65% during overcast conditions of 100% cloud cover. Similar behaviour was found to occur during July, with a lower average amplification value of ∼30% at 100% cloud cover, reflecting reduced snow cover on the ground and as a result, lower surface albedo. Amplification effects during Polar Night were also studied to assess the impact of multiple reflection effects of Artificial Light At Night (ALAN) on surface irradiance values. Comparisons of modelled and measured surface irradiance (Johnsen et al., 2021b) during a period of 100% cloud cover demonstrated an amplification factor of ∼8.5, with the measuring instrument recording more than twice as much light during overcast conditions compared with clear sky conditions.

The impact of underwater light field parameterisation in the context of biological processes was then explored. Using the modified HEIMDALL model to include the effects of snow, sea ice and surface irradiance amplification, a general broadband model for primary production (Platt et al., 1990) was utilised to calculate Pan-Arctic seasonal primary production using satellite retrieved sea ice and snow characteristics for 2018. Results showed that during clear sky conditions, in January the fraction of daily primary production per unit chlorophyll *a* occurring beneath ice accounted for only around 1.8% of total Pan-Arctic productivity, with a similar value of 1.4% in October. However during April (when spring bloom conditions are usually ongoing (Vernet et al., 2021)), this fraction increased to around 11%. In July when the sun is above horizon all day at high latitudes, results demonstrated that over 22% of Pan-Arctic productivity may be occurring in ice-covered waters with many areas of the Arctic Ocean being uninhibited by the ice cover and primary production values reached saturation levels. During overcast conditions (100% cloud cover), under-ice productivity accounted for 1.8%, 5.8%, 10.5% and 1.1% of total Pan-Arctic primary production for January, April, July and October respectively. The introduction of above surface irradiance amplification effects induced a modest increase of under-ice productivity in April and July, but had very little effect on data from January and October. Modelling primary production over a range of sea ice and snow conditions (for typical light levels in the spring) suggests that during periods of 100% ice cover, sufficiently thin ice (≤ 0.3m) still permits primary production to reach around 85% of saturation levels on clear sky days, which is comparable to open water overcast conditions. However, the presence of only a few centimetres of snow on thin ice reduces this figure by more than half, and primary production is <40% of saturation levels.

Following on from Pan-Arctic scales, daily primary production was calculated for an open water transect in the Barents Sea using a range of light field models to assess the sensitivity of diffuse attenuation parameterisation. Broadband underwater light fields were calculated using the HEIMDALL light model, a range of light models from literature designed for use in the Arctic (Banas et al., 2016, Wassmann et al., 2006, Zhang et al., 2010) and a light field model specifically tuned for conditions in the Barents Sea. Results showed the HEIMDALL model outperforming the others when comparing to irradiance measurements recorded by an autonomous glider deployed in the Barents Sea in 2018 (Kostakis et al., 2020), with models from the literature consistently demonstrating either a substantial over or under estimation of underwater light levels and the tuned model varying in performance. Using bio-optical data collected via the autonomous glider and a broadband primary production model (Platt et al., 1990), daily primary production calculated using each of the light field models showed substantial variation from those estimated by HEIMDALL, with the largest variance being a factor of 12.

Finally, modelled underwater light fields during open water conditions were calculated and used to study the impact of light on diel vertical migration (DVM) patterns of Arctic krill in Kongsfjorden, Svalbard. Using acoustic backscattering data (Häfker et al., 2022), two time series of the migration patterns of the *Thysanoessa* genus of Arctic krill from March 2018 were presented alongside underwater hyperspectral irradiances predicted by the HEIMDALL model. By weighting the spectral irradiance fields by the visual sensitivity function of the krill (Cohen et al., 2015), the perceived underwater light levels experienced by the animals was presented alongside their changing position in the water column. Converting the perceived spectra to single colour suggested that DVM patterns by the krill may be influenced by the changing spectral distribution of the above surface light field, induced by changes in solar and lunar elevations, and phase. The krill were shown to migrate deeper into the water column when there was a shift in the spectral distribution of light from a blue dominant colour to a green dominant colour. Comparing a subset of night-time migration patterns showed the animals migrating up the water column to a minimum depth of 50m when irradiance levels were in the region of $10^{-4}\,\mu\,\mathrm{mol\,m^{-2}\,s^{-1}}$ and the spectral distribution was dominant in the blue, but diving to a depth of 100m when irradiance levels were in the region of $10^{-6}\mu\,\mathrm{mol\,m^{-2}\,s^{-1}}$ and the spectral distribution was dominant in the green. These results highlighted that the spectral distribution of light may also be a controlling factor in animal behaviour in addition to absolute irradiance levels.

The work presented here has demonstrated a gap in current methods of underwater light field estimates for application to Arctic waters, and highlighted that substantial components are potentially being erroneously disregarded.

Results have shown that it is possible to build a relatively simple model of spectrally resolved underwater irradiance that captures the contributions from all important natural light sources while maintaining similar accuracy to state of the art radiative transfer models. This has facilitated the estimation of underwater light levels in the Arctic throughout the Polar Night, a period of time where existing data products or light models fail.

The construction and validation of a snow and ice transmission model has also demonstrated that although the presence of snow and sea ice significantly reduces the magnitude of under-ice light, the resulting light levels are not zero, as assumed by some existing models. Disregarding this contribution could result in a substantial underestimation of primary production during the spring and summer season. Additionally, the significance of spectral distribution in relation to animal behaviour has been demonstrated as a possible trigger mechanism of diel vertical migration in some zooplankton communities, highlighting the nuance in predicting animal migration patterns.

The construction of the HEIMDALL light field model demonstrates an ability to estimate Pan-Arctic, underwater spectral irradiance in open water and beneath snow and ice through the full calendar year, opening up new windows to explore light dependent biological process in a rapidly changing and globally influential region.

6.2 Future Work

This work has also revealed issues that remain with accurately quantifying underwater light levels. Recommendations for further improvements are noted below.

1. The implementation of cloud cover effects into the HEIMDALL model is limited and is driven by the available data products. Cloud cover estimates are generally limited to spatial-temporal scales that are too large to reflect a dynamic weather system at a specific location. Results here have also demonstrated that attempts by satellites to retrieve fractional cloud cover over snow-covered terrain are not always reliable. These limitations have the potential to impact calculated irradiance levels by up to a factor of 4. Furthermore, cloud thickness and type are not accounted for, nor are the spectral effects of cloud. For a more precise spectrally resolved underwater light field model, these issues should be explored in future studies.

2. Snow and sea ice both strongly influence underwater light levels, however accurate characterisation of these parameters is challenging on a local level. Large spatial-temporal scales mean that satellite snow and ice products are not currently able to capture the heterogeneity of snow and sea ice and are not reliable predictors of localised conditions that can be captured by *in situ* measurements. Similar to the issues identified with cloud cover products, this can cause issues with a dynamic system that requires high resolution data, such as animal behaviour patterns. Additionally, satellite data on snow and ice depth is entirely unavailable throughout the melt season, even though sea ice still covers much of the Arctic Ocean throughout the season. Although reanalysis products are available during this period of time, they exhibit similar issues of low spatial-temporal resolution and cannot be used to predict localised conditions. Although improved snow and sea ice data products would improve the accuracy of underwater light field estimates, it is possible that this scale of detail may never be possible via satellite measurements.

3. Two additional variables have been excluded entirely from analysis presented here: melt ponds and the surface scattering layer of snow and ice. Melt ponds have been shown to transmit a substantially higher fraction of above surface irradiance into the water column compared with bare ice, however melt ponds are currently unable to be identified and mapped by satellites. This issue may be addressed in the future as initial attempts to identify their presence using satellite data have recently been successful. Furthermore, very little is currently known about the surface scattering layer or how it forms, but it is known to persist widely across Arctic ice during the melt season and may effect the magnitude of light being transmitted into the water column. Any future large-scale product identifying the presence of melt ponds and the surface scattering layer should be included in light modelling efforts.

References

Aas, E. (1996). Refractive index of phytoplankton derived from its metabolite composition. *Journal of Plankton Research*, *18*(12), 2223–2249. https://doi.org/10.1093/plankt/18.12.2223

Alkama, R., Taylor, P. C., Garcia-San Martin, L., Douville, H., Duveiller, G., Forzieri, G., Swingedouw, D., & Cescatti, A. (2020). Clouds damp the radiative impacts of polar sea ice loss. *Cryosphere*, *14*(8), 2673–2686. https://doi.org/10.5194/tc-14-2673-2020

Ansari, K., Bae, T.-S., & Lee, J. (2021). Spatiotemporal variability of total cloud cover measured by visual observation stations and their comparison with ERA5 reanalysis over South Korea. *International Journal of Climatology*, *41*(S1), 1661–1679. https://doi.org/10.1002/joc.6805

Banas, N. S., Zhang, J., Campbell, R. G., Sambrotto, R. N., Lomas, M. W., Sherr, E., Sherr, B., Ashjian, C., Stoecker, D., & Lessard, E. J. (2016). Spring plankton dynamics in the Eastern Bering Sea, 1971–2050: Mechanisms of interannual variability diagnosed with a numerical model. *Journal of Geophysical Research: Oceans*, *121*(2), 1476–1501. https://doi.org/10.1002/2015JC011449

Bandara, K., Varpe, Ø., Wijewardene, L., Tverberg, V., & Eiane, K. (2021). Two hundred years of zooplankton vertical migration research. *Biological Reviews*, *96*(4), 1547–1589. https://doi.org/10.1111/brv.12715

Baran, A. J. (2004). On the scattering and absorption properties of cirrus cloud. *89*, 17–36. https://doi.org/https://doi.org/10.1016/j.jqsrt.2004.05.008

Barber, D. G., & Thomas, A. (1998). The influence of cloud cover on the radiation budget, physical properties, and microwave scattering coefficient (cr°) of first-year and multiyear sea ice. *IEEE Transactions on Geoscience and Remote Sensing*, *36*(1), 38–50. https://doi.org/10.1109/36.655316

Bartlett, J. S., Ciotti, Á. M., Davis, R. F., & Cullen, J. J. (1998). The spectral effects of clouds on solar irradiance. *Journal of Geophysical Research: Oceans*, *103*(C13), 31017–31031. https://doi.org/10.1029/1998jc900002

Beardsley, R. C., Epstein, A. W., Chen, C., Wishner, K. F., Macaulay, M. C., & Kenney, R. D. (1996). Spatial variability in zooplankton abundance near feeding right whales in the Great South Channel. *Deep-Sea Research Part II: Topical Studies in Oceanography*, *43*(7-8), 1601–1625. https://doi.org/10.1016/S0967-0645(96)00050-1

Behrenfeld, M. J., Boss, E., Siegel, D. A., & Shea, D. M. (2005). Carbon-based ocean productivity and phytoplankton physiology from space. *Global Biogeochemical Cycles*, *19*(1), 1–14. https://doi.org/10.1029/2004GB002299

Behrenfeld, M. J., & Falkowski, P. G. (1997). Photosynthetic rates derived from satellite-based chlorophyll concentration. *Limnology and Oceanography*, *42*(1), 1–20. https://doi.org/10.4319/lo.1997.42.1.0001

Bengil, F., McKee, D., Beşiktepe, S. T., Sanjuan Calzado, V., & Trees, C. (2016). A bio-optical model for integration into ecosystem models for the Ligurian Sea. *Progress in Oceanography*, *149*, 1–15. https://doi.org/10.1016/j.pocean.2016.10.007

Berge, J., Cottier, F., Varpe, Ø., Renaud, P. E., Falk-Petersen, S., Kwasniewski, S., Griffiths, C., SØreide, J. E., Johnsen, G., Aubert, A., Bjærke, O., Hovinen, J., Jung-Madsen, S., Tveit, M., & Majaneva, S. (2014). Arctic complexity: A case study on diel vertical migration of zooplankton. *Journal of Plankton Research*, *36*(5), 1279–1297. https://doi.org/10.1093/plankt/fbu059

Berge, J., Daase, M., Renaud, P. E., Ambrose, W. G., Darnis, G., Last, K. S., Leu, E., Cohen, J. H., Johnsen, G., Moline, M. A., Cottier, F., Varpe, O., Shunatova, N., Bałazy, P., Morata, N., Massabuau, J. C., Falk-Petersen, S., Kosobokova, K., Hoppe, C. J., … Callesen, T. A. (2015a). Unexpected levels of biological activity during the polar night offer new perspectives on a warming arctic. *Current Biology*, *25*(19), 2555–2561. https://doi.org/10.1016/j.cub.2015.08.024

Berge, J., Grant, S., Bjørgum, R., Cohen, J. H., McKee, D., Johnsen, G., Zolich, A., Kopec, T. P., & Vogedes, D. (2021a). Time series (2020) of irradiance in the PAR (photosynthetically active radiation) region measured under the dome of a light observatory in the Arctic (Ny-Ålesund, Svalbard, Norway) derived from an USSIMO spectroradiometer. *Norstore*. https://doi.org/10.11582/2021.00043

Berge, J., Grant, S., Bjørgum, R., Cohen, J. H., McKee, D., Johnsen, G., Zolich, A., Kopec, T. P., & Vogedes, D. (2021b). USSIMO spectroradiometer raw data time series (2018) measured under the dome of a light observatory in the Arctic (Ny-Ålesund, Svalbard, Norway). *Norstore*. https://doi.org/https://doi.org/10.11582/2021.00044

Berge, J., Renaud, P. E., Darnis, G., Cottier, F., Last, K., Gabrielsen, T. M., Johnsen, G., Seuthe, L., Weslawski, J. M., Leu, E., Moline, M., Nahrgang, J., Søreide, J. E., Varpe, Ø., Lønne, O. J., Daase, M., & Falk-Petersen, S. (2015b). In the dark: A review of ecosystem processes during the Arctic polar night. *Progress in Oceanography*, *139*, 258–271. https://doi.org/10.1016/j.pocean.2015.08.005

Bouman, H. A., Platt, T., Doblin, M., Figueiras, F. G., Gudmundsson, K., Gudfinnsson, H. G., Huang, B., Hickman, A., Hiscock, M., Jackson, T., Lutz, V. A., Mélin, F., Rey, F., Pepin, P., Segura, V., Tilstone, G. H., Van Dongen-Vogels, V., & Sathyendranath, S. (2018). Photosynthesis-irradiance parameters of marine phytoplankton:

Synthesis of a global data set. *Earth System Science Data*, *10*(1), 251–266. https://doi.org/10.5194/essd-10-251-2018

Bricaud, A., Babin, M., Morel, A., & Claustre, H. (1995). Variability in the chlorophyll-specific absorption coefficients of natural phytoplankton: analysis and parameterization. *Journal of Geophysical Research*, *100*(C7). https://doi.org/10.1029/95JC00463

Bricaud, A., Morel, A., Babin, M., Allali, K., & Claustre, H. (1998a). Variations of light absorption by suspended particles with chlorophyll a concentration in oceanic (case 1) waters : Analysis and implications for bio-optical models Abstract . Spectral absorption coefficients of total particulate matter mg m-3). As pre. *Journal of Geophysical Research*, *103*(C13), 31033–31044.

Bricaud, A., Morel, A., Babin, M., Allali, K., & Claustre, H. (1998b). Variations of light absorption by suspended particles with chlorophyll a concentration in oceanic (case 1) waters: Analysis and implications for bio-optical models. *Journal of Geophysical Research: Oceans*, *103*(C13), 31033–31044. https://doi.org/10.1029/98jc02712

Buchan, A., LeCleir, G. R., Gulvik, C. A., & González, J. M. (2014). Master recyclers: features and functions of bacteria associated with phytoplankton blooms. *Nature reviews. Microbiology*, *12*(10), 686–698. https://doi.org/10.1038/nrmicro3326

Cairns, B., Lacis, A. A., & Carlson, B. E. (2000). Absorption within Inhomogeneous Clouds and Its Parameterization in General Circulation Models, 700–714. https://doi.org/https://doi.org/10.1175/1520-0469(2000)057<0700:AWICAI>2.0.CO;2

Carr, M. E., Friedrichs, M. A., Schmeltz, M., Noguchi Aita, M., Antoine, D., Arrigo, K. R., Asanuma, I., Aumont, O., Barber, R., Behrenfeld, M., Bidigare, R., Buitenhuis, E. T., Campbell, J., Ciotti, A., Dierssen, H., Dowell, M., Dunne, J., Esaias, W., Gentili, B., … Yamanaka, Y. (2006). A comparison of global estimates of marine primary production from ocean color. *Deep-Sea Research Part II: Topical Studies in Oceanography*, *53*(5-7), 741–770. https://doi.org/10.1016/j.dsr2.2006.01.028

Castellani, G., Losch, M., Lange, B. A., & Flores, H. (2017). Modeling Arctic sea-ice algae: Physical drivers of spatial distribution and algae phenology. *Journal of Geophysical Research: Oceans*, *122*(9), 7466–7487. https://doi.org/10.1002/2017JC012828

Castellani, G., Schaafsma, F. L., Arndt, S., Lange, B. A., Peeken, I., Ehrlich, J., David, C., Ricker, R., Krumpen, T., Hendricks, S., Schwegmann, S., Massicotte, P., & Flores, H. (2020). Large-Scale Variability of Physical and Biological Sea-Ice Properties in Polar Oceans. *Frontiers in Marine Science*, *7*(August), 1–22. https://doi.org/10.3389/fmars.2020.00536

Castellani, G., Veyssière, G., Karcher, M., Stroeve, J., Banas, S. N., Bouman, A. H., Brierley, S. A., Connan, S., Cottier, F., Große, F., Hobbs, L., Katlein, C., Light, B., McKee, D., Orkney, A., Proud, R., & Schourup-Kristensen, V. (2022). Shine a light: Under-ice light and its ecological implications in a changing Arctic Ocean. *Ambio*, *51*(2), 307–317. https://doi.org/10.1007/s13280-021-01662-3

Cavalieri, D. J., & Parkinson, C. L. (2012). Arctic sea ice variability and trends, 1979-2010. *Cryosphere*, *6*(4), 881–889. https://doi.org/10.5194/tc-6-881-2012

Cawkwell, F. G., & Bamber, J. L. (2002). The impact of cloud cover on the net radiation budget of the Greenland ice sheet. *Annals of Glaciology*, *34*, 141–149. https://doi.org/10.3189/172756402781817789

Choi, Y.-S., Hwang, J., Ok, J., Park, D.-S. R., Su, H., Jiang, J. H., Huang, L., & Limpasuvan, T. (2020). Effect of Arctic clouds on the ice-albedo feedback in midsummer. *International Journal of Climatology*, *40*(10), 4707–4714. https://doi.org/10.1002/joc.6469

Choi, Y.-S., Kim, B.-M., Jur, S.-K., Kim, S.-J., Kim, J.-H., & Ho, C.-H. (2014). Connecting early summer cloud-controlled sunlight and late summer sea ice in the Arctic. *Journal of Geophysical Research*, (3), 180–198. https://doi.org/10.1002/2013JD021040.Received

Clementson, L. A., & Wojtasiewicz, B. (2019). Dataset on the in vivo absorption characteristics and pigment composition of various phytoplankton species. *Data in Brief*, *25*, 104020. https://doi.org/10.1016/j.dib.2019.104020

Cohen, J. H., Berge, J., Moline, M. A., Sørensen, A. J., Last, K., Falk-Petersen, S., Renaud, P. E., Leu, E. S., Grenvald, J., Cottier, F., Cronin, H., Menze, S., Norgren, P., Varpe, Ø., Daase, M., Darnis, G., & Johnsen, G. (2015). Is ambient light during the high Arctic polar night sufficient to act as a visual cue for zooplankton? *PLoS ONE*, *10*(6), 1–12. https://doi.org/10.1371/journal.pone.0126247

Cohen, J. H., & Forward, R. B. (2002). Spectral sensitivity of vertically migrating marine copepods. *Biological Bulletin*, *203*(3), 307–314. https://doi.org/10.2307/1543573

Cohen, J. H., & Forward, R. B. (2016). Zooplankton Diel Vertical Migration — A Review of Proximate Control. *Oceanography and Marine Biology*, 89–122.

Connan-McGinty, S., Banas, N. S., Berge, J., Cottier, F., Grant, S., Johnsen, G., Kopec, T. P., Porter, M., & McKee, D. (2022a). Midnight Sun to Polar Night: A Model of Seasonal Light in the Barents Sea. *Journal of Advances in Modeling Earth Systems*, *14*(10), 1–17. https://doi.org/10.1029/2022MS003198

Connan-McGinty, S., Banas, N. S., Berge, J., Cottier, F., Grant, S., Johnsen, G., Kopec, T. P., Porter, M., & McKee, D. (2022b). Midnight Sun to Polar Night: A model of seasonal light in the Barents Sea - HEIMDALL Model. *Zenodo*. https://doi.org/https://doi.org/10.5281/zenodo.7622686

Connan-McGinty, S., Banas, N. S., Berge, J., Cottier, F., Grant, S., Johnsen, G., Kopec, T. P., Porter, M., & McKee, D. (2022c). Midnight Sun to Polar Night: A model of seasonal light in the Barents Sea - Supplementary Data [Dataset]. *Zenodo*. https://doi.org/https://doi.org/10.5281/zenodo.7041939

Conover, J. H. (1965). Cloud and Terrestrial Albedo Determinations from TIROS Satellite Pictures. *Journal of Applied Meteorology*, *4*(3), 378–386. https://doi.org/10.1175/1520-0450(1965)004<0378:CATADF>2.0.CO;2

Cooke, S. L., Williamson, C. E., Leech, D. M., Boeing, W. J., & Torres, L. (2008). Effects of temperature and ultraviolet radiation on diel vertical migration of freshwater crustacean zooplankton. *Canadian Journal of Fisheries and Aquatic Sciences*, *65*(6), 1144–1152. https://doi.org/10.1139/F08-039

Cooper, M. G., Smith, L. C., Rennermalm, A. K., Tedesco, M., Muthyala, R., Leidman, S. Z., Moustafa, S. E., & Fayne, J. V. (2021). Spectral attenuation coefficients from measurements of light transmission in bare ice on the Greenland Ice Sheet. *Cryosphere*, *15*(4), 1931–1953. https://doi.org/10.5194/tc-15-1931-2021

Cota, G. F., Harrison, W. G., Platt, T., Sathyendranath, S., & Stuart, V. (2003). Bio-optical properties of the Labrador Sea. *Journal of Geophysical Research: Oceans*, *108*(7). https://doi.org/10.1029/2000jc000597

Cottier, F. R., Tarling, G. A., Wold, A., & Falk-Petersen, S. (2006). Unsynchronized and synchronized vertical migration of zooplankton in a high arctic fjord. *Limnology and Oceanography*, *51*(6), 2586–2599. https://doi.org/10.4319/lo.2006.51.6.2586

Cyr, H., & Sprules, W. G. (2022). The wind-driven distribution of nearshore zooplankton in a stratified lake varies with their body size. *Freshwater Biology*, *67*(6), 991–1004. https://doi.org/10.1111/fwb.13896

Daase, M., Hop, H., & Falk-Petersen, S. (2016). Small-scale diel vertical migration of zooplankton in the High Arctic. *Polar Biology*, *39*(7), 1213–1223. https://doi.org/10.1007/s00300-015-1840-7

Dall'Olmo, G., Westberry, T. K., Behrenfeld, M. J., Boss, E., & Slade, W. H. (2009). Significant contribution of large particles to optical backscattering in the open ocean. *Biogeosciences*, *6*(6), 947–967. https://doi.org/10.5194/bg-6-947-2009

Darnis, G., Hobbs, L., Geoffroy, M., Grenvald, J. C., Renaud, P. E., Berge, J., Cottier, F., Kristiansen, S., Daase, M., E. Søreide, J., Wold, A., Morata, N., & Gabrielsen, T. (2017). From polar night to midnight sun: Diel vertical migration, metabolism and biogeochemical role of zooplankton in a high Arctic fjord (Kongsfjorden, Svalbard). *Limnology and Oceanography*, *62*(4), 1586–1605. https://doi.org/10.1002/lno.10519

Davies, R. (1978). The Effect of Finite Geometry on the Three-Dimensional Transfer of Solar Irradiance in Clouds. *Journal of the Atmospheric Sciences*, *35*(9), 1712–1725. https://doi.org/10.1175/1520-0469(1978)035<1712:TEOFGO>2.0.CO;2

Durand, M., Murchie, E. H., Lindfors, A. V., Urban, O., Aphalo, P. J., & Robson, T. M. (2021). Diffuse solar radiation and canopy photosynthesis in a changing environment. *Agricultural and Forest Meteorology*, *311*(October), 108684. https://doi.org/10.1016/j.agrformet.2021.108684

Eastman, R., & Warren, S. G. (2010). Arctic cloud changes from surface and satellite observations. *Journal of Climate*, *23*(15), 4233–4242. https://doi.org/10.1175/2010JCLI3544.1

Ehn, J. K., Papakyriakou, T. N., & Barber, D. G. (2008). Inference of optical properties from radiation profiles within melting landfast sea ice. *Journal of Geophysical Research: Oceans*, *113*(9), 1–15. https://doi.org/10.1029/2007JC004656

Estilow, T. W., Young, A. H., & Robinson, D. A. (2015). A long-term Northern Hemisphere snow cover extent data record for climate studies and monitoring. *Earth System Science Data*, *7*(1), 137–142. https://doi.org/10.5194/essd-7-137-2015

Fenchel, T. (1988). Marine plankton food chains. *Annual review of ecology and systematics. Vol. 19*, 19–38. https://doi.org/10.1146/annurev.ecolsys.19.1.19

Florides, G. A., & Christodoulides, P. (2009). Global warming and carbon dioxide through sciences. *Environment International*, *35*(2), 390–401. https://doi.org/10.1016/j.envint.2008.07.007

Fortier, M. (2001). Visual predators and the diel vertical migration of copepods under Arctic sea ice during the midnight sun. *Journal of Plankton Research*, *23*(11), 1263–1278. https://doi.org/10.1093/plankt/23.11.1263

Frederiksen, M., Edwards, M., Richardson, A. J., Halliday, N. C., & Wanless, S. (2006). From plankton to top predators: Bottom-up control of a marine food web across four trophic levels. *Journal of Animal Ecology*, *75*(6), 1259–1268. https://doi.org/10.1111/j.1365-2656.2006.01148.x

Freer, J. J., Daase, M., & Tarling, G. A. (2021). Modelling the biogeographic boundary shift of Calanus finmarchicus reveals drivers of Arctic Atlantification by subarctic zooplankton. *Global Change Biology*, *28*(2), 429–440. https://doi.org/10.1111/gcb.15937

Garnier, F., Fleury, S., Garric, G., Bouffard, J., Tsamados, M., Laforge, A., Bocquet, M., Fredensborg Hansen, R. M., & Remy, F. (2021). Advances in altimetric snow depth estimates using bi-frequency SARAL and CryoSat-2 Ka-Ku measurements. *Cryosphere*, *15*(12), 5483–5512. https://doi.org/10.5194/tc-15-5483-2021

Gordon, H. R. (1989). Theoretical aspects of hydrologic optics. *Limonology And Oceanography*, *34*(8), 1389–1409. https://doi.org/10.1097/00003246-200206000-00018

Gregg, W. W., & Carder, K. L. (1990). A simple spectral solar irradiance model for cloudless maritime atmospheres. *Limnology and Oceanography*, *35*(8), 1657–1675. https://doi.org/10.4319/lo.1990.35.8.1657

Grenfell, T. C., Light, B., & Perovich, D. K. (2006). Spectral transmission and implications for the partitioning of shortwave radiation in arctic sea ice. *Annals of Glaciology*, *44*, 1–6. https://doi.org/10.3189/172756406781811763

Grenfell, T. C., & Maykut, G. A. (1977). The Optical Properties of Ice and Snow in the Arctic Basin. *Journal of Glaciology*, *18*(80), 445–463. https://doi.org/10.3189/s0022143000021122

Häfker, N. S., Connan-McGinty, S., Hobbs, L., McKee, D., Cohen, J. H., & Last, K. S. (2022). Animal behavior is central in shaping the realized diel light niche. *Communications Biology*, *5*(1), 1–8. https://doi.org/10.1038/s42003-022-03472-z

Hall, D. K., & Riggs, G. A. (2007). Accuracy assessment of the MODIS snow products. *Hydrological Processes*, *21*(12), 1534–1547. https://doi.org/10.1002/hyp.6715

Hamre, B., Winther, J. G., Gerland, S., Stamnes, J. J., & Stamnes, K. (2004). Modeled and measured optical transmittance of snow-covered first-year sea ice in Kongsfjorden, Svalbard. *Journal of Geophysical Research: Oceans*, *109*(10), 1–14. https://doi.org/10.1029/2003JC001926

Hays, G. C. (2003). A review of the adaptive significance and ecosystem consequences of zooplankton diel vertical migrations. *Hydrobiologia*, *503*, 163–170. https://doi.org/10.1023/B:HYDR.0000008476.23617.b0

He, M., Hu, Y., Chen, N., Wang, D., Huang, J., & Stamnes, K. (2019). High cloud coverage over melted areas dominates the impact of clouds on the albedo feedback in the Arctic. *Scientific Reports*, *9*(1), 1–11. https://doi.org/10.1038/s41598-019-44155-w

Hersbach, H., Bell, B., Berrisford, P., Biavati, G., Horányi, A., Muñoz Sabater, J., Nicolas, J., Peubey, C., Radu, R., Rozum, I., Schepers, D., Simmons, A., Soci, C., Dee, D., & Thépaut, J.-N. (2018). ERA5 hourly data on single levels from 1979 to present. *Copernicus Climate Change Service (C3S) Climate Data Store (CDS)*. https://doi.org/https://doi.org/10.24381/cds.adbb2d47

Hill, V. J., Light, B., Steele, M., & Zimmerman, R. C. (2018). Light Availability and Phytoplankton Growth Beneath Arctic Sea Ice: Integrating Observations and Modeling. *Journal of Geophysical Research: Oceans*, *123*(5), 3651–3667. https://doi.org/10.1029/2017JC013617

Hobbs, L., Banas, N. S., Cohen, J. H., Cottier, F. R., Berge, J., & Varpe, A. (2021). A marine zooplankton community vertically structured by light across diel to interannual timescales. *Biology Letters*, *17*(2). https://doi.org/10.1098/rsbl.2020.0810

Hu, C., Lee, Z., & Franz, B. (2012). Chlorophyll a algorithms for oligotrophic oceans: A novel approach based on three-band reflectance difference. *Journal of Geophysical Research: Oceans*, *117*(1), 1–25. https://doi.org/10.1029/2011JC007395

Huang, Y., Dong, X., Bailey, D. A., Holland, M. M., Xi, B., DuVivier, A. K., Kay, J. E., Landrum, L. L., & Deng, Y. (2019). Thicker Clouds and Accelerated Arctic Sea Ice Decline: The Atmosphere-Sea Ice Interactions in Spring. *Geophysical Research Letters*, *46*(12), 6980–6989. https://doi.org/10.1029/2019GL082791

Irish, R. R., Barker, J. L., Goward, S. N., & Arvidson, T. (2006). Characterization of the landsat-7 ETM+ automated cloud-cover assessment (ACCA) algorithm. *Photogrammetric Engineering and Remote Sensing*, *72*(10), 1179–1188. https://doi.org/10.14358/PERS.72.10.1179

Jamet, C., Ibrahim, A., Ahmad, Z., Angelini, F., Babin, M., Behrenfeld, M. J., Boss, E., Cairns, B., Churnside, J., Chowdhary, J., Davis, A. B., Dionisi, D., Duforêt-Gaurier, L., Franz, B., Frouin, R., Gao, M., Gray, D., Hasekamp, O., He, X., … Zhai, P.-W. (2019). Going Beyond Standard Ocean Color Observations: Lidar and Polarimetry. *Frontiers in Marine Science*, *6*(May). https://doi.org/10.3389/fmars.2019.00251

Jechow, A., & Hölker, F. (2019). Snowglow—the amplification of skyglow by snow and clouds can exceed full moon illuminance in suburban areas. *Journal of Imaging*, *5*(8), 1–12. https://doi.org/10.3390/jimaging5080069

Johnsen, G., Grant, S., Bjørgum, R., Cohen, J. H., McKee, D., Kopec, T. P., Vogedes, D., Berge, J., & Zolich, A. (2021a). Pictures from an all-sky camera with hourly resolution from the light observatory at Ny-Ålesund, Svalbard, Norway (complete year 2020). *Norstore*. https://doi.org/10.11582/2021.00021

Johnsen, G., Grant, S., Bjørgum, R., Cohen, J. H., McKee, D., Kopec, T. P., Vogedes, D., Berge, J., & Zolich, A. (2021b). Time series (2018) of irradiance in the PAR (photosynthetically active radiation) region measured under the dome of a light observatory in the Arctic (Ny-Ålesund, Svalbard, Norway) derived from SLR camera. *Norstore*. https://doi.org/https://doi.org/10.11582/2021.00048

Johnsen, G., Zolich, A., Grant, S., Bjørgum, R., Cohen, J. H., McKee, D., Kopec, T. P., Vogedes, D., & Berge, J. (2021c). All-sky camera system providing high temporal resolution annual time series of irradiance in the Arctic. *Applied Optics*, *60*(22), 6456. https://doi.org/10.1364/ao.424871

Josefsson, W., & Landelius, T. (2000). Effect of clouds on UV irradiance: As estimated from cloud amount, cloud type, precipitation, global radiation and sunshine duration. *Journal of Geophysical Research Atmospheres*, *105*(D4), 4927–4935. https://doi.org/10.1029/1999JD900255

Jun, S. Y., Ho, C. H., Jeong, J. H., Choi, Y. S., & Kim, B. M. (2016). Recent changes in winter Arctic clouds and their relationships with sea ice and atmospheric conditions. *Tellus, Series A: Dynamic Meteorology and Oceanography*, *68*, 1–20. https://doi.org/10.3402/tellusa.v68.29130

Kasten, F., & Czeplak, G. (1980). Solar and terrestrial radiation dependent on the amount and type of cloud. *Solar Energy*, *24*(2), 177–189. https://doi.org/10.1016/0038-092X(80)90391-6

Katlein, C., Arndt, S., Belter, H. J., Castellani, G., & Nicolaus, M. (2019). Seasonal Evolution of Light Transmission Distributions Through Arctic Sea Ice. *Journal of Geophysical Research: Oceans*, *124*(8), 5418–5435. https://doi.org/10.1029/2018JC014833

Katlein, C., Nicolaus, M., & Petrich, C. (2014). The anisotropic scattering coefficient of sea ice. *Journal of Geophysical Research: Oceans*, *119*(2), 842–855. https://doi.org/10.1002/2013JC009502

Kettle, H., & Merchant, C. J. (2008). Modeling ocean primary production: Sensitivity to spectral resolution of attenuation and absorption of light. *Progress in Oceanography*, *78*(2), 135–146. https://doi.org/10.1016/j.pocean.2008.04.002

King, J., Howell, S., Brady, M., Toose, P., Derksen, C., Haas, C., & Beckers, J. (2020). Local-scale variability of snow density on Arctic sea ice. *Cryosphere*, *14*(12), 4323–4339. https://doi.org/10.5194/tc-14-4323-2020

Kolláth, Z., Cool, A., Jechow, A., Kolláth, K., Száz, D., & Tong, K. P. (2020). Introducing the dark sky unit for multi-spectral measurement of the night sky quality with commercial digital cameras. *Journal of Quantitative Spectroscopy and Radiative Transfer*, *253*. https://doi.org/10.1016/j.jqsrt.2020.107162

Kondratyev, K. Y., Binenko, V. I., & Melnikova, I. N. (1998). Meteorology and Atmospheric Physics Absorption of Solar Radiation by Clouds and Aerosols in the Visible Wavelength Region. *10*, 1–10. https://doi.org/https://doi.org/10.1007/BF01030265

Kostakis, I., Röttgers, R., Orkney, A., Bouman, H. A., Porter, M., Cottier, F., Berge, J., & McKee, D. (2020). Development of a bio-optical model for the Barents Sea to quantitatively link glider and satellite observations: A bio-optical model for the Barents Sea. *Philosophical Transactions of the Royal Society A: Mathematical, Physical and Engineering Sciences*, *378*(2181). https://doi.org/10.1098/rsta.2019.0367

Kurtz, N. T., Farrell, S. L., Studinger, M., Galin, N., Harbeck, J. P., Lindsay, R., Onana, V. D., Panzer, B., & Sonntag, J. G. (2013). Sea ice thickness, freeboard, and snow depth products from Operation IceBridge airborne data. *Cryosphere*, *7*(4), 1035–1056. https://doi.org/10.5194/tc-7-1035-2013

Kurtz, N. T., & Harbeck, J. (2017). CryoSat-2 Level-4 Sea Ice Elevation, Freeboard, and Thickness, Version 1. [RDEFT4]. *NASA National Snow and Ice Data Center Distributed Active Archive Center.* https://doi.org/https://doi.org/10.5067/96JO0KIFDAS8

Kurtz, N. T., Markus, T., Farrell, S. L., Worthen, D. L., & Boisvert, L. N. (2011). Observations of recent Arctic sea ice volume loss and its impact on ocean-atmosphere energy exchange and ice production. *Journal of Geophysical Research*, *116*(C4), C04015. https://doi.org/10.1029/2010JC006235

Kvernvik, A. C., Hoppe, C. J. M., Lawrenz, E., Prášil, O., Greenacre, M., Wiktor, J. M., & Leu, E. (2018). Fast reactivation of photosynthesis in arctic phytoplankton during the polar night1. *Journal of Phycology*, *54*(4), 461–470. https://doi.org/10.1111/jpy.12750

Kwok, R. (2018). Arctic sea ice thickness, volume, and multiyear ice coverage: Losses and coupled variability (1958-2018). *Environmental Research Letters*, *13*(10). https://doi.org/10.1088/1748-9326/aae3ec

Kwok, R., Spreen, G., & Pang, S. (2013). Arctic sea ice circulation and drift speed: Decadal trends and ocean currents. *Journal of Geophysical Research: Oceans*, *118*(5), 2408–2425. https://doi.org/10.1002/jgrc.20191

Kyewalyanga, M., Platt, T., & Sathyendranath, S. (1992). Ocean primary production calculated by spectral and broad-band models. *Marine Ecology Progress Series*, *85*(1-2), 171–185. https://doi.org/10.3354/meps085171

Landy, J. C., Dawson, G. J., Tsamados, M., Bushuk, M., Stroeve, J. C., Howell, S. E., Krumpen, T., Babb, D. G., Komarov, A. S., Heorton, H. D., Belter, H. J., & Aksenov, Y. (2022). A year-round satellite sea-ice thickness record from CryoSat-2. *Nature*, *609*(7927), 517–522. https://doi.org/10.1038/s41586-022-05058-5

Last, K. S., Hobbs, L., Berge, J., Brierley, A. S., & Cottier, F. (2016). Moonlight Drives Ocean-Scale Mass Vertical Migration of Zooplankton during the Arctic Winter. *Current Biology*, *26*(2), 244–251. https://doi.org/10.1016/j.cub.2015.11.038

Lee, S. M., Shi, H., Sohn, B. J., Gasiewski, A. J., Meier, W. N., & Dybkjær, G. (2021). Winter Snow Depth on Arctic Sea Ice From Satellite Radiometer Measurements (2003–2020): Regional Patterns and Trends. *Geophysical Research Letters*, *48*(15), 1–11. https://doi.org/10.1029/2021GL094541

Lee, S., Stroeve, J., Tsamados, M., & Khan, A. L. (2020). Machine learning approaches to retrieve pan-Arctic melt ponds from visible satellite imagery. *Remote Sensing of Environment*, *247*(May), 111919. https://doi.org/10.1016/j.rse.2020.111919

Lee, Y. J., Matrai, P. A., Friedrichs, M. A. M., Saba, V. S., Antoine, D., Ardyna, M., Asanuma, I., Babin, M., Bélanger, S., Benoît-Gagné, M., Devred, E., Fernández-Méndez, M., Gentili, B., Hirawake, T., Kang, S.-H., Kameda, T., Katlein, C., Lee, S. H., Lee, Z., … Westberry, T. K. (2015). An assessment of phytoplankton primary productivity in the Arctic Ocean from satellite ocean color/in situ chlorophyll- a based models. *Journal of Geophysical Research: Oceans*, *120*(9), 6508–6541. https://doi.org/10.1002/2015JC011018

Lehn, W. H. (1979). The Novaya Zemlya effect: An arctic mirage. *Journal of the Optical Society of America*, *69*(5), 776. https://doi.org/10.1364/JOSA.69.000776

Li, W., Gao, K., & Beardall, J. (2012). Interactive Effects of Ocean Acidification and Nitrogen-Limitation on the Diatom Phaeodactylum tricornutum. *PLoS ONE*, *7*(12), 1–8. https://doi.org/10.1371/journal.pone.0051590

Light, B., Grenfell, T. C., & Perovich, D. K. (2008). Transmission and absorption of solar radiation by Arctic sea ice during the melt season. *Journal of Geophysical Research: Oceans*, *113*(3), 1–19. https://doi.org/10.1029/2006JC003977

Light, B., Perovich, D. K., Webster, M. A., Polashenski, C., & Dadic, R. (2015). Optical properties of melting first-year Arctic sea ice. *Journal of Geophysical Research: Oceans*, *120*(11), 7657–7675. https://doi.org/10.1002/2015JC011163

Liston, G. E., Itkin, P., Stroeve, J., Tschudi, M., Stewart, J. S., Pedersen, S. H., Reinking, A. K., & Elder, K. (2020). A Lagrangian Snow-Evolution System for Sea-Ice Applications (SnowModel-LG): Part I—Model Description. *Journal of Geophysical Research: Oceans*, *125*(10). https://doi.org/10.1029/2019JC015913

Liu, Y., Wu, W., Jensen, M. P., & Toto, T. (2011). Relationship between cloud radiative forcing, cloud fraction and cloud albedo, and new surface-based approach for determining cloud albedo. *Atmospheric Chemistry and Physics*, *11*(14), 7155–7170. https://doi.org/10.5194/acp-11-7155-2011

Liu, Y., Key, J. R., Liu, Z., Wang, X., & Vavrus, S. J. (2012). A cloudier Arctic expected with diminishing sea ice. *Geophysical Research Letters*, *39*(5), 1–5. https://doi.org/10.1029/2012GL051251

Lowry, K. E., Pickart, R. S., Selz, V., Mills, M. M., Pacini, A., Lewis, K. M., Joy-Warren, H. L., Nobre, C., Dijken, G. L. V., Grondin, P.-L., Ferland, J., & Arrigo, K. R. (2017). Under-Ice Phytoplankton Blooms Inhibited by Spring Convective Mixing in Refreezing Leads Kate. *123*(1), 90–109. https://doi.org/10.1002/2016JC012575

Ludvigsen, M., Berge, J., Geoffroy, M., Cohen, J. H., De La Torre, P. R., Nornes, S. M., Singh, H., Sørensen, A. J., Daase, M., & Johnsen, G. (2018). Use of an autonomous surface vehicle reveals small-scale diel vertical migrations of zooplankton and susceptibility to light pollution under low solar irradiance. *Science Advances*, *4*(1), 1–9. https://doi.org/10.1126/sciadv.aap9887

Lund, B., Graber, H. C., Persson, P. O., Smith, M., Doble, M., Thomson, J., & Wadhams, P. (2018). Arctic Sea Ice Drift Measured by Shipboard Marine Radar. *Journal of Geophysical Research: Oceans*, *123*(6), 4298–4321. https://doi.org/10.1029/2018JC013769

Luo, Z., & Ding, S. (2019). Object detection in remote sensing images based on GaN. *ACM International Conference Proceeding Series*, *57*(6), 499–503. https://doi.org/10.1145/3349341.3349458

Mallett, R. D., Stroeve, J. C., Tsamados, M., Landy, J. C., Willatt, R., Nandan, V., & Liston, G. E. (2021). Faster decline and higher variability in the sea ice thickness of the marginal Arctic seas when accounting for dynamic snow cover. *Cryosphere*, *15*(5), 2429–2450. https://doi.org/10.5194/tc-15-2429-2021

Markus, T., Stroeve, J. C., & Miller, J. (2009). Recent changes in Arctic sea ice melt onset, freezeup, and melt season length. *Journal of Geophysical Research: Oceans*, *114*(12), 1–14. https://doi.org/10.1029/2009JC005436

Marra, J. F., Lance, V. P., Vaillancourt, R. D., & Hargreaves, B. R. (2014). Resolving the ocean's euphotic zone. *Deep-Sea Research Part I: Oceanographic Research Papers*, *83*, 45–50. https://doi.org/10.1016/j.dsr.2013.09.005

Martin, A., Boyd, P., Buesseler, K., Cetinic, I., Claustre, H., Giering, S., Henson, S., Irigoien, X., Kriest, I., Memery, L., Robinson, C., Saba, G., Sanders, R., Siegel, D., Villa-Alfageme, M., & Guidi, L. (2020). The oceans' twilight zone must be studied now, before it is too late. *Nature*, *580*(7801), 26–28. https://doi.org/10.1038/d41586-020-00915-7

Maslanik, J., Stroeve, J., Fowler, C., & Emery, W. (2011). Distribution and trends in Arctic sea ice age through spring 2011. *Geophysical Research Letters*, *38*(13), 2–7. https://doi.org/10.1029/2011GL047735

Massicotte, P., Bécu, G., Lambert-Girard, S., Leymarie, E., & Babin, M. (2018). Estimating underwater light regime under spatially heterogeneous sea ice in the Arctic. *Applied Sciences (Switzerland)*, *8*(12), 1–19. https://doi.org/10.3390/app8122693

Meier, W. N., Fetterer, F., Windnagel, A. K., & Stewart, S. (2021). NOAA/NSIDC Climate Data Record of Passive Microwave Sea Ice Concentration, Version 4. [G02202]. *NSIDC: National Snow and Ice Data Center*. https://doi.org/https://doi.org/10.7265/efmz-2t65

Meier, W. N., Peng, G., Scott, D. J., & Savoie, M. H. (2014). Verification of a new NOAA/NSIDC passive microwave sea-ice concentration climate record. *Polar Research*, *33*(2014), 1–22. https://doi.org/10.3402/polar.v33.21004

Meirold-Mautner, I., & Lehning, M. (2004). Measurements and model calculations of the solar shortwave fluxes in snow on Summit, Greenland. *Annals of Glaciology*, *38*, 279–284. https://doi.org/10.3189/172756404781814753

Melling, H. (2022). Thickness of multi-year sea ice on the northern Canadian polar shelf: a second look after 40 years. *Cryosphere*, *16*(8), 3181–3197. https://doi.org/10.5194/tc-16-3181-2022

Miller, S. D., & Turner, R. E. (2009). A dynamic lunar spectral irradiance data set for NPOESS/VIIRS day/night band night time environmental applications. *IEEE*

Transactions on Geoscience and Remote Sensing, *47*(7), 2316–2329. https://doi.org/10.1109/TGRS.2009.2012696

Mobley, C. D. (2022). *The Oceanic Optics Book* (C. D. Mobley, Ed.). International Ocean Colour Coordinating Group (IOCCG). https://doi.org/10.25607/OBP-1710

Morel, A., & Prieur, L. (1977). Analysis of variations in ocean color. *Limnology and Oceanography*, *22*(4), 709–722. https://doi.org/10.4319/lo.1977.22.4.0709

Morel, A. (1974). Optical properties of pure water and pure sea water. In *Optical aspects of oceanography* (pp. 1–24). Academic Press.

NASA. (2014). NASA Goddard Space Flight Center, Ocean Ecology Laboratory, Ocean Biology Processing Group. *MODIS-Aqua Ocean Color Data*. https://doi.org/http://dx.doi.org/10.5067/AQUA/MOD

Newman, T., Farrell, S. L., Richter-Menge, J., Connor, L. N., Kurtz, N. T., Elder, B. C., & McAdoo, D. (2014). Assessment of radar-derived snow depth over Arctic sea ice. *Journal of Geophysical Research: Oceans*, *119*(12), 8578–8602. https://doi.org/10.1002/2014JC010284

Nicolaus, M., Petrich, C., Hudson, S. R., & Granskog, M. A. (2013). Variability of light transmission through Arctic land-fast sea ice during spring. *Cryosphere*, *7*(3), 977–986. https://doi.org/10.5194/tc-7-977-2013

Parisi, A. V., Igoe, D. P., Amar, A., & Downs, N. J. (2020). Solar blue light radiation enhancement during mid to low solar elevation periods under cloud affected skies. *Sensors (Switzerland)*, *20*(15), 1–13. https://doi.org/10.3390/s20154105

Pedersen, C. (2013). Zeppelin Webcamera Time Series [Data set]. *Norwegian Polar Institute*. https://doi.org/https://doi.org/10.21334/npolar.2013.9fd6dae0

Perovich, D. K. (2002). Seasonal evolution of the albedo of multiyear Arctic sea ice. *Journal of Geophysical Research*, *107*(C10), 8044. https://doi.org/10.1029/2000JC000438

Perovich, D. K. (2007). Spectral Light Transmittance. *Version 1.0. UCAR/NCAR - Earth Observing Laboratory*. https://doi.org/https://doi.org/10.5065/D6T1521W

Perovich, D. K., Grenfell, T. C., Light, B., Elder, B. C., Harbeck, J., Polashenski, C., Tucker, W. B., & Stelmach, C. (2009). Transpolar observations of the morphological properties of Arctic sea ice. *Journal of Geophysical Research: Oceans*, *114*(1). https://doi.org/10.1029/2008JC004892

Perovich, D. K., Light, B., Eicken, H., Jones, K. F., Runciman, K., & Nghiem, S. V. (2007). Increasing solar heating of the Arctic Ocean and adjacent seas, 1979-2005: Attribution and role in the ice-albedo feedback. *Geophysical Research Letters*, *34*(19), 1–5. https://doi.org/10.1029/2007GL031480

Perovich, D. K., & Richter-Menge, J. A. (2009). Loss of sea ice in the arctic. *Annual Review of Marine Science*, *1*, 417–441. https://doi.org/10.1146/annurev.marine.010908.163805

Petty, A. A., Webster, M., Boisvert, L., & Markus, T. (2018). The NASA Eulerian Snow on Sea Ice Model (NESOSIM) v1.0: Initial model development and analysis. *Geoscientific Model Development*, *11*(11), 4577–4602. https://doi.org/10.5194/gmd-11-4577-2018

Pfister, G., McKenzie, R. L., Liley, J. B., Thomas, A., Forgan, B. W., & Long, C. N. (2003). Cloud coverage based on all-sky imaging and its impact on surface solar irradiance. *Journal of Applied Meteorology*, *42*(10), 1421–1434. https://doi.org/10.1175/1520-0450(2003)042<1421:CCBOAI>2.0.CO;2

Pithan, F., & Mauritsen, T. (2014). Arctic amplification dominated by temperature feedbacks in contemporary climate models. *Nature Geoscience*, *7*(3), 181–184. https://doi.org/10.1038/ngeo2071

Platt, T., Sathyendranath, S., & Ravindran, P. (1990). Primary production by phytoplankton: Analytic solutions for daily rates per unit area of water surface. *Proceedings of the Royal Society B: Biological Sciences*, *241*(1301), 101–111. https://doi.org/10.1098/rspb.1990.0072

Platt, T., Sathyendranath, S., Forget, M. H., White, G. N., Caverhill, C., Bouman, H., Devred, E., & Son, S. H. (2008). Operational estimation of primary production at large geographical scales. *Remote Sensing of Environment*, *112*(8), 3437–3448. https://doi.org/10.1016/j.rse.2007.11.018

Ponce, V. M., Lohani, A. K., & Huston, P. T. (1997). Surface Albedo and Water Resources: Hydroclimatological Impact of Human Activities. *Journal of Hydrologic Engineering*, *2*(4), 197–203. https://doi.org/10.1061/(asce)1084-0699(1997)2:4(197)

Pope, R. M., & Fry, E. S. (1997). Absorption spectrum (380–700 nm) of pure water II Integrating cavity measurements. *Applied Optics*, *36*(33), 8710. https://doi.org/10.1364/AO.36.008710

Popova, E. E., Yool, A., Coward, A. C., Aksenov, Y. K., Alderson, S. G., De Cuevas, B. A., & Anderson, T. R. (2010). Control of primary production in the Arctic by nutrients and light: Insights from a high resolution ocean general circulation model. *Biogeosciences*, *7*(11), 3569–3591. https://doi.org/10.5194/bg-7-3569-2010

Popova, E. E., Yool, A., Coward, A. C., Dupont, F., Deal, C., Elliott, S., Hunke, E., Jin, M., Steele, M., & Zhang, J. (2012). What controls primary production in the Arctic Ocean? Results from an intercomparison of five general circulation models with biogeochemistry. *Journal of Geophysical Research: Oceans*, *117*(1), 1–16. https://doi.org/10.1029/2011JC007112

Porter, M., Cottier, F. R., Dumont, E., & Venables, E. (2020). Arctic PRIZE mission three near-real time glider dataset in the Barents Sea Spring 2018. *British Oceanographic Data Centre, National Oceanography Centre*. https://doi.org/https://doi.org/10.5285/9e4a232d-b59e-7e87-e053-6c86abc0f29f

Randelhoff, A., Lacour, L., Marec, C., Leymarie, E., Lagunas, J., Xing, X., Darnis, G., Penkerc, C., Sampei, M., Fortier, L., D'Ortenzio, F., Claustre, H., & Babin, M. (2020). Arctic mid-winter phytoplankton growth revealed by autonomous profilers. *Science Advances*, *6*(39), 1–10. https://doi.org/10.1126/sciadv.abc2678

Rantanen, M., Karpechko, A. Y., Lipponen, A., Nordling, K., Hyvärinen, O., Ruosteenoja, K., Vihma, T., & Laaksonen, A. (2022). The Arctic has warmed nearly four times faster than the globe since 1979. *Communications Earth and Environment*, *3*(1), 1–10. https://doi.org/10.1038/s43247-022-00498-3

Reda, I., & Andreas, A. (2004). Solar position algorithm for solar radiation applications. *Solar Energy*, *76*(5), 577–589. https://doi.org/10.1016/j.solener.2003.12.003

Rhodes. (2019). Skyfield: High precision research-grade positions for planets and Earth satellites generator. *Astrophysics Source Code Library*. https://doi.org/.

Ricker, R., Hendricks, S., Kaleschke, L., Tian-Kunze, X., King, J., & Haas, C. (2017). A weekly Arctic sea-ice thickness data record from merged CryoSat-2 and SMOS satellite data. *Cryosphere*, *11*(4), 1607–1623. https://doi.org/10.5194/tc-11-1607-2017

Ronneberger, O., Fischer, P., & Brox, T. (2015). U-Net: Convolutional Networks for Biomedical Image Segmentation. https://doi.org/10.1007/978-3-319-24574-4_28

Rösel, A., Kaleschke, L., & Birnbaum, G. (2012). Melt ponds on Arctic sea ice determined from MODIS satellite data using an artificial neural network. *Cryosphere*, *6*(2), 431–446. https://doi.org/10.5194/tc-6-431-2012

Rösel, A., Itkin, P., King, J., Divine, D., Wang, C., Granskog, M. A., Krumpen, T., & Gerland, S. (2018). Thin Sea Ice, Thick Snow, and Widespread Negative Freeboard Observed During N-ICE2015 North of Svalbard. *Journal of Geophysical Research: Oceans*, *123*(2), 1156–1176. https://doi.org/10.1002/2017JC012865

Rösel, A., & Kaleschke, L. (2011). Comparison of different retrieval techniques for melt ponds on Arctic sea ice from Landsat and MODIS satellite data. *Annals of Glaciology*, *52*(57 PART 2), 185–191. https://doi.org/10.3189/172756411795931606

Röttgers, R., & Doerffer, R. (2007). Measurements of optical absorption by chromophoric dissolved organic matter using a point-source integrating-cavity absorption meter.

Limnology and Oceanography: Methods, *5*(MAY), 126–135. https://doi.org/10.4319/lom.2007.5.126

Röttgers, R., McKee, D., & Utschig, C. (2014). Temperature and salinity correction coefficients for light absorption by water in the visible to infrared spectral region. *Optics Express*, *22*(21), 25093. https://doi.org/10.1364/oe.22.025093

Rouse, W. R. (1987). Examples of Enhanced Global Solar Radiation Through Multiple Reflection from an Ice-Covered Arctic Sea. *Journal of Climate and Applied Meteorology*, *26*(6), 670–674. https://doi.org/10.1175/1520-0450(1987)026<0670:EOEGSR>2.0.CO;2

Rousso, B. Z., Bertone, E., Stewart, R. A., Rinke, K., & Hamilton, D. P. (2021). Light-induced fluorescence quenching leads to errors in sensor measurements of phytoplankton chlorophyll and phycocyanin. *Water Research*, *198*, 117133. https://doi.org/10.1016/j.watres.2021.117133

Roy, R., Pratihary, A., Mangesh, G., & Naqvi, S. W. (2006). Spatial variation of phytoplankton pigments along the southwest coast of India. *Estuarine, Coastal and Shelf Science*, *69*(1-2), 189–195. https://doi.org/10.1016/j.ecss.2006.04.006

Rozwadowska, A., & Górecka, I. (2012). The impact of a non-uniform land surface on the radiation environment over an Arctic fjord - A study with a 3D radiative transfer model for stratus clouds over the Hornsund fjord, Spitsbergen. *Oceanologia*, *54*(4), 509–544. https://doi.org/10.5697/oc.54-4.509

Rozwadowska, A., & Górecka, I. (2017). Impact of reflecting land surface on radiation environment over Hornsund, Spitsbergen - A model study for cloudless skies. *Polish Polar Research*, *38*(2), 149–174. https://doi.org/10.1515/popore-2017-0008

Saba, V. S., Friedrichs, M. A., Antoine, D., Armstrong, R. A., Asanuma, I., Behrenfeld, M. J., Ciotti, A. M., Dowell, M., Hoepffner, N., Hyde, K. J., Ishizaka, J., Kameda, T., Marra, J., Mlin, F., Morel, A., O'Reilly, J., Scardi, M., Smith, W. O., Smyth, T. J., … Westberry, T. K. (2011). An evaluation of ocean color model estimates of marine primary productivity in coastal and pelagic regions across the globe. *Biogeosciences*, *8*(2), 489–503. https://doi.org/10.5194/bg-8-489-2011

Sabine, C. L., Feely, R. A., Gruber, N., Key, R. M., Lee, K., Bullister, J. L., Wanninkhof, R., Wong, C. S., R Wallace, D. W., Tilbrook, B., Millero, F. J., Peng, T.-H., Kozyr, A., & Ono, T. (2004). The Oceanic Sink for Anthropogenic CO 2 Author(s). *Rios Source: Science, New Series*, *305*(5682), 367–371.

Sallila, H., Farrell, S. L., McCurry, J., & Rinne, E. (2019). Assessment of contemporary satellite sea ice thickness products for Arctic sea ice. *Cryosphere*, *13*(4), 1187–1213. https://doi.org/10.5194/tc-13-1187-2019

Sathyendranath, S., & Platt, T. (1988). The spectral irradiance field at the surface and in the interior of the ocean: a model for applications in oceanography and remote sensing. *Journal of Geophysical Research*, *93 C*(8), 9270–9280. https://doi.org/10.1029/jc093ic08p09270

Sathyendranath, S., Platt, T., Caverhill, C. M., Warnock, R. E., & Lewis, M. R. (1989). Remote sensing of oceanic primary production: computations using a spectral model. *Deep Sea Research Part A, Oceanographic Research Papers*, *36*(3), 431–453. https://doi.org/10.1016/0198-0149(89)90046-0

Schäfer, B., Carlsen, T., Hanssen, I., Gausa, M., & Storelvmo, T. (2022). Observations of cold-cloud properties in the Norwegian Arctic using ground-based and spaceborne lidar. *Atmospheric Chemistry and Physics*, *22*(14), 9537–9551. https://doi.org/10.5194/acp-22-9537-2022

Schneider, S. H., & Dickinson, R. E. (1976). Parameterization of Fractional Cloud Amounts in Climatic Models: The Importance of Modeling Multiple Reflections. *Journal of Applied Meteorology*, *15*(10), 1050–1056. https://doi.org/10.1175/1520-0450(1976)015<1050:POFCAI>2.0.CO;2

Schweiger, A. J. (2004). Changes in seasonal cloud cover over the Arctic seas from satellite and surface observations. *Geophysical Research Letters*, *31*(12), 1–5. https://doi.org/10.1029/2004GL020067

Serreze, M. C., & Stroeve, J. (2015). Arctic sea ice trends, variability and implications for seasonal ice forecasting. *Philosophical Transactions of the Royal Society A: Mathematical, Physical and Engineering Sciences*, *373*(2045). https://doi.org/10.1098/rsta.2014.0159

Shiozaki, T., Ito, S. I., Takahashi, K., Saito, H., Nagata, T., & Furuya, K. (2014). Regional variability of factors controlling the onset timing and magnitude of spring algal blooms in the northwestern North Pacific. *Journal of Geophysical Research: Oceans*, *119*(1), 253–265. https://doi.org/10.1002/2013JC009187

Shkuratov, Y., Starukhina, L., Hoffmann, H., & Arnold, G. (1999). A Model of Spectral Albedo of Particulate Surfaces: Implications for Optical Properties of the Moon. *Icarus*, *137*(2), 235–246. https://doi.org/10.1006/icar.1998.6035

Provides spectral albedo of ”average moon” from satellite based observations and lab measurements of lunar soils.

Simon, N., Cras, A. L., Foulon, E., & Lemée, R. (2009). Diversity and evolution of marine phytoplankton. *Comptes Rendus - Biologies*, *332*(2-3), 159–170. https://doi.org/10.1016/j.crvi.2008.09.009

Sloughter, T. M., Banas, N. S., & Sambrotto, R. N. (2019). Seasonal variation in light response of polar phytoplankton. *Journal of Marine Systems*, *191*(December 2018), 64–75. https://doi.org/10.1016/j.jmarsys.2018.12.003

Smith, M. M., Light, B., Macfarlane, A. R., Perovich, D. K., Holland, M. M., & Shupe, M. D. (2022). Sensitivity of the Arctic Sea Ice Cover to the Summer Surface Scattering Layer. *Geophysical Research Letters*, *49*(9). https://doi.org/10.1029/2022GL098349

Smith, T., & Guild, J. (1931). The C.I.E. colorimetric standards and their use. *Transactions of the Optical Society*, *33*(3), 73–134. https://doi.org/10.1088/1475-4878/33/3/301

Smyth, T. J., Tilstone, G. H., & Groom, S. B. (2005). Integration of radiative transfer into satellite models of ocean primary production. *Journal of Geophysical Research C: Oceans*, *110*(10), 1–11. https://doi.org/10.1029/2004JC002784

Spitschan, M., Aguirre, G. K., Brainard, D. H., & Sweeney, A. M. (2016). Variation of outdoor illumination as a function of solar elevation and light pollution. *Scientific Reports*, *6*, 1–14. https://doi.org/10.1038/srep26756

Spreen, G., Kwok, R., & Menemenlis, D. (2011). Trends in Arctic sea ice drift and role of wind forcing: 1992-2009. *Geophysical Research Letters*, *38*(19), 1–6. https://doi.org/10.1029/2011GL048970

Stedmon, C. A., Amon, R. M., Rinehart, A. J., & Walker, S. A. (2011). The supply and characteristics of colored dissolved organic matter (CDOM) in the Arctic Ocean: Pan Arctic trends and differences. *Marine Chemistry*, *124*(1-4), 108–118. https://doi.org/10.1016/j.marchem.2010.12.007

Steinberg, D. K., & Landry, M. R. (2017). Zooplankton and the Ocean Carbon Cycle. *Annual Review of Marine Science*, *9*(1), 413–444. https://doi.org/10.1146/annurev-marine-010814-015924

Stillinger, T., Roberts, D. A., Collar, N. M., & Dozier, J. (2019). Cloud Masking for Landsat 8 and MODIS Terra Over Snow-Covered Terrain: Error Analysis and Spectral Similarity Between Snow and Cloud. *Water Resources Research*, *55*(7), 6169–6184. https://doi.org/10.1029/2019WR024932

Stramski, D., Babin, M., & Woźniak, S. B. (2007). Variations in the optical properties of terrigenous mineral-rich particulate matter suspended in seawater. *Limnology and Oceanography*, *52*(6), 2418–2433. https://doi.org/10.4319/lo.2007.52.6.2418

Stroeve, J., Barrett, A., Serreze, M., & Schweiger, A. (2014a). Using records from submarine, aircraft and satellites to evaluate climate model simulations of Arctic sea ice thickness. *Cryosphere*, *8*(5), 1839–1854. https://doi.org/10.5194/tc-8-1839-2014

Stroeve, J., Kattsov, V., Barrett, A., Serreze, M., Pavlova, T., Holland, M., & Meier, W. N. (2012). Trends in Arctic sea ice extent from CMIP5, CMIP3 and observations. *Geophysical Research Letters*, *39*(16), 1–7. https://doi.org/10.1029/2012GL052676

Stroeve, J., Liston, G. E., Buzzard, S., Zhou, L., Mallett, R., Barrett, A., Tschudi, M., Tsamados, M., Itkin, P., & Stewart, J. S. (2020). A Lagrangian Snow Evolution System for Sea Ice Applications (SnowModel-LG): Part II—Analyses. *Journal of Geophysical Research: Oceans*, *125*(10). https://doi.org/10.1029/2019JC015900

Stroeve, J., Markus, T., Boisvert, L., Miller, J., & Barrett, A. (2014b). Changes in Arctic melt season and implications for sea ice loss. *Geophysical Research Letters*, *41*(4), 1216–1225. https://doi.org/10.1002/2013GL058951

Stroeve, J., & Notz, D. (2018). Changing state of Arctic sea ice across all seasons. *Environmental Research Letters*, *13*(10). https://doi.org/10.1088/1748-9326/aade56

Stroeve, J., Serreze, M., Drobot, S., Gearheard, S., Holland, M., Maslanik, J., Meier, W., & Scambos, T. (2008). Arctic sea ice extent plummets in 2007. *Eos*, *89*(2), 13–14. https://doi.org/10.1029/2008EO020001

Stroeve, J., Vancoppenolle, M., Veyssiere, G., Lebrun, M., Castellani, G., Babin, M., Karcher, M., Landy, J., Liston, G. E., & Wilkinson, J. (2021). A Multi-Sensor and Modeling Approach for Mapping Light Under Sea Ice During the Ice-Growth Season. *Frontiers in Marine Science*, *7*(February), 1–28. https://doi.org/10.3389/fmars.2020.592337

Summers, N., Berge, J., Johnsen, G., Mogstad, A., Lovas, H., & Fragoso, G. (2022). Underwater Hyperspectral Imaging of Arctic Macroalgal Habitats during the Polar Night Using a Novel Mini-ROV-UHI Portable System. *Remote Sensing*, *14*(1325).

Taylor, P. C., Cai, M., Hu, A., Meehl, J., Washington, W., & Zhang, G. J. (2013). A decomposition of feedback contributions to polar warming amplification. *Journal of Climate*, *26*(18), 7023–7043. https://doi.org/10.1175/JCLI-D-12-00696.1

Tedesco, L., Vichi, M., & Scoccimarro, E. (2019). Sea-ice algal phenology in a warmer Arctic. *Science Advances*, *5*(5). https://doi.org/10.1126/sciadv.aav4830

Tilling, R., Kurtz, N. T., Bagnardi, M., Petty, A. A., & Kwok, R. (2020). Detection of Melt Ponds on Arctic Summer Sea Ice From ICESat-2. *Geophysical Research Letters*, *47*(23), 1–10. https://doi.org/10.1029/2020GL090644

Timco, G. W., & Frederking, R. M. (1996). A review of sea ice density. *Cold Regions Science and Technology*, *24*(1), 1–6. https://doi.org/10.1016/0165-232X(95)00007-X

Urmy, S. S., Horne, J. K., & Barbee, D. H. (2012). Measuring the vertical distributional variability of pelagic fauna in Monterey Bay. *ICES Journal of Marine Science*, *69*(2), 184–196. https://doi.org/10.1093/icesjms/fsr205

Uttal, T., Curry, J. A., Mcphee, M. G., Perovich, D. K., Moritz, R. E., Maslanik, J. A., Guest, P. S., Stern, H. L., Moore, J. A., Turenne, R., Heiberg, A., Serreze, M. C., Wylie, D. P., Persson, O. G., Paulson, C. A., Halle, C., Morison, J. H., Wheeler, P. A., Makshtas, A., … Grenfeld, T. C. (2002). Surface Heat Budget of the Arctic Ocean. *Bulletin of the American Meteorological Society*, *83*(2), 255–275. https://doi.org/10.1175/1520-0477(2002)083<0255:SHBOTA>2.3.CO;2

Vernet, M., Ellingsen, I., Marchese, C., Simon, B., Cape, M., Slagstad, D., & Matrai, P. A. (2021). Progress in Oceanography Spatial variability in rates of net primary production (NPP) and onset of the spring bloom in Greenland shelf waters. *198*(July).

Veyssière, G., Castellani, G., Wilkinson, J., Karcher, M., Hayward, A., Stroeve, J. C., Nicolaus, M., Kim, J.-H., Yang, E.-J., Valcic, L., Kauker, F., Khan, A. L., Rogers, I., & Jung, J. (2022). Under-Ice Light Field in the Western Arctic Ocean During

Late Summer. *Frontiers in Earth Science*, *9*(February), 1–19. https://doi.org/10.3389/feart.2021.643737

Wang, X., Key, J., Kwok, R., & Zhang, J. (2016). Comparison of Arctic sea ice thickness from satellites, aircraft, and PIOMAS data. *Remote Sensing*, *8*(9), 1–17. https://doi.org/10.3390/rs8090713

Wang, X., & Key, J. R. (2005). Arctic surface, cloud, and radiation properties based on the AVHRR polar pathfinder dataset. Part II: Recent trends. *Journal of Climate*, *18*(14), 2575–2593. https://doi.org/10.1175/JCLI3439.1

Wang, Y., Bi, H., Huang, H., Liu, Y., Liu, Y., Liang, X., Fu, M., & Zhang, Z. (2019). Satellite-observed trends in the Arctic sea ice concentration for the period 1979–2016. *Journal of Oceanology and Limnology*, *37*(1), 18–37. https://doi.org/10.1007/s00343-019-7284-0

Warren, S. G. (2019). Optical properties of ice and snow. *Philosophical Transactions of the Royal Society A: Mathematical, Physical and Engineering Sciences*, *377*(2146). https://doi.org/10.1098/rsta.2018.0161

Warren, S. G., Rigor, I. G., Untersteiner, N., Radionov, V. F., Bryazgin, N. N., Aleksandrov, Y. I., & Colony, R. (1999). Snow depth on Arctic sea ice. *Journal of Climate*, *12*(6), 1814–1829. https://doi.org/10.1175/1520-0442(1999)012<1814:SDOASI>2.0.CO;2

Warren, S. G., & Wiscombe, W. J. (1980). A Model for the Spectral Albedo of Snow. II: Snow Containing Atmospheric Aerosols. *Journal of the Atmospheric Sciences*, *37*(12), 2734–2745. https://doi.org/10.1175/1520-0469(1980)037<2734:AMFTSA>2.0.CO;2

Wassmann, P., Slagstad, D., Riser, C. W., & Reigstad, M. (2006). Modelling the ecosystem dynamics of the Barents Sea including the marginal ice zone II . Carbon flux and interannual variability. *59*(1-2), 1–24. https://doi.org/https://doi.org/10.1016/j.jmarsys.2005.05.006

Wei, T., Yan, Q., Qi, W., Ding, M., & Wang, C. (2020). Projections of Arctic sea ice conditions and shipping routes in the twenty-first century using CMIP6 forcing scenarios. *Environmental Research Letters*, *15*(10). https://doi.org/10.1088/1748-9326/abb2c8

Wendler, G., Eaton, F. D., & Ohtake, T. (1981). Multiple reflection effects on irradiance in the presence of Arctic stratus clouds (Barrow, Alaska). *Journal of Geophysical Research*, *86*(C3), 2049–2057. https://doi.org/10.1029/JC086iC03p02049

Wendler, G., Moore, B., Hartmann, B., Stuefer, M., & Flint, R. (2004). Effects of multiple reflection and albedo on the net radiation in the pack ice zones of Antarctica. *Journal of Geophysical Research: Atmospheres*, *109*(6), 1–8. https://doi.org/10.1029/2003jd003927

Werdell, P. J., McKinna, L. I., Boss, E., Ackleson, S. G., Craig, S. E., Gregg, W. W., Lee, Z., Maritorena, S., Roesler, C. S., Rousseaux, C. S., Stramski, D., Sullivan, J. M., Twardowski, M. S., Tzortziou, M., & Zhang, X. (2018). An overview of approaches and challenges for retrieving marine inherent optical properties from ocean color remote sensing. *Progress in Oceanography*, *160*(October 2017), 186–212. https://doi.org/10.1016/j.pocean.2018.01.001

Westberry, T., Behrenfeld, M. J., Siegel, D. A., & Boss, E. (2008). Carbon-based primary productivity modeling with vertically resolved photoacclimation. *Global Biogeochemical Cycles*, *22*(2), 1–18. https://doi.org/10.1029/2007GB003078

Williamson, C. E., Fischer, J. M., Bollens, S. M., Overholt, E. P., & Breckenridgec, J. K. (2011). Toward a more comprehensive theory of zooplankton diel vertical migration: Integrating ultraviolet radiation and water transparency into the biotic paradigm. *Limnology and Oceanography*, *56*(5), 1603–1623. https://doi.org/10.4319/lo.2011.56.5.1603

Winder, M., & Sommer, U. (2012). Phytoplankton response to a changing climate. *Hydrobiologia*, *698*(1), 5–16. https://doi.org/10.1007/s10750-012-1149-2

Xie, W., Liu, D., Yang, M., Chen, S., Wang, B., Wang, Z., Xia, Y., Liu, Y., Wang, Y., & Zhang, C. (2020). SegCloud: A novel cloud image segmentation model using a deep convolutional neural network for ground-based all-sky-view camera observation. *Atmospheric Measurement Techniques*, *13*(4), 1953–1961. https://doi.org/10.5194/amt-13-1953-2020

Xie, Y., & Liu, Y. (2013). A new approach for simultaneously retrieving cloud albedo and cloud fraction from surface-based shortwave radiation measurements. *Environmental Research Letters*, *8*(4). https://doi.org/10.1088/1748-9326/8/4/044023

Zhang, J., Liu, P., Zhang, F., & Song, Q. (2018). CloudNet: Ground-Based Cloud Classification With Deep Convolutional Neural Network. *Geophysical Research Letters*, *45*(16), 8665–8672. https://doi.org/10.1029/2018GL077787

Zhang, J., & Rothrock, D. A. (2003). Modeling global sea ice with a thickness and enthalpy distribution model in generalized curvilinear coordinates. *Monthly Weather Review*, *131*(5), 845–861. https://doi.org/10.1175/1520-0493(2003)131<0845:MGSIWA>2.0.CO;2

Zhang, J., Spitz, Y. H., Steele, M., Ashjian, C., Campbell, R., Berline, L., & Matrai, P. (2010). Modeling the impact of declining sea ice on the Arctic marine planktonic ecosystem. *115*(10), 1–24. https://doi.org/10.1029/2009JC005387

Zhang, X., Hu, L., & He, M.-X. (2009). Scattering by pure seawater: Effect of salinity. *Optics Express*, *17*(7), 5698. https://doi.org/10.1364/oe.17.005698

Zhou, L., Stroeve, J., Xu, S., Petty, A., Tilling, R., Winstrup, M., Rostosky, P., Lawrence, I. R., Liston, G. E., Ridout, A., Tsamados, M., & Nandan, V. (2021). Intercomparison of snow depth over Arctic sea ice from reanalysis reconstructions and satellite retrieval. *Cryosphere*, *15*(1), 345–367. https://doi.org/10.5194/tc-15-345-2021